frontiers | Research Topics

Insights in microbiological chemistry and geomicrobiology 2022/2023

Edited by
Ruiyong Zhang

Published in
Frontiers in Microbiology

ISSN 1664-8714
ISBN 978-2-8325-5231-5
DOI 10.3389/978-2-8325-5231-5

About Frontiers

Frontiers is more than just an open access publisher of scholarly articles: it is a pioneering approach to the world of academia, radically improving the way scholarly research is managed. The grand vision of Frontiers is a world where all people have an equal opportunity to seek, share and generate knowledge. Frontiers provides immediate and permanent online open access to all its publications, but this alone is not enough to realize our grand goals.

Frontiers journal series

The Frontiers journal series is a multi-tier and interdisciplinary set of open-access, online journals, promising a paradigm shift from the current review, selection and dissemination processes in academic publishing. All Frontiers journals are driven by researchers for researchers; therefore, they constitute a service to the scholarly community. At the same time, the *Frontiers journal series* operates on a revolutionary invention, the tiered publishing system, initially addressing specific communities of scholars, and gradually climbing up to broader public understanding, thus serving the interests of the lay society, too.

Dedication to quality

Each Frontiers article is a landmark of the highest quality, thanks to genuinely collaborative interactions between authors and review editors, who include some of the world's best academicians. Research must be certified by peers before entering a stream of knowledge that may eventually reach the public - and shape society; therefore, Frontiers only applies the most rigorous and unbiased reviews. Frontiers revolutionizes research publishing by freely delivering the most outstanding research, evaluated with no bias from both the academic and social point of view. By applying the most advanced information technologies, Frontiers is catapulting scholarly publishing into a new generation.

What are Frontiers Research Topics?

Frontiers Research Topics are very popular trademarks of the *Frontiers journals series*: they are collections of at least ten articles, all centered on a particular subject. With their unique mix of varied contributions from Original Research to Review Articles, Frontiers Research Topics unify the most influential researchers, the latest key findings and historical advances in a hot research area.

Find out more on how to host your own Frontiers Research Topic or contribute to one as an author by contacting the Frontiers editorial office: frontiersin.org/about/contact

Insights in microbiological chemistry and geomicrobiology: 2022/2023

Topic editor
Ruiyong Zhang — Institute of Oceanology, Chinese Academy of Sciences (CAS), China

Citation
Zhang, R., ed. (2024). *Insights in microbiological chemistry and geomicrobiology: 2022/2023*. Lausanne: Frontiers Media SA. doi: 10.3389/978-2-8325-5231-5

Table of contents

frontiers | Frontiers in Microbiology

TYPE Editorial
PUBLISHED 17 July 2024
DOI 10.3389/fmicb.2024.1446765

OPEN ACCESS

EDITED AND REVIEWED BY
David Emerson,
Bigelow Laboratory for Ocean Sciences, United States

*CORRESPONDENCE
Ruiyong Zhang
ruiyong.zhang@qdio.ac.cn

RECEIVED 10 June 2024
ACCEPTED 01 July 2024
PUBLISHED 17 July 2024

CITATION
Zhang R (2024) Editorial: Insights in microbiological chemistry and geomicrobiology: 2022/2023. *Front. Microbiol.* 15:1446765. doi: 10.3389/fmicb.2024.1446765

Editorial: Insights in microbiological chemistry and geomicrobiology: 2022/2023

Ruiyong Zhang[1,2]*

[1]Key Laboratory of Advanced Marine Materials, Key Laboratory of Marine Environmental Corrosion and Bio-Fouling, Institute of Oceanology, Chinese Academy of Sciences, Qingdao, China, [2]Guangxi Key Laboratory of Marine Environmental Science, Institute of Marine Corrosion Protection, Guangxi Academy of Sciences, Nanning, China

KEYWORDS

extreme microbiology, microbial communities, biodegradation, geomicrobiology, biogeochemistry

Editorial on the Research Topic
Insights in microbiological chemistry and geomicrobiology: 2022/2023

Microbes are crucial in balancing and improving environmental systems in the lithosphere, hydrosphere, biosphere, and atmosphere, by shaping the surrounding geochemical and mineralogical components through their metabolic action (Druschel and Kappler, 2015). Further, the growth and metabolic activities of microbial communities are generally dictated by the surrounding environmental systems (Diener and Gibbons, 2023; Yang et al., 2023). Changes in the geochemical and mineralogical components of environmental systems, influenced by natural and anthropogenic activities, may affect the microbial communities. In particular, the resistance and adaptive ability of microbial communities to extreme conditions through diverse physiological and molecular functions have become crucial in mitigating and restoring ecosystems (Shade, 2023; Caro-Astorga et al., 2024; Song et al., 2024; Turrini et al., 2024). Exploring the interactions between microbial communities and geochemical components and other biota of different ecosystems, as well as uncovering the secrets hidden in them, is an ideal way to identify and solve problems in ecosystem management. This *Research Topic* "*Insights in microbiological chemistry and geomicrobiology: 2022/2023*" includes ten papers connected to the microbial community structure and assembly, physiological and molecular adaptive strategies to various extreme environments, and biogeochemical cycling role of the microbial community.

It is noteworthy that the composition and association of microbial communities are mainly affected by contaminants in ecosystems. Zhang W. et al. studied the diversity and composition of microbial communities in sediment and soil samples of heavily polluted estuarine karst environment and revealed that diversity, abundance, and structure of microbial communities are governed by the concentrations of organic pollutants [polycyclic aromatic hydrocarbons (PAHs) and hazardous trace elements (HTEs)] present in the estuarine environment. The variations in diversity and assembly of bacterial and fungal communities that respond to environmental factors at different altitudes and depths of mountain ecosystems were observed by Kang et al.. Their study revealed that the distribution of bacterial and fungal communities at soil depth varied and their assembly process was significantly related to DOC and C:N ratio of soil. For instance, bacterial community assembly processes were related to soil DOC and C:N ratio, while fungal community assembly was related to soil C:N ratio.

The diversity and abundance of microbes in ecosystems are influenced by environmental factors that vary over time and seasonally. Changes in environmental factors due to seasonally changing weather conditions can have negative effects on microbial communities. Xu et al. investigated the composition and distribution of *Massilia* bacterial species in constructed wetland ecosystems in different seasons and found that the richness of *Massilia* bacteria varied significantly in different environments and different seasons, with a greater abundance of *Massilia* bacterial species observed in summer and autumn than in spring and winter. Also, their study revealed that seasonal variation of bacterial species in different compartments of constructed wetland ecosystems correlated with environmental factors.

Various positive (mutualism, symbiosis, commensalism, and proto-cooperation) and negative (predation, parasitism, competition, and ammensalism) interactions between microbial communities and other biotas (animals, plants, humans, etc.) are driven by various physiological and molecular processes, which play an important role in balancing the ecosystems. Feng et al. investigated the relationships between epibiotic bacterial communities with various species of deep-sea squat lobsters (*Shinkaia crosnieri* and *Munidopsis Verrilli*) from cold-seep ecosystems and revealed the differences in epibiotic bacterial communities among the lobster species. Also, this study reported that epibiotic bacterial communities on lobster species use chemical fluxes near cold seeps in more efficient ways, which benefits the host's nutrient strategies.

Adaptation and resistance of microbial communities to extreme conditions through various internal and external processes are important in the environmental management and the bio-metallurgical field. In particular, the detoxification capability of indigenous microbial communities against organic and inorganic contaminants has attracted significant attention in the remediation of contaminated environments. Understanding the interactions and detoxification mechanisms of microbial communities on contaminants can help improve microbial bioremediation technology for environmental restoration. da Silva et al. studied the microbial action on reduction and oxidation of iron in hematite and goethite with four different treatment systems and found biofilm formation by microbes alters the levels of iron oxyhydroxides precipitation. Furthermore, their research found that iron-reducing families such as Enterobacteriaceae dominated the treatment samples. Their research results suggested that the ability of microbes to dissolve iron could help reduce the environmental effects of the iron mining industry and thereby restore the ecosystem. Shi et al. observed that glutathione reductase (GR) plays a key role in *Acidithiobacillus caldus* defense against reactive oxygen species caused by heavy metals.

Hydrothermal vent systems offer habitats that support microbial life due to their diverse chemical energy sources and steep physical and chemical gradients. Investigating the structure of microbial communities and their interaction with the physical and chemical gradients of hydrothermal vent systems helps to understand the biochemical cycling role of microbial communities in terrestrial and marine ecosystems. Nakano et al. used metagenomic analysis to identify magentosome-producing microorganisms, as well as mineralogical and geochemical studies to understand their role at deep-sea hydrothermal vent chimney samples from the South Mariana Trough. It is necessary to develop techniques to study microbial progress in the environment. Yin et al. developed a method of in situ and quantitative gas (methane) detection using Raman spectroscopy. This technology may be a powerful complementary tool to gas chromatography for monitoring microbiological progresses.

To verify whether the isotopic ratio in cell water is controlled by metabolic water produced by cellular respiration, Weiner et al. conducted experiments with varying the $\delta^{18}O$ and by measuring the $\delta^{18}O$ of cell phosphate. The authors provide evidence to show that the deviation from isotopic equilibrium between the ambient water and the oxygen in phosphate is not derived from the contribution of metabolic water to the cell water.

Lastly, a mini review article of this Research Topic touches the hot spot of research dealing with nuclear waste storage. Zhang Q. et al. proposed a method to prevent hydrogen embrittlement via reduce of hydrogen by the induced hydrogen consuming microorganisms. Nevertheless, more work has to be conducted to test the efficiency of this approach.

It is crucial from an ecological perspective to comprehend the diversity, structure, and assembly of microbial communities in ecosystems, as well as their interactions with one another. Environmental restoration by microbial communities requires knowledge of the resistance and adaptive strategies of microbial communities to inorganic and organic contaminants in ecosystems, their interaction, and the detoxification mechanism. The metal solubilizing and adsorbing properties of microbial communities can be sustainable and efficient in the extraction of metals from solid materials (ores and e-waste) in the metallurgical industry and environmental remediation (Amendola and Acharjee, 2022; Ayilara and Babalola, 2023; Pakostova et al., 2024). Therefore, studies related to the enhancement of metal solubilization and metal absorption capacity of microbial communities are highly needed. Efficient use of microbial communities for environmental management and the metallurgical industry requires in-depth knowledge of the interaction between environmental systems and microbial communities, the role of microbes in environmental management, and the interaction of microbes with the geochemical and mineralogical components of ecosystems.

Author contributions

RZ: Writing – original draft, Writing – review & editing.

Funding

The author(s) declare that no financial support was received for the research, authorship, and/or publication of this article.

Acknowledgments

The author thanks the peer-review experts for their insightful comments and suggestions. Katrin Ansorge is acknowledged for her assistance with this Research Topic.

Conflict of interest

The author declares that the research was conducted in the absence of any commercial or financial relationships that could be construed as a potential conflict of interest.

The author(s) declared that they were an editorial board member of Frontiers, at the time of submission. This had no impact on the peer review process and the final decision.

Publisher's note

References

Amendola, R., and Acharjee, A. (2022). Microbiologically influenced corrosion of copper and its alloys in anaerobic aqueous environments: a review. *Front. Microbiol.* 13:806688. doi: 10.3389/fmicb.2022.806688

Ayilara, M. S., and Babalola, O. O. (2023). Bioremediation of environmental wastes: the role of microorganisms. *Front. Agron.* 5:1183691. doi: 10.3389/fagro.2023.1183691

Caro-Astorga, J., Meyerowitz, J. T., Stork, D. A., Nattermann, U., Piszkiewicz, S., Vimercati, L., et al. (2024). Polyextremophile engineering: a review of organisms that push the limits of life. *Front. Microbiol.* 15:1341701. doi: 10.3389/fmicb.2024.1341701

Diener, C., and Gibbons, S. M. (2023). More is different: metabolic modeling of diverse microbial communities. *mSystems* 8, e01270–e01222. doi: 10.1128/msystems.01270-22

Druschel, G. K., and Kappler, A. (2015). Geomicrobiology and microbial geochemistry. *Elements* 11, 389–394. doi: 10.2113/gselements.11.6.389

Pakostova, E., Falagan, C., and Zhang, R. (2024). "The geomicrobiology of biomining," in *Geomicrobiology: Natural and Anthropogenic Settings*, eds. L. C. Staicu, and L. L. Barton (Cham: Springer), 171–194.

Shade, A. (2023). Microbiome rescue: directing resilience of environmental microbial communities. *Curr. Opin. Microbiol.* 72:102263. doi: 10.1016/j.mib.2022.102263

Song, A., Liang, S., Li, H., and Yan, B. (2024). Effects of biodiversity on functional stability of freshwater wetlands: a systematic review. *Front. Microbiol.* 15:1397683. doi: 10.3389/fmicb.2024.1397683

Turrini, P., Chebbi, A., Riggio, F. P., and Visca, P. (2024). The geomicrobiology of limestone, sulfuric acid speleogenetic, and volcanic caves: basic concepts and future perspectives. *Front. Agron.* 15:1370520. doi: 10.3389/fmicb.2024.1370520

Yang, P. F., Spanier, N., Aldredge, P., Shahid, N., Coleman, A., Lyons, J., et al. (2023). Will free-living microbial community composition drive biogeochemical responses to global change? *Biogeochemistry* 162, 285–307. doi: 10.1007/s10533-023-01015-0

frontiers | Frontiers in Microbiology

TYPE Original Research
PUBLISHED 09 February 2023
DOI 10.3389/fmicb.2023.1126612

OPEN ACCESS

EDITED BY
Ruiyong Zhang,
Institute of Oceanology (CAS), China

REVIEWED BY
Artur Banach,
The John Paul II Catholic University of Lublin, Poland
Hongchang Liu,
Central South University, China

*CORRESPONDENCE
Zaixing Huang
✉ zhuang@uwyo.edu
Gordana Medunić
✉ gordana.medunic@geol.pmf.hr
Huan He
✉ hehuan6819@cumt.edu.cn

SPECIALTY SECTION
This article was submitted to Microbiological Chemistry and Geomicrobiology, a section of the journal Frontiers in Microbiology

RECEIVED 18 December 2022
ACCEPTED 23 January 2023
PUBLISHED 09 February 2023

CITATION
Zhang W, Mo Q, Huang Z, Sabar MA, Medunić G, Ivošević T, He H, Urynowicz M, Liu F-J, Guo H, Haider R, Ali MI and Jamal A (2023) Contaminants from a former Croatian coal sludge dictate the structure of microbiota in the estuarine (Raša Bay) sediment and soil. *Front. Microbiol.* 14:1126612. doi: 10.3389/fmicb.2023.1126612

Contaminants from a former Croatian coal sludge dictate the structure of microbiota in the estuarine (Raša Bay) sediment and soil

Weiting Zhang[1], Qianyun Mo[1], Zaixing Huang[1,2]*, Muhammad Adnan Sabar[3], Gordana Medunić[4]*, Tatjana Ivošević[5], Huan He[1]*, Michael Urynowicz[2], Fang-Jing Liu[1], Hongguang Guo[6], Rizwan Haider[7], Muhammad Ishtiaq Ali[8] and Asif Jamal[8]

[1]Key Laboratory of Coal Processing and Efficient Utilization of Ministry of Education, School of Chemical Engineering and Technology, China University of Mining and Technology, Xuzhou, China, [2]Department of Civil and Architectural Engineering, University of Wyoming, Laramie, WY, United States, [3]Environmental Risk Control Engineering Laboratory, Division of Environmental Design, Kanazawa University, Kanazawa, Japan, [4]Department of Geology, Faculty of Science, University of Zagreb, Zagreb, Croatia, [5]Faculty of Maritime Studies, University of Rijeka, Rijeka, Croatia, [6]College of Safety and Emergency Management and Engineering, Taiyuan University of Technology, Taiyuan, China, [7]Institute of Energy & Environmental Engineering, University of the Punjab, Lahore, Pakistan, [8]Department of Microbiology, Quaid-i-Azam University, Islamabad, Pakistan

Introduction: Croatian superhigh-organic-sulfur Raša coal had been mined for nearly 400 years. The release of hazardous trace elements (HTEs) and toxic organic pollutants (TOPs) into the local environment by coal mining, preparation, and combustion activities has resulted in pollution.

Methods: In this study, the diversity and composition of microbial communities in estuarine sediment and soil samples as well as community function responses to the pollutants were investigated.

Results: The results showed that PAH degradation does occur following 60 years of natural attenuation, the location is still heavily polluted by polycyclic aromatic hydrocarbons (PAHs) and HTEs. Microbial analyses have shown that high concentrations of PAHs have reduced the diversity and abundance of microbial communities. The pollution exerted an adverse, long-term impact on the microbial community structure and function in the brackish aquatic ecosystem. Microorganisms associated with the degradation of PAHs and sulfur-containing compounds have been enriched although the diversity and abundance of the microbial community have reduced. Fungi which are believed to be the main PAH degrader may play an important role initially, but the activity remains lower thereafter. It is the high concentrations of coal-derived PAHs, rather than HTEs, that have reduced the diversity and abundance of microbial communities and shaped the structure of the local microbiota.

Discussion: This study could provide a basis for the monitoring and restoration of ecosystems impacted by coal mining activities considering the expected decommission of a large number of coal plants on a global scale in the coming years due to growing global climate change concerns.

KEYWORDS

Raša coal, microbial diversity, estuary, PAHs, hazardous trace elements, natural attenuation

1. Introduction

Coal is the second largest fuel accounting for ~30% of the world's total primary energy, with a consumption of 150 EJ in 2020 (BP, 2021). However, coal mining, processing, and combustion have led to the release of hazardous trace elements (HTEs) (e.g., chromium, selenium, molybdenum, vanadium) and toxic organic pollutants (TOPs, e.g., polycyclic aromatic hydrocarbons [PAHs], sulfur heterocycles, nitrogen heterocycles, oxygen heterocycles) into aquatic and terrestrial ecosystems, which may have a long-term impact on the local microflora. Studies have shown that elevated levels of HTEs and TOPs persist in the environment, accumulate in soils, sediments, and organisms, and deteriorate many inland and coastal aquatic environments; many are also potential human mutagens (Addink and Olie, 1995; Johnson, 1995; Nadal et al., 2004; Medunić et al., 2018, 2021; Yu et al., 2019; Fei et al., 2020; Zhang J. et al., 2020; Li, 2021; Li et al., 2021).

The reduction of microbial diversity in the local environments, due to the release of TOPs and HTEs from coal mining, processing, and combustion processes, has been well documented (Ma et al., 2016; Zhao et al., 2019; Hamidović et al., 2020). In addition, microbes capable of degrading PAHs [e.g., *Pseudomonas putida* (Ghiorse et al., 1995; Herrick et al., 1997), *Alphaproteobacteria*, *Betaproteobacteria*, *Cupriavidus*, *Luteimonas* (Ma et al., 2016)] and resistant/tolerant to HTEs [e.g., Proteobacteria, Firmicutes (Huang et al., 2019; Roth et al., 2019; Zhao et al., 2019), Acidobacteria, Bacteroidetes (Roth et al., 2019; Zhao et al., 2020)] have been found in coal-contaminated soils and sediments. While the effects of HTEs and TOPs on microorganisms in coal-contaminated environments have received considerable attention, the ecological consequences of the complex combined pollution associated with coal wastes on microbial assemblages in natural settings, especially aquatic environments, remain largely unknown.

Croatian superhigh-organic-sulfur (SHOS) Raša coal has a very long mining history of nearly 400 years (Medunić et al., 2019b). A Raša coal separation and washing facility (RCSW), situated within Raša Bay (**Figure 1**), was in operation till the 1960s. Although mining of Raša coal ceased on November 29, 1999, due to economic and construction difficulties, a total of about 40 Mt of coal has been excavated, while an estimate of more than 4 Mt of Raša coal remains underground (Medunić et al., 2020a). Studies have shown that Raša coal has SHOS content of up to 9-11%. Previous publications characterized the detrimental impacts of Raša coal on the local environment regarding elevated levels of HTEs (Se, U, Mo, and V in particular) and PAHs in local soil, crops, groundwater, surface water, and sediments (Medunić et al., 2016, 2020a,b, 2019a,b, 2021). However, the extent of the impact of the RCSW on downstream estuarine ecosystems including Raša Bay has remained unknown. In an effort to investigate these effects, soil and sediment samples were collected from the site where Raša coal sludge (wastewater from coal preparation) was disposed of directly into Raša Bay between the 1930s and 1960s, and thereafter remained abandoned. Downstream sediment samples were also collected for comparison. The objectives of this study were as follows: 1) to examine the composition of collected soil and sediment samples in terms of HTEs and PAHs; 2) to explore the long-term effects of the coal-derived contaminants on the structure and function of the microbial community of the local estuarine environment. The site provides a unique opportunity to get an insight into a microbial community structure in a karst aquatic ecosystem that has been affected by coal-derived pollutants following long-term (>60 years) natural attenuation processes.

2. Materials and methods

2.1. Study site and sampling

The study site is an estuarine karst environment that can be characterized by wetland features. It is located inside Raša Bay (**Figure 1**) belonging to the north part of the Adriatic Sea, in a Štalije settlement, coordinates of 45°02′50″N and 14°02′82″E. The area is characterized by hard carbonate bedrock overlain by reddish clay-loam cambic type of soil. The karst topography and residue of variable thickness from the weathering of carbonate strata typify the terrain. The study area has a Mediterranean type of climate, with mild humid winters (annual precipitation of 900–1000 mm), hot dry summers, and prevailing NE winds (the so-called bora) (Durn et al., 1999; Peh et al., 2010). Since the local area is composed mainly of highly vulnerable karst, its environmental quality should be carefully monitored (Medunić et al., 2020a).

The sampling campaign was carried out on October 5, 2021. Sediment and soil samples were collected from sites (No. 1–8) within some 500–700 m from the RCSW as indicated in **Figure 1**. Samples No. 1-7 were collected from surface soil and sediment (0-5 cm). The position of samples No. 6–8 corresponds to the site of former lagoons (a naturally shallow part of the estuary) that received coal sludge (coal processing wastewater) some 60-90 years ago. There, huge quantities of wastewater were stored and gradually filled up with coal and mud particles. Today, it is partly covered by grass and shrub vegetation. Samples No. 2–5 were collected downstream from the lagoon along Raša River. Sample No. 1 was collected from the estuary sediment located halfway between the local road and the coastline, partly wetland. Three samples with different depths were collected at site No. 8 with a stainless soil core sampler that was partly filled with groundwater. The samples were designated as No. 8-10, 8-20 and 8-30, corresponding to the depths of 15–20, 20–30, and 30–40 cm. Following the return to the lab, the samples were divided into two portions. One subset was stored at −80 °C for microbial DNA extraction. The other subset was air-dried, and then carefully packed in sterile bags for further analyses.

2.2. Analytical methods

2.2.1. Characterizations of soil and sediment samples

Water content, total organic carbon (TOC, dissolved), total nitrogen (TN), total sulfur (TS), total organic sulfur (TOS), and pH of the samples were determined. Briefly, the samples were dried at 105°C to determine the moisture. Any animal and plant residues, and stones were removed after drying. The samples were ground and passed through a 2-mm sieve. Then, the samples were mixed with DI water at a sample-to-water ratio of 1:5 (w/v) with continuous mixing for 4 h, and filtered with membrane filters (0.45 μm, F513132, Sangon Biotech Co. Ltd) prior to TOC and TN analyses (TOC-L TNM-L CSN, Shimadzu, Japan) (Jones and Willett, 2006; Li et al., 2017). TS and TOS were measured using an automatic sulfur meter (CTS3000, Xuzhou Terui Instrument and Equipment Co., Ltd., Xuzhou, China)

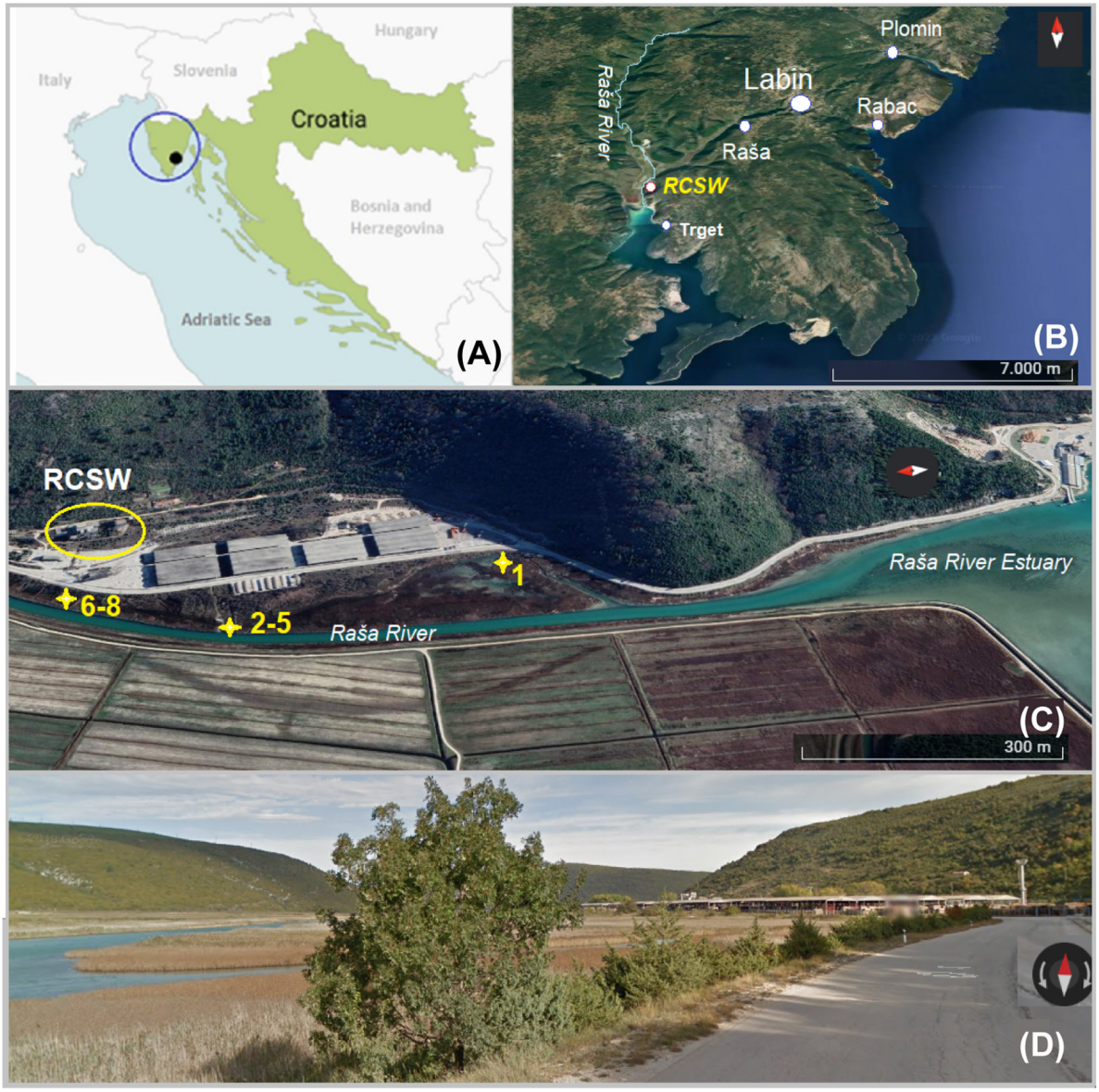

FIGURE 1
Map of the study area: **(A)** Position of the study area (black dot) on Istrian Peninsula (blue circle) in Croatia (Europe); **(B)** position of sampling sites on the eastern part of Istria with Raša River and position of coal processing facility (RCSW); **(C)** position of sampling sites No. 1-8; **(D)** street view of the sampling area.

(Lange and Brumsack, 1977; Bohn et al., 2002). Sample pH was determined with a soil-to-water ratio of 1:2.5 (w/v) using a pH meter (PHS-25, Shanghai INESA Scientific Instrument Co., Ltd., Shanghai, China) (Liang et al., 2017).

2.2.2. Heavy metal analysis

Heavy metals including Se, Mo, Pb, U, V, Cr, Cu, Zn, Sr, and Cd were determined using an inductively coupled plasma mass spectrometry (ICP-MS). An aliquot of 0.5 g dry samples was digested in a TeFlon-coated vessel with 10 mL of digestion solution. The digestion solution was prepared by mixing 2 volumes of hydrofluoric acid, 1 volume of hydrogen peroxide, 1 volume of nitric acid, and 1 volume of perchloric acid. Then, the samples were sequentially heated in a microwave oven under the following conditions: 150°C for 30 min, 180°C for 60 min, 190°C for 60 min, and 210°C for 30 min. After heating, the samples were allowed to cool down before filtering. The filtrate was transferred to a 100 mL volumetric flask with 5.0% v/v HNO_3 as the makeup solution. Then the concentrations of these metals were determined using an ICP-MS (ICP-RQ, Thermo Scientific, USA). Certified standards of these elements were purchased from Solarbio Science and Technology Co., Ltd (Beijing, China) and used for calibration. Rhodium served as an internal standard (Medunić et al., 2021).

2.2.3. Organic pollutants analysis

PAHs were determined with the S-PAHGMS01 method based on the US EPA 8270 and ISO 18287 with a GC/MS. The GC/MS (8890/5977B, Agilent, USA) was equipped with an HP-MS column (30 m × 0.25 μm × 0.25 mm, Agilent, USA). 10 g dried samples were extracted with 50 mL dichloromethane three times with ultrasonication. The GC/MS was run as follows: injection volume, 1 μL; injection inlet temperature, 300 °C; running mode, split mode

with a split ratio of 10:1. Helium was used as the carrier gas with a constant flow rate of 1.0 mL/min. The initial temperature of the column was 40 °C and held for 4 min. Then the column was heated to 300 °C at a rate of 10 °C/min and held at 300 °C for 2 min. The MS was operated in an electron ionization (EI) mode at 70 eV. The temperature of the ion source was set at 230 °C. The fragmental ions were scanned in the quadrupole analyzer at 150 °C at a range of m/z 30–500. The solvent delay was set at 3 min. Total ion chromatograms (TICs) and mass spectra were processed using MSD Productivity ChemStation software (Agilent, USA). NIST11 library was used for compound identification (Gworek et al., 2018).

2.2.4. DNA extraction and sequencing

The DNA samples were extracted with an E.Z.N.A.® soil DNA kit (Omega Bio-Tek, Norcross, GA, USA) according to the manufacturer's instructions. The bacterial and archaeal 16S rRNA genes and fungal ITS1 genes were respectively amplified with the primer pairs 338F (ACTCCTACGGGAGGCAGCAG)/806R (GGACTACHVGGGTWTCTA-AT) (Claesson et al., 2009), 524F10extF (TGYCAGCCGCCGCGGTA-A)/Arch958RmodR (YCCGGC-GTT-GAVTCCAATT) (Zhang J. et al., 2020), and ITS1F (CTTGGTCAT-TTAGAG-GAAGTAA)/ITS2R (GCTGCGTTCTTCATCG-ATGC) (Orgiazzi et al., 2012) using a therm-ocycler PCR system (GeneAmp 9700, ABI, U.S). Then the purified PCR amplicons were pooled in equimolar and paired-end sequenced (2 300) on an Illumina Miseq platform (Illumina, San Diego, USA) at Majio Bioinformatics Technology Co., Ltd. (Shang hai, China). Operational taxonomic units (OTUs) were clustered with a 97% similarity cutoff using the UPARSE pipeline (version 7.1). Sequences of OTUs were classified within the Sliva database release 138 for bacteria and archaea, and Unite INSD release 8.0 (Unite and International Nucleotide and Sequence Databases) for fungi. The data were analyzed on the Majorbio I-Sanger Cloud Platform (www.i-sanger.com). The sequencing data for our study are available in the NCBI Sequence Read Archive under accession no. PRJNA880742.

2.2.5. Predicted metagenomic analysis

Marker gene data and reference genomes can be used to predict genes' functions in a genome. As a computational tool, PICRUSt 2 (phylogenetic investigation of communities by reconstruction of unobserved states) was used to predict the functional potential of the microbial community. In this study, the sediment microbial assemblages exhibited a relatively low mean NSTI (Nearest Sequenced Taxon Index) value (0.18+−0.06), implying that the prediction was reliable for subsequent functional analysis of the microbial community. The predicted genes were then used to compare with the Kyoto Encyclopedia of Genes and Genomes (KEGG) pathways. However, it does have limitations for fungi, as it only provides information on enzymes (Langille et al., 2013; Douglas et al., 2020).

2.2.6. Statistical analysis

Bivariate correlation (2-tailed) analyses including Pearson or Spearman coefficients were performed for the correlations between microbial diversities and environmental factors, as well as between different environmental factors of soil and sediment samples. To explain the correlation between fungal guilds and Naphthalene, PAHs and sulfur genes, Person and bivariate correlation (2-tailed) analyses were used. Levene's test was applied to test the equality of variances. Subsequently, the mean difference was checked by the appropriate t-test method. All statistical analyses were performed on SPSS 26.0 with a P-value less than 0.05 considered statistically significant.

3. Results

3.1. Physicochemical characteristics and levels of PAHs and HTEs in samples

The physiochemical properties of the collected samples and their PAH concentrations are shown in **Table 1**. The samples had generally alkaline pH (7.6-8.3). Depending on the collection sites, moisture ranged widely from 19% to 77%. Total organic carbon ranging from 98 to 268 mg/kg and C:N ratio between 4.8 and 26.0 were recorded in the samples. Elevated levels of TS (up to 9.3%) and OS (up to 4.2%) were detected in samples No. 6-8 (**Figure 1**), which represent the former coal sludge-receiving site. Interestingly, the pH, moisture, C:N ratio, TS and OS of sampling sites No. 1-5 were significantly different from No. 6-8 (ANOVA, $P < 0.05$).

Two types of PAHs including naphthalene and its derivatives [naphthalenes], and dibenzothiophene [DBT]) were quantified (**Table 1**). PAHs and heavy metals in an uncontaminated soil sample in the same area from our previous studies were served as references (Medunić et al., 2016). Results revealed that the samples contained extremely high concentrations of naphthalene (26.3-40.1 mg/kg) and DBT (7.4-8.9 μg/kg) from the coal sludge-receiving site compared to downstream locations (0 μg/kg) and control sample (0.1 μg/kg). The correlations of physicochemical properties with PAHs (**Supplementary Table 1**) were not significantly affected by the depth at site No. 8 except for TS and OS. In addition, for samples from all sites, correlation analysis revealed that C:N ratio and PAHs (Spearman $\rho = 0.692, P = 0.027$), TS and PAHs (Spearman $\rho = 0.925, P = 0.000$), OS and PAHs (Spearman $\rho = 0.937, P = 0.000$) were positively correlated (**Supplementary Table 2**). Although the concentrations of specific PAH congeners varied from site to site, the anomalously high levels of PAHs in No. 6-8 samples indicate that the site is still heavily polluted from the former coal sludge disposal.

Table 1 also shows that the concentrations of major HTEs in the samples are considerably higher compared with the references (Medunić et al., 2016). The concentrations of selenium, uranium and vanadium in samples No. 6-8 are significantly higher than that in samples No. 1-5, while lead and zinc showed the opposite (ANOVA, $\rho < 0.05$). Furthermore, positive correlations of Se-U-V (Spearman $\rho > 0.69, P < 0.05$) and Pb-Zn-Cu (Spearman $\rho > 0.71, P < 0.05$) were observed which might be worthy of further investigation.

3.2. Diversity and abundance of microbial communities

A total of 610,122, 682,950, and 788,679 high-quality bacterial, archaeal, and fungal sequences were obtained and grouped into 8,231, 607 and 4,722 OTUs using a 97% sequence similarity cutoff. Then OTU tables were, respectively, rarified to the minimum depth of sequences of 30,709, 43,999, and 52,799 per sample.

TABLE 1 Physiochemical characteristics, concentrations of toxic organic pollutants and hazardous trace elements of samples.

Sample ID	1	2	3	4	5	6	7	8-20	8-30	8-40	a	b	c	Unit
pH	7.59	7.69	7.70	7.87	7.84	8.21	8.22	8.21	8.28	8.23	/	/		/
Moisture	77.22	32.80	30.40	30.80	34.00	23.25	15.11	18.87	19.52	22.47	/	/		%
TOC	123.2	106.0	146.7	268.7	106.8	97.7	123.5	153.1	132.6	120.2	/	/		mg/kg
C/N	17.3	11.1	14.6	5.0	4.8	25.9	22.6	14.6	20.3	24.3	/	/		/
TS	1.2	1.3	1.4	1.3	1.5	9.3	4.8	4.6	3.8	3.0	/	/		%
OS	0.2	0.2	0.3	0.2	0.4	3.7	4.2	3.4	2.9	2.3	/	/		%
Naphthalenes	0.0	0.0	0.0	0.0	0.0	35.8	40.1	33.6	31.3	26.3	/	0.03		mg/kg
Dibenzothio-phene	0.0	0.0	0.0	0.0	0.0	8.9	7.6	7.9	7.5	7.4	/	/		mg/kg
PAHs	0.0	0.0	0.0	0.0	0.0	44.8	47.7	41.5	38.7	33.7	/	0.1		mg/kg
Se	19.9	21.9	32.7	22.9	22	38.5	34.1	32.8	26.9	28.2	0.3 2.3	1.3	/	mg/kg
Mo	58.3	55.5	27.7	16.4	12	20.5	8.9	12.1	9.4	8.5	/ /	2.4	/	mg/kg
Pb	28.2	26.4	21.3	18.6	19.7	12.3	19.7	15.9	15.4	19.3	17 26	37.1	48	mg/kg
U	6.9	3.7	3.4	2.9	2.9	42.9	33.9	20	9.9	8.4	2.7 5.0	4.4	/	mg/kg
V	72.9	86.2	73.1	75.9	73.6	199.3	86.3	139.7	105.2	121.6	90 98	203.5	148	mg/kg
Cr	119.9	217.7	181.8	167.1	188.6	115.9	114.7	137.3	143.3	170.7	80 64	181.8	60	mg/kg
Cu	80.8	40.6	36.3	37.7	36.2	18.7	31	42.6	30.7	37	25 19	31.9	31	mg/kg
Zn	210.5	80.7	67.2	100.4	93	23.6	42.3	49.8	39.7	59.7	70 80	126.2	108	mg/kg
Sr	247.2	333.9	300	264.7	262.8	303.5	261	306.1	292.3	322.4	240 187	99.2	117	mg/kg
Cd	0.2	0.2	0.2	0.2	0.2	0.2	0.2	0.3	0.3	0.2	0.3 1.8	0.9	0.4	mg/kg

TOC, total organic carbon (dissolved); C/N, C:N ratio; TS, total sulfur; OS, organic sulfur; Naphthalenes, including Naphthalene, 2-methyl-, Naphthalene, 1-methyl-, Naphthalene, 1, 5-dimethyl-, Naphthalene, 1, 3-dimethyl-, Naphthalene, 2, 7-dimethyl- and Naphthalene, 2, 3-dimethyl-. a: soil and sediment (<2 mm, total world median data); b: uncontaminated topsoil in Rabin as a reference; c: element values representative of the coastal Croatian background. Underlined values refer to sediment reference levels (Medunić et al., 2016).

10.3389/fmicb.2023.1126612

Figure 2A shows alpha-diversity levels of bacteria, archaea, and fungi which were all higher in samples No. 1-5 than in samples No. 6-8, except for the Shannon index for the archaea. The community diversity and abundance of bacteria, archaea and fungi were not significantly affected by the depth, suggesting that bacterial, archaeal and fungal communities were not sensitive to the soil and sediment depth at site No. 8. These were confirmed by the correlation analysis (Supplementary Table 1). Furthermore, the differences in the alpha-diversity indices between the coal sludge-receiving site and the downstream locations were confirmed via the Wilcoxon rank sum test (Figure 2A). It appears that except for archaeal diversity, the microbial diversities and abundance were significantly higher in the downstream locations than in the contaminated site.

Non-metric multidimensional scaling (NMDS) analysis revealed that samples No. 1-5 and No. 6-8 formed distinct clusters (Figure 2B), with significant differences being found at OTU levels (analysis of similarity test [ANOSIM]). These differences among samples No. 1-5 and No. 6-8 were the highest for bacterial communities, followed by archaeal and fungal communities, indicating that the coal wastewater discharge impacted the bacterial communities the most.

3.3. Microbial community analyses

Figure 3 shows the microbial community composition at the phylum level for a relative abundance greater than 0.1%. Bacterial sequences were primarily composed of the phyla Proteobacteria (27.92%), Chloroflexi (15.47%), Actinobacteriota (9.59%), Desulfobacterota (9.15%), Acidobacteriota (7.25%), and Bacteroidota (7.12%). The majority of the archaeal sequences belonged to the phyla Crenarchaeota (54.19%), Halobacterota (21.27%), and Thermoplasmatota (11.48%). The most abundant fungal phyla were Ascomycota (72.06%), Rozellomycota (7.45%) and Basidiomycota (6.98%).

Microbial community profiles at the genus level were demonstrated by a hierarchically clustered heatmap (Figures 4A–C). The top 30 genera and 10 samples were both hierarchically clustered based on the Bray-Curtis similarity index. Bray-Curtis dissimilarity analysis revealed that microbial communities of the 10 samples were clustered into two groups. The bacterial and archaeal clustering indicated that samples 1-5 (the downstream locations) were closely related while samples 6-8 (the coal sludge-receiving site) shared a close relationship. Conversely, samples No. 6, 8-30 cm, and 8-40 cm exhibited a distant relationship with samples No. 7 and 8-20 cm in fungal communities. This affinity relationship was also intuitively demonstrated by the NMDS analysis. As shown in Figures A–C, the most representative bacterial and archaeal genera in samples No. 6-8 were *Blastococcus* and *Halogranum*, respectively. In samples No. 1-5, *Sulfurovum*, *Sulfurimonas*, norank_f_Desulfurococcaceae, *Methanosarcina*, and *Methanobacterium* were the most abundant genera. Although most of the dominant genera of samples No. 1-5 and No. 6-8 were different, the top 30 genera were shared by all the samples. This may represent the ecological coherence of the water and sediment of Raša river.

Wilcoxon Rank Sum tests were conducted (double tail test, fdr multiple correction) to determine the difference in abundance of the classified bacterial, archaeal and fungal taxa between the sample groups of No. 1-5 and No. 6-8. The species with significant differences in the sum of the means in the top 15 genera are presented in Figures 4D–F. Interestingly, most of these bacteria and archaea were significantly enriched in samples No. 6-8. Specifically, *Blatococcus*, "Subgroup 10" from Thermoanaerobaculaceae, *Nitrosococcus*, *Ferruginivarius*, *Nitrosopumilus*, *Methanomassiliicoccus*, *Halogranum*, Halobacterales (order), *Haladaptatus*, *Haloterrigena*, and *Natronomonas* were enriched in samples No. 6-8 (all $P < 0.05$). The same members in samples 1-5 were all less than 0.1%. Conversely, most fungi were significantly enriched in samples No. 1-5, while only one genus showed an abundant advantage in samples No. 6-8, i.e., *Neocamarosporium*. In comparison, members of *Sulfurovum*, Anaerolineaceae (family), Rhodobacteraceae (family) and Bathyarchaeia (class) were enriched in samples No. 1-5. The members belonging to *Sulfurovum* and Bathyarchaeia (class) accounted for 3.54% and 60.6% of the population in samples No. 1-5 but less than 0.01% samples No. 6-8.

3.4. Impacts of sample properties on the microbial community structure and function

Canonical correspondence analysis (CCA) was used to determine the relationship between biochemical factors and bacterial, archaeal or fungal communities. Because the strong multicollinearity was detected among nine HTEs (variance inflation factor (VIF) value > 10), VIF analysis was performed prior to the CCA analysis (threshold value = 2). As shown in Supplementary Table 3, two HTEs' environmental factors, Zn and U, were ruled out. As shown in Figure 5, for the eight environmental variables, acute angles were formed among variables of PAHs, U, C:N ratio (C/N), pH, and OS, indicating that these variables had a synergetic impact on the microbial community. On the contrary, sample moisture and Zn showed an opposite relationship in obtuse angles on the microbial composition with the other five variables (PAHs, U, C/N, pH, OS). Apparently, the microbial composition of samples No. 6-8 is positively correlated with the levels of PAHs, U, C/N, pH, and OS, and negatively associated with the sample moisture, thus implying that a higher level of PAHs, U, C/N, pH, and OS, and lower moisture might reduce the abundance and diversity of microbial communities in soils and sediments. All the edaphic variables explained 92.3, 93.4, and 88.1% of the bacterial, archaeal, and fungal variance, respectively. The key environmental factors impacting microbial communities in the samples were pH, OS, and PAHs ($P < 0.05$).

Provided that the microbial diversity and community composition are different between sample groups No. 1-5 and No. 6-8, the key functional microorganisms between the two groups were compared and presented in Figure 4G. Notably, 21 genes (including pcaG, pcaH, ligA, ligB, phdF), 23 genes (including adh, frmA, ADH5, nahF), and 16 genes (including dmsB, dmsC, ssuE, msuE, and cysJ) were affiliated with important enzyme categories (dehydrogenase, hydroxylase, aldolase, decarboxylase, hydrolase) involved in the degradation of PAHs (Supplementary Figure 1), naphthalene (Supplementary Figure 2), and sulfur-containing compounds (Supplementary Figure 3). These pathways were predicted to be harbored by the soil and sediment bacteria and archaea. Among these genes, the sulfur degradation-related genes generally showed the highest abundance followed by naphthalene and PAHs (Figure 4G). The abundance of functional genes associated

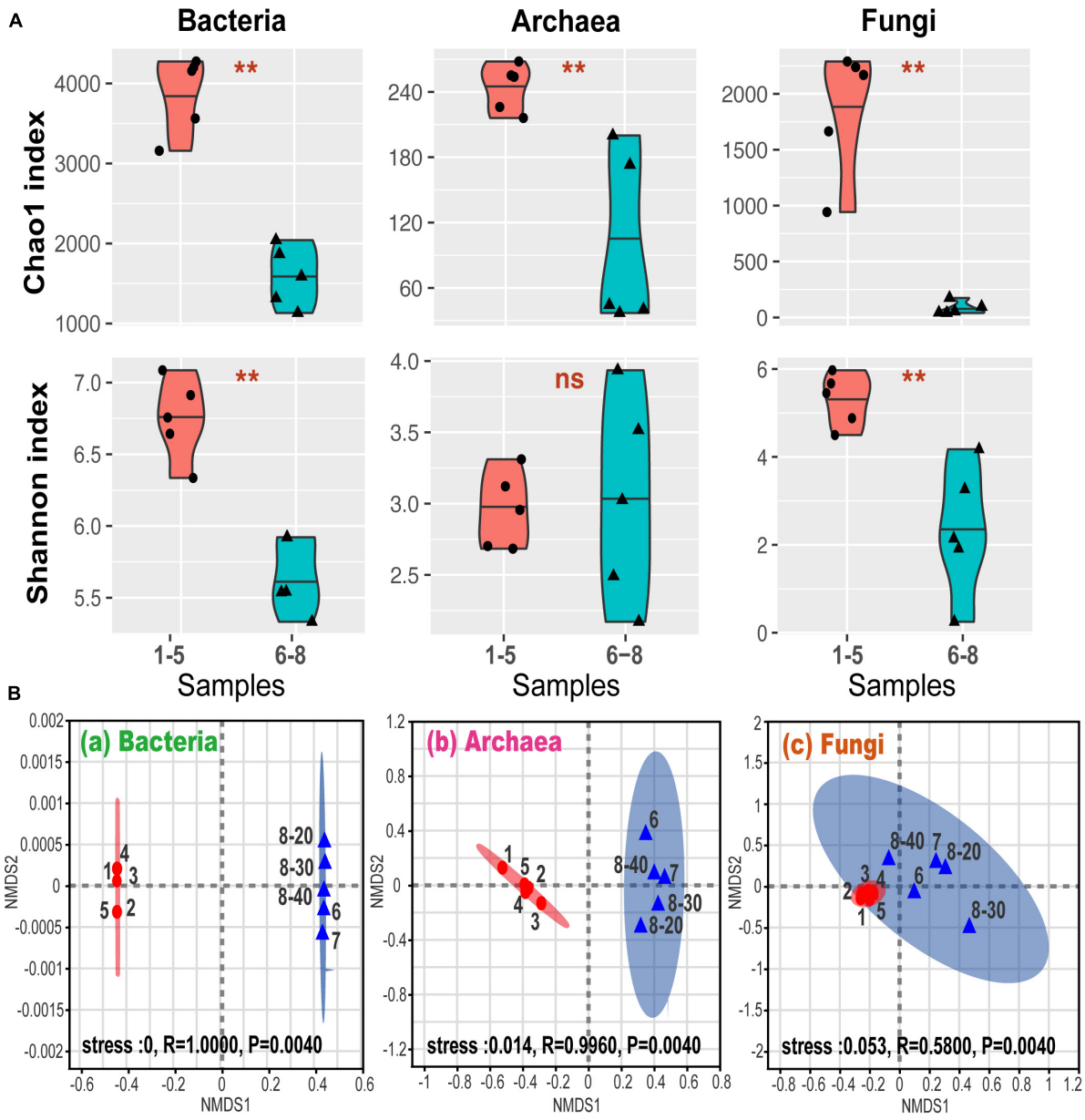

FIGURE 2
(A) Alpha-diversity via Wilcoxon rank sum test. $^{**}P < 0.01$; ns, $P > 0.05$; **(B)** general patterns of microbial beta-diversity. NMDS showed the structure of microbial community for sample bacteria (a), archaea (b), and fungi (c). 95% confidence ellipses were shown around the samples. Similarity values among the samples between ex-coal separation unit and other place were examined via the ANOSIM test, which are shown in each plot.

with naphthalene and sulfur degradation in samples No. 6-8 was greater than that in samples No. 1-5. Notably, most of the genera with significant differences in the top 15 bacterial and archaeal genera have functional genes that are related to the degradation of naphthalene, PAHs, or sulfur-containing compounds. Specifically, the genus, *Ferruginivarius* can degrade all three substances while the other 5 genera (*Natronomona*, *Blastococcus*, *Halogranum*, *Haladaptatus*, *Haloterrigena*) could degrade two substances (Naphthalene/PAHs, sulfur-containing compounds). Both groups exhibited a large number of genes that are involved in sulfur metabolism. In addition, total enzymes and enzymes capable of PAHs degradation for fungi in the two sample groups have shown almost no difference (Table 2), suggesting that indigenous fungi contribute little to the degradation of PAHs in the long run.

4. Discussion

4.1. High concentrations of PAHs and HTEs in the contaminated samples

Elevated concentrations of HTEs were documented in all collected samples (Table 1), thus indicating that the Raša Bay area in the vicinity of the RCSW is severely polluted with HTEs as a result of the legacy of coal sludge. Previous publications report that the local environment (e.g., groundwater, soil, wild plants, crops, and aquatic sediment) is polluted with HTEs due to former coal mining, processing, and combustion activities (Sando et al., 2015; Medunić et al., 2016, 2020a,b, 2021). Interestingly, the concentrations of Mo,

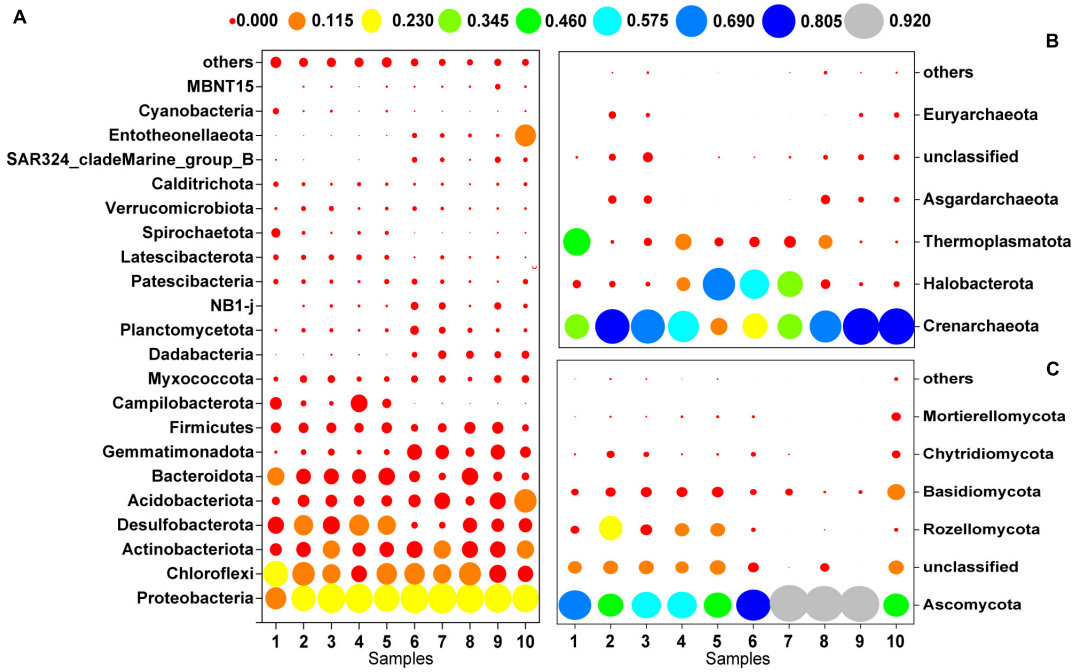

FIGURE 3
Microbial community composition at the phylum level (>0.1%); **(A)** bacteria, **(B)** archaea, **(C)** fungi.

Cu, Zn, Cr, and Pb in samples No. 1-5, especially Zn and Pb, were higher than that in samples No. 6-8, suggesting migration occurred possibly from the erosion and upstream leaching of the coal sludge-receiving site (No. 6-8), while Se, U, and V are coalphilic elements (Yudovich and Ketris, 2006). However, Mo, Cu, Zn, Cr, and Pb are less coalphilic, and more soluble in water (Medunić et al., 2016). Therefore, leaching of Mo, Cu, Zn, Cr, and Pb from coal debris contained in the sludge-receiving site soil could have happened. A previous study (Medunić et al., 2016) also indicated positive correlation ($P < 0.05$) between Cu-Pb-Zn and Se-U-V clusters in soil polluted by Raša coal.

PAHs are components of fossil fuels such as coal. DBT and its derivatives are the main sulfur-containing aromatic compounds in fuels (Kertesz and Wietek, 2001). These aromatic compounds and their degradation products have been found in groundwater, seawater, sediment, soil and atmospheric samples related to old gas plants, industrial waste sites and wood treatment facilities (Warshawsky, 1992; He et al., 2009), which can persist in the environment (Xu et al., 2006; He et al., 2009). According to the classification proposed by Maliszewska-Kordybach (1996), the former coal sludge-receiving site (samples No. 6-8) is heavily polluted (> > 1,000 μg/kg, **Table 1**). On the contrary, PAHs were not detected in the downstream samples (samples No. 1-5). Notably, the PAH composition of coal is commonly dominated by an average of 4.5-ring PAHs (Dong et al., 2012), while those detected in the analyzed samples were dominated by a lower number of rings (2-rings). In addition, concentrations of PAHs were also lower compared with raw Raša coal (53,407.7 μg/kg) (Medunić et al., 2016). These results indicate that PAHs were not migration-prone and were naturally attenuated by the soil and sediment microbes (Schneider et al., 1996; Coates et al., 1997; Yagi et al., 2010). However, the concentration of naphthalene from the polluted coal sludge-receiving site was apparently higher than coal-tar waste (Yagi et al., 2010). This is likely due to slow desorption rates for PAH compounds in coal-contaminated floodplain soils (Achten et al., 2011).

Complex variation occurred in sample properties due to coal processing wastewater, such as increases in sample pH and C:N ratio. These changes could be partly explained by microorganisms, whose activities have proven essential for the functioning of these nutrient cycles (Falkowski et al., 2008; Dai et al., 2018; Jiao et al., 2018). Studies have shown that when pH was between 8 and 9, the activities of phenanthrene, pyrene and naphthalene-degrading microorganisms were highest (Song et al., 2012; Lian et al., 2015). Furthermore, a suitable C:N ratio is beneficial for the continuous growth and proliferation of PAH-degrading microorganisms in soil and sediment (Cai et al., 2021). However, these environmental changes can also lead to an alteration of microbial communities (Schneider et al., 1996; Chaput et al., 2015; Jiao et al., 2018; Liu et al., 2018), as shown by the canonical correspondence analysis (**Figure 5**). On the other hand, a high concentration of sulfur was detected in the polluted coal sludge receiving site, attributed to Raša coal which has exceptionally high values of sulfur (up to 9-11%). Noteworthy, previous study also confirmed that sulfur and PAHs were strongly correlated in soil polluted with Raša coal as a consequence of a local coal-fired power plant (Spearman, $P < 0.01$) (Medunić et al., 2016).

4.2. PAHs reducing the diversity and abundance of microbial community in the polluted site

HTEs have been repeatedly illustrated to have significant impacts on microbial community structure and function across diverse habitat types (Nicomrat et al., 2006; Weber et al., 2008; Khan et al., 2010; Liu et al., 2018; Zhao et al., 2021). Although this study showed that the levels of HTEs were elevated in all samples, CCA

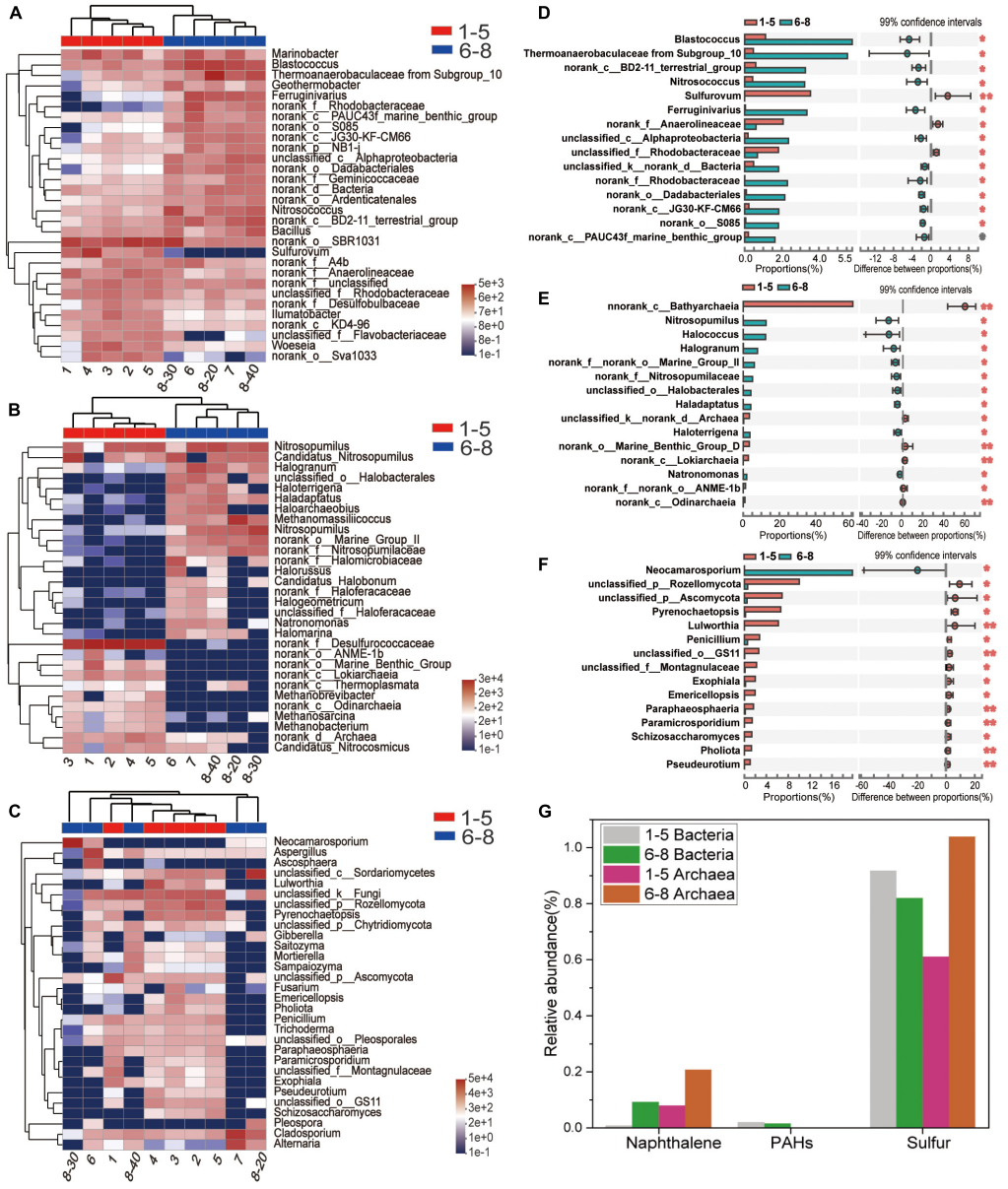

FIGURE 4
(A–C) Heatmap diagrams of the dominant 30 genera; **(A)** bacteria, **(B)** archaea, **(C)** fungi; **(D–F)** comparisons of **(D)** bacterial, **(E)** archaeal and **(F)** fungal abundances with significant differences at the genus level. **(G)** Relative abundance (%) of PAHs-, Naphthalene- and sulfur-degradation genes inferred by PICRUSt 2 in the communities from coal-waste contaminated site.

analysis revealed that HTEs may not have played an important role in the change of microbial communities (**Figure 5**, all $P > 0.05$). On the contrary, the accumulation of PAHs has been the main cause for changing the structure of microbial communities and thus their functions. Since HTEs cannot be degraded like TOPs, they may not participate in the basic element cycle of cells (Nies, 1999). Furthermore, it has been reported that microbial cells have ubiquitously defensive mechanisms against HTEs in such environments (Nies, 2003). In this study, there are bacteria and archaea with intrinsic high-level resistance to HTEs that have been reported in other studies [e.g., *Bacillus* sp. (Amoozegar et al., 2005), *Marinobacter* sp., *Halococcus* sp. (Voica et al., 2016)].

This study shows that PAHs decreased the biodiversity of sample microbiomes, which is in accordance with the fact that high concentrations of PAHs negatively affect the total microbial populations (Zoppini et al., 2016; Picariello et al., 2020). PAHs have detrimental impacts on microbial metabolic processes, enzyme activities (Picariello et al., 2020), and cell functional integrity (Zoppini et al., 2016). For example, PAHs can inhibit oxidative phosphorylation processes by preventing the ATP-forming mechanism (Zoppini et al., 2016). This would explain why the PAH pollution of the Raša coal sludge-receiving site is one of the key factors affecting the microbial community at this study locality. Studies showed that fungal biomass and enzyme activities associated with PAH degradation (e.g., laccase, peroxidase, cytochrome P450 monooxygenase) increased in the early PAH contamination (Marco-Urrea et al., 2015; Mineki et al., 2015; Jové et al., 2016; Bellino et al., 2019; Picariello et al., 2020). However, a minuscule difference in enzyme activity related to PAH degradation was observed in this study. This suggests that fungi have few roles to play in the later

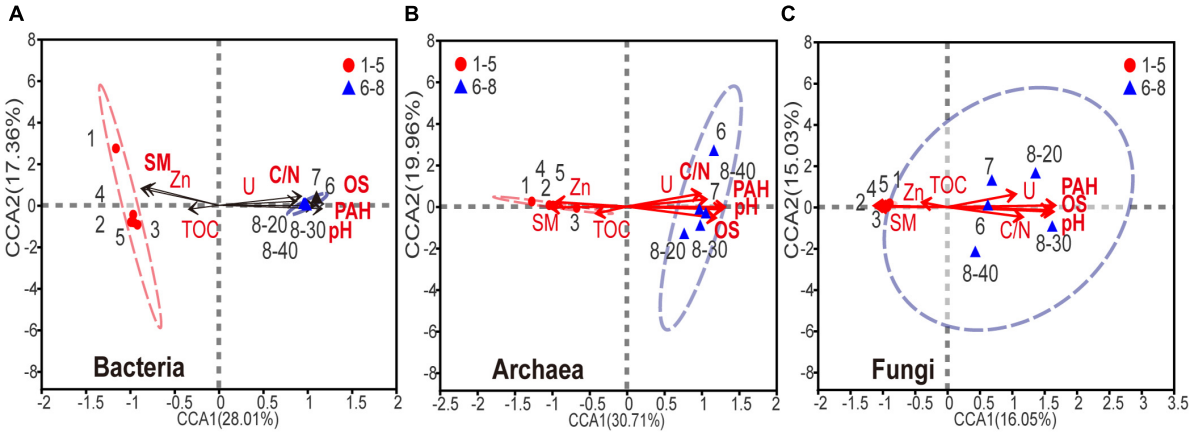

FIGURE 5
Canonical correspondence analysis of **(A)** bacterial, **(B)** archaeal, **(C)** fungal community composition and the subset of seven environmental variables (including SM, PAHs, DBT, OS, TS, Se, V, C/N and pH). The environmental variable in bold font represents $P < 0.05$.

TABLE 2 Enzyme abundance of fungi by PICRUSt 2.

Enzyme description	1.10.3.2 laccase	1.11.1.7 peroxidase	Total
1	258,963	69,508	81,588,426
2	175,760	39,306	82,295,204
3	187,184	42,986	79,146,167
4	218,509	46,861	81,964,137
5	201,701	43,532	74,664,812
6	211,914	51,321	75,415,107
7	397,246	99,963	73,362,268
8-20	256,325	63,343	77,798,089
8-30	307,892	102,323	71,780,019
8-40	208,579	32,854	75,643,813

stage of the degradation of PAHs, while bacterial communities were more responsive and adaptive to contamination than fungi. This could be ascribed to the high intrinsic growth rates and resilience in disturbances and perturbations of bacteria, rendering a more rapid response to environmental changes such as coal processing wastewater pollution in this study. This contrasting pattern could reflect that bacteria and archaea were more sensitive to PAH pollution from the coal sludge-receiving site (No. 6-8).

4.3. Enrichment of genera capable of degrading organic pollutants

Recent research has revealed significant influences of coal waste-associated pollution on the composition and diversity of indigenous soil microbial communities (Ghiorse et al., 1995; Yagi et al., 2010; Roth et al., 2019; Hamidović et al., 2020). This study shows that Proteobacteria, Chloroflexi (bacteria), Crenarchaeota, Halobacterota (archaea), Ascomycota, and Basidiomycota (fungi) were the dominant phyla in the coal sludge-receiving site (affected by the RCSW). Similar phyla have previously been found to dominate the soil microbiota in coal-related wastes (Yagi et al., 2010).

Noteworthy, while the top 30 genera were shared by all samples, a very different distribution pattern of dominant genera was observed. Specifically, *Blastococcus*, "Subgroup 10" from Thermoanaerobaculaceae, *Nitrosococcus*, Ferruginivarius (bacteria), *Nitrosopumilus*, *Methanomassiliicoccus*, *Halodaptatus*, Halobacterales (order) (archaea), and *Neocamarosporium* (fungi) were significantly more abundant in the polluted coal sludge samples ($P < 0.01$). Interestingly, *Blastococcus*, *Ferruginivarius*, "Subgroup 10" from Thermoanaerobaculaceae, *Methanomassiliicoccus*, *Halodaptatus*, and Halobacterales (order) have shown the ability to catabolize complex aromatic compounds or simple hydrocarbons (Joo and Kim, 2005; Youssef et al., 2012; Dyksma et al., 2016; Zárate et al., 2021; Vidal-Verdú et al., 2022). Additionally, "Subgroup 10" from Thermoanaerobaculaceae (Basen et al., 2018), *Nitrosococcus* (Dyksma et al., 2016), *Ferruginivarius* (Wiese et al., 2020), *Halodaptatus* and Halobacterales (order) (Wang et al., 2022) are involved in the sulfur oxidation process. "Subgroup 10" from Thermoanaerobaculaceae has strong viability in polluted coal sludge soil and may have participated at the end of the sulfur cycle in the degradation of TOPs and benefit the growth of other microorganisms (Basen et al., 2018). Besides, *Nitrosococcus* can release nitrogen and nitrogen oxides (Watson, 1965), which explains why samples No. 6-8 have a higher C:N ratio. Subsequent functional inference of communities further revealed that *Blastococcus*, *Ferruginivarius*, "Subgroup 10" from Thermoanaerobaculaceae, *Methanomassiliicoccus*, *Halodaptatus*, and Halobacterales (order) may have relevant genes involved in the PAH and naphthalene degradation. "Subgroup 10" from Thermoanaerobaculaceae, *Nitrosococcus*, *Ferruginivarius*, *Halodaptatus* and Halobacterales (descending order) may have relevant genes involved in the sulfur-metabolism pathways. Overall, our results demonstrate that the native community in the study area contains microbes that can tolerate high concentrations of HTEs and degrade PAHs and sulfur-containing organic compounds. Notably, the microorganisms that can degrade refractory and sulfur-containing organics may have been enriched as they adapt to the surrounding environment. However,

the restoration (biodegradation process) of the polluted ecosystem is slow as extremely high levels of PAHs and HTEs are still observed today, following some 60 years of natural attenuation processes. This study shows that polluting organic compounds mostly shape the microbial structures in the local estuarine environment.

5. Conclusion

In the present study, we have quantified PAHs and HTEs in estuarine sediments and soils polluted by coal sludge that has been abandoned for over 60 years. The effects of the two classes of contaminations on microbial diversity and community structure have been investigated. The results show that PAH degradation does occur by the natural attenuation as indicated by the lower number of mean PAH rings and lower concentrations of PAHs compared with raw Raša coal. However, the site is still heavily polluted by extremely high concentrations of PAHs, while fingerprint elements (Se, U, Mo, and V) of superhigh-organic-sulfur Raša coal were also elevated in the analyzed samples. Microbial analyses revealed that the community structure of the polluted coal sludge-receiving site was significantly different from the downstream. Gemmatimonadota, Dadabacteria and Halobacterota at the phylum level and *Blastococcus*, "Subgroup 10" from Thermoanaerobaculaceae, *Nitrosococcus*, *Ferruginivarius*, *Ntrosopumilus*, *Methanomassiliicoccus*, *Natronomonas, Halogranum*, *Haladaptatus* and *Haloterrigena* at the genus level were the dominant microorganisms in the polluted samples. Further analysis of microbial functionalities has shown that microorganisms associated with the degradation of PAHs and sulfur-containing compounds have been enriched although the diversity and abundance of the microbial community have reduced. Fungi which are believed to be the main PAH degrader may play an important role initially, but the activity remains lower thereafter. It is the high concentrations of coal-derived PAHs, rather than HTEs, that have reduced the diversity and abundance of microbial communities and shaped the structure of the local microbiota. Furthermore, this study also revealed that the restoration of sites polluted by persistent chemicals like PAHs and HTEs by natural attenuation processes is not sufficiently effective. Further anthropogenic intervention may be needed to expedite the remediation process. This study also contributes to the ecological risk assessment of coal-related pollution and bioremediation of such environments. Although the analyses are limited by one-time sampling, a well-planned long-term monitoring program is strongly recommended.

Data availability statement

The data presented in this study are deposited in the NCBI Sequence Read Archive repository, accession number: PRJNA880742.

Author contributions

WZ: data curation, formal analysis, investigation, methodology, visualization, conceptualization, and writing—original draft/reviewing and editing. HH: formal analysis, resources, and writing—original draft/reviewing and editing. QM: data curation, methodology, and writing—original draft/reviewing and editing. MS: data curation, formal analysis, and visualization. GM: data curation, formal analysis, investigation, methodology, visualization, and writing—reviewing and editing. TI: data curation and visualization. MU: formal analysis and writing—original draft/reviewing and editing. F-JL: resources and methodology. HG, RH, MA, and AJ: writing—original draft/reviewing and editing. ZH: formal analysis, conceptualization, supervision, resources, and writing—original draft/reviewing and editing. All authors contributed to the article and approved the submitted version.

Funding

This work was supported by National Key Research and Development Program of China (2019YFC1805400 and 2021YFC2902603), Fundamental Research Funds for the Central Universities of China (2021ZDPY0210 and 2022ZZCX01K1), National Natural Science Foundation of China (No. 42172187), and Key Research Development Program of in Modern Agriculture (KC21137).

Acknowledgments

We are grateful to Dalibor Kvaternik and Dražen Vratarić for their generous help with digital maps of Raša and sampling work.

Conflict of interest

The authors declare that the research was conducted in the absence of any commercial or financial relationships that could be construed as a potential conflict of interest.

Publisher's note

Supplementary material

The Supplementary Material for this article can be found online at: https://www.frontiersin.org/articles/10.3389/fmicb.2023.1126612/full#supplementary-material

References

Achten, C., Cheng, S., Straub, K. L., and Hofmann, T. (2011). The lack of microbial degradation of polycyclic aromatic hydrocarbons from coal-rich soils. *Environ. Poll.* 159, 623–629. doi: 10.1016/j.envpol.2010.09.035

Addink, R., and Olie, K. (1995). Mechanisms of Formation and Destruction of Polychlorinated Dibenzo-p-dioxins and Dibenzofurans in Heterogeneous Systems. *Environ. Sci. Technol.* 29:1425. doi: 10.1021/es00006a002

Amoozegar, M. A., Hamedi, J., Dadashipour, M., and Shariatpanahi, S. (2005). Effect of salinity on the tolerance to toxic metals and oxyanions in native moderately halophilic spore-forming bacilli. *World J. Microbiol. Biotechnol.* 21, 1237–1243. doi: 10.1007/s11274-005-1804-0

Basen, M., Geiger, I., Henke, L., and Müller, V. (2018). A Genetic System for the Thermophilic Acetogenic Bacterium *Thermoanaerobacter kivui*. *Appl. Environ. Microbiol.* 84, e02210–e02217. doi: 10.1128/aem.02210-17

Bellino, A., Baldantoni, D., Picariello, E., Morelli, R., Alfani, A., and De Nicola, F. (2019). Role of different microorganisms in remediating PAH-contaminated soils treated with compost or fungi. *J. Environ. Manage.* 252:109675. doi: 10.1016/j.jenvman.2019.109675

Bohn, H. L., Myer, R. A., and O'Connor, G. A. (2002). *Soil chemistry*. Hoboken, NJ: John Wiley & Sons Press.

BP (2021). *BP statistical review of world energy*. Available online at: https://www.bp.com/en/global/corporate/energy-economics/statistical-review-of-world-energy.html (accessed September 10, 2022).

Cai, Y., Li, W., Zuo, X., Cui, L., Lei, Y., Zhao, X., et al. (2021). Distribution characteristics and influencing factors of polycyclic aromatic hydrocarbons in Yancheng Coastal Wetland (in Chinese). *Ecol. Environ. Sci.* 30, 1249–1259. doi: 10.16258/j.cnki.1674-5906.2021.06.016

Chaput, D. L., Hansel, C. M., Burgos, W. D., and Santelli, C. M. (2015). Profiling microbial communities in manganese remediation systems treating coal mine drainage. *Appl. Environ. Microbiol.* 81, 2189–2198. doi: 10.1128/aem.03643-14

Claesson, M. J., O'Sullivan, O., Wang, Q., Nikkilä, J., Marchesi, J. R., Smidt, H., et al. (2009). Comparative analysis of pyrosequencing and a phylogenetic microarray for exploring microbial community structures in the human distal intestine. *PLoS One* 4:e6669. doi: 10.1371/journal.pone.0006669

Coates, J. D., Woodward, J., Allen, J., Philp, P., and Lovley, D. R. (1997). Anaerobic degradation of polycyclic aromatic hydrocarbons and alkanes in petroleum-contaminated marine harbor sediments. *Appl. Environ. Microbiol.* 63, 3589–3593. doi: 10.1128/aem.63.9.3589-3593.1997

Dai, K., Zhang, F., Zhang, Y., and Zeng, R. J. (2018). The chemostat metabolite spectra of alkaline mixed culture fermentation under mesophilic, thermophilic, and extreme-thermophilic conditions. *Bioresour. Technol.* 249, 322–327. doi: 10.1016/j.biortech.2017.10.035

Dong, J., Li, F., and Xie, K. (2012). Study on the source of polycyclic aromatic hydrocarbons (PAHs) during coal pyrolysis by PY–GC–MS. *J. Hazard. Mater.* 243, 80–85. doi: 10.1016/j.jhazmat.2012.09.073

Douglas, G. M., Maffei, V. J., Zaneveld, J. R., Yurgel, S. N., Brown, J. R., Taylor, C. M., et al. (2020). PICRUSt2 for prediction of metagenome functions. *Nat. Biotechnol.* 38, 685–688. doi: 10.1038/s41587-020-0548-6

Durn, G., Ottner, F., and Slovenec, D. (1999). Mineralogical and geochemical indicators of the polygenetic nature of terra rossa in Istria. *Croatia. Geoderma* 91, 125–150. doi: 10.1016/S0016-7061(98)00130-X

Dyksma, S., Bischof, K., Fuchs, B. M., Hoffmann, K., Meier, D., Meyerdierks, A., et al. (2016). Ubiquitous Gammaproteobacteria dominate dark carbon fixation in coastal sediments. *ISME J.* 10, 1939–1953. doi: 10.1038/ismej.2015.257

Falkowski, P., Fenchel, T., and Delong, E. (2008). The microbial engines that drive Earth's biogeochemical cycles. *Science* 320, 1034–1039. doi: 10.1126/science.1153213

Fei, J. J., Wan, Y. Y., He, X. Y., Zhang, Z. H., and Ying, Y. X. (2020). Unitary and binary remediations by plant and microorganism on refining oil-contaminated soil. *Environ. Sci. Poll. Res.* 27, 41253–41264. doi: 10.1007/s11356-020-10025-6

Ghiorse, W. C., Herrick, J. B., Sandoli, R. L., and Madsen, E. L. (1995). Natural selection of PAH-degrading bacterial guilds at coal-tar disposal sites. *Environ. Health Perspect.* 103 (Suppl. 5), 107–111. doi: 10.1289/ehp.95103s4107

Gworek, B., Baczewska-Dabrowska, A. H., Kalinowski, R., Gorska, E. B., Rekosz-Burlaga, H., Gozdowski, D., et al. (2018). Ecological risk assessment for land contaminated by petrochemical industry. *PLoS One* 13:e0204852. doi: 10.1371/journal.pone.0204852

Hamidović, S., Cvijović, G. G., Waisi, H., Životić, L., Šoja, S. J., Raičević, V., et al. (2020). Response of microbial community composition in soils affected by coal mine exploitation. *Environ. Monit. Assess.* 192:364. doi: 10.1007/s10661-020-08305-2

He, F., Zhang, Z., Wan, Y., Lu, S., Wang, L., and Bu, Q. (2009). Polycyclic aromatic hydrocarbons in soils of Beijing and Tianjin region: Vertical distribution, correlation with TOC and transport mechanism. *J. Environ. Sci.* 21, 675–685. doi: 10.1016/S1001-0742(08)62323-2

Herrick, J. B., Stuart-Keil, K. G., Ghiorse, W. C., and Madsen, E. L. (1997). Natural horizontal transfer of a naphthalene dioxygenase gene between bacteria native to a coal tar-contaminated field site. *Appl. Environ. Microbiol.* 63, 2330–2337. doi: 10.1128/aem.63.6.2330-2337.1997

Huang, J., Zhu, X. Y., Lu, J., Sun, Y., and Zhao, X. Q. (2019). Effects of Different Land Use Types on Microbial Community Diversity in the Shizishan Mining Area (in Chinese). *Environ. Sci.* 40, 5550–5560. doi: 10.13227/j.hjkx.201905050

Jiao, S., Chen, W., Wang, J., Du, N., Li, Q., and Wei, G. (2018). Soil microbiomes with distinct assemblies through vertical soil profiles drive the cycling of multiple nutrients in reforested ecosystems. *Microbiome* 6, 1–13. doi: 10.1186/s40168-018-0526-0

Johnson, J. (1995). Dioxin risk: Are we sure yet? *Environ. Sci. Technol.* 29, 24A–25A. doi: 10.1021/es00001a750

Jones, D. L., and Willett, V. B. (2006). Experimental evaluation of methods to quantify dissolved organic nitrogen (DON) and dissolved organic carbon (DOC) in soil. *Soil Biol. Biochem.* 38, 991–999. doi: 10.1016/j.soilbio.2005.08.012

Joo, W. A., and Kim, C. W. (2005). Proteomics of Halophilic archaea. *J. Chromatogr. B Analyt. Technol. Biomed. Life Sci.* 815, 237–250. doi: 10.1016/j.jchromb.2004.10.041

Jové, P., Olivella, M., Camarero, S., Caixach, J., Planas, C., Cano, L., et al. (2016). Fungal biodegradation of anthracene-polluted cork: A comparative study. *J. Environ. Sci. Health A Toxic Hazard. Subst. Environ. Eng.* 51, 70–77. doi: 10.1080/10934529.2015.1079114

Kertesz, M., and Wietek, C. (2001). Desulfurization and desulfonation: Applications of sulfur-controlled gene expression in bacteria. *Appl. Microbiol. Biotechnol.* 57, 460–466. doi: 10.1007/s002530100800

Khan, S., El-Latif Hesham, A., Qiao, M., Rehman, S., and He, J.-Z. (2010). Effects of Cd and Pb on soil microbial community structure and activities. *Environ. Sci. Poll. Res.* 17, 288–296. doi: 10.1007/s11356-009-0134-4

Lange, J., and Brumsack, H.-J. (1977). Total sulphur analysis in geological and biological materials by coulometric titration following combustion. *Anal. Bioanal. Chem.* 286, 361–366. doi: 10.1007/bf00431198

Langille, M. G., Zaneveld, J., Caporaso, J. G., McDonald, D., Knights, D., Reyes, J. A., et al. (2013). Predictive functional profiling of microbial communities using 16S rRNA marker gene sequences. *Nat. Biotechnol.* 31, 814–821. doi: 10.1038/nbt.2676

Li, Q. (2021). The view of technological innovation in coal industry under the vision of carbon neutralization. *Int. J. Coal Sci. Technol.* 8, 1197–1207. doi: 10.1007/s40789-021-00458-w

Li, T., Guo, Z., Kou, C., Lu, J., Zhang, X., and Yang, X. (2017). Effect of extraction methods on the determination results of soil soluble organic carbon. *Ecol. Environ. Sci.* 26, 1878–1883. doi: 10.16258/j.cnki.1674-5906.2017.11.008

Li, X., Cai, J., Chen, D., and Feng, Q. (2021). Characteristics of water contamination in abandoned coal mines: A case study on Yudong River area, Kaili, Guizhou Province, China. *Int. J. Coal Sci. Technol.* 8, 1491–1503. doi: 10.1007/s40789-021-00466-w

Lian, J., Lu, B., Liu, J., Shi, X., and Huang, L. (2015). Isolation and identification of naphthalene-degrading bacteria and its application in bioremediation of contaminated soil. *Acta Sci. Nat. Univ. Nankaiensis* 048, 92–98. doi: 10.1021/es051024e

Liang, X., Ren, H., Sheng, L., Leng, X., and Yao, X. (2017). Soil bacterial community structure and co-occurrence pattern during vegetation restoration in karst rocky desertification area. *Front. Microbiol.* 2017:8. doi: 10.3389/fmicb.2017.02377

Liu, J., Chen, X., Shu, H. Y., Lin, X. R., Zhou, Q. X., Bramryd, T., et al. (2018). Microbial community structure and function in sediments from e-waste contaminated rivers at Guiyu area of China. *Environ. Poll.* 235, 171–179. doi: 10.1016/j.envpol.2017.12.008

Ma, J., Zhang, W., Chen, Y., Zhang, S., Feng, Q., Hou, H., et al. (2016). Spatial Variability of PAHs and Microbial Community Structure in Surrounding Surficial Soil of Coal-Fired Power Plants in Xuzhou, China. *Int. J. Environ. Res. Public Health* 13:878. doi: 10.3390/ijerph13090878

Maliszewska-Kordybach, B. (1996). Polycyclic aromatic hydrocarbons in agricultural soils in Poland: Preliminary proposals for criteria to evaluate the level of soil contamination. *Appl. Geochem.* 11, 121–127. doi: 10.1016/0883-2927(95)00076-3

Marco-Urrea, E., García-Romera, I., and Aranda, E. (2015). Potential of non-ligninolytic fungi in bioremediation of chlorinated and polycyclic aromatic hydrocarbons. *N. Biotechnol.* 32, 620–628. doi: 10.1016/j.nbt.2015.01.005

Medunić, G., Bilandžić, N., Sedak, M., Fiket, Ž., Crnić, A. P., and Geng, V. (2021). Elevated selenium levels in vegetables, fruits, and wild plants affected by the Raša coal mine water chemistry. *Min. Geol. Petrol. Eng. Bull.* 36, 1–13. doi: 10.17794/rgn.2021.1.1

Medunić, G., Buckovi, D., Crnic, A. P., Bituh, T., and Zgorelec, Z. (2020a). Sulfur, metal(loid)s, radioactivity, and cytotoxicity in abandoned karstic Raša coal-mine discharges (the north Adriatic Sea). *Rudarsko Geolosko Naftni Zbornik* 35, 1–16.

Medunić, G., Kuharić, Ž, Fiket, Ž, Bajramović, M., Singh, A. L., Krivohlavek, A., et al. (2020b). Selenium and other potentially toxic elements in vegetables and tissues of three non-migratory birds exposed to soil, water, and aquatic sediment contaminated with seleniferous Raša coal. *Rudarsko Geološko Naftni Zbornik* 35, 1–16. doi: 10.17794/rgn.2020.3.1

Medunić, G., Singh, P. K., Singh, A. L., Rai, A., Rai, S., Jaiswal, M. K., et al. (2019b). Use of bacteria and synthetic zeolites in remediation of soil and water polluted with superhigh-organic-sulfur Raša coal (Raša Bay. North Adriatic, Croatia). *Water* 11:1419. doi: 10.3390/w11071419

Medunić, G., Grigore, M., Dai, S., Berti, D., and Hower, J. C. (2019a). Characterization of superhigh-organic-sulfur Raša coal, Istria, Croatia, and its environmental implication. *Int. J. Coal Geol.* 217:103344. doi: 10.1016/j.coal.2019.103344

Medunić, G., Kuharić, Ž, Krivohlavek, A., Đuroković, M., Dropučić, K., Rađenović, A., et al. (2018). Selenium, sulphur, trace metal, and BTEX levels in soil, water, and lettuce from the croatian raša bay contaminated by superhigh-organic-sulphur coal. *Geosciences* 8:408. doi: 10.3390/geosciences8110408

Medunić, G, Ahel, M, Mihali, I B, Srèek, VG, Kopjar, N, Fiket, Ž, et al. (2016). Toxic airborne S, PAH, and trace element legacy of the superhigh-organic-sulphur Raša coal combustion: Cytotoxicity and genotoxicity assessment of soil and ash. *Sci. Total Environ.* 566-567, 306–319. doi: 10.1016/j.scitotenv.2016.05.096

Mineki, S., Suzuki, K., Iwata, K., Nakajima, D., and Goto, S. (2015). Degradation of polyaromatic hydrocarbons by fungi isolated from soil in Japan. *Polycycl. Aromat. Compd.* 35, 120–128. doi: 10.1080/10406638.2014.937007

Nadal, M., Schuhmacher, M., and Domingo, J. (2004). Metal pollution of soils and vegetation in an area with petrochemical industry. *Sci. Total Environ.* 321, 59–69. doi: 10.1016/j.scitotenv.2003.08.029

Nicomrat, D., Dick, W. A., and Tuovinen, O. H. (2006). Assessment of the microbial community in a constructed wetland that receives acid coal mine drainage. *Microb. Ecol.* 51, 83–89. doi: 10.1007/s00248-005-0267-z

Nies, D. H. (1999). Microbial heavy-metal resistance. *Appl. Microbiol. Biotechnol.* 51, 730–750. doi: 10.1007/s002530051457

Nies, D. H. (2003). Efflux-mediated heavy metal resistance in prokaryotes. *FEMS Microbiol. Rev.* 27, 313–339. doi: 10.1016/s0168-6445(03)00048-2

Orgiazzi, A., Lumini, E., Nilsson, R. H., Girlanda, M., Vizzini, A., Bonfante, P., et al. (2012). Unravelling soil fungal communities from different Mediterranean land-use backgrounds. *PLoS One* 7:e34847. doi: 10.1371/journal.pone.0034847

Peh, Z., Miko, S., and Hasan, O. (2010). Geochemical background in soils: A linear process domain? An example from Istria (Croatia). *Environ. Earth Sci.* 59:1367. doi: 10.1007/s12665-009-0125-2

Picariello, E., Baldantoni, D., and De Nicola, F. (2020). Acute effects of PAH contamination on microbial community of different forest soils. *Environ. Poll.* 262:114378. doi: 10.1016/j.envpol.2020.114378

Roth, H., Gallo, S., Badger, P., and Hillwig, M. (2019). Changes in microbial communities of a passive coal mine drainage bioremediation system. *Can. J. Microbiol.* 65, 775–782. doi: 10.1139/cjm-2018-0612

Sando, S. K., Clark, M. L., Cleasby, T. E., and Barnhart, E. P. (2015). *Water-quality trends for selected sites in the Boulder River and Tenmile Creek watersheds, Montana, based on data collected during water years 1997-2013.* Reston, VA: US Geological Survey.

Schneider, J., Grosser, R., Jayasimhulu, K., Xue, W., and Warshawsky, D. (1996). Degradation of pyrene, benz[a]anthracene, and benzo[a]pyrene by Mycobacterium sp. strain RJGII-135, isolated from a former coal gasification site. *Appl. Environ. Microbiol.* 62, 13–19. doi: 10.1128/aem.62.1.13-19.1996

Song, L., Liu, L., Li, P., Liu, W., and Zhang, Y. (2012). Screening and degradation characteristics of polycyclic aromatic hydrocarbons (PAHs) degrading bacteria in saline-alkali soil (in Chinese). *Acta Petrolei Sinica* 28, 161–166.

Vidal-Verdú, À, Latorre-Pérez, A., Molina-Menor, E., Baixeras, J., Peretó, J., and Porcar, M. (2022). Living in a bottle: Bacteria from sediment-associated Mediterranean waste and potential growth on polyethylene terephthalate. *Microbiologyopen* 11:e1259. doi: 10.1002/mbo3.1259

Voica, D. M., Bartha, L., Banciu, H. L., and Oren, A. (2016). Heavy metal resistance in halophilic Bacteria and Archaea. *FEMS Microbiol. Lett.* 363:fnw146. doi: 10.1093/femsle/fnw146

Wang, B., Kuang, S., Shao, H., Cheng, F., and Wang, H. (2022). Improving soil fertility by driving microbial community changes in saline soils of Yellow River Delta under petroleum pollution. *J. Environ. Manage.* 304:114265. doi: 10.1016/j.jenvman.2021.114265

Warshawsky, D. (1992). Environmental sources, carcinogenicity, mutagenicity, metabolism and DNA binding of nitrogen and sulfur heterocyclic aromatics. *J. Environ. Sci. Health Part C Environ. Carcinog. Rev.* 10, 1–71. doi: 10.1080/10590509209373411

Watson, S. W. (1965). Characteristics of a marine nitrifying bacterium. Nitrosocystis oceanus sp. N. 1. *Limnol. Oceanogr.* 10, R274–R289. doi: 10.4319/lo.1965.10.suppl2.r274

Weber, K. P., Gehder, M., and Legge, R. L. (2008). Assessment of changes in the microbial community of constructed wetland mesocosms in response to acid mine drainage exposure. *Water Res.* 42, 180–188. doi: 10.1016/j.watres.2007.06.055

Wiese, J., Imhoff, J. F., Horn, H., Borchert, E., Kyrpides, N. C., Göker, M., et al. (2020). Genome analysis of the marine bacterium *Kiloniella laminariae* and first insights into comparative genomics with related Kiloniella species. *Arch. Microbiol.*202, 815–824. doi: 10.1007/s00203-019-01791-0

Xu, P., Yu, B., Li, F. L., Cai, X. F., and Ma, C. Q. (2006). Microbial degradation of sulfur, nitrogen and oxygen heterocycles. *Trends Microbiol.* 14, 398–405. doi: 10.1016/j.tim.2006.07.002

Yagi, J. M., Neuhauser, E. F., Ripp, J. A., Mauro, D. M., and Madsen, E. L. (2010). Subsurface ecosystem resilience: Long-term attenuation of subsurface contaminants supports a dynamic microbial community. *ISME J.* 4, 131–143. doi: 10.1038/ismej.2009.101

Youssef, N. H., Ashlock-Savage, K. N., and Elshahed, M. S. (2012). Phylogenetic diversities and community structure of members of the extremely halophilic Archaea (order Halobacteriales) in multiple saline sediment habitats. *Appl. Environ. Microbiol.* 78, 1332–1344. doi: 10.1128/aem.07420-11

Yu, H., Li, T., Liu, Y., and Ma, L. (2019). Spatial distribution of polycyclic aromatic hydrocarbon contamination in urban soil of China. *Chemosphere* 230, 498–509. doi: 10.1016/j.chemosphere.2019.05.006

Yudovich, Y. E., and Ketris, M. P. (2006). Selenium in coal: A review. *Int. J. Coal Geol.* 67, 112–126. doi: 10.1016/j.coal.2005.09.003

Zárate, A., Dorador, C., Valdés, J., Molina, V., Icaza, G., Pacheco, A. S., et al. (2021). Benthic microbial diversity trends in response to heavy metals in an oxygen-deficient eutrophic bay of the humboldt current system offshore the atacama desert. *Environ. Poll.* 286:117281. doi: 10.1016/j.envpol.2021.117281

Zhang, J., Liu, F., Huang, H., Wang, R., and Xu, B. (2020). Occurrence, risk and influencing factors of polycyclic aromatic hydrocarbons in surface soils from a large-scale coal mine. Huainan China. *Sci. Total Environ.* 192:110269. doi: 10.1016/j.ecoenv.2020.110269

Zhang, Y., Jiang, Q., Gong, L., Liu, H., Cui, M., and Zhang, J. (2020). In-situ mineral CO(2) sequestration in a methane producing microbial electrolysis cell treating sludge hydrolysate. *J. Hazard. Mater* 394:122519. doi: 10.1016/j.jhazmat.2020.122519

Zhao, Q., Xu, Z., and Yu, Z. (2021). Straw-derived biochar as the potential adsorbent for U(VI) and Th(IV) removal in aqueous solutions. *Biomass Convers. Biorefin.* 1–12. doi: 10.1007/s13399-021-01810-5

Zhao, X., Huang, J., Lu, J., and Sun, Y. (2019). Study on the influence of soil microbial community on the long-term heavy metal pollution of different land use types and depth layers in mine. *Ecotoxicol Environ. Saf.* 170, 218–226. doi: 10.1016/j.ecoenv.2018.11.136

Zhao, X., Huang, J., Zhu, X., Chai, J., and Ji, X. (2020). Ecological effects of heavy metal pollution on soil microbial community structure and diversity on both sides of a river around a mining area. *Int. J. Environ. Res. Public Health* 17:5680. doi: 10.3390/ijerph17165680

Zoppini, A., Ademollo, N., Amalfitano, S., Capri, S., Casella, P., Fazi, S., et al. (2016). Microbial responses to polycyclic aromatic hydrocarbon contamination in temporary river sediments: Experimental insights. *Sci. Total Environ.* 541, 1364–1371. doi: 10.1016/j.scitotenv.2015.09.144

frontiers | Frontiers in Microbiology

TYPE Original Research
PUBLISHED 06 April 2023
DOI 10.3389/fmicb.2023.1128064

OPEN ACCESS

EDITED BY
Greg Druschel,
Indiana University,
Purdue University Indianapolis,
United States

REVIEWED BY
Delong Meng,
Central South University,
China
Fanghua Liu,
Guangdong Institute of Eco-environmental and Soil Sciences (CAS),
China
Isabelle Daniel,
Université Claude Bernard Lyon 1,
France

*CORRESPONDENCE
Xin Zhang
✉ xzhang@qdio.ac.cn

SPECIALTY SECTION
This article was submitted to Microbiological Chemistry and Geomicrobiology, a section of the journal Frontiers in Microbiology

RECEIVED 20 December 2022
ACCEPTED 20 March 2023
PUBLISHED 06 April 2023

CITATION
Yin Z, Zheng R, Li L, Xi S, Luan Z, Sun C and Zhang X (2023) *In situ* Raman quantitative monitoring of methanogenesis: Culture experiments of a deep-sea cold seep methanogenic archaeon. *Front. Microbiol.* 14:1128064. doi: 10.3389/fmicb.2023.1128064

In situ Raman quantitative monitoring of methanogenesis: Culture experiments of a deep-sea cold seep methanogenic archaeon

Ziyu Yin[1,2,3], Rikuan Zheng[1,2], Lianfu Li[1,2], Shichuan Xi[1,2], Zhendong Luan[1,2,3], Chaomin Sun[1,2,3] and Xin Zhang[1,2,3]*

[1]CAS Key Laboratory of Marine Geology and Environment and CAS Key Laboratory of Experimental Marine Biology and Center of Deep Sea Research, Institute of Oceanology, Chinese Academy of Sciences, Qingdao, China, [2]Laboratory for Marine Geology and Laboratory for Marine Biology and Biotechnology, Pilot Laboratory for Marine Science and Technology, Qingdao, China, [3]University of Chinese Academy of Sciences, Beijing, China

Gas production from several metabolic pathways is a necessary process that accompanies the growth and central metabolism of some microorganisms. However, accurate and rapid nondestructive detection of gas production is still challenging. To this end, gas chromatography (GC) is primarily used, which requires sampling and sample preparation. Furthermore, GC is expensive and difficult to operate. Several researchers working on microbial gases are looking forward to a new method to accurately capture the gas trends within a closed system in real-time. In this study, we developed a precise quantitative analysis for headspace gas in Hungate tubes using Raman spectroscopy. This method requires only a controlled focus on the gas portion inside Hungate tubes, enabling nondestructive, real-time, continuous monitoring without the need for sampling. The peak area ratio was selected to establish a calibration curve with nine different CH_4–N_2 gaseous mixtures and a linear relationship was observed between the peak area ratio of methane to nitrogen and their molar ratios ($A(CH_4)/A(N_2)=6.0739\times n(CH_4)/n(N_2)$). The results of *in situ* quantitative analysis using Raman spectroscopy showed good agreement with those of GC in the continuous monitoring of culture experiments of a deep-sea cold seep methanogenic archaeon. This method significantly improves the detection efficiency and shows great potential for *in situ* quantitative gas detection in microbiology. It can be a powerful complementary tool to GC.

KEYWORDS

Raman spectroscopy, quantitative analysis, *in situ*, CH_4–N_2 gas system, deep-sea methanogenic archaea, culture experiment

1. Introduction

The deep sea is extremely rich in microbial resources, and several microbial communities remain undiscovered, especially in the deep-sea extreme environments (Jorgensen and Boetius, 2007). Because microbial communities are believed to be related to the origin of life and the vast majority of microorganisms are not yet known to us, such a wide range of microbial resources has great potential for exploitation and use. In recent years, researchers have isolated a variety of methanogenic archaea from various habitats (Simankova et al., 2001; Lyimo et al., 2009;

Zhilina et al., 2013). Methanogenic archaea and methanogens have great phylogenetic and ecological diversity despite their limited range of metabolic diversity (Liu and Whitman, 2008; Yang et al., 2020). Recently, our team also isolated a novel strain of methanogenic archaea from a deep-sea cold seep. Our preliminary studies have suggested that different environmental conditions can greatly affect its metabolic methanogenic processes. Therefore, to more conveniently and quickly investigate whether methane can be produced under different conditions and to identify under which conditions methane production is the most efficient, *in situ* detection methods for methane production should be developed. Furthermore, in microbiology, in addition to methanogenic bacteria, other types of gases produced through several metabolic pathways by the microorganisms, such as hydrogen sulfide (Kalenitchenko et al., 2017), hydrogen (Jiang et al., 2014), and carbon dioxide (La Ferla and Azzaro, 2001), can be detected using a similar method. The identification of gas production by these organisms can then be quickly performed. This will also bring great convenience to various subsequent biological studies and will certainly assist in rapidly exploring the best reaction conditions and monitoring the reaction process.

In conventional anaerobic culture experiments of marine microorganisms, the Hungate tube is a commonly used small anaerobic culture equipment. The Hungate tube is convenient for setting various substrate conditions to investigate the fermentation process, culture conditions, and optimal reaction conditions (Bowles et al., 2011). However, the gas generated in the tube cannot yet be measured nondestructively using *in situ* methods. Instead, it can only be measured using a typical procedure of collecting a sample with a syringe or gas-tight needle and testing it using gas chromatography (GC) (Ahamed and Ahring, 2011). GC is widely used for evaluating the gas composition because of its high sensitivity and small sample requirements. However, when the number of samples is large and the detection frequency is high, sample preparation is cumbersome and time-consuming for GC testing in addition to being expensive (Chen et al., 2003). Furthermore, GC requires sampling prior to determination, which is followed by a multistep gas-transfer procedure (Drozd and Novák, 1979).

Laser Raman spectroscopy is an excellent method for studying gases (Wang et al., 2011; Hanf et al., 2014), fluids (Facq et al., 2014; Li et al., 2018), and mineral components (Ma et al., 2021). In recent years, Raman spectroscopy has been gradually applied in the studies of microbiology because of its unique advantages of being inexpensive, nondestructive, requiring a short time, exhibiting high accuracy, and enabling *in situ* monitoring (Shope et al., 1987; Picard et al., 2007; Wu et al., 2015; Schalk et al., 2017; Jehlicka et al., 2019; Shi et al., 2020; Osman et al., 2021; Wang et al., 2022). Furthermore, owing to the ability of Raman spectroscopy to detect rapidly the characteristic peaks of several gas–and liquid-phase substances from a closed system, it can be used for the long-term monitoring of gas production. Quantitative analysis of fermentation gases using Raman spectroscopy was achieved by Numata et al. (2013), and they conducted a detailed study on the ratios of gaseous mixtures. Fang et al. (2018) studied the Raman spectral parameters of H_2 and CH_4 gaseous mixtures. They found that the peak area and height ratios between CH_4 and H_2 were sensitive to composition (i.e., the molar ratio between CH_4 and H_2) but were almost independent of pressure. These two studies provided a reference for our study; we considered simulating the real gas production process by using gaseous mixtures to build a calibration curve, followed by the application of the curve to the actual biological sample testing process. Our objective was to propose a new, simple, and fast method that does not require device interfacing. In this method, the test environment and equipment depend entirely on the common conditions in microbiology experiments. Thus, the use of custom devices can be avoided, which ensures the versatility and simplicity.

In this study, we established a quantitative calibration curve for methane and nitrogen in a binary-mixture system based on Raman spectroscopy. The methane content in the culture experiments of a deep-sea cold seep methanogenic archaeon can be monitored quantitatively in real time. This method has the potential to become a novel method for gas quantification alone or in combination with GC in microbiology, with the advantages of being nondestructive, fast, and inexpensive.

2. Materials and methods

2.1. Strains and culture conditions

Following the process reported in previous studies (Zheng et al., 2021, 2022), deep-sea sediment samples were collected by *RV KEXUE* from a typical cold seep in the South China Sea. These sediment samples were cultured at 28°C for 2 months in an anaerobic enrichment medium containing (per liter of seawater) the following: yeast extract, 0.1 g; peptone, 0.1 g; methanol, 10 mL; cysteine hydrochloride, 0.6 g; and resazurin, 500 μL 0.1% (w/v; the pH was adjusted to 7.0). The cultures were purified via the repeated use of the Hungate roll-tube method. Single colonies were picked using sterilized bamboo skewers, which were then cultured in the anaerobic enrichment medium. The purity of the isolate was confirmed via repeated partial sequencing of the 16S rRNA gene. Thereafter, a strain of methanogenic archaea (strain ZRKC1), which belongs to the genus *Methanolobus*, was isolated from the deep-sea surficial sediments. Cells of ZRKC1 were motile cocci. This strain grew between 12 and 42°C (optimum 37°C), at pH between 6.5 and 8.2 (optimum pH 7.0) and salinity from 20 to 120 gL^{-1} NaCl (optimum 45 gL^{-1}). To study the production of methane from methanol by strain ZRKC1, 100 μL of freshly incubated cells were inoculated in 10 mL of basal medium (including 2.0 g of the yeast extract, 1.0 g of NH_4Cl, 1.0 g of $NaHCO_3$, 1.0 g of CH_3COONa, 0.5 g of KH_2PO_4, 0.2 g of $MgSO_4$ $7H_2O$, 0.6 g of cysteine hydrochloride, 500 μL of 0.1% (w/v) resazurin in 1 L filtered seawater, and pH = 7.0) supplemented with 100 μL methanol at 25°C for 12 days.

2.2. Raman spectrometer and data processing

In the experiment, a Raman insertion probe (RiP) system was used to collect the Raman spectra of the gas above the liquid medium in the Hungate tubes. The system description has been detailed in the study by Zhang et al. (2017) and a similar concept for this system was first proposed by Brewer et al. (2004). The system primarily consists of a diode-pumped neodymium-doped yttrium aluminum garnet pulsed laser with a power of 150 mW and wavelength of 532 nm (Kaiser Optical Systems, Inc.) and cooled charge-coupled device

(CCD) of 2,048 × 512 pixels (Andor Technology, Inc.). The spectral range (100–4,325 cm^{-1}) was split into two regions (100–2,100 and 2,100–4,325 cm^{-1}) on the surface of the CCD. The acquired spectra were a combination of these two regions. The Raman spectra were collected using HoloGRAMS 4.1 (Kaiser Optical Systems, Inc.) with an exposure time of 6 s and five accumulations, which is an appropriate monitoring mode based on multiple previous experiments. Spectra were collected 3–5 times per tube at the same focus position using Raman non-contact optics (Kaiser Optical Systems, Inc.) in a dark room with the focus adjusted to the gas above the liquid inside the Hungate tubes. We then used GRAMS/AI® 9.1 software (Thermo Fisher Scientific, Inc.) for the baseline calibration of the Raman spectra. The peak position, height, and area were determined using the GRAMS/AI "Peak fitting" and "Integrate" routine.

2.3. Sample preparation and experimental procedures

In the evaluation procedure of gas component samples with known ratios, we configured nine sets of binary mixtures of methane (>99.9%) and nitrogen (>99.9%) (Qingdao Deyi Gas Co., Ltd.) at different ratios (9:1, 8:2, 7:3, 6:4, 5:5, 4:6, 3:7, 2:8, and 1:9) at a normal temperature and pressure (25°C and 1 atm, respectively) using a multicomponent high-precision dynamic gas distribution system (Suzhou Friend Experimental Equipment Co., Ltd.). Pre-experiments revealed that these ratios adequately covered the dynamics of the gas in the tube during the subsequent methanogenesis of methanogenic archaea. The gas mixture was collected in a large water tank by draining it into the same tube as that used in the subsequent experiments. After stabilization, the Raman spectrum of the gas in the tube was collected by controlling the focus point (Figure 1), and a standard curve of the Raman peak area ratio and gas mixture molar ratio was obtained after processing. Subsequently, additional sets of binary mixtures with different ratios were randomly generated to test the curve accuracy.

A total of 16 tubes (Hungate tube, 15 ml) with identical initial conditions were configured for the detection of unknown gas production in the actual samples, and a continuous observation period of 10–12 days was planned. The specific operation was to fix the same interval and select one tube for Raman spectroscopy acquisition every day. Subsequently, approximately 5 mL of gas was immediately transferred into a small customized gas bag with a syringe. After this two-step procedure, the sample was not used. After the completion of data collection and sampling, some samples were selected for GC testing as needed (Figure 2), and excess tubes and gas bags were used as spares. In addition to this, for control validation, we selected several tubes for Raman spectra collection at random times in the later stages of the process, and the gas collection was switched to a vacuum blood collection tube directly from the Hungate tube. This method avoids retaining the gas in the syringe and reduces a gas transit step, which may reduce errors and can be used with GC to validate the curve again.

3. Results and discussion

3.1. Raman spectra of the gaseous mixtures and quantitative theory

The C–H symmetric stretching band at 2,921 cm^{-1} was the dominant Raman peak used to identify methane in the CH_4–N_2 gas mixture in this study. For nitrogen, the N–N stretching band located at 2,332 cm^{-1} was considered (Figure 3). We uniformly controlled the left and right endpoints of the acquired spectra in the ranges of 2,900–2,940 cm^{-1} for methane and 2,310–2,350 cm^{-1} for nitrogen. All subsequent spectral processing was limited and performed within the respective spectral ranges. The Raman intensity normalization theory of Wopenka and Pasteris laid the foundation for the quantitative analysis of the Raman spectra based on the normalized intensities

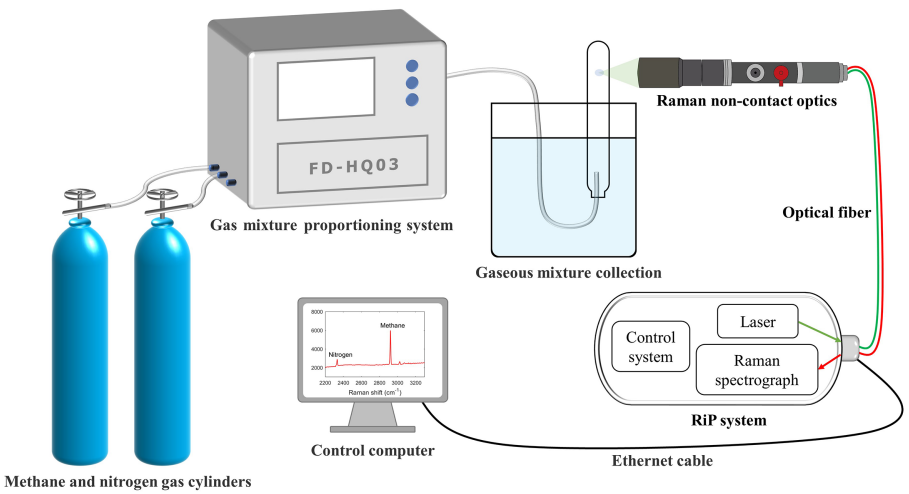

FIGURE 1
Schematic of the experimental system for establishing the calibration curve. The system is equipped with gas-mixing, RiP, and Raman non-contact optical systems.

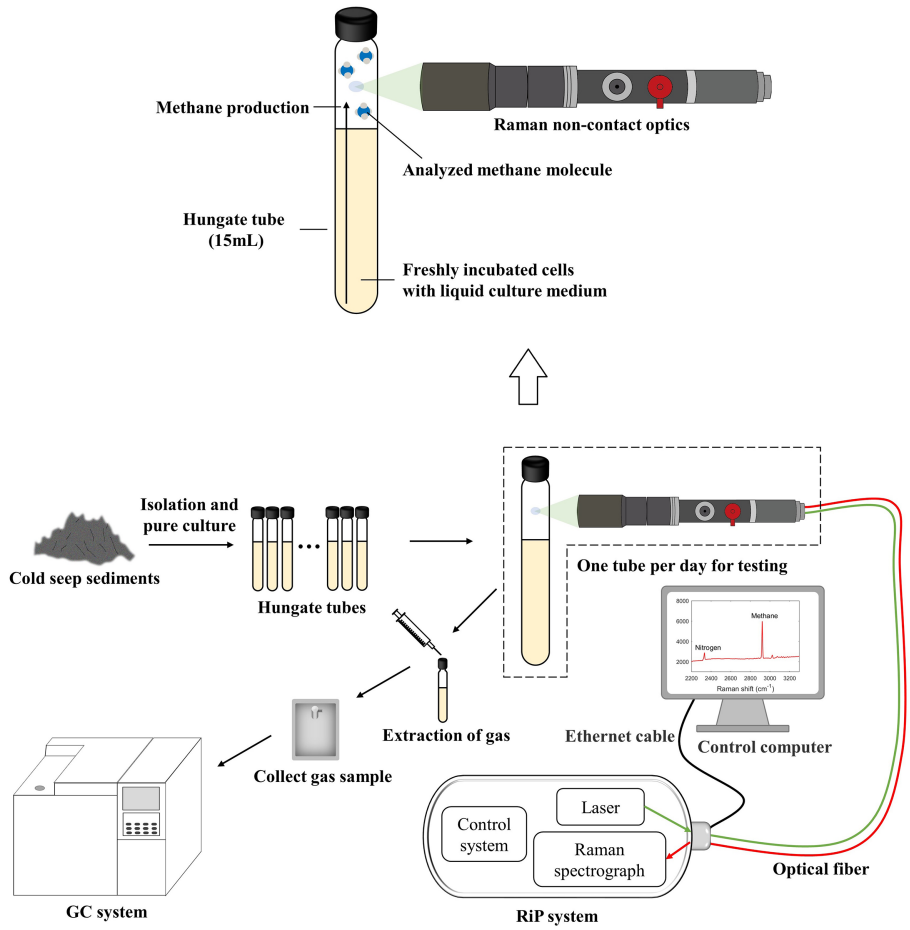

FIGURE 2
Schematic of the experimental system for the application of the calibration curve to the culture experiments. It shows real-time online *in situ* monitoring of methanogenesis using Raman spectroscopy. The partially enlarged insets illustrate the collection of gas Raman spectra. Raman spectra can easily be acquired by focusing the laser through Raman non-contact optics on the gas portion above the interior of the Hungate tube.

(intensity ratios) (Wopenka and Pasteris, 1987), which has led to the development of qualitative Raman spectroscopy for quantification. In our experiments, the Raman scattering intensity reflected the amount of gas within the closed system; however, it was also influenced by other factors. The molar ratios of the two Raman-active species, a and b, in a homogeneous phase can be calculated from the peak areas of one of their specific vibrational bands based on the following equation:

$$\frac{A_a}{A_b} = \frac{C_a}{C_b} \times \frac{\sigma_a}{\sigma_b} \times \frac{\eta_a}{\eta_b} = \frac{C_a}{C_b} \times \frac{F_a}{F_b},$$

where A is the peak area corresponding to the selected vibration band, C is the molar concentration, σ is the Raman scattering coefficient, η is the instrumental efficiency factor, and F is the Raman quantification factor (Wopenka and Pasteris, 1987). This calculation method was widely utilized in the quantitative analysis of gaseous mixtures (Chou et al., 1990; Seitz et al., 1993; Lu et al., 2006; Fang et al., 2018; Chen and Chou, 2022).

To quantify the concentration of methane, known or constant concentrations of Raman-active substances in the sample should be simultaneously measured as a standard reference (Szostak and Mazurek, 2002; Zhang et al., 2016). The Raman peak of nitrogen is a good choice for the procedure of establishing a calibration curve, where it can be used as a quantity of a known concentration. The amount of substance remains constant during the application. Furthermore, nitrogen does not participate in any reactions in this experiment, and it is considered as an inert gas. Consequently, it is well suited to the conditions of the internal standard. In addition, we consistently controlled the environmental conditions. We did not adjust or move the Raman system during the entire experimental cycle and only changed the samples in the sample holder. Therefore, the laser intensity and optical path conditions were consistent. Therefore, the ratio $F(CH_4)/F(N_2)$ can be approximated as a constant. The gas space inside the Hungate tube was always controlled to be maintained at 5 mL. Thus, $C(CH_4)/C(N_2)$ can be calculated from the ratio $A(CH_4)/A(N_2)$, which is also equal to the ratio $n(CH_4)/n(N_2)$.

3.2. Establishment and validation of the Raman quantitative curve

Based on our RiP system, Raman spectra of nine different binary mixtures (molar ratios of CH_4 to N_2 = 9:1, 8:2, 7:3, 6:4, 5:5, 4:6, 3:7, 2:8,

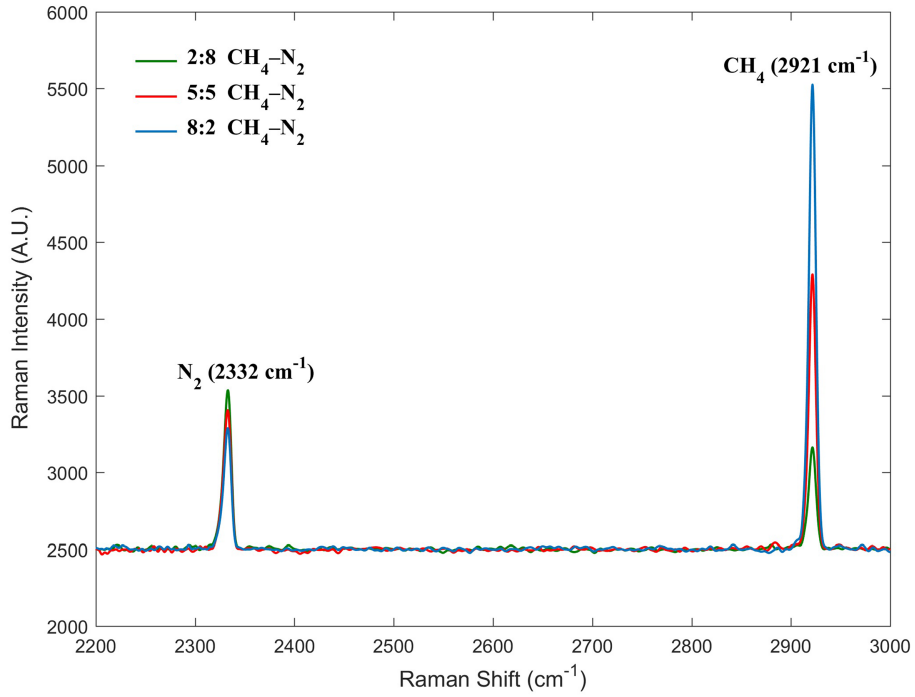

FIGURE 3
Raman spectra of three molar ratios of methane and nitrogen. The peaks at 2332 and 2,921cm^{-1} were assigned to nitrogen and methane, respectively.

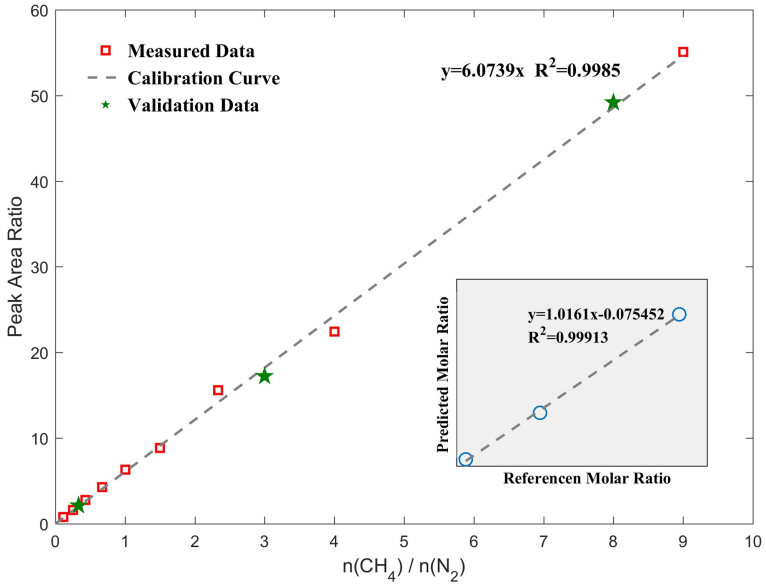

FIGURE 4
Quantitative calibration curve of the molar ratio of the gaseous mixtures to the Raman peak area ratio. Error bars are within the symbol size; therefore, the relevant values are shown in Table 1. The green stars are validation data that are randomly mixed to test the difference between the theoretical and measured values, and they are close to the calibration curve. The lower-right corner shows the molar ratio predicted by the calibration curve versus the actual value.

and 1:9) were collected at normal temperature and pressure. We regressed the peak area ratio of methane and normalized nitrogen on the molar ratio of methane to nitrogen to obtain the calibration curve shown in Figure 4. Relevant data are shown in Table 1. In general, different laboratories reported different F values due to different Raman systems and optical paths. The slope of the calibration curve is 6.0739 ($R^2 = 0.9985$), which is representative of $F(CH_4)/F(N_2)$ in this study.

Thereafter, three different ratios of gaseous mixtures were randomly configured, and the volume ratios calculated with their

TABLE 1 Molar ratio of methane to nitrogen and the corresponding peak area ratio.

Serial number	Molar ratio	Peak area ratio	Standard deviation
1	1:9	0.780	0.068
2	2:8	1.637	0.074
3	3:7	2.812	0.220
4	4:6	4.230	0.166
5	5:5	6.337	0.350
6	6:4	8.849	0.749
7	7:3	15.630	1.067
8	8:2	22.455	0.062
9	9:1	55.086	1.190

measured peak area ratios were 0.35, 2.84, and 8.10, which were close to the actual values of 0.33, 3.00, and 8.00, respectively. These data are marked with green stars in the standard curve, as shown in Figure 4. The root-mean-square error of the molar ratio based on the calibration curve of the peak area ratio was 0.1095. The slopes of the fitting lines were close to 1.0, which indicates that the curve-predicted and actual values are generally consistent and demonstrates the accuracy of the calibration curve. When only a qualitative detection is required, a signal-to-noise ratio of 3:1 is generally used as the detection limit. In this case, CH_4 with a volume fraction of 5% in this experiment could be detected by our system. Converting it to a concentration unit is 2.05 mmol/L. A quantitative limit is generally based on a signal-to-noise ratio greater than 10:1. In this study, the signal-to-noise ratios of Raman spectra for both CH_4 and N_2 in the detection interval were considerably larger than 10; therefore, the conditions for quantification were available from the spectroscopic point of view. Based on this curve, we could then quantitatively monitor the CH_4 concentrations in the 10–90% interval in our experiment.

To achieve nondestructive *in situ* real-time monitoring, we used Raman non-contact optics, which have the advantage of a wide range of working distances for remote measurements either directly or through sight glasses and translucent packaging. However, because of its characteristics for remote measurements, other regions through which the laser passes beside the focal point partially excite the scattering effect. This scattering effect will also be reflected in the Raman spectrum, that is, the information in the optical path. Nonetheless, this effect can be eliminated using a simple spectral treatment. Specifically, in this experiment, we used the nitrogen peak area in the Raman spectrum of a Hungate tube filled with pure methane as the reference value of the optical path. The reason for this treatment is that the optical path passes through air containing nitrogen but no methane. This reference value was subtracted from all the peak areas of nitrogen in the subsequent spectral processing to obtain the Raman signal excited only by the nitrogen in the tube under ideal conditions. If we ignore the influence of the optical path, the attempted calibration curve has an R^2 of only 0.8, and nine points appear to have a logarithmic trend, which is inconsistent with the ideal situation. The results showed that the effect of the gas in the optical path cannot be neglected. This data treatment is closer to the actual ideal conditions and more conducive to the establishment of an accurate quantitative curve.

In addition, the Raman spectrum is highly sensitive to pressure and temperature changes (Peercy and Morosin, 1973; Pironon et al., 2003), particularly in a gas (Lallemand et al., 1966; Lu et al., 2007). Therefore, in our experiments, the pressure and temperature were controlled. The characteristics of the methane peaks were systematically investigated by Petrov (2017) in the range of 1–55 bar. The half width of the C–H symmetric stretching band (ν_1) increased only slightly with increasing pressure (~0.005 cm^{-1}/bar). Furthermore, the peak position of the C–H symmetric stretching band shifted toward lower wavenumbers for 1.1 cm^{-1} in the range of 1–55 bar. Two other studies have arrived at similar conclusions (Lin et al., 2007a,b). In our study, the pressure in the culture experiments was estimated to be no more than 5 bar. This was roughly inferred by the insertion of the syringe through the rubber plug into the Hungate tube. Based on Petrov's model, we showed that both the Raman shift and half-width variations in this range were less than 0.1 cm^{-1}. The ν_1 peak of methane in this range was largely unaffected by pressure; therefore, the effect of pressure on the experiment could be ignored. The study by Lu et al. (2007) contains data that confirm our opinion. Therefore, we did not perform experiments under different pressures in our quantitative analysis. The same concerns applied to the temperature: the culture temperature of the strain was set to normal room temperature (25°C). It is the same temperature as in the previous analysis, and the subsequent continuous observation experiments were also performed at this temperature. Even if there was an error in the controlled temperature, such a small temperature change would not have a significant effect on the experimental results. The claim is also supported by the temperature data reported in a former study (Lu et al., 2007). Therefore, the temperature had no effect on any of the spectra in our experiments.

3.3. Application in continuous observation of methanogenesis

In the microbiological experiments, the Raman spectra of the gas above the liquid in the Hungate tube were collected over a period of 12 consecutive days. Daily data showed good repeatability. Considering the data of the second day with low methane concentrations in the early stage as an example, the peak area ratio data obtained from five replicates were 0.656, 0.664, 0.697, 0.633, and 0.646, respectively. Figure 5A shows the Raman spectra of the methane peaks collected in the Hungate tube for 5 out of the 12 consecutive days. A clear trend in the intensity of the methane peaks with time were observed, and this trend is presented in two forms in Figure 5B. Based on the trend analysis and the figure, we can surmise that strain ZRKC1 may not have undergone methanogenesis in the first 5 days. At this stage, the observed methane production was low, and the parameters related to the methane peak did not change significantly. From the sixth day, the methane production was noticeable (Supplementary Video S1). In the later stages, methane dominated the gas composition in the tubes. Methanogenesis was suppressed owing to a high production of methane. Furthermore, methanol was almost completely consumed, resulting in the stabilization of the final methane volume fraction. The gas environment inside the tube for the first 5 days was consistent with that of the initial environment, which was a mixed-gas system inside the anaerobic operating table. In the later days, because of a significant

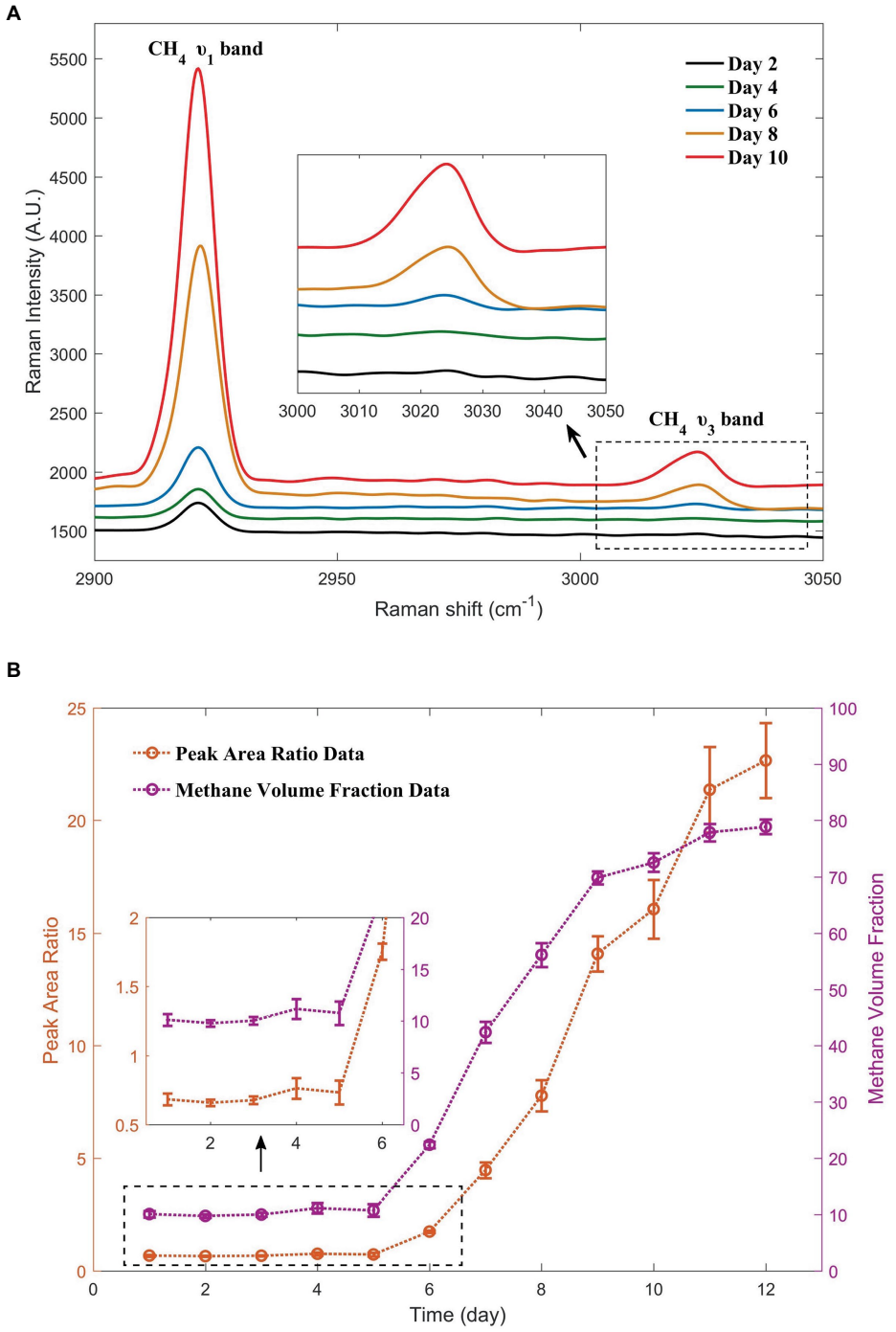

FIGURE 5
Changes in the methane peaks during the 5days selected from the 12-day monitoring. The Raman spectra with simultaneous inclusion of nitrogen peaks were shown in Supplementary Figure S1 **(A)**. Methane production, as demonstrated by the methane peak area ratio with nitrogen and methane volume fractions calculated from the curve over a period of 12days **(B)**.

methane production, we used the curve to calculate the methane and nitrogen volume fraction data in the tube at various time points. The data are shown in Table 2. The purpose of using volume fractions as units was to enable a better comparison with the GC data.

Because the sampling procedure was performed in parallel, we selected several samples for GC testing. Specifically, one sample from day 10 and two samples from the backup group with unknown culture times were selected and sent for testing, yielding methane volume fractions of 78.73, 69.40, and 77.33%, respectively. The peak area ratios for these three data sets were 16.070, 17.931, and 22.357, respectively, and the volume fractions of methane calculated after incorporating them into the curve were 72.57, 74.70, and 78.64%, respectively, which were close to the actual values (Figure 6). A p-value of 0.968 obtained from the t-test of paired data for the two data sets was considerably greater than 0.05, indicating that there was no significant difference between the two sets of data. Thus, the accuracy

of this *in situ* detection method meets the requirements of the observation experiments.

Currently, there are five methanogenic pathways for methanogenic archaea, and the corresponding research is abundant. A majority of methanogenic processes are accompanied by the production of carbon dioxide according to the literature (Liu and Whitman, 2008; Zhou et al., 2022). Therefore, when we analyzed the obtained spectra, we focused on the peak of CO_2, which also showed a slightly increasing trend throughout the 12-day monitoring (5 out of 12-day data are shown in Figure 7). However, we inferred from the qualitative analysis that its production is extremely small. The production of CO_2 was insignificant compared with the production of CH_4. Therefore, we neglected the CO_2 content in the calculated data presented in Table 2. The measured data may not match the theoretical situation in most of the literature, which is an interesting finding. Thus, a trace amount of CO_2 has a minimum effect on the spectral parameters of methane and nitrogen and can be neglected, which also indicates the need for further metabolic studies on this strain. However, it also shows that a small part of the pressure increase in the tubes during the culture experiments is contributed by the production of CO_2.

TABLE 2 Volume fraction of methane and nitrogen calculated from the curve.

Days	Peak area ratio	Nitrogen volume fraction (%)	Methane volume fraction (%)
1	0.684	89.884	10.116
2	0.659	90.210	9.790
3	0.678	89.965	10.035
4	0.764	88.830	11.170
5	0.734	89.225	10.775
6	1.752	77.614	22.386
7	4.470	57.607	42.393
8	7.779	43.845	56.155
9	14.089	30.124	69.876
10	16.070	27.429	72.571
11	21.363	22.138	77.862
12	22.663	21.137	78.863

During the continuous observation of methanogenesis, we prepared multiple tubes in the same batch with identical initial conditions for one tube per day of testing. This selection might have incorporated some chance errors, and our data (e.g., the first 5 days provided fluctuating results, and the results on some days were lower than predicted) confirmed the existence of these errors. However, unlike the theoretically ideal method of concentrating on the same tube for daily monitoring with multiple samplings, we discard the tube after collecting the spectrum and taking the sample in the current method. This method does not require multisampling and, therefore, avoids the accompanying problems of signal-to-noise ratio reduction (Numata et al., 2013), pressure reduction (Seitz et al., 1996), and culture contamination. Consequently, this processing allows us to obtain Raman data that are more accurate. We also aim to adopt the former ideal method in subsequent studies that do not require GC validation. Because of the convenience of this method,

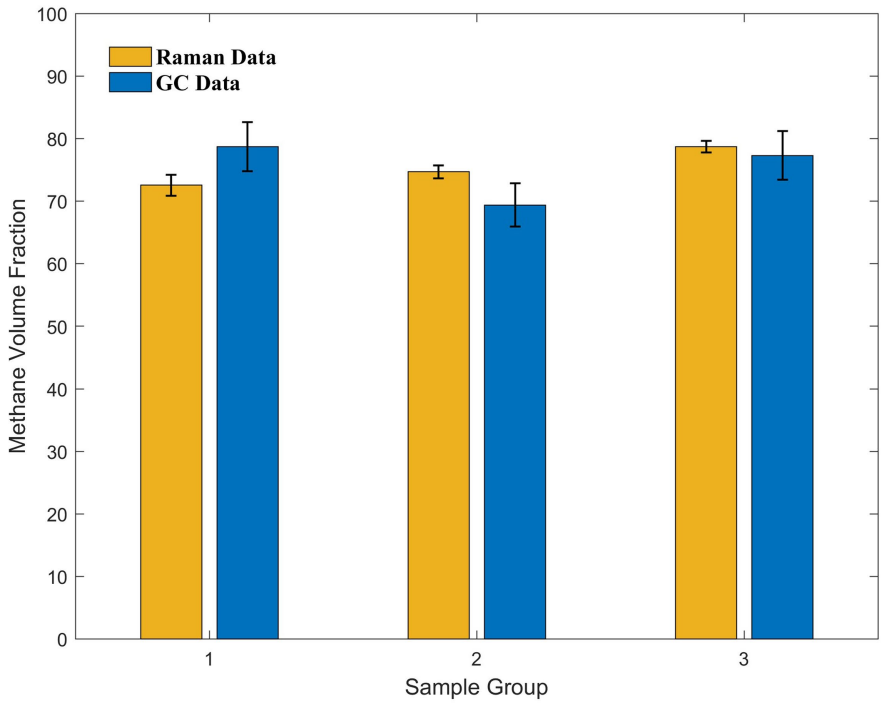

FIGURE 6
Comparison of the Raman and GC data acquired from three sets of samples with different culture times in the later stages of the culture experiments. The methane volume fraction calculated from the curve using Raman data and methane volume fraction measured using GC show good agreement.

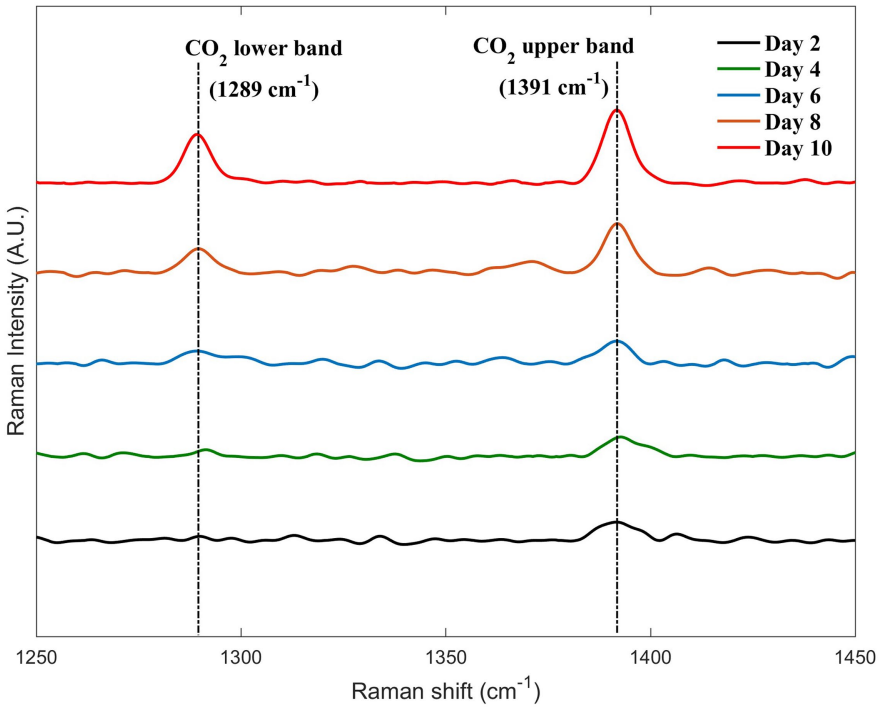

FIGURE 7
Changes in the carbon dioxide peaks during the 5days selected from the 12-day monitoring.

we can quickly explore whether the strain can produce methane from other organic or inorganic substances apart from methanol, such as shrimp shells and lignin. This method makes it possible to reduce the cost and speed up the assay and facilitates the setting of a wide range of initial conditions, which is ideal for the initial screening of a large number of substances. After the initial screening, further small-scale studies in combination with GC can result in significant time and cost savings.

4. Conclusion

In this study, we first established a quantitative Raman curve of methane with nitrogen in a binary mixture system by configuring different mixture ratios. Based on this curve, we quantitatively monitored the metabolism of a novel methanogenic archaeon isolated from a cold seep and successfully demonstrated an *in situ* quantitative detection method for gas production. The curve and its application were separately validated, with fair accuracy. Compared with GC, the proposed method has the following advantages: sampling, gas separation, and transfer are not required and this method enables fast detection and continuous long-term monitoring at fixed time intervals. This will bring great convenience to similar studies by reducing the operational difficulty and threshold. In the future, simulations of gaseous mixtures, including methane and hydrogen, at different temperatures and pressures can be conducted. Combined with Raman immersion probes, this method is expected to be better adapted for *in situ* monitoring of microbial fermentation and metabolic processes in extreme environments.

Data availability statement

The original contributions presented in the study are included in the article/Supplementary material, further inquiries can be directed to the corresponding author.

Author contributions

XZ and ZY contributed to the conception and design of the study. Material preparation, data collection, and analysis were performed by ZY, RZ, LL, and SX. The first draft of the manuscript was written by ZY, and all authors commented on previous versions of the manuscript. XZ contributed to the funding acquisition, project administration, supervision, writing, reviewing, and editing. CS and ZL participated in funding acquisition, project administration, and supervision. All authors contributed to the article and approved the submitted version.

Funding

This research was supported by the following grants: the National Natural Science Foundation of China (92058206 and 41822604), the Strategic Priority Research Program of Chinese Academy of Sciences (XDA22050000 and XDA19060402), Key Project of Ocean Research Center, Chinese Academy of Sciences (COMS2020J03), and the Young Taishan Scholars Program (tsqn201909158).

Acknowledgments

The authors thank all the crews onboard the *RV KEXUE* for their assistance in sample collection and all the laboratory staff for continuous experimental help and technical discussions.

Conflict of interest

The authors declare that the research was conducted in the absence of any commercial or financial relationships that could be construed as a potential conflict of interest.

Publisher's note

All claims expressed in this article are solely those of the authors and do not necessarily represent those of their affiliated organizations, or those of the publisher, the editors and the reviewers. Any product that may be evaluated in this article, or claim that may be made by its manufacturer, is not guaranteed or endorsed by the publisher.

Supplementary material

The Supplementary material for this article can be found online at: https://www.frontiersin.org/articles/10.3389/fmicb.2023.1128064/full#supplementary-material

References

Ahamed, A., and Ahring, B. K. (2011). Production of hydrocarbon compounds by endophytic fungi Gliocladium species grown on cellulose. *Bioresour. Technol.* 102, 9718–9722. doi: 10.1016/j.biortech.2011.07.073

Bowles, M. W., Samarkin, V. A., and Joye, S. B. (2011). Improved measurement of microbial activity in deep-sea sediments at in situ pressure and methane concentration. *Limnol. Oceanogr. Methods* 9, 499–506. doi: 10.4319/lom.2011.9.499

Brewer, P. G., Malby, G., Pasteris, J. D., White, S. N., Peltzer, E. T., Wopenka, B., et al. (2004). Development of a laser Raman spectrometer for deep-ocean science. *Deep-Sea Res. I Oceanogr. Res. Pap.* 51, 739–753. doi: 10.1016/j.dsr.2003.11.005

Chen, Y., and Chou, I. M. (2022). Quantitative Raman spectroscopic determination of the composition, pressure, and density of CO_2–CH_4 gas mixtures. *J. Spectrosc.* 2022, 1–18. doi: 10.1155/2022/7238044

Chen, P. C., Joyner, C. C., Patrick, S. T., Royster, R. M., and Ingham, L. L. (2003). Gas chromatography-multiplex coherent Raman spectroscopy. *Anal. Chem.* 75, 3066–3072. doi: 10.1021/ac0207123

Chou, I. M., Pasteris, J. D., and Seitz, J. C. (1990). High-density volatiles in the system C-O-H-N for the calibration of a laser Raman microprobe. *Geochim. Cosmochim. Acta* 54, 535–543. doi: 10.1016/0016-7037(90)90350-t

Drozd, J., and Novák, J. (1979). Headspace gas analysis by gas chromatography. *J. Chromatogr. A* 165, 141–165. doi: 10.1016/s0021-9673(00)90938-5

Facq, S., Daniel, I., Montagnac, G., Cardon, H., and Sverjensky, D. A. (2014). *In situ* Raman study and thermodynamic model of aqueous carbonate speciation in equilibrium with aragonite under subduction zone conditions. *Geochim. Cosmochim. Acta* 132, 375–390. doi: 10.1016/j.gca.2014.01.030

Fang, J., Chou, I. M., and Chen, Y. (2018). Quantitative Raman spectroscopic study of the H_2–CH_4 gaseous system. *J. Raman Spectrosc.* 49, 710–720. doi: 10.1002/jrs.5337

Hanf, S., Keiner, R., Yan, D., Popp, J., and Frosch, T. (2014). Fiber-enhanced Raman multigas spectroscopy: A versatile tool for environmental gas sensing and breath analysis. *Anal. Chem.* 86, 5278–5285. doi: 10.1021/ac404162w

Jehlicka, J., Culka, A., Mana, L., and Oren, A. (2019). Comparison of miniaturized Raman spectrometers for discrimination of carotenoids of halophilic microorganisms. *Front. Microbiol.* 10:1155. doi: 10.3389/fmicb.2019.01155

Jiang, L., Long, C., Wu, X., Xu, H., Shao, Z., and Long, M. (2014). Optimization of thermophilic fermentative hydrogen production by the newly isolated Caloranaerobacter azorensis H53214 from deep-sea hydrothermal vent environment. *Int. J. Hydrog. Energy* 39, 14154–14160. doi: 10.1016/j.ijhydene.2014.05.025

Jorgensen, B. B., and Boetius, A. (2007). Feast and famine—microbial life in the deep-sea bed. *Nat. Rev. Microbiol.* 5, 770–781. doi: 10.1038/nrmicro1745

Kalenitchenko, D., Le Bris, N., Dadaglio, L., Peru, E., Besserer, A., and Galand, P. E. (2017). Bacteria alone establish the chemical basis of the wood-fall chemosynthetic ecosystem in the deep-sea. *ISME J.* 12, 367–379. doi: 10.1038/ismej.2017.163

La Ferla, R., and Azzaro, M. (2001). Microbial respiration in the Levantine Sea: Evolution of the oxidative processes in relation to the main Mediterranean water masses. *Deep-Sea Res. I Oceanogr. Res. Pap.* 48, 2147–2159. doi: 10.1016/s0967-0637(01)00009-7

Lallemand, P., Simova, P., and Bret, G. (1966). Pressure-induced line shift and collisional narrowing in hydrogen gas determined by stimulated Raman emission. *Phys. Rev. Lett.* 17, 1239–1241. doi: 10.1103/PhysRevLett.17.1239

Li, L., Zhang, X., Luan, Z., du, Z., Xi, S., Wang, B., et al. (2018). *In situ* quantitative Raman detection of dissolved carbon dioxide and sulfate in Deep-Sea high-temperature hydrothermal vent fluids. *Geochem. Geophys. Geosyst.* 19, 1809–1823. doi: 10.1029/2018gc007445

Lin, F., Bodnar, R. J., and Becker, S. P. (2007a). Experimental determination of the Raman CH_4 symmetric stretching (ν_1) band position from 1–650 bar and 0.3–22 °C: Application to fluid inclusion studies. *Geochim. Cosmochim. Acta* 71, 3746–3756. doi: 10.1016/j.gca.2007.05.016

Lin, F., Sum, A. K., and Bodnar, R. J. (2007b). Correlation of methane Raman ν_1 band position with fluid density and interactions at the molecular level. *J. Raman Spectrosc.* 38, 1510–1515. doi: 10.1002/jrs.1804

Liu, Y., and Whitman, W. B. (2008). Metabolic, phylogenetic, and ecological diversity of the methanogenic archaea. *Ann. N. Y. Acad. Sci.* 1125, 171–189. doi: 10.1196/annals.1419.019

Lu, W., Chou, I. M., Burruss, R. C., and Song, Y. (2007). A unified equation for calculating methane vapor pressures in the CH_4–H_2O system with measured Raman shifts. *Geochim. Cosmochim. Acta* 71, 3969–3978. doi: 10.1016/j.gca.2007.06.004

Lu, W. J., Chou, I. M., Burruss, R. C., and Yang, M. Z. (2006). *In situ* study of mass transfer in aqueous solutions under high pressures via Raman spectroscopy: A new method for the determination of diffusion coefficients of methane in water near hydrate formation conditions. *Appl. Spectrosc.* 60, 122–129. doi: 10.1366/000370206776023278

Lyimo, T. J., Pol, A., Jetten, M. S., and den Camp, H. J. (2009). Diversity of methanogenic archaea in a mangrove sediment and isolation of a new Methanococcoides strain. *FEMS Microbiol. Lett.* 291, 247–253. doi: 10.1111/j.1574-6968.2008.01464.x

Ma, L., Xi, S., Zhang, X., Luan, Z., Du, Z., Li, L., et al. (2021). Influence of vapor-phase fluids on the geochemical characterization of hydrothermal sulfides in the shimmering waters of the southern Okinawa trough. *Ore Geol. Rev.* 139:104496. doi: 10.1016/j.oregeorev.2021.104496

Numata, Y., Shinohara, Y., Kitayama, T., and Tanaka, H. (2013). Rapid and accurate quantitative analysis of fermentation gases by Raman spectroscopy. *Process Biochem.* 48, 569–574. doi: 10.1016/j.procbio.2013.02.018

Osman, J. R., Cardon, H., Montagnac, G., Picard, A., and Daniel, I. (2021). Pressure effects on sulfur-oxidizing activity of Thiobacillus thioparus. *Environ. Microbiol. Rep.* 13, 169–175. doi: 10.1111/1758-2229.12922

Peercy, P. S., and Morosin, B. (1973). Pressure and temperature dependences of the Raman-active phonons in SnO_2. *Phys. Rev. B* 7, 2779–2786. doi: 10.1103/PhysRevB.7.2779

Petrov, D. V. (2017). Pressure dependence of peak positions, half widths, and peak intensities of methane Raman bands (ν_2, $2\nu_4$, ν_1, ν_3, and $2\nu_2$). *J. Raman Spectrosc.* 48, 1426–1430. doi: 10.1002/jrs.5141

Picard, A., Daniel, I., Montagnac, G., and Oger, P. (2007). *In situ* monitoring by quantitative Raman spectroscopy of alcoholic fermentation by Saccharomyces cerevisiae under high pressure. *Extremophiles* 11, 445–452. doi: 10.1007/s00792-006-0054-x

Pironon, J., Grimmer, J. O. W., Teinturier, S., Guillaume, D., and Dubessy, J. (2003). Dissolved methane in water: Temperature effect on Raman quantification in fluid inclusions. *J. Geochem. Explor.* 78–79, 111–115. doi: 10.1016/s0375-6742(03)00136-5

Schalk, R., Braun, F., Frank, R., Radle, M., Gretz, N., Methner, F. J., et al. (2017). Non-contact Raman spectroscopy for in-line monitoring of glucose and ethanol during yeast fermentations. *Bioprocess Biosyst. Eng.* 40, 1519–1527. doi: 10.1007/s00449-017-1808-9

Seitz, J. C., Pasteris, J. D., and Chou, I. M. (1993). Raman spectroscopic characterization of gas mixtures; I, quantitative composition and pressure determination of CH_4, N_2 and their mixtures. *Am. J. Sci.* 293, 297–321. doi: 10.2475/ajs.293.4.297

Seitz, J. C., Pasteris, J. D., and Chou, I. M. (1996). Raman spectroscopic characterization of gas mixtures; II, quantitative composition and pressure determination of the CO_2–CH_4 system. *Am. J. Sci.* 296, 577–600. doi: 10.2475/ajs.296.6.577

Shi, L., Xu, L., Xiao, R., Zhou, Z., Wang, C., Wang, S., et al. (2020). Rapid, quantitative, high-sensitive detection of Escherichia coli O157:H7 by gold-Shell silica-Core

Nanospheres-based surface-enhanced Raman scattering lateral flow immunoassay. *Front. Microbiol.* 11:596005. doi: 10.3389/fmicb.2020.596005

Shope, T. B., Vickers, T. J., and Mann, C. K. (1987). The direct analysis of fermentation products by Raman spectroscopy. *Appl. Spectrosc.* 41, 908–912. doi: 10.1366/0003702874448373

Simankova, M. V., Parshina, S. N., Tourova, T. P., Kolganova, T. V., Zehnder, A. J., and Nozhevnikova, A. N. (2001). Methanosarcina lacustris sp. nov., a new psychrotolerant methanogenic archaeon from anoxic lake sediments. *Syst. Appl. Microbiol.* 24, 362–367. doi: 10.1078/0723-2020-00058

Szostak, R., and Mazurek, S. (2002). Quantitative determination of acetylsalicylic acid and acetaminophen in tablets by FT-Raman spectroscopy. *Analyst* 127, 144–148. doi: 10.1039/b108240j

Wang, X., Chou, I. M., Hu, W., Burruss, R. C., Sun, Q., and Song, Y. (2011). Raman spectroscopic measurements of CO_2 density: Experimental calibration with high-pressure optical cell (HPOC) and fused silica capillary capsule (FSCC) with application to fluid inclusion observations. *Geochim. Cosmochim. Acta* 75, 4080–4093. doi: 10.1016/j.gca.2011.04.028

Wang, S., Xi, S., Pan, R., Yang, Y., Luan, Z., Yan, J., et al. (2022). One-step method to prepare coccinellaseptempunctate-like silver nanoparticles for high sensitivity SERS detection. *Surf. Interfaces* 35:102440. doi: 10.1016/j.surfin.2022.102440

Wopenka, B., and Pasteris, J. D. (1987). Raman intensities and detection limits of geochemically relevant gas mixtures for a laser Raman microprobe. *Anal. Chem.* 59, 2165–2170. doi: 10.1021/ac00144a034

Wu, Z., Xu, E., Long, J., Wang, F., Xu, X., Jin, Z., et al. (2015). Measurement of fermentation parameters of Chinese rice wine using Raman spectroscopy combined with linear and non-linear regression methods. *Food Control* 56, 95–102. doi: 10.1016/j.foodcont.2015.03.015

Yang, S., Lv, Y., Liu, X., Wang, Y., Fan, Q., Yang, Z., et al. (2020). Genomic and enzymatic evidence of acetogenesis by anaerobic methanotrophic archaea. *Nat. Commun.* 11:3941. doi: 10.1038/s41467-020-17860-8

Zhang, X., Du, Z. F., Zheng, R. E., Luan, Z. D., Qi, F. J., Cheng, K., et al. (2017). Development of a new deep-sea hybrid Raman insertion probe and its application to the geochemistry of hydrothermal vent and cold seep fluids. *Deep-Sea Res. I Oceanogr. Res. Pap.* 123, 1–12. doi: 10.1016/j.dsr.2017.02.005

Zhang, Y., Zou, Y., Liu, F., Xu, Y., Wang, X., Li, Y., et al. (2016). Stable graphene-isolated-au-nanocrystal for accurate and rapid surface enhancement Raman scattering analysis. *Anal. Chem.* 88, 10611–10616. doi: 10.1021/acs.analchem.6b02958

Zheng, R., Cai, R., Wang, C., Liu, R., and Sun, C. (2022). Characterization of the first cultured representative of "Candidatus Thermofonsia" clade 2 within Chloroflexi reveals its phototrophic lifestyle. *MBio* 13:e0028722. doi: 10.1128/mbio.00287-22

Zheng, R., Liu, R., Shan, Y., Cai, R., Liu, G., and Sun, C. (2021). Characterization of the first cultured free-living representative of Candidatus Izemoplasma uncovers its unique biology. *ISME J.* 15, 2676–2691. doi: 10.1038/s41396-021-00961-7

Zhilina, T. N., Zavarzina, D. G., Kevbrin, V. V., and Kolganova, T. V. (2013). Methanocalculus natronophilus sp. nov., a new alkaliphilic hydrogenotrophic methanogenic archaeon from a soda lake, and proposal of the new family Methanocalculaceae. *Microbiology* 82, 698–706. doi: 10.1134/s0026261713060131

Zhou, Z., Zhang, C. J., Liu, P. F., Fu, L., Laso-Perez, R., Yang, L., et al. (2022). Non-syntrophic methanogenic hydrocarbon degradation by an archaeal species. *Nature* 601, 257–262. doi: 10.1038/s41586-021-04235-2

frontiers | Frontiers in Microbiology

TYPE Original Research
PUBLISHED 02 June 2023
DOI 10.3389/fmicb.2023.1152818

OPEN ACCESS

EDITED BY
Ruiyong Zhang,
Institute of Oceanology,
Chinese Academy of Sciences (CAS), China

REVIEWED BY
Jian Liu,
Shandong University, China
Junhong Bai,
Beijing Normal University, China
Sunil Mundra,
United Arab Emirates University,
United Arab Emirates

*CORRESPONDENCE
Haitao Wu
✉ wuhaitao@iga.ac.cn

RECEIVED 28 January 2023
ACCEPTED 29 March 2023
PUBLISHED 02 June 2023

CITATION
Kang Y, Wu H, Zhang Y, Wu Q, Guan Q, Lu K and Lin Y (2023) Differential distribution patterns and assembly processes of soil microbial communities under contrasting vegetation types at distinctive altitudes in the Changbai Mountain.
Front. Microbiol. 14:1152818.
doi: 10.3389/fmicb.2023.1152818

Differential distribution patterns and assembly processes of soil microbial communities under contrasting vegetation types at distinctive altitudes in the Changbai Mountain

Yujuan Kang[1,2], Haitao Wu[1]*, Yifan Zhang[1,3], Qiong Wu[1,3], Qiang Guan[1], Kangle Lu[1] and Yiling Lin[1]

[1]Key Laboratory of Wetland Ecology and Environment, Northeast Institute of Geography and Agroecology, Chinese Academy of Sciences, Changchun, China, [2]College of Resources and Environment, University of Chinese Academy of Sciences, Beijing, China, [3]College of Tourism and Geography Sciences, Jilin Normal University, Siping, China

Diversity patterns and community assembly of soil microorganisms are essential for understanding soil biodiversity and ecosystem processes. Investigating the impacts of environmental factors on microbial community assembly is crucial for comprehending the functions of microbial biodiversity and ecosystem processes. However, these issues remain insufficiently investigated in related studies despite their fundamental significance. The present study aimed to assess the diversity and assembly of soil bacterial and fungal communities to altitude and soil depth variations in mountain ecosystems by using 16S and ITS rRNA gene sequence analyses. In addition, the major roles of environmental factors in determining soil microbial communities and assembly processes were further investigated. The results showed a U-shaped pattern of the soil bacterial diversity at 0–10 cm soil depth along altitudes, reaching a minimum value at 1800m, while the fungal diversity exhibited a monotonically decreasing trend with increasing altitude. At 10–20 cm soil depth, the soil bacterial diversity showed no apparent changes along altitudinal gradients, while the fungal Chao1 and phylogenetic diversity (PD) indices exhibited hump-shaped patterns with increasing altitude, reaching a maximum value at 1200m. Soil bacterial and fungal communities were distinctively distributed with altitude at the same depth of soil, and the spatial turnover rates in fungi was greater than in bacteria. Mantel tests suggested soil physiochemical and climate variables significantly correlated with the β diversity of microbial community at two soil depths, suggesting both soil and climate heterogeneity contributed to the variation of bacterial and fungal community. Correspondingly, a novel phylogenetic null model analysis demonstrated that the community assembly of soil bacterial and fungal communities were dominated by deterministic and stochastic processes, respectively. The assembly processes of bacterial community were significantly related to the soil DOC and C:N ratio, while the fungal community assembly processes were significantly related to the soil C:N ratio. Our results provide a new perspective to assess the responses of soil microbial communities to variations with altitude and soil depth.

KEYWORDS

altitudinal gradient, spatial scaling, assembly processes, soil depth, soil microbiota

1. Introduction

The spatial distribution patterns of biome structure and diversity, as well as their underlying mechanisms that regulate spatiotemporal changes are the core theme of biogeography (Green and Bohannan, 2006; Chu et al., 2020). Numerous biogeographical studies have focused on the responses of ecosystems to large-scale environmental changes (Fukami and Wardle, 2005; Walker et al., 2010). Altitude gradients provided a verification platform for models to accurately predict biodiversity responses to global change (McCain and Colwell, 2011). Soil microorganisms play an essential role in biogeochemical cycles within terrestrial ecosystems and are sensitive to environmental changes. Therefore, it is crucial to reveal the fundamental mechanisms underlying the microbial community diversity and distribution patterns to assess their relationships with community stability and ecosystem functions, which are the main central goal in community ecology (Hanson et al., 2012; Meyer et al., 2018). In this context, spatial variations in the soil microbial community at large spatial scales have been continually investigated in different ecosystems, including farmland (Constancias et al., 2015), woodland (Singh et al., 2014; Schnecker et al., 2015), grassland (Baker et al., 2009), tundra (Bjork et al., 2008; Kim et al., 2014), and deserts (Andrew et al., 2012). Studies have highlighted the inconsistent conclusions on the altitudinal distribution patterns of microbial communities, such as monotonous (Bryant et al., 2008; Wang et al., 2011), unimodal (Singh et al., 2012), concave (Singh et al., 2014), and no altitude pattern (Shen et al., 2013). Although the influence of spatial distance on microbial distribution was confirmed (Whitaker et al., 2003; Papke and Ward, 2004), few studies have investigated the impacts of spatial distance on microbial evolution in mountain ecosystems considering the strong diffusion ability of soil microorganisms.

Natural selection, dispersal, drift, species formation, and extinction rates showed the strongest effects on microbial altitude diversity patterns (Kassen and Rainey, 2004; Hanson et al., 2012; Nemergut et al., 2013). Previous studies have showed that microbial communities are influenced by both biotic factors (e.g., terrestrial vegetation characteristics) and abiotic factors (e.g., climatic factors and soil physicochemical properties) (Bezemer et al., 2010; Orwin et al., 2010; Thoms et al., 2010; de Vries et al., 2012). Previous studies have revealed clearly spatial distribution patterns of soil microbial communities and diversity (Green et al., 2004; Fierer and Jackson, 2006; Fierer et al., 2009; Lauber et al., 2009; Nemergut et al., 2011). Soil pH, C:N ratio, and vegetation types were the key factors controlling the altitudinal distribution pattern of soil microbial diversity (Rousk et al., 2010; Shen et al., 2016; Bahram et al., 2018).

The Changbai Mountain area is one of the most biodiversity-rich temperate regions, making it a suitable area for studying biodiversity patterns (Yang and Xu, 2003; Shen et al., 2014; Zou et al., 2017). The main objective of this study is to investigate variations in soil microbial (bacterial and fungal) community structures and their assemblies at four altitudes (800, 1200, 1800, and 2300 m) and two soil depths (0–10 cm and 10–20 cm), as well as their responses to environmental factors on Changbai Mountain. The distance-decay relationships (DDRs) were used to explore changes in spatial turnover rates, while a null model was applied to measure microbial assemblies in different soil samples. The following hypotheses were examined in this study: (i) Altitudinal gradients and soil depths have a substantial impact on the diversities and communities of soil microorganism, as well as the spatial turnover rates of their communities. (ii) Altitudinal gradients and soil depths can distinctly influence the mechanisms of microbial community assembly, which are shaped by distinct environmental factors.

2. Materials and methods

2.1. Site selection and soil sampling

This study was conducted in autumn 2021 on Changbai Mountain (126°55′-129°00′E; 41°23′- 42°36′N), Jilin, northeast China. The study area has a temperate continental monsoon climate with altitudinal variability, whereas the winter is long and cold, and the summer is short and cool. The annual temperature and precipitation range from 2.9 to 4.8°C and 632 to 1154 mm, respectively. The main vegetation types, which exhibit an altitudinal distribution from low 800 m to high 2300 m, consist of mixed coniferous broad-leaved forest (MCB), coniferous spruce forest (CS), Erman's birch forest (EB), and alpine tundra (AT; Figure 1). The climate and main vegetation characteristics of each habitat are reported in Supplementary Table S1. Three plots (25 m × 25 m each) were established for each vegetation type. To minimize the heterogeneity, we divided each plot into three subplots for soil sampling. The collected soil samples from the three subplots were mixed to obtain one composite soil sample from each plot. In total, 72 subplots were established in the field experiment (4 altitudes × 3 subplots × 3 replicates × 2 depths), from which 24 composite soil samples were collected (4 altitudes × 2 depths × 3 replicates). The collected composite soil samples were placed in plastic bags on ice and transported to the laboratory for further analysis. Soil samples were sieved through 2-mm sieve after the removal of visible debris, such as roots and litter and stored at 4°C for chemical analysis or at −80°C for DNA extraction.

2.2. Determination of soil physicochemical properties

Soil pH was measured using a PHS-3C pH meter (PHS-3C pH acidometer) after shaking the soil solution (soil: water = 1: 5) for 30 min. Soil TC and TN contents were determined using a Carlo Erba FLASHEA 1112 CHN-S analyzer according to the instruction manual. Soil total organic (TOC) contents were determined using the external heating-potassium dichromate titration method. Soil total phosphorus (TP) contents were determined using the nitric acid-perchloric acid digestion method combined with a continuous flow analytical system (San++ System, Skalar, Holland) according to the instruction manual. Soil dissolved organic carbon (DOC) contents were determined using a total organic carbon analyzer (TOC VCPH, Shimadzu) according to the instruction manual.

2.3. DNA extraction and bar-coded pyrosequencing of the 16S rRNA genes

DNA was first extracted from 0.5 g soil samples using the FastDNA SPIN Kit for soil (MP Biomedicals, Santa Ana, CA, United States), then purified using the UltraClean Soil DNA Kit (MOBIO Laboratories, Carlsbad, CA, United States) following the manufacturer's instructions. Bacterial 16S rRNA gen V3–V4 region was amplified using the 338F and 806R primers, while the ITS1 region of fungal ITS gene were

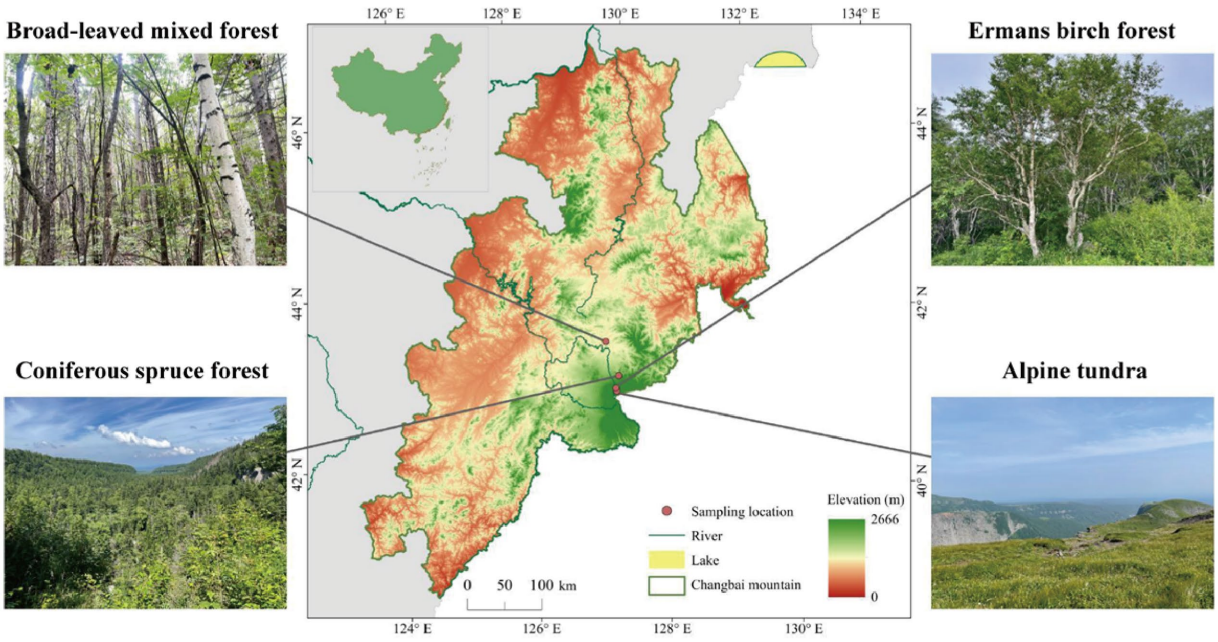

FIGURE 1
Vegetation types at the study sites on the northern slope of Changbai Mountain, northeast China.

amplified using the ITS1F and ITS2R primers (Adams et al., 2013). The PCR reactions were performed in triplicate. The PCR product was first extracted from 2% agarose gel, then purified using the AxyPrep DNA Gel Extraction Kit (Axygen Biosciences, Union City, CA, United States) and quantified using an Quantus™ Fluorometer (Promega, United States). NEXTFLEX® Rapid DNA-Seq Kit was used to build the library. Purified amplicons were pooled in equimolar amounts and paired-end sequencing was performed on an Illumina MiSeq platform (Illumina, San Diego, United States) in the Majorbio Bio-Pharm Technology Co. Ltd. (Shanghai, China) according to its standard protocols.

2.4. Sequence data processing

Raw sequence data were processed and analyzed using the QIIME software package (Caporaso et al., 2010). The extraction of non-repeated sequences from the optimized sequence was convenient for reducing the redundant calculation in the intermediate process of analysis. Operational taxonomic unit (OTU) clustering was performed according to 97% similarity on non-repeated sequences (excluding single sequence). Chimeras were removed prior to the clustering process to obtain a representative OTU sequence. In order to classify species according to OTU sequences, the RDP classifier Bayesian algorithm was used to classify the representative OTU sequences at a 97% sequence similarity level.

2.5. Statistical analysis

The one-way analysis of variance (ANOVA), with the least significant difference (LSD) method, was performed using SPSS 19.0 to determine whether the differences between treatments were significant at the $p < 0.05$ level. The analysis of similarity (ANOSIM) was performed based on the Bray-Curtis distance using the *vegan* package in R (Version 3.3.1). The Mantel test was performed based on Bray-Curtis in QIIME software (Version 1.9.1). QIIME was used to calculate the β diversity distance matrix, while the *vegan* package was used for Nonmetric Multidimensional Scaling (NMDS). The Shannon and Chao1 indices were calculated in R to estimate α-diversity of the soil bacterial and fungal communities. The Phylogenetic diversity (PD) indices were analyzed on the online tool of Majorbio Cloud Platform.[1] Distance-based redundancy analysis (db-RDA) was performed using the *vegan* package in R. The distance-decay relationships (DDRs) were investigated based on taxonomic dissimilarities (Sorensen distance) (Oksanen et al., 2020).

The slope of the ordinary least-squares regression between the log-transformed geographic distance and microbial community similarity was used to quantify the distance-decay rate of the microbial community using the *vegan* R package (Dixon, 2003). One-way ANOVA was performed to examine the significance of the slopes of the two curves using the *lsmeans* R package (Lenth, 2016). Null modeling-based approaches were performed to infer community assembly mechanisms (Chase and Myers, 2011; Stegen et al., 2013; Chase et al., 2019). First, representative OTU sequences were introduced into MEGA software (Version 10.2.4) to build a phylogenetic tree using the maximum likelihood method, then the *ape* R package was loaded to read the phylogenetic tree (.tre) and OTU-table (.csv) files. The mean nearest phylogenetic taxon distance (MNTD) and nearest taxon index (NTI) indices were calculated using the *Picante* package (Kembel et al., 2010).

1 https://cloud.majorbio.com/page/tools/

An average NTI value greater than 0 indicates sample aggregation and the next step calculation can be performed, while an average NTI value lower than 0 indicates sample dispersion requiring further re-grouping. In addition, the βMNTD and βNTI indices of different samples were calculated using the same calculation method. The last operation is the RCbray index (Stegen et al., 2013). The *Picante* package was used to further quantify the deterministic (heterogeneous and homogenous selections) and randomness processes (diffusion limits and co-diffusion). The null model, based on the βNTI and RCbray indices, was applied to quantify the contributions of the deterministic and randomness processes to soil microbial community assembly. βNTI values that were lower than −2 or higher than 2 indicated that the communities were driven by homogeneous or heterogenous processes. In addition, a |βNTI| value lower than 2 suggested a stochastic assembly process of microbial community, and the diffusion limit (RCbray >0.95), isotropic diffusion (RCbray < −0.95), and uncertain process (−0.95 < RCbray <0.95) were determined according to the size of RCbray index in the assembly processes of microbial communities (Stegen et al., 2015).

3. Results

3.1. Diversity, composition and structure of microbial communities

The minimal bacterial Shannon, Chao1, and PD diversity indices at 0–10 cm depth were observed at 1800 m, showing a U-shaped altitudinal pattern, while the fungal α-diversity indices decreased with altitude (Figure 2 and Supplementary Figure S1). The bacterial diversity showed no obvious altitude pattern at 10–20 cm depth, while the fungal Chao1 and PD indices showed hump patterns with increasing altitude (Figure 2 and Supplementary Figure S2). The two most abundant bacterial phyla were Acidobacteria and Proteobacteria, accounting for 48.41–64.58% of the pyrosequences, followed in abundance by Actinobacteriota (12.31–27.48%), Chloroflexi (2.34–14.33%), Verrucomicrobiota (2.50–4.78%; Figure 3). The two most abundant fungal phyla were Basidiomycota and Ascomycota, accounting for 69.82–99.37% of the pyrosequences, followed by Mortierellomycota (0.52–21.14%), unclassified_k__Fungi (0.1–8.96%), and Rozellomycota (0.01–4.52%; Figure 3). The relative abundance of Proteobacteria at 0–10 cm depth was significantly higher than that at 10–20 cm soil depth at all altitudes ($F = 13.77$, $p < 0.05$, 800 m; $F = 18.77$, $p < 0.05$, 1800 m; $F = 15.35$, $p < 0.05$, 2300 m), except for 1200 m (Supplementary Figure S3). At 1800 m, the relative abundance of Basidiomycota at 0–10 cm soil depth was significantly lower ($F = 9.17$, $p < 0.05$) than that at 10–20 cm soil depth (Supplementary Figure S3). The NMDS plots showed different soil microbial compositions in the collected soil samples with respect to different altitudes (Figure 4). In addition, both soil depths showed significant variability along the altitude gradient (Figure 4 and Table 1).

3.2. Correlations between microbial communities and soil properties

The Mental test showed significant correlations between community composition and environmental variables (Table 2). The C:N ratio showed significant positive correlations with the soil

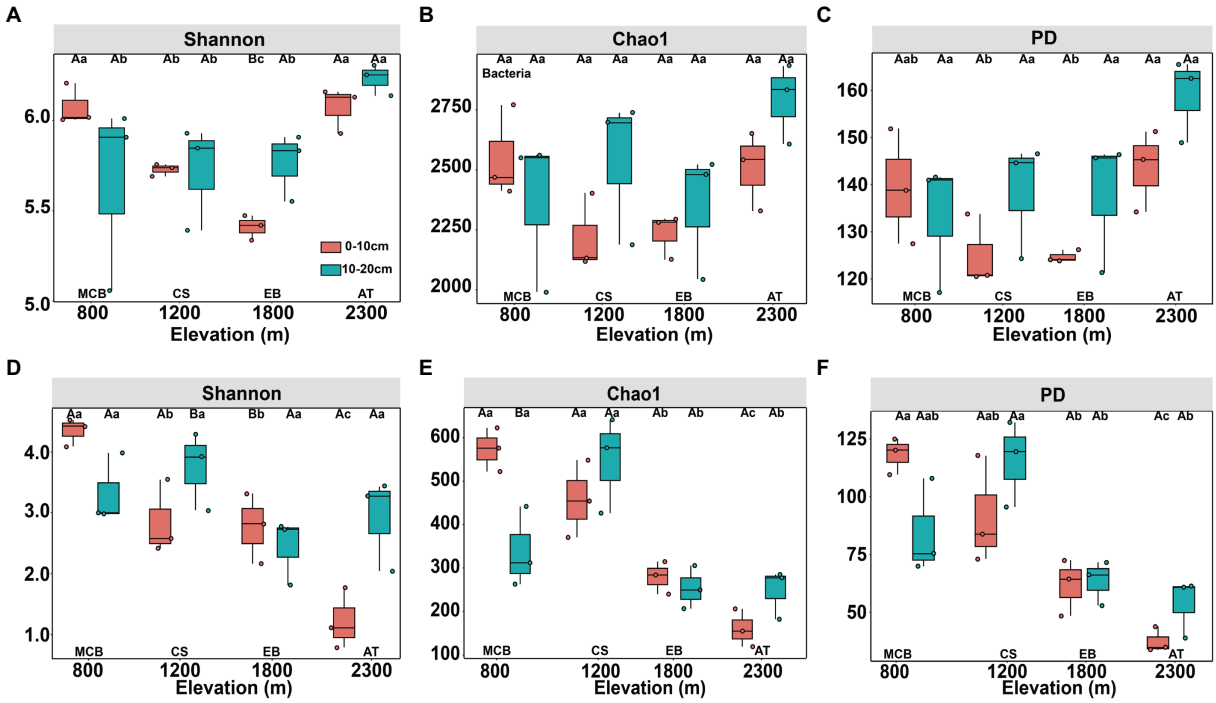

FIGURE 2
Changes in diversity of soil bacterial **(A–C)** and fungal **(D–F)** communities along altitudinal gradient and soil depth on Changbai Mountain. Capital letters indicate significant differences ($p<0.05$) between soil depth treatments, lower case letters indicate significant differences ($p<0.05$) between altitude treatments.

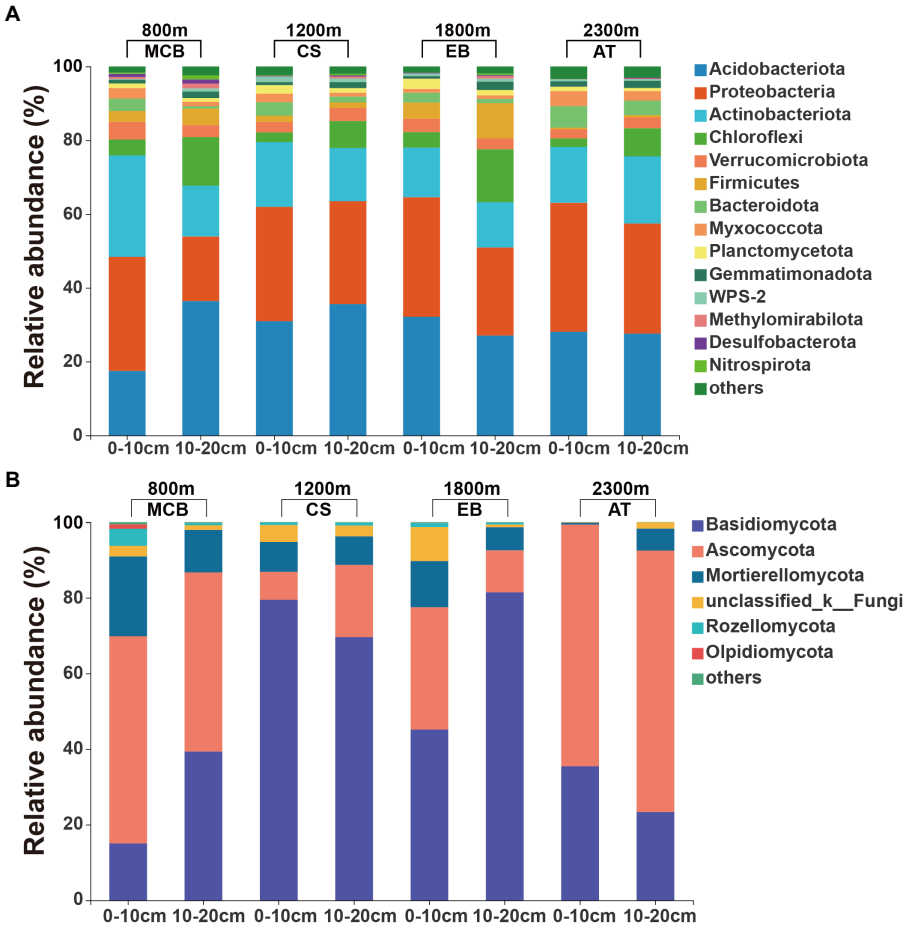

FIGURE 3
Relative abundances of the major soil **(A)** bacterial and **(B)** fungal communities at the phylum level.

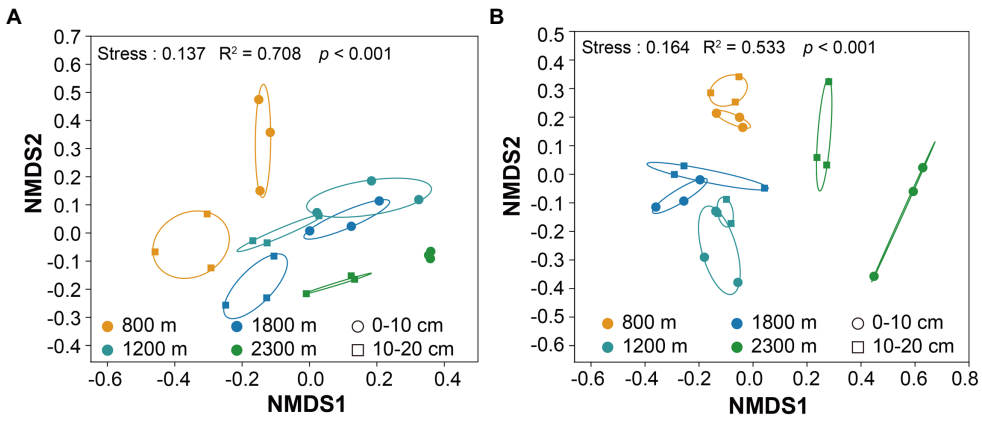

FIGURE 4
Non-metric multidimensional scaling (NMDS) of the bacterial **(A)** and fungal **(B)** communities along altitudes and soil depths.

bacterial community compositions at 0–10 cm ($r = 0.757$, $p < 0.001$) and 10–20 cm ($r = 0.387$, $p < 0.05$) soil depths (Table 2). Soil TP contents exhibited a significant positive correlation with the soil fungal community composition at 0–10 cm soil depth ($r = 0.451$, $p < 0.001$), while TOC was the most relevant soil variables to the soil fungal community at 10–20 cm soil depth ($r = 0.341$, $p < 0.01$; Table 2).

TABLE 1 Anosim and Adonis analysis of altitude and soil depth in shaping the bacterial and fungal communities structure.

	Bacteria				Fungi			
	Anosim		Adonis		Anosim		Adonis	
	F	*p*	*F*	*p*	*F*	*p*	*F*	*p*
0–10 cm	0.864	<0.001	0.651	<0.001	0.877	<0.001	0.525	<0.001
10–20 cm	0.941	<0.001	0.641	<0.001	0.966	<0.001	0.494	<0.001

TABLE 2 Results of Mantel test on the correlation between community composition (Bray-Curtis) and environmental variables for bacteria and fungi.

Variable	Bacteria				Fungi			
	0–10cm		10–20cm		0–10cm		10–20cm	
	r	*p*	*r*	*p*	*r*	*p*	*r*	*p*
TP	**0.387**	**0.014**	−0.035	0.812	**0.451**	**0.001**	**0.214**	**0.027**
DOC	**0.274**	**0.050**	0.210	0.114	0.101	0.359	**0.258**	**0.027**
AN	0.244	0.064	0.066	0.648	**0.378**	**0.005**	0.022	0.825
pH	**0.301**	**0.021**	0.124	0.313	**0.279**	**0.018**	**0.261**	**0.022**
TN	**0.292**	**0.035**	−0.022	0.866	**0.369**	**0.003**	0.163	0.130
TC	**0.325**	**0.031**	0.258	0.051	0.172	0.154	**0.320**	**0.011**
TOC	**0.264**	**0.037**	**0.301**	**0.028**	0.097	0.413	**0.341**	**0.007**
C:N ratio	**0.757**	**0.001**	**0.387**	**0.015**	**0.350**	**0.005**	**0.339**	**0.008**
MAT	**0.605**	**0.001**	**0.632**	**0.001**	**0.630**	**0.001**	**0.590**	**0.001**
MAP	**0.575**	**0.008**	**0.674**	**0.001**	**0.622**	**0.001**	**0.625**	**0.001**
Altitude	**0.668**	**0.001**	**0.697**	**0.001**	**0.545**	**0.001**	**0.606**	**0.001**

r, correlation coefficient of environmental factors with microbial communities; *p*-value, statistical significance; values in bold indicate significant correlations ($p < 0.05$). TP, total phosphorus; DOC, dissolved organic carbon; AN, available nitrogen; pH: pondus Hydrogenii; TN, total nitrogen; TC, total carbon; TOC, total organic carbon; C:N ratio, TC:TN; MAT: mean annual temperature; MAP: mean annual precipitation.

Distance-based redundancy analysis (db-RDA) demonstrated the stronger effects of the soil pH and C:N ratio on the bacterial and fungal communities, respectively (Figure 5). Among the abiotic factors, C:N ratio and soil pH were the two major soil variables contributing to the bacterial α-diversity variation (Figure 6A), while C:N ratio and altitude were the two major soil variables contributing to the fungal α-diversity variations (Figure 6B).

3.3. Assembly processes and driving factors for microbial communities

Community dissimilarity and geographic distance for each pairwise sample set showed a significant distance-decay relationship (DDR) of the microbial communities (Figures 7A,B). At the same soil depth, the spatial turnover rate of fungal community ($\beta = 0.134–0.138$) was higher than that of bacterial community ($\beta = 0.056–0.065$; Figures 7A,B). However, there was no significant difference in the turnover rates of soil bacterial and fungal communities between different soil depths (Figure 7C). Bacterial community assembly was determined by deterministic process (53.47%), while assembly processes of soil fungal communities was mainly determined by stochastic process (90.62%; Figure 8A). At 0–10 cm depth, the effect of the deterministic process (heterogeneous selection) on soil bacterial community assembly was dominated at the lowest altitude (800 m), while that of the stochastic process (undominated and dispersal limitation) exhibited a gradual dominance at the remaining altitudes (Figure 8B). The soil bacterial community assembly was mostly driven by the stochastic process at 10–20 cm soil depth (Figure 8B). In contrast, the fungal community assembly was dominated by the stochastic process among all selected altitudes and soil depths (Figure 8C).

The main explanatory soil variables were selected to determine the correlations between the assembly processes of microbial communities and environmental variables (based on Euclidean distance matrices; Table 3). For bacterial community, the significant positive correlations of βNTI with DOC ($r^2 = 0.206$, $p < 0.001$) and C:N ratio ($r^2 = 0.141$, $p < 0.001$; Figure 9). Whereas for fungal community, a significant positive correlation was observed between the soil C:N ratio and βNTI ($r^2 = 0.141$, $p < 0.001$; Figure 9).

The multiple regression model (MRM) was used to further assess the relative contributions of each environmental factor to the soil bacterial and fungal communities (Table 4). According to the obtained results, the soil C:N ratio ($R^2 = 0.419$, $p < 0.001$) and altitude ($R^2 = 0.534$, $p < 0.001$) significantly explained the variations of soil bacterial community dissimilarities at the upper and deeper soil depths, respectively (Table 4). Whereas MAP significantly explained the variations in the soil fungal community dissimilarities at both soil depths (Table 4).

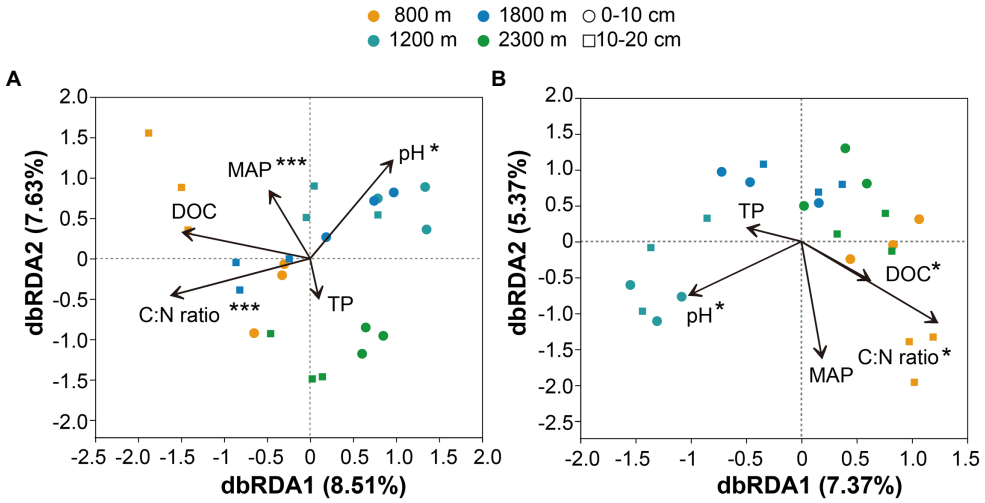

FIGURE 5
Distance-based redundancy analysis of soil bacterial **(A)** and fungal **(B)** communities along altitudinal gradient and soil depth as related to environmental variables. pH: pondus Hydrogenii; DOC, dissolved organic carbon; TP, total phosphorus; C:N ratio, TC/TN; MAP, mean annual precipitation. *p<0.05; **p<0.01; ***p<0.001.

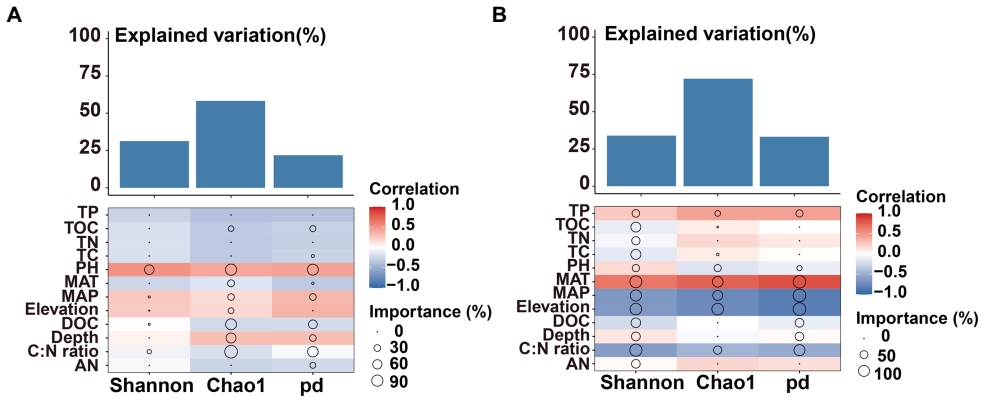

FIGURE 6
Contributions of environmental factors to bacterial bacterial **(A)** and fungal **(B)** α-diversity based on correlation and random forest model. Circle size represents the variable's importance (i.e., percentage of increase of mean square error calculated *via* random forest model). Colors represent spearman's correlations.

4. Discussion

The altitudinal diversity pattern is one of the most fundamental patterns in animal and plant biogeography (Denef et al., 2009). Here we observed that soil bacterial diversity appeared a U-shaped pattern with altitude at 0–10 cm soil depth, which is in line with the previous results (Singh et al., 2014). The α-diversity of soil bacterial communities did not show an obvious distribution pattern with altitudes at 10–20 cm soil depth, which was consistent with the results revealed in previous studies (Fierer et al., 2011). The peak pattern (Miyamoto et al., 2014; Wang et al., 2015; Ogwu et al., 2019) or U-shaped pattern (Liu et al., 2018) of soil fungal community were observed in previous studies, showing the highest and lowest diversity observed at mid-altitude. The α-diversity of fungal community at 0–10 cm soil depth exhibited a monotonically decreasing trend with altitude (Figure 2 and Supplementary Figure S2), while the Chao1 and PD indices of the fungal communities at 10–20 cm soil depth showed a hump-shaped pattern (Figure 2 and Supplementary Figure S3). In addition, the significant differences of ectomycorrhizal fungi distribution between soil depths might resulted in different substrate utilization patterns (Dickie et al., 2002).

Both bacterial and fungal communities were significantly different among the selected altitudes and soil depth (Figure 4 and Table 1). We found bacterial and fungal communities have significant correlation with altitude (Table 2). Previous research found that bacterial community composition varied with elevation (Fierer et al., 2011). The fungal community composition had significant differences along the altitude gradient (Kivlin et al., 2014), which might be due to the different selection of soil habitats by different fungal groups, with obvious ecological niche differentiation (Cook and Quinn, 1995). It had been reported that the spatial distribution pattern of fungal community was closely related to environmental heterogeneity (pH,

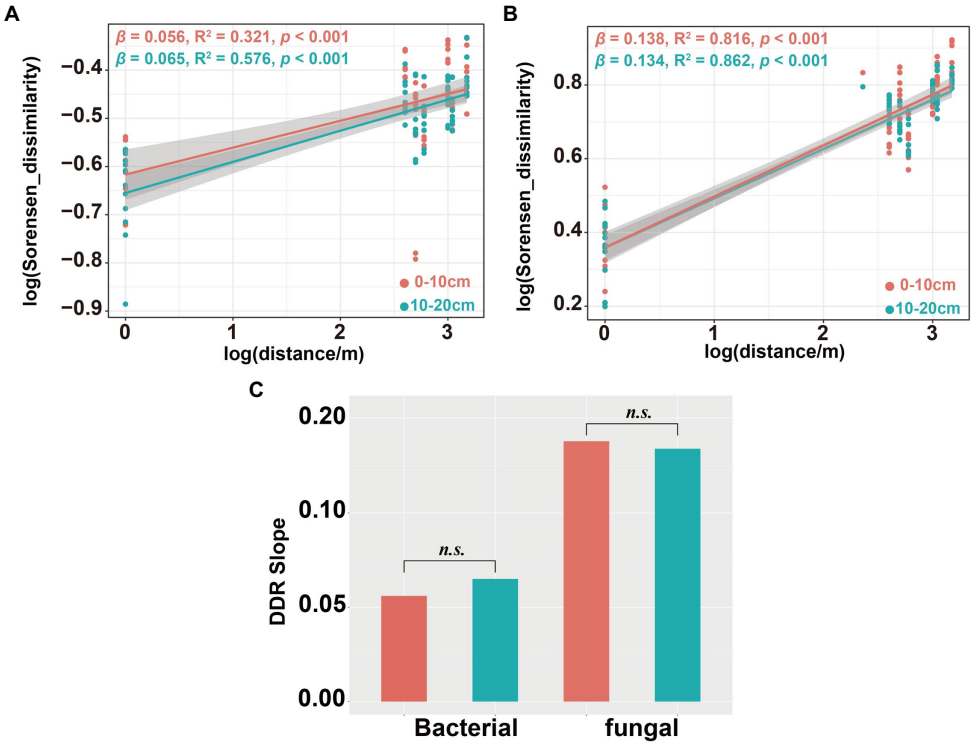

FIGURE 7
Distance-decay relationship (DDR) for the soil bacterial and fungal communities. DDR based on Sorensen dissimilarity along geographic distances for the bacterial community **(A)**; DDR for the fungal community **(B)** and DDR slope significance test of soil bacterial and fungal communities **(C)**. The slope β of DDR represent the spatial turnover rate of species.

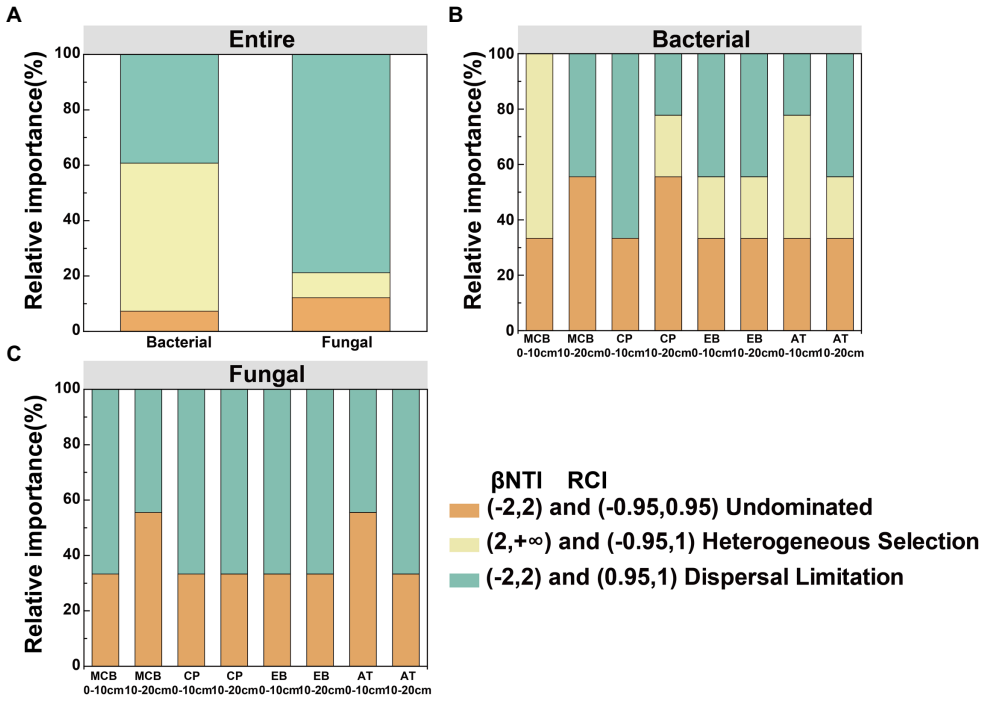

FIGURE 8
Deterministic and stochastic processes in the assembly of soil bacterial and fungal communities in the Changbai Mountain. These two processes were both detected using the β-Nearest Taxon Index (βNTI) and Raup-Crick Index (RCI). **(A)** Relative influences of deterministic and stochastic assembly processes in shaping a bacterial and fungal community. Relative influences of deterministic and stochastic assembly processes in shaping bacterial community **(B)** and fungal community **(C)** for different treatments.

TABLE 3 Mantel tests of environmental variables against the phylogenetic turnover (β-nearest taxon index) of the soil bacterial and fungal communities.

Variable	Bacteria		Fungi	
	Mantel r	*p*	Mantel r	*p*
TP	−0.0380	0.9952	0.0057	0.2145
DOC	0.0408	0.0004	0.0131	0.0082
AN	0.0054	0.3130	0.0082	0.0740
pH	0.0048	0.3630	0.0355	0.0001
TN	−0.0100	0.7858	−0.0017	0.5988
TC	−0.0098	0.7484	−0.0048	0.7798
TOC	−0.0140	0.8465	−0.0020	0.6018
C:N ratio	0.0306	0.0354	0.1039	0.0001
MAP	0.0443	0.0680	−0.0054	0.6798
MAT	0.0478	0.0456	−0.0059	0.6886
Altitude	−0.0129	0.8735	0.0003	0.4556

TP, total phosphorus; DOC, dissolved organic carbon; AN, available nitrogen; pH: pondus Hydrogenii; TN, total nitrogen; TC, total carbon; TOC, total organic carbon; C:N ratio, TC:TN; MAT: mean annual temperature; MAP: mean annual precipitation.

soil nutrition and altitude) (Cox et al., 2010; Polme et al., 2013). Acidobacteria and Proteobacteria were the major soil microorganisms on Changbai Mountain (Figure 3), which was consistent with the findings reported in previous studies (Shen et al., 2013). This might be due to the crucial role of Acidobacteria in organic matter decomposition and nutrient cycling (Eichorst et al., 2018). Proteobacteria have high morphological and metabolic diversity, which enables them to easily utilize soil organic carbon and nitrogen (Bryant and Frigaard, 2006; Mukhopadhya et al., 2012). Basidiomycetes and Ascomycetes were the dominant soil fungal groups due to the presence of a thicker litter layer in the upper soil layer than in the deeper soil layer. Indeed, Basidiomycetes can decompose complex lignocellulosic components (Lundell et al., 2010). Ascomycetes can use more resources to better tolerate environmental pressure (Yang et al., 2017; Egidi et al., 2019).

Soil nitrogen (N) and phosphorus (P) are important nutrients for bacterial growth and activity, influencing the spatial distribution of soil microorganisms (Wang et al., 2018; Zhang et al., 2019). Soil fungal diversity in forests was related to plant diversity, temperature, and altitude (Geml et al., 2014; Wang et al., 2015; Wan and He, 2020). Previous studies have pointed out that soil pH was a main factor

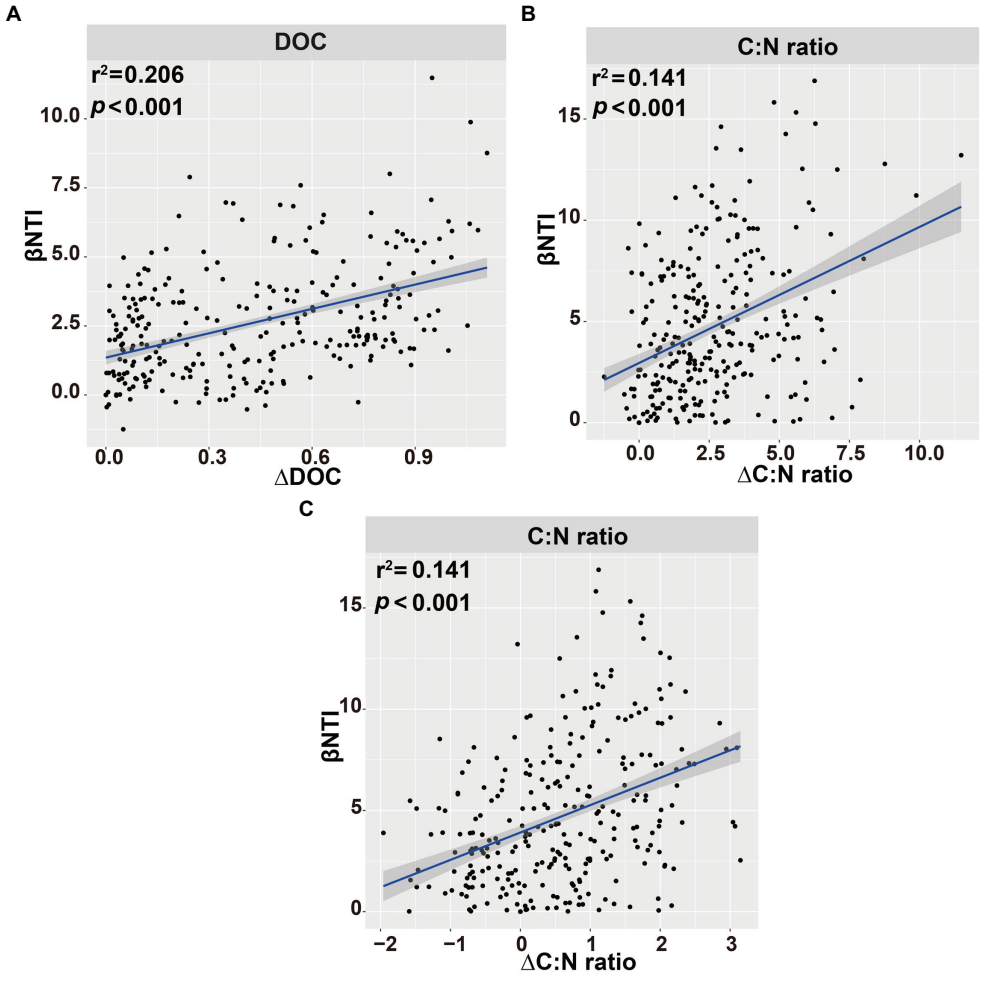

FIGURE 9
Linear regression analysis of the connections between β-nearest taxon index (βNTI) of soil bacterial **(A,B)** or fungal **(C)** communities and soil variables. Blue shaded area indicates 95% confidence interval (Spearman's $p<0.05$).

TABLE 4 Results of the multiple regression analysis on matrices analysis (MRM) for the microbial community composition.

	Bacteria				Fungi			
Variable	0–10cm		10–20cm		0–10cm		10–20cm	
	R^2	p	R^2	p	R^2	p	R^2	p
TP	0.132	0.036	0.004	0.698	0.189	0.003	0.034	0.103
DOC	0.044	0.099	0.027	0.225	0.015	0.405	0.028	0.154
AN	0.094	0.046	0.059	0.092	0.390	<0.001	0.019	0.222
pH	0.161	0.006	0.005	0.590	0.009	0.435	0.045	0.066
TN	0.058	0.109	0.012	0.451	0.435	0.002	0.009	0.387
TC	0.102	0.102	0.011	0.456	0.043	0.116	0.046	0.066
TOC	0.079	0.040	0.014	0.376	0.018	0.344	0.051	0.055
C:N ratio	0.419	<0.001	0.215	0.005	0.247	0.002	0.106	0.015
MAP	0.254	0.005	0.424	<0.001	0.711	<0.001	0.531	<0.001
MAT	0.335	0.004	0.394	<0.001	0.668	<0.001	0.480	<0.001
Altitude	0.346	<0.001	0.534	<0.001	0.437	<0.001	0.521	<0.001

The proportion of variation in Sorensen dissimilarity matrices is explained by the remaining variables.TP, total phosphorus; DOC, dissolved organic carbon; AN, available nitrogen; pH: pondus Hydrogenii; TN, total nitrogen; TC, total carbon; TOC, total organic carbon; C:N ratio, TC:TN; MAT, mean annual temperature; MAP, mean annual precipitation.

affected the distribution pattern of soil microbial communities along altitudinal gradients (Baath and Anderson, 2003; Lauber et al., 2009; Delgado-Baquerizo et al., 2017). Climatic factors (MAT and MAP) were dominant variables affected the diversity and community composition of bacteria (Singh et al., 2014; Xu et al., 2014; Nottingham et al., 2018; Frindte et al., 2019). The results of this study showed significant positive correlations of TP, DOC, pH, TN, TC, TOC, C:N ratio, MAT, MAP and altitudes with the bacterial community composition at upper soil depth, while TOC, C:N ratio, MAT, MAP and altitudes exhibited significant positive correlations with the bacterial community at deeper soil depth (Table 2). It is noteworthy that the soil fungal community composition exhibited significant positive correlations with soil TP and TOC contents at the upper and deeper soil depths, respectively (Table 2). Soil pH leads to niche differentiation of soil microbial and controls their patterns along altitude gradients (Shen et al., 2013; Bahram et al., 2018). Whereas soil C:N ratio and phosphorus contents could significantly affect the soil fungal diversity in forests and farmland (Lauber et al., 2013; Shen et al., 2017; Li et al., 2018; Delgado-Baquerizo and Eldridge, 2019). The importance of MAT had been widely reported at both horizontal and vertical scales (Yang et al., 2014; Delgado-Baquerizo et al., 2016; Zhou et al., 2016). Among the abiotic factors considered in this study, soil pH and C:N ratio were the major factors contributing to the variation in the soil bacterial α-diversity (Figure 6A), which is consistent with the results observed in Southwest Tibet (Peay et al., 2017; Shen et al., 2019), indicating that soil pH was the main factor controlling soil microbial diversity. Besides soil pH, soil C:N ratio and altitude showed correlations with microbial diversity (Singh et al., 2014; Shen et al., 2017; Li et al., 2018; Delgado-Baquerizo and Eldridge, 2019). This study demonstrated the contributions of the soil C:N ratio and altitudes to the variations in the fungal α-diversity (Figure 6B).

Several studies have shown that soil microbial community have obvious spatial scale patterns in DDRs (Soininen et al., 2007; Morlon et al., 2008; Deng et al., 2016). We observed steeper turnover slopes in the fungal community (β=0.134–0.138) than that in the bacterial community (β=0.056–0.065). This indicates greater dissimilarity of the soil fungal community over geographic distance than that of the soil bacterial community (Figures 7A,B). In addition, we also observed significant DDR for both bacterial (0–10 cm: R^2=0.321, p<0.001;10–20 cm: R^2=0.576, p<0.001) and fungal (0–10 cm: R^2=0.816, p<0.001;10–20 cm: R^2=0.862, p<0.001) communities, but soil depth had no significant effects on spatial turnover rate of either bacterial or fungal communities (Figure 7C). These spatial turnover patterns might be due to vegetation characteristics, geographic distance, and environmental conditions (Noss, 1990; Whittaker et al., 2001). Several studies have highlighted two primary factors that alter the spatial turnover rates of microorganisms (Deng et al., 2016). The first factor was niche selection which affects soil microorganism species through environmental heterogeneity, leading to variations in the community composition (Bell, 2010). The second factor was the restriction of spatial microbial dispersion (Cho and Tiedje, 2000; Peay et al., 2010), resulting in disparate soil microbial community (Zhou and Ning, 2017).

Quantifying the relative contributions of the microbial community to its construction provides an understanding of the spatiotemporal distribution patterns of the microbial community (Stegen et al., 2012). Our observation that deterministic assembly in the soil bacterial community was the dominant process (53.47%) and random assembly contributed substantially to the soil fungal community (90.62%; Figure 8), which was in line with the findings of previous studies (Zhang et al., 2018; Liu et al., 2020). This pointed out that soil bacterial community assembly was mainly driven by a deterministic process. Soil fungi require external forces to reproduce, such as wind, underground mycelial proliferation, plant transplantation, and animal activities (Liu et al., 2020).

It is essential to reveal the factors that lead to the dominance of different microbial community assembly processes. Previous studies have pointed out that assembly processes were related to soil chemical properties, such as pH, and NH_4^+-N (Jiang et al., 2019; Wan et al., 2021). In this study, the βNTI of bacteria was associated with the soil DOC contents and C:N ratio, while that of fungi was associated with the soil C:N ratio, suggesting that the assembly processes of soil bacterial and fungal communities were affected by soil parameters

(Figure 9). Soil organic carbon and nitrogen contents could be readily absorbed by Proteobacteria (Bryant and Frigaard, 2006; Mukhopadhya et al., 2012). The relative abundance of Bacteroidetes was positively correlated with resource availability, which could preferentially consume soil active organic carbon (Fierer et al., 2007).

5. Conclusion

Our study revealed changes in the soil microbial community along the altitudinal gradient and soil depth on Changbai Mountain, as well as the main mechanisms controlling the soil microbial community assembly. The obtained results revealed significant differences in the diversity, community composition, and structure of soil microorganisms between altitudes and soil depths. The soil bacterial and fungal communities exhibited clear spatial patterns without showing differences in their spatial turnover rates between soil depths. The community assembly of soil bacteria and fungi were dominated by deterministic and stochastic processes, respectively. The assembly processes of soil bacterial and fungal communities differed along the altitude gradient and soil depth, which were due to the spatial variability in soil factors that control the aggregation of bacterial and fungal communities.

Data availability statement

The data presented in the study are deposited in the National Center for Biotechnology Information (NCBI) repository, accession number PRJNA936073.

Author contributions

YK and HW designed the study, conducted the statistical analysis, and wrote the manuscript. YK, YZ, QW, QG, KL, and YL performed the field investigation and collected the data. All authors contributed to the article and approved the submitted version.

Funding

This work was supported by the National Natural Science Foundation of China (U20A2083), the National Key R&D Program of China (2022YFF1300900), and Jilin Scientific and Technological Development Program (20210509037RQ).

Acknowledgments

We are very grateful to Xiuxue Chen for making the sampling point map on this paper. We also thank Dandan Liu, Weiqiang Guo, and Zhiyu Zhang assistance in with field soil sampling.

Conflict of interest

The authors declare that the research was conducted in the absence of any commercial or financial relationships that could be construed as a potential conflict of interest.

Publisher's note

All claims expressed in this article are solely those of the authors and do not necessarily represent those of their affiliated organizations, or those of the publisher, the editors and the reviewers. Any product that may be evaluated in this article, or claim that may be made by its manufacturer, is not guaranteed or endorsed by the publisher.

Supplementary material

The Supplementary material for this article can be found online at: https://www.frontiersin.org/articles/10.3389/fmicb.2023.1152818/full#supplementary-material

References

Adams, R. I., Miletto, M., Taylor, J. W., and Bruns, T. D. (2013). Dispersal in microbes: fungi in indoor air are dominated by outdoor air and show dispersal limitation at short distances. *ISME J.* 7, 1262–1273. doi: 10.1038/ismej.2013.28

Andrew, D. R., Fitak, R. R., Munguia-Vega, A., Racolta, A., Martinson, V. G., and Dontsova, K. (2012). Abiotic factors shape microbial diversity in Sonoran Desert soils. *Appl. Environ. Microbiol.* 78, 7527–7537. doi: 10.1128/AEM.01459-12

Baath, E., and Anderson, T. H. (2003). Comparison of soil fungal/bacterial ratios in a pH gradient using physiological and PLFA-based techniques. *Soil Biol. Biochem.* 35, 955–963. doi: 10.1016/S0038-0717(03)00154-8

Bahram, M., Hildebrand, F., Forslund, S. K., Anderson, J. L., Soudzilovskaia, N. A., Bodegom, P. M., et al. (2018). Structure and function of the global topsoil microbiome. *Nature* 560, 233–237. doi: 10.1038/s41586-018-0386-6

Baker, K. L., Langenheder, S., Nicol, G. W., Ricketts, D., Killham, K., Campbell, C. D., et al. (2009). Environmental and spatial characterisation of bacterial community composition in soil to inform sampling strategies. *Soil Biol. Biochem.* 41, 2292–2298. doi: 10.1016/j.soilbio.2009.08.010

Bell, T. (2010). Experimental tests of the bacterial distance-decay relationship. *ISME J.* 4, 1357–1365. doi: 10.1038/ismej.2010.77

Bezemer, T. M., Fountain, M. T., Barea, J. M., Christensen, S., Dekker, S. C., Duyts, H., et al. (2010). Divergent composition but similar function of soil food webs of individual plants: plant species and community effects. *Ecology* 91, 3027–3036. doi: 10.1890/09-2198.1

Bjork, R. G., Bjorkman, M. P., Andersson, M. X., and Klemedtsson, L. (2008). Temporal variation in soil microbial communities in Alpine tundra. *Soil Biol. Biochem.* 40, 266–268. doi: 10.1016/j.soilbio.2007.07.017

Bryant, D. A., and Frigaard, N. U. (2006). Prokaryotic photosynthesis and phototrophy illuminated. *Trends Microbiol.* 14, 488–496. doi: 10.1016/j.tim.2006.09.001

Bryant, J. A., Lamanna, C., Morlon, H., Kerkhoff, A. J., Enquist, B. J., and Green, J. L. (2008). Microbes on mountainsides: contrasting elevational patterns of bacterial and plant diversity. *Proc. Natl. Acad. Sci. U. S. A.* 105, 11505–11511. doi: 10.1073/pnas.0801920105

Caporaso, J. G., Kuczynski, J., Stombaugh, J., Bittinger, K., Bushman, F. D., Costello, E. K., et al. (2010). QIIME allows analysis of high-throughput community sequencing data. *Nat. Methods* 7, 335–336. doi: 10.1038/nmeth.f.303

Chase, J. M., Kraft, N., Smith, K. G., Vellend, M., and Inouye, B. D. (2019). Using null models to disentangle variation in community dissimilarity from variation in a-diversity. *Ecosphere* 2, 1–11. doi: 10.1890/es10-00117.1

Chase, J. M., and Myers, J. A. (2011). Disentangling the importance of ecological niches from stochastic processes across scales. *Philos. Trans. Roy. Soc. B. Biol. Sci.* 366, 2351–2363. doi: 10.1098/rstb.2011.0063

Cho, J. C., and Tiedje, J. M. (2000). Biogeography and degree of endemicity of fluorescent Pseudomonas strains in soil. *Appl. Environ. Microbiol.* 66, 5448–5456. doi: 10.1128/AEM.66.12.5448-5456.2000

Chu, H., Gao, G. F., Ma, Y., Fan, K., and Delgado-Baquerizo, M. (2020). Soil microbial biogeography in a changing world: recent advances and future perspectives. *mSystems* 5:e00803-19. doi: 10.1128/mSystems.00803-19

Constancias, F., Saby, N. P., Terrat, S., Dequiedt, S., Horrigue, W., Nowak, V., et al. (2015). Contrasting spatial patterns and ecological attributes of soil bacterial and archaeal taxa across a landscape. *Microbiology* 4, 518–531. doi: 10.1002/mbo3.256

Cook, R. R., and Quinn, J. F. (1995). The influence of colonization in nested species subsets. *Oecologia* 102, 413–424. doi: 10.1007/BF00341353

Cox, F., Barsoum, N., Lilleskov, E. A., and Bidartondo, M. I. (2010). Nitrogen availability is a primary determinant of conifer mycorrhizas across complex environmental gradients. *Ecol. Lett.* 13, 1103–1113. doi: 10.1111/j.1461-0248.2010.01494.x

de Vries, F. T., Manning, P., Tallowin, J. R. B., Mortimer, S. R., Pilgrim, E. S., Harrison, K. A., et al. (2012). Abiotic drivers and plant traits explain landscape-scale patterns in soil microbial communities. *Ecol. Lett.* 15, 1230–1239. doi: 10.1111/j.1461-0248.2012.01844.x

Delgado-Baquerizo, M., and Eldridge, D. J. (2019). Cross-biome drivers of soil bacterial alpha diversity on a worldwide scale. *Ecosystems* 22, 1220–1231. doi: 10.1007/s10021-018-0333-2

Delgado-Baquerizo, M., Maestre, F. T., Reich, P. B., Jeffries, T. C., Gaitan, J. J., Encinar, D., et al. (2016). Microbial diversity drives multifunctionality in terrestrial ecosystems. *Nat. Commun.* 7:10541. doi: 10.1038/ncomms10541

Delgado-Baquerizo, M., Reich, P. B., Khachane, A. N., Campbell, C. D., Thomas, N., Freitag, T. E., et al. (2017). It is elemental: soil nutrient stoichiometry drives bacterial diversity. *Environ. Microbiol.* 19, 1176–1188. doi: 10.1111/1462-2920.13642

Denef, K., Roobroeck, D., Wadu, M., Lootens, P., and Boeckx, P. (2009). Microbial community composition and rhizodeposit-carbon assimilation in differently managed temperate grassland soils. *Soil Biol. Biochem.* 41, 144–153. doi: 10.1016/j.soilbio.2008.10.008

Deng, Q., Cheng, X. L., Hui, D. F., Zhang, Q., Li, M., and Zhang, Q. F. (2016). Soil microbial community and its interaction with soil carbon and nitrogen dynamics following afforestation in Central China. *Sci. Total Environ.* 541, 230–237. doi: 10.1016/j.scitotenv.2015.09.080

Dickie, I. A., Xu, B., and Koide, R. T. (2002). Vertical niche differentiation of ectomycorrhizal hyphae in soil as shown by T-RFLP analysis. *New Phytol.* 156, 527–535. doi: 10.1046/j.1469-8137.2002.00535.x

Dixon, P. (2003). VEGAN, a package of R functions for community ecology. *J. Veg. Sci.* 14, 927–930. doi: 10.1111/j.1654-1103.2003.tb02228.x

Egidi, E., Delgado-Baquerizo, M., Plett, J. M., Wang, J. T., Eldridge, D. J., Bardgett, R. D., et al. (2019). A few Ascomycota taxa dominate soil fungal communities worldwide. *Nat. Commun.* 10:2369. doi: 10.1038/s41467-019-10373-z

Eichorst, S. A., Trojan, D., Roux, S., Herbold, C., Rattei, T., and Woebken, D. (2018). Genomic insights into the Acidobacteria reveal strategies for their success in terrestrial environments. *Environ. Microbiol.* 20, 1041–1063. doi: 10.1111/1462-2920.14043

Fierer, N., Bradford, M. A., and Jackson, R. B. (2007). Toward an ecological classification of soil bacteria. *Ecology* 88, 1354–1364. doi: 10.1890/05-1839

Fierer, N., and Jackson, R. B. (2006). The diversity and biogeography of soil bacterial communities. *Proc. Natl. Acad. Sci. U. S. A.* 103, 626–631. doi: 10.1073/pnas.0507535103

Fierer, M. C., McCain, C. M., Meir, P., Zimmermann, M., Rapp, J. M., Silman, M. R., et al. (2011). Microbes do not follow the elevational diversity patterns of plants and animals. *Ecology* 92, 797–804. doi: 10.1890/10-1170.1

Fierer, N., Strickland, M. S., Liptzin, D., Bradford, M. A., and Cleveland, C. C. (2009). Global patterns in belowground communities. *Ecol. Lett.* 12, 1238–1249. doi: 10.1111/j.1461-0248.2009.01360.x

Frindte, K., Pape, R., Werner, K., Loffler, J., and Knief, C. (2019). Temperature and soil moisture control microbial community composition in an arctic-alpine ecosystem along elevational and micro-topographic gradients. *ISME J.* 13, 2031–2043. doi: 10.1038/s41396-019-0409-9

Fukami, T., and Wardle, D. A. (2005). Long-term ecological dynamics: reciprocal insights from natural and anthropogenic gradients. *Proc. Roy. Soc. B. Biol. Sci.* 272, 2105–2115. doi: 10.1098/rspb.2005.3277

Geml, J., Pastor, N., Fernandez, L., Pacheco, S., Semenova, T. A., Becerra, A. G., et al. (2014). Large-scale fungal diversity assessment in the Andean Yungas forests reveals strong community turnover among forest types along an altitudinal gradient. *Mol. Ecol.* 23, 2452–2472. doi: 10.1111/mec.12765

Green, J., and Bohannan, B. J. M. (2006). Spatial scaling of microbial biodiversity. *Trends Ecol. Evol.* 21, 501–507. doi: 10.1016/j.tree.2006.06.012

Green, J. L., Holmes, A. J., Westoby, M., Oliver, I., Briscoe, D., Dangerfield, M., et al. (2004). Spatial scaling of microbial eukaryote diversity. *Nature* 432, 747–750. doi: 10.1038/nature03034

Hanson, C. A., Fuhrman, J. A., Horner-Devine, M. C., and Martiny, J. B. H. (2012). Beyond biogeographic patterns: processes shaping the microbial landscape. *Nat. Rev. Microbiol.* 10, 497–506. doi: 10.1038/nrmicro2795

Jiang, Y., Song, H., Lei, Y., Korpelainen, H., and Li, C. (2019). Distinct co-occurrence patterns and driving forces of rare and abundant bacterial subcommunities following a glacial retreat in the eastern Tibetan Plateau. *Biol. Fertil. Soils* 55, 351–364. doi: 10.1007/s00374-019-01355-w

Kassen, R., and Rainey, P. B. (2004). The ecology and genetics of microbial diversity. *Annu. Rev. Microbiol.* 58, 207–231. doi: 10.1146/annurev.micro.58.030603.123654

Kembel, S. W., Cowan, P. D., Helmus, M. R., Cornwell, W. K., Morlon, H., Ackerly, D. D., et al. (2010). Picante: R tools for integrating phylogenies and ecology. *Bioinformatics* 26, 1463–1464. doi: 10.1093/bioinformatics/btq166

Kim, H. M., Jung, J. Y., Yergeau, E., Hwang, C. Y., Hinzman, L., Nam, S., et al. (2014). Bacterial community structure and soil properties of a subarctic tundra soil in council, Alaska. *FEMS Microbiol. Ecol.* 89, 465–475. doi: 10.1111/1574-6941.12362

Kivlin, S. N., Winston, G. C., Goulden, M. L., and Treseder, K. K. (2014). Environmental filtering affects soil fungal community composition more than dispersal limitation at regional scales. *Fungal Ecol.* 12, 14–25. doi: 10.1016/j.funeco.2014.04.004

Lauber, C. L., Hamady, M., Knight, R., and Fierer, N. (2009). Pyrosequencing-based assessment of soil pH as a predictor of soil bacterial community structure at the continental scale. *Appl. Environ. Microbiol.* 75, 5111–5120. doi: 10.1128/AEM.00335-09

Lauber, C. L., Ramirez, K. S., Aanderud, Z., Lennon, J., and Fierer, N. (2013). Temporal variability in soil microbial communities across land-use types. *ISME J.* 7, 1641–1650. doi: 10.1038/ismej.2013.50

Lenth, R. V. (2016). Least-squares means: the R package lsmeans. *J. Stat. Softw.* 69, 1–33. doi: 10.18637/jss.v069.i01

Li, J. B., Shen, Z. H., Li, C. N., Kou, Y. P., Wang, Y. S., Tu, B., et al. (2018). Stair-step pattern of soil bacterial diversity mainly driven by pH and vegetation types along the elevational gradients of Gongga Mountain, China. *Front. Virol.* 9:569. doi: 10.3389/fmicb.2018.00569

Liu, Y. R., Delgado-Baquerizo, M., Wang, J. T., Hu, H. W., Yang, Z. M., and He, J. Z. (2018). New insights into the role of microbial community composition in driving soil respiration rates. *Soil Biol. Biochem.* 118, 35–41. doi: 10.1016/j.soilbio.2017.12.003

Liu, K. S., Liu, Y. Q., Hu, A. Y., Wang, F., Chen, Y. Y., Gu, Z. Q., et al. (2020). Different community assembly mechanisms underlie similar biogeography of bacteria and microeukaryotes in Tibetan lakes. *FEMS Microbiol. Ecol.* 96:fiaa071. doi: 10.1093/femsec/fiaa071

Lundell, T. K., Makela, M. R., and Hilden, K. (2010). Lignin-modifying enzymes in filamentous basidiomycetes - ecological, functional and phylogenetic review. *J. Basic Microbiol.* 50, 5–20. doi: 10.1002/jobm.200900338

McCain, C. M., and Colwell, R. K. (2011). Assessing the threat to montane biodiversity from discordant shifts in temperature and precipitation in a changing climate. *Ecol. Lett.* 14, 1236–1245. doi: 10.1111/j.1461-0248.2011.01695.x

Meyer, K. M., Memiaghe, H., Korte, L., Kenfack, D., Alonso, A., and Bohannan, B. J. M. (2018). Why do microbes exhibit weak biogeographic patterns? *ISME J.* 12, 1404–1413. doi: 10.1038/s41396-018-0103-3

Miyamoto, Y., Nakano, T., Hattori, M., and Nara, K. (2014). The mid-domain effect in ectomycorrhizal fungi: range overlap along an elevation gradient on Mount Fuji, Japan. *ISME J.* 8, 1739–1746. doi: 10.1038/ismej.2014.34

Morlon, H., Chuyong, G., Condit, R., Hubbell, S., Kenfack, D., Thomas, D., et al. (2008). A general framework for the distance-decay of similarity in ecological communities. *Ecol. Lett.* 11, 904–917. doi: 10.1111/j.1461-0248.2008.01202.x

Mukhopadhya, I., Hansen, R., El-Omar, E. M., and Hold, G. L. (2012). IBD-what role do Proteobacteria play? *Nat. Rev. Gastroenterol. Hepatol.* 9, 219–230. doi: 10.1038/nrgastro.2012.14

Nemergut, D. R., Costello, E. K., Hamady, M., Lozupone, C., Jiang, L., Schmidt, S. K., et al. (2011). Global patterns in the biogeography of bacterial taxa. *Environ. Microbiol.* 13, 135–144. doi: 10.1111/j.1462-2920.2010.02315.x

Nemergut, D. R., Schmidt, S. K., Fukami, T., O'Neill, S. P., Bilinski, T. M., Stanish, L. F., et al. (2013). Patterns and processes of microbial community assembly. *Microbiol. Mol. Biol. Rev.* 77, 342–356. doi: 10.1128/MMBR.00051-12

Noss, R. F. (1990). Indicators for monitoring biodiversity: a hierarchical approach. *Conserv. Biol.* 4, 355–364. doi: 10.1111/j.1523-1739.1990.tb00309.x

Nottingham, A. T., Fierer, N., Turner, B. L., Whitaker, J., Ostle, N. J., McNamara, N. P., et al. (2018). Microbes follow Humboldt: temperature drives plant and soil microbial diversity patterns from the Amazon to the Andes. *Ecology* 99, 2455–2466. doi: 10.1002/ecy.2482

Ogwu, M. C., Takahashi, K., Dong, K., Song, H. K., Moroenyane, I., Waldman, B., et al. (2019). Fungal elevational Rapoport pattern from a High Mountain in Japan. *Sci. Rep.* 9:6570. doi: 10.1038/s41598-019-43025-9

Oksanen, J., Blanchet, F.G., Friendly, M., Kindt, R., and Wagner, H.H. (2020). Vegan: community ecology package. R Package Version 2.5-7. Available at: https://CRAN.R-project.org/package=vegan

Orwin, K. H., Bertram, J. E., Clough, T. J., Condron, L. M., Sherlock, R. R., O'Callaghan, M., et al. (2010). Impact of bovine urine deposition on soil microbial activity, biomass, and community structure. *Appl. Soil Ecol.* 44, 89–100. doi: 10.1016/j.apsoil.2009.10.004

Papke, R. T., and Ward, D. M. (2004). The importance of physical isolation to microbial diversification. *FEMS Microbiol. Ecol.* 48, 293–303. doi: 10.1016/j.femsec.2004.03.013

Peay, K. G., Garbelotto, M., and Bruns, T. D. (2010). Evidence of dispersal limitation in soil microorganisms: isolation reduces species richness on mycorrhizal tree islands. *Ecology* 91, 3631–3640. doi: 10.1890/09-2237.1

Peay, K. G., von Sperber, C., Cardarelli, E., Toju, H., Francis, C. A., Chadwick, O. A., et al. (2017). Convergence and contrast in the community structure of Bacteria, Fungi and Archaea along a tropical elevation-climate gradient. *FEMS Microbiol. Ecol.* 93:fix045. doi: 10.1093/femsec/fix045

Polme, S., Bahram, M., Yamanaka, T., Nara, K., Dai, Y. C., Grebenc, T., et al. (2013). Biogeography of ectomycorrhizal fungi associated with alders (Alnus spp.) in relation to biotic and abiotic variables at the global scale. *New Phytol.* 198, 1239–1249. doi: 10.1111/nph.12170

Rousk, J., Baath, E., Brookes, P. C., Lauber, C. L., Lozupone, C., Caporaso, J. G., et al. (2010). Soil bacterial and fungal communities across a pH gradient in an arable soil. *ISME J.* 4, 1340–1351. doi: 10.1038/ismej.2010.58

Schnecker, J., Wild, B., Takriti, M., Alves, R. J. E., Gentsch, N., Gittel, A., et al. (2015). Microbial community composition shapes enzyme patterns in topsoil and subsoil horizons along a latitudinal transect in Western Siberia. *Soil Biol. Biochem.* 83, 106–115. doi: 10.1016/j.soilbio.2015.01.016

Shen, C. C., Ge, Y., Yang, T., and Chu, H. Y. (2017). Verrucomicrobial elevational distribution was strongly influenced by soil pH and carbon/nitrogen ratio. *J. Soils Sediments* 17, 2449–2456. doi: 10.1007/s11368-017-1680-x

Shen, C. C., Liang, W. J., Shi, Y., Lin, X. G., Zhang, H. Y., Wu, X., et al. (2014). Contrasting elevational diversity patterns between eukaryotic soil microbes and plants. *Ecology* 95, 3190–3202. doi: 10.1890/14-0310.1

Shen, C. C., Shi, Y., Fan, K. K., He, J. S., Adams, J. M., Ge, Y., et al. (2019). Soil pH dominates elevational diversity pattern for bacteria in high elevation alkaline soils on the Tibetan Plateau. *FEMS Microbiol. Ecol.* 95:fiz003. doi: 10.1093/femsec/fiz003

Shen, C. C., Shi, Y., Ni, Y. Y., Deng, Y., Van Nostrand, J. D., He, Z. L., et al. (2016). Dramatic increases of soil microbial functional gene diversity at the treeline ecotone of Changbai Mountain. *Front. Microbiol.* 7:1184. doi: 10.3389/fmicb.2016.01184

Shen, C. C., Xiong, J. B., Zhang, H. Y., Feng, Y. Z., Lin, X. G., Li, X. Y., et al. (2013). Soil pH drives the spatial distribution of bacterial communities along elevation on Changbai Mountain. *Soil Biol. Biochem.* 57, 204–211. doi: 10.1016/j.soilbio.2012.07.013

Singh, D., Lee-Cruz, L., Kim, W.-S., Kerfahi, D., Chun, J.-H., and Adams, J. M. (2014). Strong elevational trends in soil bacterial community composition on Mt. Halla, South Korea. *Soil Biol. Biochem.* 68, 140–149. doi: 10.1016/j.soilbio.2013.09.027

Singh, D., Takahashi, K., and Adams, J. M. (2012). Elevational patterns in archaeal diversity on Mt. Fuji. *PLoS One* 7:e44494. doi: 10.1371/journal.pone.0044494

Soininen, J., McDonald, R., and Hillebrand, H. (2007). The distance decay of similarity in ecological communities. *Ecography* 30, 3–12. doi: 10.1111/j.0906-7590.2007.04817.x

Stegen, J. C., Lin, X. J., Fredrickson, J. K., Chen, X. Y., Kennedy, D. W., Murray, C. J., et al. (2013). Quantifying community assembly processes and identifying features that impose them. *ISME J.* 7, 2069–2079. doi: 10.1038/ismej.2013.93

Stegen, J. C., Lin, X. J., Fredrickson, J. K., and Konopka, A. E. (2015). Estimating and mapping ecological processes influencing microbial community assembly. *Front. Microbiol.* 6:370. doi: 10.3389/fmicb.2015.00370

Stegen, J. C., Lin, X. J., Konopka, A. E., and Fredrickson, J. K. (2012). Stochastic and deterministic assembly processes in subsurface microbial communities. *ISME J.* 6, 1653–1664. doi: 10.1038/ismej.2012.22

Thoms, C., Gattinger, A., Jacob, M., Thomas, F. M., and Gleixner, G. (2010). Direct and indirect effects of tree diversity drive soil microbial diversity in temperate deciduous forest. *Soil Biol. Biochem.* 42, 1558–1565. doi: 10.1016/j.soilbio.2010.05.030

Walker, L. R., Wardle, D. A., Bardgett, R. D., and Clarkson, B. D. (2010). The use of chronosequences in studies of ecological succession and soil development. *J. Ecol.* 98, 725–736. doi: 10.1111/j.1365-2745.2010.01664.x

Wan, W., Gadd, G. M., Yang, Y., Yuan, W., Gu, J., Ye, L., et al. (2021). Environmental adaptation is stronger for abundant rather than rare microorganisms in wetland soils from the Qinghai-Tibet Plateau. *Mol. Ecol.* 30, 2390–2403. doi: 10.1111/mec.15882

Wan, P., and He, R. R. (2020). Soil microbial community characteristics under different vegetation types at the national nature reserve of Xiaolongshan Mountains, Northwest China. *Ecol Inform* 55:101020. doi: 10.1016/j.ecoinf.2019.101020

Wang, J. T., Cao, P., Hu, H. W., Li, J., Han, L. L., Zhang, L. M., et al. (2015). Altitudinal distribution patterns of soil bacterial and archaeal communities along Mt. Shegyla on the Tibetan Plateau. *Microb. Ecol.* 69, 135–145. doi: 10.1007/s00248-014-0465-7

Wang, J. J., Soininen, J., Zhang, Y., Wang, B. X., Yang, X. D., and Shen, J. (2011). Contrasting patterns in elevational diversity between microorganisms and macroorganisms. *J. Biogeogr.* 38, 595–603. doi: 10.1111/j.1365-2699.2010.02423.x

Wang, Q., Wang, C., Yu, W. W., Turak, A., Chen, D. W., Huang, Y., et al. (2018). Effects of nitrogen and phosphorus inputs on soil bacterial abundance, diversity, and community composition in Chinese fir plantations. *Front. Microbiol.* 9:1543. doi: 10.3389/fmicb.2018.01543

Whitaker, R. J., Grogan, D. W., and Taylor, J. W. (2003). Geographic barriers isolate endemic populations of hyperthermophilic archaea. *Science* 301, 976–978. doi: 10.1126/science.1086909

Whittaker, R. J., Willis, K. J., and Field, R. (2001). Scale and species richness: towards a general, hierarchical theory of species diversity. *J. Biogeogr.* 28, 453–470. doi: 10.1046/j.1365-2699.2001.00563.x

Xu, M., Li, X. L., Cai, X. B., Gai, J. P., Li, X. L., Christie, P., et al. (2014). Soil microbial community structure and activity along a montane elevational gradient on the Tibetan Plateau. *Eur. J. Soil Biol.* 64, 6–14. doi: 10.1016/j.ejsobi.2014.06.002

Yang, T., Adams, J. M., Shi, Y., He, J. S., Jing, X., Chen, L. T., et al. (2017). Soil fungal diversity in natural grasslands of the Tibetan Plateau: associations with plant diversity and productivity. *New Phytol.* 215, 756–765. doi: 10.1111/nph.14606

Yang, Y., Gao, Y., Wang, S., Xu, D., Yu, H., Wu, L., et al. (2014). The microbial gene diversity along an elevation gradient of the Tibetan grassland. *ISME J.* 8, 430–440. doi: 10.1038/ismej.2013.146

Yang, X., and Xu, M. (2003). Biodiversity conservation in Changbai Mountain biosphere reserve, northeastern China: status, problem, and strategy. *Biodivers. Conserv.* 12, 883–903. doi: 10.1023/A:1022841107685

Zhang, Q., Goberna, M., Liu, Y. G., Cui, M., Yang, H. S., Sun, Q. X., et al. (2018). Competition and habitat filtering jointly explain phylogenetic structure of soil bacterial communities across elevational gradients. *Environ. Microbiol.* 20, 2386–2396. doi: 10.1111/1462-2920.14247

Zhang, B., Xue, K., Zhou, S. T., Che, R. X., Du, J. Q., Tang, L., et al. (2019). Phosphorus mediates soil prokaryote distribution pattern along a small-scale elevation gradient in Noijin Kangsang Peak, Tibetan Plateau. *FEMS Microbiol. Ecol.* 95:fiz076. doi: 10.1093/femsec/fiz076

Zhou, J. Z., Deng, Y., Shen, L. N., Wen, C. Q., Yan, Q. Y., Ning, D. L., et al. (2016). Temperature mediates continental-scale diversity of microbes in forest soils. *Nat. Commun.* 7:12083. doi: 10.1038/ncomms12083

Zhou, J. Z., and Ning, D. L. (2017). Stochastic community assembly: does it matter in microbial ecology? *Microbiol. Mol. Biol. Rev.* 81:e00002-17. doi: 10.1128/mmbr.00002-17

Zou, Y., Sang, W., Bai, F., and Axmacher, J. C. (2017). Relationships between plant diversity and the abundance and a-diversity of predatory ground beetles (coleoptera: carabidae) in a mature asian temperate forest ecosystem. *PLoS One* 8:e82792. doi: 10.1371/journal.pone.0082792

frontiers | Frontiers in Microbiology

TYPE Original Research
PUBLISHED 27 June 2023
DOI 10.3389/fmicb.2023.1174899

OPEN ACCESS

EDITED BY
Ruiyong Zhang,
Chinese Academy of Sciences (CAS), China

REVIEWED BY
Jinhua Li,
Chinese Academy of Sciences (CAS), China
Hongmiao Pan,
Chinese Academy of Sciences (CAS), China
L. F. Wu,
Centre National de la Recherche Scientifique (CNRS), France

*CORRESPONDENCE
Yohey Suzuki
✉ yohey-suzuki@eps.s.u-tokyo.ac.jp

RECEIVED 27 February 2023
ACCEPTED 16 May 2023
PUBLISHED 27 June 2023

CITATION
Nakano S, Furutani H, Kato S, Kouduka M, Yamazaki T and Suzuki Y (2023) Bullet-shaped magnetosomes and metagenomic-based magnetosome gene profiles in a deep-sea hydrothermal vent chimney.
Front. Microbiol. 14:1174899.
doi: 10.3389/fmicb.2023.1174899

Bullet-shaped magnetosomes and metagenomic-based magnetosome gene profiles in a deep-sea hydrothermal vent chimney

Shinsaku Nakano[1], Hitoshi Furutani[1], Shingo Kato[2], Mariko Kouduka[1], Toshitsugu Yamazaki[3] and Yohey Suzuki[1]*

[1]Graduate School of Science, The University of Tokyo, Tokyo, Japan, [2]Japan Collection of Microorganisms, RIKEN BioResource Research Center, Tsukuba, Ibaraki, Japan, [3]Atmosphere and Ocean Research Institute, The University of Tokyo, Chiba, Japan

Magnetosome-producing microorganisms can sense and move toward the redox gradient and have been extensively studied in terrestrial and shallow marine sediment environments. However, given the difficulty of sampling, magnetotactic bacteria (MTB) are poorly explored in deep-sea hydrothermal fields. In this study, a deep-sea hydrothermal vent chimney from the Southern Mariana Trough was collected using a remotely operated submersible. The mineralogical and geochemical characterization of the vent chimney sample showed an internal iron redox gradient. Additionally, the electron microscopy of particles collected by magnetic separation from the chimney sample revealed MTB cells with bullet-shaped magnetosomes, and there were minor occurrences of cuboctahedral and hexagonal prismatic magnetosomes. Genome-resolved metagenomic analysis was performed to identify microorganisms that formed magnetosomes. A metagenome-assembled genome (MAG) affiliated with *Nitrospinae* had magnetosome genes such as *mamA*, *mamI*, *mamM*, *mamP*, and *mamQ*. Furthermore, a diagnostic feature of MTB genomes, such as magnetosome gene clusters (MGCs), including *mamA*, *mamP*, and *mamQ*, was also confirmed in the *Nitrospinae*-affiliated MAG. Two lines of evidence support the occurrence of MTB in a deep-sea, inactive hydrothermal vent environment.

KEYWORDS

magnetotactic bacteria, *Nitrospinae*-related sequences, magnetosome gene cluster, redox gradient, electron microscopy

Introduction

Magnetotactic bacteria (MTB) produce membrane-enveloped single-domain magnetite (Fe_3O_4), greigite (Fe_3S_4), or both, which are called magnetosomes (Blakemore, 1975). MTB are phylogenetically affiliated within six major lineages: the *Alpha-*, *Gamma-*, and *Candidatus* (*Ca.*) Etaproteobacteria classes of the *Proteobacteria* phylum, the *Desulfobacterota* phylum, the *Nitrospirae* phylum, and the *Ca.* Omnitrophica phylum (Lefèvre and Bazylinski, 2013; Lin et al., 2014a). Although the morphological features of magnetosomes are different among taxonomic groups, all magnetosomes function as a compass needle for moving along the Earth's geomagnetic field (Frankel et al., 1997). This phenomenon is called magnetotaxis, which enables MTB to inhabit the redox gradient

(Frankel et al., 1997; Lefèvre and Bazylinski, 2013). MTB have access to various electron donors and acceptors along the redox gradient. Most of the major lineages use reduced sulfur compounds as energy sources, such as hydrogen sulfide, thiosulfate, and sulfite, whereas O_2, sulfate, and fumarate are utilized as electron acceptors (Lefèvre et al., 2013; Goswami et al., 2022). Carbon fixation is mediated by *Proteobacteria*, *Desulfobacterota*, and *Nitrospirae* via the Calvin-Benson cycle or Wood-Ljungdahl (Lefèvre et al., 2013; Goswami et al., 2022). As a result, MTB play an important role in the biogeochemical cycling of iron, sulfur, carbon, and other redox-sensitive elements (Li et al., 2020). Recent studies have reported that MTB are involved in the intracellular deposition of silica (Li et al., 2022), poly-β-hydroxybutyrate (Li et al., 2021), and polymetaphosphate (Schulz-Vogt et al., 2019).

MTB from shallow marine and land environments have been intensively studied for sampling feasibility (Lin et al., 2014a, 2017). Light and electron microscopy was used to observe magnetically separated MTB cells, the taxonomic affiliations of which were determined using fluorescence *in situ* hybridization (FISH) targeting cells containing single-domain magnets (Li et al., 2017). Single-cell genomics and metagenomics combined with light and electron microscopy have been applied to identify MTB by examining the presence of magnetosome gene clusters (MGCs; Kolinko et al., 2012, 2013; Lin et al., 2014b, 2018, 2020). MGCs are consecutively arranged gene sets in MTB genomes that control magnetosome biogenesis (Grünberg et al., 2001; Uebe and Schüler, 2016; McCausland and Komeili, 2020). MGCs have recently been discovered in metagenome-assembled genomes (MAGs) that have been taxonomically classified into previously unknown bacterial lineages for MTB, such as *Nitrospinae*, *Ca. Latescibacteria*, *Planctomycetes*, *Fibrobacteres*, and *Ca. Riflebacteria* (Lin et al., 2020; Uzun et al., 2020).

In contrast, MTB in deep-sea environments is largely unknown, partly because the low cell density of MTB hinders the magnetic recovery of magnetotactic cells sufficiently for FISH and single-cell genomics. In deep-sea sediments, magnetosomes have been observed with microbial cells (Liu et al., 2017; McGlynn et al., 2018; Cui et al., 2021), whereas magnetosomes have been observed without microbial cells (Dong et al., 2016; Yamazaki et al., 2019). Although the previous deep-sea studies attempted to clarify the taxonomy of MTB involved in the formation of magnetosomes by 16S rRNA gene sequences, metagenomic analysis was performed to characterize MTB, the presence of which has been demonstrated by electron microscopy in deep-sea hydrothermal sediments (Chen et al., 2022). However, their metagenomic approach was unsuccessful in revealing the taxonomic affiliations of magnetosome genes and their arrangement into MGCs. It has been demonstrated by our previous studies of deep-sea hydrothermal vent chimneys that chimney samples with high cell densities are predominantly colonized by microorganisms closely related to known MTB lineages (Suzuki et al., 2004; Kato et al., 2010, 2018; Takamiya et al., 2022). In this study, magnetic separation and electron microscopy analyses were performed to detect MTB cells in a metal sulfide chimney sample from the South Mariana Trough (SMT). A genome-resolved metagenomic analysis was also performed to search for MGCs in metagenome-assembled genomes (MAGs) from the vent chimney community.

Materials and methods

The site, sample descriptions, and handling

A metal sulfide chimney examined in this study was described in previous research (Kato et al., 2019). The chimney was collected from a hydrothermal vent field at the Pika site (12°55.130′N, 143°38.972′E) in SMT, a back-arc basin where the Philippine Sea Plate is subducted. Sampling was conducted during the Japan Agency for Marine-Earth Science and Technology (JAMSEC) Scientific Cruises NT12-24 of the R/V *Natsushima* in September 2012. The sample size was at a water depth of 2,787 m, and the *in situ* temperature of the deep seawater was 1.7°C. No fluid emanating from the chimney was observed on the sample during video observations. The chimney structure unassociated with fluid venting was collected by the manipulator arm of the remotely operated vehicle, *Hyper Dolphin* (HPD). The chimney structure was enclosed in an HPD container to minimize contamination from the surrounding seawater during transportation to the sea surface.

After the retrieval, the chimney structure was named Pika55, which was also described as IPdc by Kato et al. (2019) and was immediately subsampled onboard in a cold room at 4°C. First, the tip of the metal sulfide chimney sample (shown by a white arrow in Figure 1A) was soaked two times in 100% ethanol for 5 min to dehydrate, and the chimney sample was infiltrated four times with LR White Resin for 30 min and solidified in an oven at 50°C for 48 h. Solidified blocks were cut into thin sections and polished with corundum powder and diamond paste. Then, after the removal of the chimney tip, the interior and exterior portions of the chimney sample were separated using sterile chisels and spatulas. The exterior portion was named Pika55ext. Subsequently, Pika55ext was ground into powder using a sterile pestle and mortar and stored at −80°C for magnetic separation and metagenomic analysis. Finally, some ground samples were fixed with 3.7% formamide in seawater onboard for magnetic separation.

Magnetic separation and electron microscopy

Magnetic particles were separated from the Pika55ext ground sample by sonicated dispersion in a sodium hexametaphosphate buffer solution, followed by sample collection by Nd magnets. The extracted magnetic particles dispersed in ethanol were mounted on a carbon-coated copper grid. A JEM-1400 transmission electron microscope (TEM; JEOL, Tokyo, Japan) was used to observe magnetic particles at an operation voltage of 120 kV. The extracted magnetic particles were prefiltered through 8.0-μm pore size nitrocellulose filters and then filtered through 0.2-μm pore size polycarbonate filters. The filtered magnetic particles were carbon-coated and observed using the S4500 scanning electron microscope (SEM; Hitachi, Ibaragi, Japan) at an accelerating voltage of 10 kV. Finally, secondary electron imaging coupled to energy-dispersive x-ray spectroscopy (EDS) was performed to clarify the chemical compositions of magnetosomes.

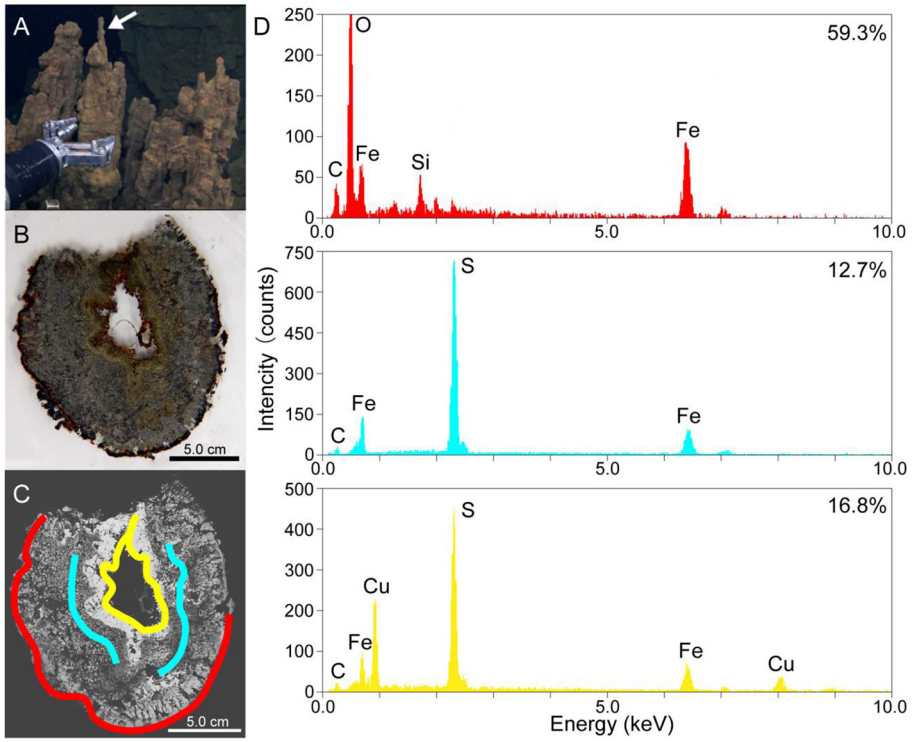

FIGURE 1
(A) A photo of the metal sulfide chimney collected from the Pika site (Pika55). An arrow shows the site where thin sections were made. **(B)** A photo of the thin horizontal section of Pika55. **(C)** A back-scattered electron image obtained by scanning electron microscopy of the thin section of Pika55. Colored bands show the areas drilled for the quantification of amorphous ferric iron. **(D)** Energy-dispersive x-ray spectroscopy spectra from the colored bands in **(C)**. The percentages shown with the spectra indicate the amount of amorphous ferric iron in total iron.

Metagenomic analysis

As described in a previous study, DNA extraction, library construction, and shotgun sequencing were performed (Kato et al., 2019). Using an UltraClean Soil DNA Isolation Kit (MoBio Laboratories, Carlsbad, CA, USA), genomic DNA was extracted from Pika55ext without the use of magnetic separation. Hirai et al. (2017) constructed a shotgun library for the extracted DNA using a KAPA Hyper Prep kit for Illumina (KAPA Biosystems, Wilmington, MA, USA). Library sequencing was performed on an Illumina MiSeq platform (MiSeq PE300). The following steps were taken to reconstruct MAGs using MetaWRAP v.1.3.2 (Uritskiy et al., 2018). First, the Read_QC module included in MetaWRAP was used to trim and filter reads from the library. Following that, high-quality reads were assembled into contigs using SPAdes version 3.13.0 with the options "–meta, -k 55,77,99,111,121" (Bankevich et al., 2012). Then, the contigs were binned into metagenome-assembled genomes (MAGs) using the Binning module [including metabat2 (Kang et al., 2015), maxbin2 (Wu et al., 2016), and concoct (Alneberg et al., 2014)] included in MetaWRAP. The MAGs from the binning tools were then refined using the bin refinement module included in MetaWRAP. For phylogenomic analysis, MAGs with a completeness of >70% and a contamination of <5% were selected (Supplementary Table 1). The taxonomic classification was performed based on the National Center for Biotechnology Information (NCBI) taxonomy (Sayers et al., 2021) and the Genome Taxonomy Database (GTDB) taxonomy (Parks et al., 2022). Magnetosome genes were searched against the MAGs using the FeGenie program with a lower maximum distance of 1 or 5 (Garber et al., 2020). BLASTP (Gish and States, 1993) was also used to search for magnetosome genes in the MAGs from this study and the NCBI database (Gish and States, 1993). Relative abundances of the MAGs in the metagenome were estimated based on the normalized read coverage values using the Quant Bins module included in MetaWRAP.

Phylogenetic analysis of magnetosome genes

Known MTB genomes were downloaded from the NCBI database against which magnetosome genes were searched using the FeGenie program (Garber et al., 2020). Then, the amino acid sequences of magnetosome genes were aligned using Muscle v.3.8.8425 (Edgar, 2004) within the ARB software (Ludwig et al., 2004) and filtered using the TrimAl program (Capella-Gutierrez et al., 2009) with the "-gappyout" option. Additionally, maximum-likelihood phylogenetic protein trees were constructed using RAxML v.8.2.11 (Stamatakis, 2014) in the Geneious Prime software. The maximum-likelihood trees were obtained using the 1,000 bootstrap-resampling approaches. Protein trees were visualized using FigTree v.1.4.4 (http://tree.bio.ed.ac.uk/software/figtree/) and were rooted at the midpoint.

Based on 120 concatenated bacterial single-copy marker proteins, a maximum-likelihood tree was constructed for *Nitrospinae* genomes downloaded from the GTDB database (Parks et al., 2017). With the "-gappyout" option, the TrimAl program was used to trim concatenated sequences. The Geneious Prime software's RAxML v.8.2.11 was used to build the maximum-likelihood tree. The maximum-likelihood tree was obtained using the 1,000 bootstrap-resampling approach. The tree was rooted with *Thermodesulfovibrio yellowstonii* DSM 11347 and visualized using FigTree v.1.4.4.

Metabolic predictions

A curated set of genes involved in carbon, nitrogen, and sulfur metabolism were searched using METABOLIC v.4.0 (Zhou et al., 2022), which annotates genes through the Kyoto Encyclopedia of Genes and Genomes (KEGG; Ogata et al., 1999), TIGRfam (Selengut et al., 2007), Pfam (Finn et al., 2014), and custom hidden Markov model profiles. Using DiSCo, genes involved in sulfur metabolism, such as *dsrABCDEFHJKMOP*, *aprAB*, and *sat*, were annotated (Neukirchen and Sousa, 2021). KEGG was used to annotate *sir,* which METABOLIC and DiSCo did not annotate. In Supplementary Table 2, the complete names of metabolic genes and the related annotation tools are presented.

Results and discussion

Internal redox gradient indicated by amorphous Fe(III) quantification

Thin sections of the metal sulfide chimney collected from SMT called Pika55 were examined to reveal the redox gradient, which is potentially important for magnetotaxis in the chimney. Light microscopy observations showed that the internal structure was concentrated in three layers (Figures 1A, B). The outermost layer was reddish, and a gray layer was present inside the reddish layer. Moreover, the innermost metallic gold layer had a reddish inner rim. The combination of these layers is typical for metal sulfide chimneys found at deep-sea hydrothermal vents (Haymon, 1983). Additionally, SEM observations with back-scattered electron imaging and EDS analysis were performed to show that the chimney mainly comprises iron and sulfur or iron, copper, and sulfur (Figures 1C, D). In the outer layer, a dark contrast phase relative to metal sulfides was composed of Fe, Si, and O (Figures 1C, D). In contrast, the two inner layers were unassociated with the iron silicate phase.

As the iron silicate phase is likely composed of ferric iron due to the oxidative alteration of iron-bearing sulfides, the valence state of iron was clarified by a colorimetric ferrozine-based assay (Lovley and Phillips, 1986) coupled with the micron-scale drilling technique (Sakai and Kodan, 2011). The reddish layer contained 59.3% of amorphous ferric iron in the total iron extracted with 0.5-M HCl (red band and EDS spectrum in Figures 1C, D), whereas the inner and outer portions of the gray layer contained 12.7% (blue bands and EDS spectrum in Figures 1C, D). The innermost metallic layer contained 16.8% amorphous ferric iron in total iron extracted with 0.5-N HCl (yellow band and EDS spectrum in Figures 1C, D). Finally, there appears to be a redox gradient between the outermost and innermost parts of the chimney structure.

Microbial cells with bullet-shaped magnetosomes found in the metal sulfide chimney

First, magnetic separation of the metal sulfide chimney sample from SMT was performed. TEM observations of the magnetically separated particles revealed microbial cells with bullet-shaped magnetosomes (Figures 2A–C). The bullet-shaped magnetosomes in ~200-nm-wide and 500-nm-long microbial cells were arranged into a single chain (Figure 2A). SEM observations and EDS analysis of a microbial cell with bullet-shaped magnetosomes, similarly observed by TEM, revealed that the bullet-shaped magnetosomes were composed of Fe and O without S (Figures 2D, E). The observed morphology types of the magnetosomes without microbial cells were categorized as bullet-shaped, cuboctahedral, and hexagonal prismatic (Figures 2B, C). Enumeration of each morphology type revealed the dominance of bullet-shaped magnetosomes in the chimney sample (Figure 2F). As the composition of cuboctahedral and hexagonal prismatic magnetosomes was not examined, the possibility that these particles were not magnetosomes cannot be ruled out. Based on TEM images, the length and width of bullet-shaped crystals associated with and without microbial cells ($n = 253$) were measured. The median length and axial ratio (width/length) were 65.2 nm and 0.525, respectively (Figure 2G). The distribution of crystal size is significantly uniform, relative to that of bullet-shaped magneto fossils in surface marine sediments from the Japan Sea (Yamazaki, 2020). These results indicate the inhabitation of a limited species of MTB in a metal sulfide chimney.

Metagenomic evidence of the production of magnetosomes in the chimney by *Nitrospinae*

Metagenomic analysis was performed to obtain MAGs from the vent chimney samples (Table 1). Based on reading coverage values, abundant NCBI-based taxonomic groups were *Nitrospirae* (p_Nitrospirota; c_Thermodesulfovibrionia; o_Thermodesulfovibrionales; f_JdFR-85; and g__BMS3Bbin07 based on the GTDB taxonomy) represented by a MAG named Idc_ex_meta_mg7 and *Gammaproteobacteria* (p_Proteobacteria; c_Gammaproteobacteria; o_Arenicellales; and f-s_BMS3Bbin11 based on the GTDB taxonomy) represented by a MAG named Idc_ex_meta_mg1 (Table 1). 16S rRNA gene sequences were not found in all MAGs except for the MAG Idc_ex_meta_mg1. Based on the 16S rRNA gene sequence, the MAG Idc_ex_meta_mg1 had no close MTB relatives. All MAGs were subjected to a FeGenie search against *mamABEIKLMOPQ*. *mamABEIKLMOPQ* were selected because these magnetosome genes are universal for magnetite production by MTB (Kolinko et al., 2016; Uebe and Schüler, 2016). As a result, it was revealed that *mamA*,

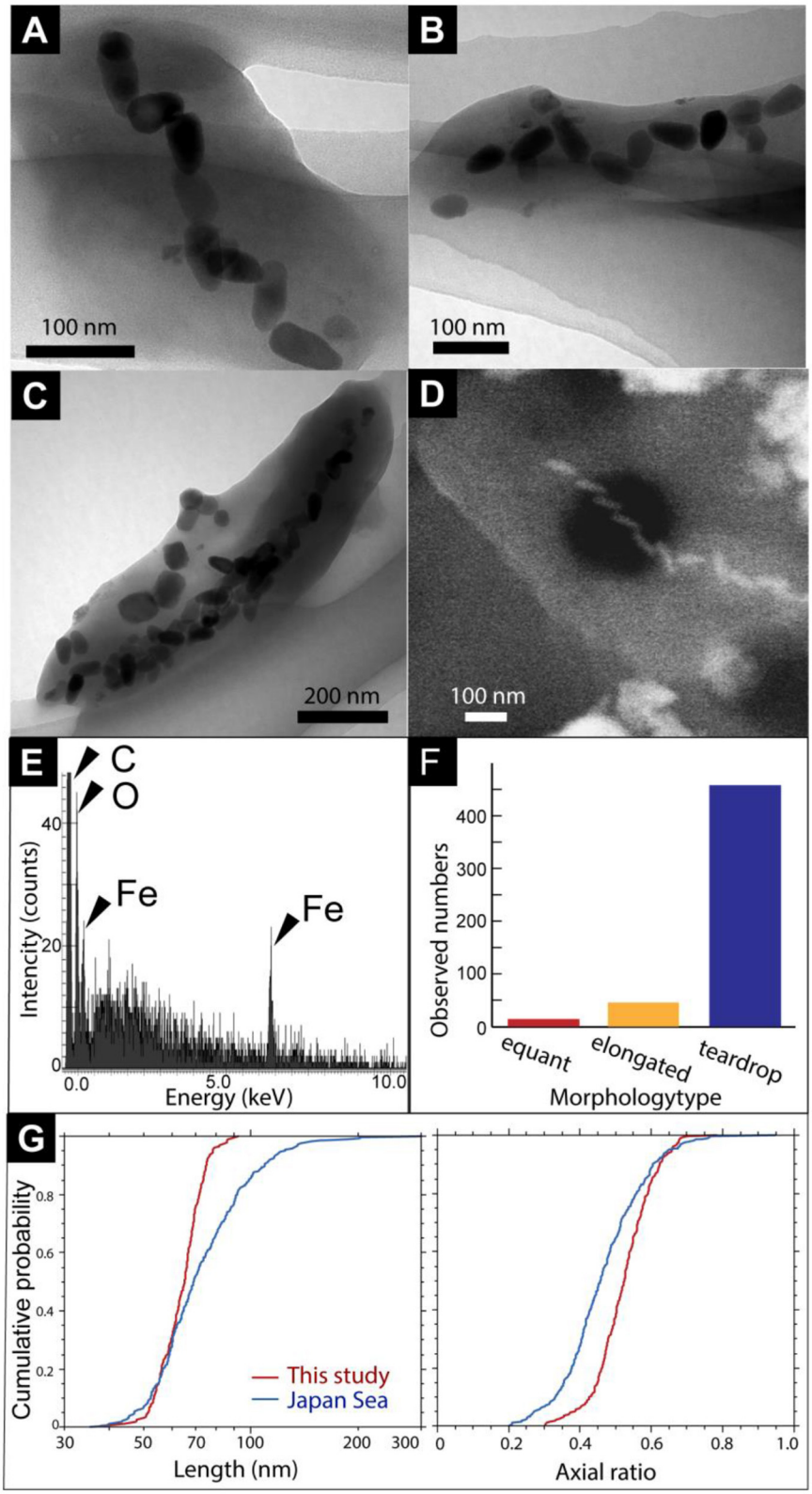

FIGURE 2
(A) A TEM image of a cell with bullet-shaped magnetosomes. **(B, C)** TEM images of magnetosomes unassociated with cells. Black arrows show cubo-octahedral magnetosomes. White arrowheads show hexagonal prismatic magnetosomes. **(D)** Secondary electron image of a microbial cell with bullet-shaped magnetosomes. **(E)** Energy dispersive x-ray spectrum from a red circle in **(D)**. **(F)** Observed a number of morphology types of magnetosomes. **(G)** Cumulative probability distribution of length and axial ratio (width/length) for bullet-shaped crystals extracted from the chimney sample in this study (red) and from Japan Sea surface sediments (blue; Yamazaki, 2020).

TABLE 1 List of metagenome-assembled genomes and their genomic features.

MAG ID	Genome size (bp)	Numbers of contigs	Completeness (%)	Contamination (%)	Coverage (x)	Accession	Taxonomy based on NCBI	Taxonomy based on GTDB	Magnetosome genes identified by FeGenie
Idc_ex_meta_mg1	2,572,058	165	98.17	2.08	21.19	DRZ059048	p_Proteobacteria; c_Gammaproteobacteria	p_Proteobacteria; c_Gammaproteobacteria; o_Arenicellales; f_BMS3Bbin11; g_BMS3Bbin11; s_BMS3Bbin11 sp002897635	*mamE*
Idc_ex_meta_mg2	2,014,408	355	90.5	3.59	3.41	DRZ059049	p_Nitrospinae; c_Nitrospinia; o_Nitrospinales	p_Nitrospinota; c_UBA7883; o_UBA7883	*mamA, mamI, mamM, mamP, mamQ*
Idc_ex_meta_mg3	1,412,330	531	83.1	3.96	2.74	DRZ059050	p_Proteobacteria; c_Epsilonproteobacteria	p_Campylobacterota; c_Desulfurellia; o_JAADFJ01; f_JAADFJ01; g_JAADFJ01	*mamE*
Idc_ex_meta_mg6	2,753,789	141	97.85	0.67	8.72	DRZ059051	p_Bacteroidetes; c_Bacteroidia; o_Bacteroidales	p_Bacteroidota; c_Bacteroidia; o_Bacteroidales; f_F082; g_SZUA-53	*mamA, mamE*
Idc_ex_meta_mg7	2,256,723	191	97.22	0.91	37.38	DRZ059052	p_Nitrospirae	p_Nitrospirota; c_Thermodesulfovibrionia; o_Thermodesulfovibrionales; f_JdFR-85; g_BMS3Bbin07	*mamA, mamE*
Idc_ex_meta_mg8	3,037,378	1,316	74.38	3.36	2.66	DRZ059053	p_Spirochaetes; c_Spirochaetia	p_Spirochaetota; c_UBA6919; o_UBA6919; f_UBA6919	*mamE*

10.3389/fmicb.2023.1174899

mamI, *mamM*, *mamP*, and *mamQ* were found in a MAG called Idc_ex_meta_mg2 affiliated with *Nitrospinae* (p_Nitrospinota; c-o_UBA7883 based on the GTDB taxonomy). The consecutive arrangement of *mamP*, *mamA*, and *mamQ* with locus tags of Idc_ex_meta_mg2_1352 to 1354 in the *Nitrospinae*-affiliated MAG supports the presence of an MGC (Supplementary Table 1). Other magnetosome genes previously found in *Nitrospinae*-affiliated MAGs (nPCR_bin9 and nNGH_bin12; Lin et al., 2020) were searched, and the arrangement of the MGC (*mamP*, *mamA*, and *mamQ*) in Idc_ex_meta_mg2 is similar to those from the other *Nitrospinae*-affiliated MAGs (Figure 3 and Supplementary Table 1). As a result, the presence of two other MGC clusters was due to the composition of *mamI*, *mamH*, *mmsF*, *mms6*, *mamT*, and *mamS*, and *man3* and *mamM* (Figure 3 and Supplementary Table 1). The former cluster was similar to that found in nNGH_bin12, whereas the latter cluster was similar to that in nPCR_bin9 (Figure 3). It should be noted that the MGCs found in the *Nitrospinae*-affiliated MAGs were similar to those in *Alphaproteobacteria* and *Ca.* Etaprotebacteria but clearly different from those in *Desulfobacteria*, *Nitrospirae*, and *Ca.* Omnitrophica. Although *mamA* and *mamE* were detected in MAGs other than *Nitrospinae* (non-*Nitrospinae* MAGs) by FeGenie, the detected *mamA* and *mamE* were not consecutively arranged without forming MGCs. Although *mamA* and *mamE* found in non-*Nitrospinae* MAGs may function in magnetosome formation, the functions of *mamA* and *mamE* in non-*Nitrospinae* MAGs need to be clarified.

Phylogenetic congruency of magnetosome genes in the *Nitrospinae* genome

Phylogenetic trees were constructed for *mamAMQ* found in the *Nitrospinae*-affiliated MAG obtained in this study (Figure 4). *MamAMQ* genes were selected because the gene sequences are present in most MTB genomes with sufficient sequence lengths for phylogenetic analysis (Lin et al., 2020). Consequently, the *mamAMQ* sequences from the chimney *Nitrospinae* formed a monophyletic clade with those from *Nitrospinae*-affiliated genomes from public databases rather than those from the other major taxonomic groups of MTB, except for the *mamQ* gene (Figure 4). The low bootstrap values might have resulted from the genetic divergence of magnetosome genes in *Nitrospinae*. Based on the relatedness of the *Nitrospinae*-affiliated magnetosome genes, the MGC appears to be encoded in the chimney *Nitrospinae* genome. Although the presence of MGC is a prerequisite for MTB, it remains to be determined whether the chimney *Nitrospinae* is capable of producing magnetosomes.

The metabolic potential of the chimney *Nitrospinae*

Genes involved in energy-yielding metabolic pathways were annotated using METABOLIC and DiSCo (Supplementary Table 2). The presence of *nrfH* (locus tag: Idc_ex_meta_mg2_0657) in the chimney *Nitrospinae* genome indicates nitrite reduction as the terminal electron-accepting process (Idc_ex_meta_mg2 in Figure 5). In mediating nitrite reduction, *nrfA* is essentially present at the consecutive downstream of *nrfH*. *nrfA* was found downstream of the *Nitrospinae* genome (locus tag: Idc_ex_meta_mg2_0656), wherein lysine, a motif sequence, was substituted with histidine. This substitution has also been found in a *nrfA*-like gene in *Campylobacter jejuni* (Einsle et al., 2000), whose nitrite-reducing ability has been demonstrated (Pittman et al., 2007). Thus, the chimney *Nitrospinae* may depend on nitrite as the electron acceptor. As for the energy source, sulfur oxidizers have an operon, including *dsrEFH* and a Dsr-Apr-Sat system, typically possessed by sulfate reducers (Dahl et al., 2008). In the *Nitrospinae* genome, *dsrA* (locus tag: Idc_ex_meta_mg2_1291), *dsrE* (locus tag: Idc_ex_meta_mg2_1294), *dsrF* (locus tag: Idc_ex_meta_mg2_1293), *dsrH* (locus tag: Idc_ex_meta_mg2_1292), *sat* (locus tag: Idc_ex_meta_mg2_1547), and *aprB* (locus tag: Idc_ex_meta_mg2_0024) were found (Figure 5). These results indicate the potential that the chimney *Nitrospinae* is a nitrite-reducing sulfur oxidizer.

Nitrospina gracilis, a cultivated member of the phylum *Nitrospinae*, is a chemolithoautotroph that generates energy by oxidizing nitrite (Lucker et al., 2013). Draft *Nitrospinae* genomes were submitted to comparative genomic analysis to clarify the variation of metabolic pathways in phylogenetically diverse members of the phylum *Nitrospinae* (Figure 5 and Supplementary Table 3). Three class-level clades were identified using a maximum likelihood tree from the concatenated sequences of 120 bacterial single-copy marker genes. Clade A included *N. gracilis*, whereas Clade B and Clade C included uncultivated taxa. The chimney genome (Idc_ex_meta_mg2) and the other MGC-encoding genomes were found in Clade C. *N. gracilis* uses the reductive tricarboxylic acid (rTCA) cycle for CO_2 fixation. *Acl* is a key enzyme in the rTCA, and *N. gracilis* has an *aclAB* with low sequence similarities to known *aclABs* (Lucker et al., 2013). The low sequence similarities caused *aclAB* to be undetected by most of the Clade A genomes, including *N. gracilis* by METABOLIC.

In contrast, *aclAB* was detected in many Clade B and C genomes, including the chimney *Nitrospinae*. Thus, the chimney *Nitrospinae* is most likely a chemolithautotroph that uses rTCA for CO_2 fixation. *nxrAB,* which is involved in nitrite oxidation by *N. gracilis* (Lucker et al., 2013), was present in 11 genomes affiliated with Clade A, but *nxrAB* was absent in 13 genomes affiliated with Clades B and C, except for HyVt-426. *sir*, indicated to be involved in assimilatory sulfite reduction by *N. gracilis* (Lucker et al., 2013), was detected in many genomes from Clade A and Clade C. Sulfur oxidation genes such as *dsrEFH* were not found in Clade A genomes, which is consistent with the use of nitrite as an energy source.

In contrast, many genomes affiliated with Clades B and C contained *dsrEFH*, as well as *aprAB* and *sat*. According to these results, the metabolic potential of the chimney *Nitrospinae* appears to be common in Clade C but is clearly distinct from that of Clade A, which includes *N.*

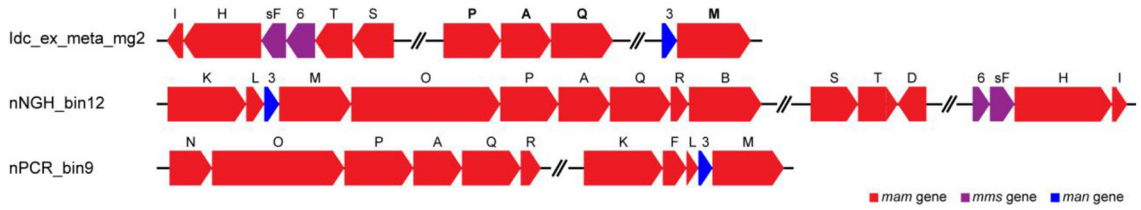

FIGURE 3
Comparison of magnetosome gene cluster arrangements in *Nitrospinae*-affiliated MAGs from this study (Idc_ex_meta_mg2) and a previous study (Lin et al., 2020). Magnetosome genes annotated by FeGenie, in addition to BLASTP scoring, are indicated in bold font (Table 1 and Supplementary Table 1).

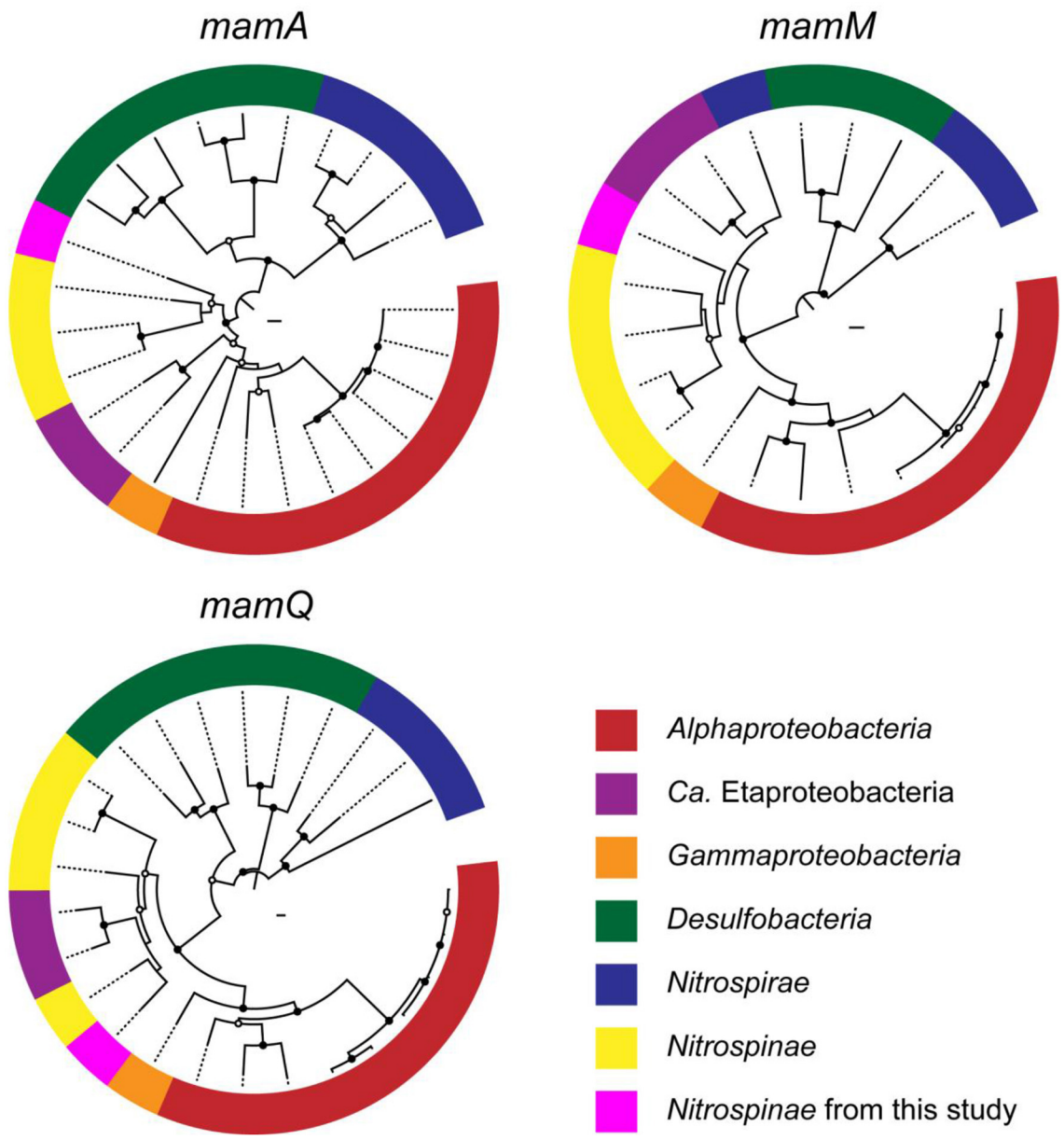

FIGURE 4
Phylogenetic trees of magnetosome genes, *mamAMQ*. The trees were constructed with the *mam* genes of known MTB (*Proteobacteria*, *Desulfobacteria*, and *Nitrospirae*) and *Nitrospinae* genomes. Filled and open black circles at nodes represent 1,000 pseudoreplicate bootstrap values higher than 75 and 50%, respectively. Complete trees are shown in Supplementary Figures 1–3.

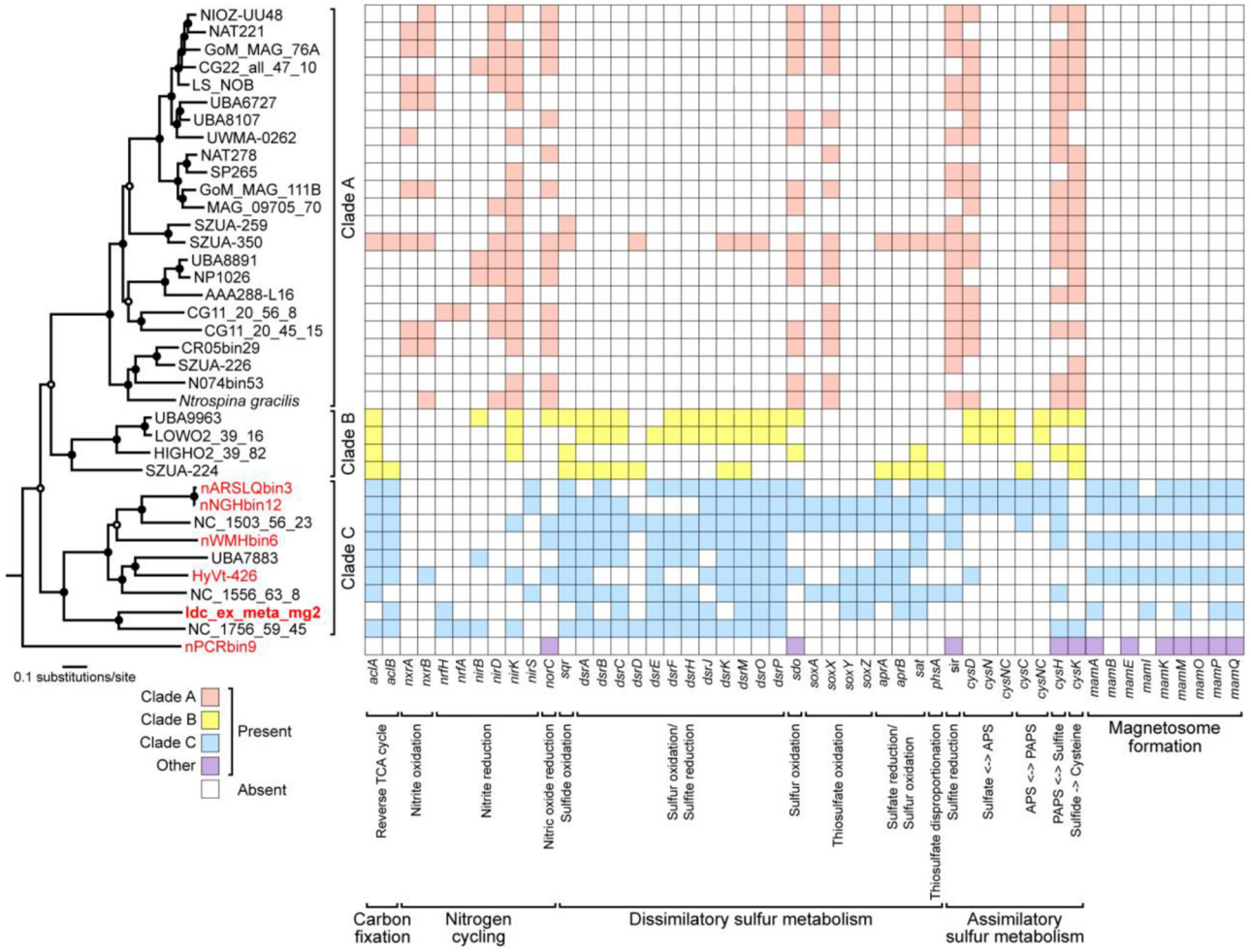

FIGURE 5
A maximum-likelihood tree of 120 concatenated bacterial single-copy marker proteins from *Nitrospinae* genomes, as well as a heat map of *Nitrospinae* genomes showing the presence or absence of genes involved in carbon, nitrogen, and sulfur metabolisms as well as magnetosome genes. Genes involved in magnetosome formation were annotated by FeGenie. Other genes were annotated by METABOLIC and DiSCo. A concatenated sequence obtained in this study is indicated in bold letters, whereas concatenated sequences containing MGCs are indicated in red letters. At nodes in the tree, filled and open black circles represent 1,000 pseudoreplicate bootstrap values higher than 75 and 50%, respectively. The absence of *aclAB* in Clade A may be due to the low similarity of *aclAB* sequences in Clade A genomes to known *aclAB* sequences.

gracilis. Taken together, the bacteria from the phylum *Nitrospinae* play an important role in carbon fixation in dark deep-sea environments.

Conclusion

In this study, magnetosomes in a metal sulfide chimney were demonstrated through direct observations of magnetically separated cells. Based on the genome-resolved metagenomic analysis, some of these magnetosomes could have originated from *Nitrospinae*-affiliated populations possessing genes involved in magnetosome production. Thus, our results expand the ecological diversity of magnetosome-producing MTB. However, it is still unclear what the ecological advantage of magnetosomes in the metal sulfide chimney is. To answer this question, further culture-dependent and culture-independent analyses are needed.

Data availability statement

The original contributions presented in the study are included in the article/Supplementary material. The MAG sequences presented in this study can be found in online repositories. The names of the repository/repositories and accession number can be found at: www.ncbi.nlm.nih.gov under the accession number, PRJDB13464.

Author contributions

SN and YS designed the study and co-wrote the manuscript. YS, HF, and SK collected and analyzed the chimney sample as shipboard scientists during JAMSTEC Scientific Cruises NT12-24. SN, HF, and YS performed mineralogical characterizations. SN and TY conducted magnetic separation and electron microscopy. SN, MK, HF, SK, and YS performed single-gene and metagenomics

analyses and data analyses. All authors discussed the results and commented on the manuscript. All authors contributed to the article and approved the submitted version.

Funding

This research was supported by the TAIGA project, a Grant-in-Aid for Scientific Research on Innovative Areas (#20109006) from the Ministry of Education, Culture, Sports, Science, and Technology (MEXT), Japan, a Grant-in-Aid for Scientific Research (B) (#19H03310) from MEXT, and JSPS KAKENHI (Grant Numbers: 25287137 and 16K13896).

Acknowledgments

We are grateful to Atsushi Arakaki at the Tokyo University of Agriculture and Technology for providing us with a culture of *Magnetospirillum magneticum* and to Koji Ichimura and Seiya Yamashita at the University of Tokyo for technical support for mineralogical analyses. The authors would like to thank Enago (www.enago.jp) for the English language review.

Conflict of interest

The authors declare that the research was conducted in the absence of any commercial or financial relationships that could be construed as a potential conflict of interest.

Publisher's note

All claims expressed in this article are solely those of the authors and do not necessarily represent those of their affiliated organizations, or those of the publisher, the editors and the reviewers. Any product that may be evaluated in this article, or claim that may be made by its manufacturer, is not guaranteed or endorsed by the publisher.

Supplementary material

The Supplementary Material for this article can be found online at: https://www.frontiersin.org/articles/10.3389/fmicb.2023.1174899/full#supplementary-material

References

Alneberg, J., Bjarnason, B. S., de Bruijn, I., Schirmer, M., Quick, J., Ijaz, U. Z., et al. (2014). Binning metagenomic contigs by coverage and composition. *Nat. Methods* 11, 1144–1146. doi: 10.1038/nmeth.3103

Bankevich, A., Nurk, S., Antipov, D., Gurevich, A. A., Dvorkin, M., Kulikov, A. S., et al. (2012). SPAdes: A new genome assembly algorithm and its applications to single-cell sequencing. *J. Comput. Biol.* 19, 455–477. doi: 10.1089/cmb.2012.0021

Blakemore, R. (1975). Magnetotactic bacteria. *Science* 190, 377–379. doi: 10.1126/science.170679

Capella-Gutierrez, S., Silla-Martinez, J. M., and Gabaldon, T. (2009). trimAl: A tool for automated alignment trimming in large-scale phylogenetic analyses. *Bioinformatics* 25, 1972–1973. doi: 10.1093/bioinformatics/btp348

Chen, S., Yu, M., Zhang, W., He, K., Pan, H., Cui, K., et al. (2022). Metagenomic and microscopic analysis of magnetotactic bacteria in tangyin hydrothermal field of okinawa trough. *Front. Microbiol.* 13, 887136. doi: 10.3389/fmicb.2022.887136

Cui, K., Zhang, W., Liu, J., Xu, C., Zhao, Y., Chen, S., et al. (2021). Characterization and diversity of magnetotactic bacteria from sediments of Caroline Seamount in the Western Pacific Ocean. *J. Oceanol. Limnol.* 39, 2027–2043. doi: 10.1007/s00343-021-0029-x

Dahl, C., Schulte, A., Stockdreher, Y., Hong, C., Grimm, F., Sander, J., et al. (2008). Structural and molecular genetic insight into a widespread sulfur oxidation pathway. *J. Mol. Biol.* 384, 1287–1300. doi: 10.1016/j.jmb.2008.10.016

Dong, Y., Li, J., Zhang, W., Zhang, W., Zhao, Y., Xiao, T., et al. (2016). The detection of magnetotactic bacteria in deep sea sediments from the east Pacific Manganese Nodule Province. *Environ. Microbiol. Rep.* 8, 239–249. doi: 10.1111/1758-2229.12374

Edgar, R. C. (2004). MUSCLE: Multiple sequence alignment with high accuracy and high throughput. *Nucleic Acids Res.* 32, 1792–1797. doi: 10.1093/nar/gkh340

Einsle, O., Stach, P., Messerschmidt, A., Simon, J., Kroger, A., Huber, R., et al. (2000). Cytochrome c nitrite reductase from *Wolinella succinogenes*. Structure at 1.6 A resolution, inhibitor binding, and heme-packing motifs. *J. Biol. Chem.* 275, 39608–39616. doi: 10.1074/jbc.M006188200

Finn, R. D., Bateman, A., Clements, J., Coggill, P., Eberhardt, R. Y., Eddy, S. R., et al. (2014). Pfam: The protein families database. *Nucleic Acids Res.* 42, D222–D230. doi: 10.1093/nar/gkt1223

Frankel, R. B., Bazylinski, D. A., Johnson, M. S., and Taylor, B. L. (1997). Magneto-aerotaxis in marine coccoid bacteria. *Biophys. J.* 73, 994–1000. doi: 10.1016/S0006-3495(97)78132-3

Garber, A. I., Nealson, K. H., Okamoto, A., McAllister, S. M., Chan, C. S., Barco, R. A., et al. (2020). FeGenie: A comprehensive tool for the identification of iron genes and iron gene neighborhoods in genome and metagenome assemblies. *Front. Microbiol.* 11, 37. doi: 10.3389/fmicb.2020.00037

Gish, W., and States, D. J. (1993). Identification of protein coding regions by database similarity search. *Nat. Genet.* 3, 266–272. doi: 10.1038/ng0393-266

Goswami, P., He, K., Li, J., Pan, Y., Roberts, A. P., and Lin, W. (2022). Magnetotactic bacteria and magnetofossils: Ecology, evolution and environmental implications. *NPJ Biofilms Microbiomes* 8, 43. doi: 10.1038/s41522-022-00304-0

Grünberg, K., Wawer, C., Tebo, B. M., and Schüler, D. (2001). A large gene cluster encoding several magnetosome proteins is conserved in different species of magnetotactic bacteria. *Appl. Environ. Microbiol.* 67, 4573–4582. doi: 10.1128/AEM.67.10.4573-4582.2001

Haymon, R. M. (1983). Growth history of hydrothermal black smoker chimneys. *Nature* 301, 695–698. doi: 10.1038/301695a0

Hirai, M., Nishi, S., Tsuda, M., Sunamura, M., Takaki, Y., and Nunoura, T. (2017). Library construction from subnanogram DNA for pelagic sea water and deep-sea sediments. *Microbes Environ.* 32, 336–343. doi: 10.1264/jsme2.ME17132

Kang, D. D., Froula, J., Egan, R., and Wang, Z. (2015). MetaBAT, an efficient tool for accurately reconstructing single genomes from complex microbial communities. *PeerJ* 3, e1165. doi: 10.7717/peerj.1165

Kato, S., Nakano, S., Kouduka, M., Hirai, M., Suzuki, K., Itoh, T., et al. (2019). Metabolic potential of as-yet-uncultured archaeal lineages of candidatus hydrothermarchaeota thriving in deep-sea metal sulfide deposits. *Microbes Environ.* 34, 293–303. doi: 10.1264/jsme2.ME19021

Kato, S., Shibuya, T., Takaki, Y., Hirai, M., Nunoura, T., and Suzuki, K. (2018). Genome-enabled metabolic reconstruction of dominant chemosynthetic colonizers in deep-sea massive sulfide deposits. *Environ. Microbiol.* 20, 862–877. doi: 10.1111/1462-2920.14032

Kato, S., Takano, Y., Kakegawa, T., Oba, H., Inoue, K., Kobayashi, C., et al. (2010). Biogeography and biodiversity in sulfide structures of active and inactive vents at deep-sea hydrothermal fields of the Southern Mariana Trough. *Appl. Environ. Microbiol.* 76, 2968–2979. doi: 10.1128/AEM.00478-10

Kolinko, S., Jogler, C., Katzmann, E., Wanner, G., Peplies, J., and Schuler, D. (2012). Single-cell analysis reveals a novel uncultivated magnetotactic bacterium within the candidate division OP3. *Environ. Microbiol.* 14, 1709–1721. doi: 10.1111/j.1462-2920.2011.02609.x

Kolinko, S., Richter, M., Glockner, F. O., Brachmann, A., and Schuler, D. (2016). Single-cell genomics of uncultivated deep-branching magnetotactic bacteria reveals a conserved set of magnetosome genes. *Environ. Microbiol.* 18, 21–37. doi: 10.1111/1462-2920.12907

Kolinko, S., Wanner, G., Katzmann, E., Kiemer, F., Fuchs, B. M., and Schuler, D. (2013). Clone libraries and single cell genome amplification reveal extended diversity of uncultivated magnetotactic bacteria from marine and freshwater environments. *Environ. Microbiol.* 15, 1290–1301. doi: 10.1111/1462-2920.12004

Lefèvre, C. T., and Bazylinski, D. A. (2013). Ecology, diversity, and evolution of magnetotactic bacteria. *Microbiol. Mol. Biol. Rev.* 77, 497–526. doi: 10.1128/MMBR.00021-13

Lefèvre, C. T., Trubitsyn, D., Abreu, F., Kolinko, S., Jogler, C., de Almeida, L. G., et al. (2013). Comparative genomic analysis of magnetotactic bacteria from the Deltaproteobacteria provides new insights into magnetite and greigite magnetosome genes required for magnetotaxis. *Environ. Microbiol.* 15, 2712–2735. doi: 10.1111/1462-2920.12128

Li, J., Liu, P., Menguy, N., Zhang, X., Wang, J., Benzerara, K., et al. (2022). Intracellular silicification by early-branching magnetotactic bacteria. *Sci. Adv.* 8, eabn6045. doi: 10.1126/sciadv.abn6045

Li, J., Liu, P., Tamaxia, A., Zhang, H., Liu, Y., Wang, J., et al. (2021). Diverse intracellular inclusion types within magnetotactic bacteria: Implications for biogeochemical cycling in aquatic environments. *J. Geophys. Res.* 126, 2021JG006310. doi: 10.1029/2021JG006310

Li, J., Liu, P., Wang, J., Roberts, A. P., and Pan, Y. (2020). Magnetotaxis as an adaptation to enable bacterial shuttling of microbial sulfur and sulfur cycling across aquatic oxic-anoxic interfaces. *J. Geophys. Res.* 125. doi: 10.1029/2020JG006012

Li, J., Zhang, H., Menguy, N., Benzerara, K., Wang, F., Lin, X., et al. (2017). Single-cell resolution of uncultured magnetotactic bacteria via fluorescence-coupled electron microscopy. *Appl. Environ. Microbiol.* 83, 17. doi: 10.1128/AEM.00409-17

Lin, W., Bazylinski, D. A., Xiao, T., Wu, L. F., and Pan, Y. (2014a). Life with compass: Diversity and biogeography of magnetotactic bacteria. *Environ. Microbiol.* 16, 2646–2658. doi: 10.1111/1462-2920.12313

Lin, W., Deng, A., Wang, Z., Li, Y., Wen, T., Wu, L. F., et al. (2014b). Genomic insights into the uncultured genus "Candidatus Magnetobacterium" in the phylum Nitrospirae. *ISME J.* 8, 2463–2477. doi: 10.1038/ismej.2014.94

Lin, W., Pan, Y., and Bazylinski, D. A. (2017). Diversity and ecology of and biomineralization by magnetotactic bacteria. *Environ. Microbiol. Rep.* 9, 345–356. doi: 10.1111/1758-2229.12550

Lin, W., Zhang, W., Paterson, G. A., Zhu, Q., Zhao, X., Knight, R., et al. (2020). Expanding magnetic organelle biogenesis in the domain Bacteria. *Microbiome* 8, 152. doi: 10.1186/s40168-020-00931-9

Lin, W., Zhang, W., Zhao, X., Roberts, A. P., Paterson, G. A., Bazylinski, D. A., et al. (2018). Genomic expansion of magnetotactic bacteria reveals an early common origin of magnetotaxis with lineage-specific evolution. *ISME J.* 12, 1508–1519. doi: 10.1038/s41396-018-0098-9

Liu, J., Zhang, W., Li, X., Li, X., Chen, X., Li, J. H., et al. (2017). Bacterial community structure and novel species of magnetotactic bacteria in sediments from a seamount in the Mariana volcanic arc. *Sci. Rep.* 7, 17964. doi: 10.1038/s41598-017-17445-4

Lovley, D. R., and Phillips, E. J. (1986). Organic matter mineralization with reduction of ferric iron in anaerobic sediments. *Appl. Environ. Microbiol.* 51, 683–689. doi: 10.1128/aem.51.4.683-689.1986

Lucker, S., Nowka, B., Rattei, T., Spieck, E., and Daims, H. (2013). The genome of *Nitrospina gracilis* illuminates the metabolism and evolution of the major marine nitrite oxidizer. *Front. Microbiol.* 4, 27. doi: 10.3389/fmicb.2013.00027

Ludwig, W., Strunk, O., Westram, R., Richter, L., Meier, H., Yadhukumar, A., et al. (2004). ARB: A software environment for sequence data. *Nucleic Acids Res.* 32, 1363–1371. doi: 10.1093/nar/gkh293

McCausland, H. C., and Komeili, A. (2020). Magnetic genes: Studying the genetics of biomineralization in magnetotactic bacteria. *PLoS Genet.* 16, e1008499. doi: 10.1371/journal.pgen.1008499

McGlynn, S. E., Chadwick, G. L., O'Neill, A., Mackey, M., Thor, A., Deerinck, T. J., et al. (2018). Subgroup characteristics of marine methane-oxidizing ANME-2 archaea and their syntrophic partners as revealed by integrated multimodal analytical microscopy. *Appl. Environ. Microbiol.* 84, 18. doi: 10.1128/AEM.00399-18

Neukirchen, S., and Sousa, F. L. (2021). DiSCo: A sequence-based type-specific predictor of Dsr-dependent dissimilatory sulphur metabolism in microbial data. *Microb. Genom.* 7, 603. doi: 10.1099/mgen.0.000603

Ogata, H., Goto, S., Sato, K., Fujibuchi, W., Bono, H., and Kanehisa, M. (1999). KEGG: Kyoto encyclopedia of genes and genomes. *Nucleic Acids Res.* 27, 29–34. doi: 10.1093/nar/27.1.29

Parks, D. H., Chuvochina, M., Rinke, C., Mussig, A. J., Chaumeil, P. A., and Hugenholtz, P. (2022). GTDB: An ongoing census of bacterial and archaeal diversity through a phylogenetically consistent, rank normalized and complete genome-based taxonomy. *Nucleic Acids Res.* 50, D785–D794. doi: 10.1093/nar/gkab776

Parks, D. H., Rinke, C., Chuvochina, M., Chaumeil, P. A., Woodcroft, B. J., Evans, P. N., et al. (2017). Recovery of nearly 8,000 metagenome-assembled genomes substantially expands the tree of life. *Nat. Microbiol.* 2, 1533–1542. doi: 10.1038/s41564-017-0012-7

Pittman, M. S., Elvers, K. T., Lee, L., Jones, M. A., Poole, R. K., Park, S. F., et al. (2007). Growth of *Campylobacter jejuni* on nitrate and nitrite: Electron transport to NapA and NrfA via NrfH and distinct roles for NrfA and the globin Cgb in protection against nitrosative stress. *Mol. Microbiol.* 63, 575–590. doi: 10.1111/j.1365-2958.2006.05532.x

Sakai, S., and Kodan, T. (2011). Micropowder collecting technique for stable isotope analysis of carbonates. *Rapid Commun. Mass Spectrom.* 25, 1205–1208. doi: 10.1002/rcm.4980

Sayers, E. W., Beck, J., Bolton, E. E., Bourexis, D., Brister, J. R., Canese, K., et al. (2021). Database resources of the national center for biotechnology information. *Nucleic Acids Res.* 49, D10–D17. doi: 10.1093/nar/gkaa892

Schulz-Vogt, H. N., Pollehne, F., Jurgens, K., Arz, H. W., Beier, S., Bahlo, R., et al. (2019). Effect of large magnetotactic bacteria with polyphosphate inclusions on the phosphate profile of the suboxic zone in the Black Sea. *ISME J.* 13, 1198–1208. doi: 10.1038/s41396-018-0315-6

Selengut, J. D., Haft, D. H., Davidsen, T., Ganapathy, A., Gwinn-Giglio, M., Nelson, W. C., et al. (2007). TIGRFAMs and genome properties: Tools for the assignment of molecular function and biological process in prokaryotic genomes. *Nucleic Acids Res.* 35, D260–D264. doi: 10.1093/nar/gkl1043

Stamatakis, A. (2014). RAxML version 8: A tool for phylogenetic analysis and post-analysis of large phylogenies. *Bioinformatics* 30, 1312–1313. doi: 10.1093/bioinformatics/btu033

Suzuki, Y., Inagaki, F., Takai, K., Nealson, K. H., and Horikoshi, K. (2004). Microbial diversity in inactive chimney structures from deep-sea hydrothermal systems. *Microb. Ecol.* 47, 186–196. doi: 10.1007/s00248-003-1014-y

Takamiya, H., Kouduka, M., Furutani, H., Mukai, H., Nakagawa, K., Yamamoto, T., et al. (2022). Copper-nanocoated ultra-small cells in grain boundaries inside an extinct vent chimney. *Front. Microbiol.* 13, 864205. doi: 10.3389/fmicb.2022.864205

Uebe, R., and Schüler, D. (2016). Magnetosome biogenesis in magnetotactic bacteria. *Nat. Rev. Microbiol.* 14, 621–637. doi: 10.1038/nrmicro.2016.99

Uritskiy, G. V., DiRuggiero, J., and Taylor, J. (2018). MetaWRAP-a flexible pipeline for genome-resolved metagenomic data analysis. *Microbiome* 6, 158. doi: 10.1186/s40168-018-0541-1

Uzun, M., Alekseeva, L., Krutkina, M., Koziaeva, V., and Grouzdev, D. (2020). Unravelling the diversity of magnetotactic bacteria through analysis of open genomic databases. *Sci. Data* 7, 252. doi: 10.1038/s41597-020-00593-0

Wu, Y. W., Simmons, B. A., and Singer, S. W. (2016). MaxBin 2.0: An automated binning algorithm to recover genomes from multiple metagenomic datasets. *Bioinformatics* 32, 605–607. doi: 10.1093/bioinformatics/btv638

Yamazaki, T. (2020). Reductive dissolution of biogenic magnetite. *Earth Planets Space* 72, 3. doi: 10.1186/s40623-020-01290-3

Yamazaki, T., Suzuki, Y., Kouduka, M., and Kawamura, N. (2019). Dependence of bacterial magnetosome morphology on chemical conditions in deep-sea sediments. *Earth Planet Sci. Lett.* 513, 135–143. doi: 10.1016/j.epsl.2019.02.015

Zhou, Z., Tran, P. Q., Breister, A. M., Liu, Y., Kieft, K., Cowley, E. S., et al. (2022). METABOLIC: High-throughput profiling of microbial genomes for functional traits, metabolism, biogeochemistry, and community-scale functional networks. *Microbiome* 10, 33. doi: 10.1186/s40168-021-01213-8

frontiers | Frontiers in Microbiology

TYPE Original Research
PUBLISHED 28 June 2023
DOI 10.3389/fmicb.2023.1197476

OPEN ACCESS

EDITED BY
David Emerson,
Bigelow Laboratory for Ocean Sciences,
United States

REVIEWED BY
Jiwen Liu,
Ocean University of China, China
Hongmei Jing,
Institute of Deep-Sea Science and Engineering,
China

*CORRESPONDENCE
Chaolun Li
✉ lcl@qdio.ac.cn

RECEIVED 31 March 2023
ACCEPTED 25 May 2023
PUBLISHED 28 June 2023

CITATION
Feng W, Wang M, Dong D, Hui M, Zhang H, Fu L, Zhong Z, Xu Z and Li C (2023) Variation in epibiotic bacteria on two squat lobster species of Munidopsidae.
Front. Microbiol. 14:1197476.
doi: 10.3389/fmicb.2023.1197476

Variation in epibiotic bacteria on two squat lobster species of Munidopsidae

Wenze Feng[1,2,3,4], Minxiao Wang[1,2,3], Dong Dong[5], Min Hui[5], Huan Zhang[1,2], Lulu Fu[1,2], Zhaoshan Zhong[1,2], Zheng Xu[6] and Chaolun Li[1,2,3,4]*

[1]CAS Key Laboratory of Marine Ecology and Environmental Sciences, Institute of Oceanology, Chinese Academy of Sciences, Qingdao, China, [2]Center of Deep Sea Research, Institute of Oceanology, Chinese Academy of Sciences, Qingdao, China, [3]University of Chinese Academy of Sciences, Beijing, China, [4]South China Sea Institute of Oceanology, Chinese Academy of Sciences, Guangzhou, China, [5]Department of Marine Organism Taxonomy and Phylogeny, Institute of Oceanology, Chinese Academy of Sciences, Qingdao, China, [6]College of Life Sciences, Zaozhuang University, Zaozhuang, China

The relationships between epibiotic bacteria on deep-sea hosts and host lifestyle factors are of particular interest in the field of deep-sea chemoautotrophic environmental adaptations. The squat lobsters *Shinkaia crosnieri* and *Munidopsis verrilli* are both dominant species in cold-seep ecosystems, and they have different distributions and feeding behaviors. These species may have evolved to have distinct epibiotic microbiota. Here, we compared the epibiotic bacterial communities on the *M. verrilli* carapace ($MV_{carapace}$), *S. crosnieri* carapace ($SC_{carapace}$), and *S. crosnieri* ventral plumose setae (SC_{setae}). The epibiotic bacteria on SC_{setae} were dense and diverse and had a multi-layer configuration, while those on $MV_{carapace}$ and $SC_{carapace}$ were sparse and had a monolayer configuration. Chemoautotrophic bacteria had the highest relative abundance in all epibiotic bacterial communities. The relative abundance of amplicon sequence variant 3 (ASV3; unknown species in order *Thiotrichales*), which is associated with sulfide oxidation, was significantly higher in SC_{setae} than $MV_{carapace}$ and $SC_{carapace}$. *Thiotrichales* species seemed to be specifically enriched on SC_{setae}, potentially due to the synthetic substrate supply, adhesion preference, and host behaviors. We hypothesize that the *S. crosnieri* episymbionts use chemical fluxes near cold seeps more efficiently, thereby supporting the host's nutrient strategies, resulting in a different distribution of the two species of squat lobster.

KEYWORDS

cold seep, squat lobster, epibiotic microbiome, sulfide, adaptation

1. Introduction

Deep-Sea chemoautotrophic ecosystems, including cold seeps, are often characterized by extreme environmental conditions and endemic fauna. Decapod crustaceans, such as alvinocaridid shrimps (Komai et al., 2005), lithodid crabs (Niemann et al., 2013), and squat lobsters (Chevaldonne and Olu, 1996), are common macrofauna in cold seeps. Squat lobsters, as one of the dominant microbenthic crustaceans, are key components of deep-sea chemosynthetic ecosystems, considering their wide distribution and high abundance (Martin and Haney, 2005). Squat lobsters belong to the superfamilies Galatheoidea and Chirostyloidea, with over 1,000 species (Baba and Fujita, 2017). They are found at all depths, and the

Munidopsidae (Galatheoidea) species almost completely dominate at extreme depths, with typical adaptations such as eye degeneration (Warrant and Locket, 2004). The Munidopsidae species occupy various ecological niches in the deep sea, including in cold seeps (Martin and Haney, 2005). Most of those observed at cold seeps [such as *Munidopsis andamanica* (Hoyoux et al., 2012) and *Munidopsis* sp. (Macavoy et al., 2008)] have a wide distribution around the vents, with an omnivorous diet. Others [such as *Kiwa puravida* (Thurber et al., 2011) and *Kiwa hirsute* (Macpherson et al., 2005)] are concentrated around vents, with distinctive dense setae on their body surfaces. Numerous invertebrate species have formed symbiotic associations with their microbiomes, which can exert a range of effects on their hosts, predominantly beneficial ones (Mioduchowska et al., 2018). Goffredi et al. proposed that the bacteria that clustered on the plumose setae of *Kiwa hirsute* could be used as a nutrient resource to meet the energetic demands of the host (Goffredi et al., 2008). The provision of nutrients is a major feature of host–microbe interactions (Schwartzman et al., 2015). Dattagupta et al. found that *Niphargus ictus,* a freshwater cave amphipod, developed a nutritional strategy involving scraping epibiotic bacteria (by grooming itself with its gnathopods) to use as food, and it was adapted to environments with high concentrations of sulfides (Dattagupta et al., 2009). Specialized nutritional strategies might have driven the evolution of some Munidopsidae species (Hoyoux et al., 2009). Munidopsidae species' epibiotic bacterial communities, as a source of nutrients, might be drivers of speciation in squat lobsters.

Shinkaia crosnieri (Galatheoidea: Munidopsidae) was first recorded in hydrothermal vents in the Okinawa Trough, mainly dwelling in chemosynthetic ecosystems in the west Pacific Ocean (Baba and Williams, 1998). *Munidopsis verrilli* (Galatheoidea: Munidopsidae) has been widely reported in various deep-sea ecosystems around the world, such as the San Clemente Basin (Williams et al., 2000), Tasmania Island (Baba and Poore, 2002), eastern Hokkaido (Komai and Matsuzaki, 2016), and northeastern South China Sea (Dong and Li, 2015). These two species are closely evolutionarily related and belong to different genera of the same family (Cheng et al., 2020). The plumose setae on *S. crosnieri* (SC_{setae}), which harbors dense epibiotic bacterial communities, are the main basis for distinguishing between the two squat lobsters (Wehrtmann and Acuna, 2011). According to a previous study conducted by Watsuji, the host can use the abundant episymbionts that attach to the setae as dense biofilm to obtain nutrients through *in vitro* digestion experiments (Watsuji et al., 2015). Some of these epibiotic bacteria were found to be thioautotrophic based on FISH and Nano-SIMS analysis, as suggested by Watsuji et al. (2012). On the other hand, *M. verrilli*'s underside was smooth without dense plumose setae. Leinberger et al. found evidence for a possible beneficial relationship between *Munidopsis alvisca* and its epibiotic bacteria (Leinberger et al., 2022). However, *Munidopsis* are not generally considered to have a close symbiotic association with their microbiomes but an opportunist. The two species also differ in their distribution in the chemosynthetic ecosystems. *Shinkaia crosnieri* forms impressive aggregations around cold seeps (refs) and hydrothermal vents in the Okinawa Trough (Tsuchida et al., 2003). In contrast, *M. verrilli,* associated with whale carcasses, appears to be an opportunist with a much broader geological range (Williams et al., 2000). It is evident that the concentration of reductive materials is higher in the core regions of vents and seeps, which can lead to higher primary productivity. The distance from the seepages may have influenced the microbiological communities in different squat lobsters. The microbiome's composition and abundance may, in turn, influence the behavior and evolution of squat lobsters. Thus, we hypothesized that the establishment of symbiosis in SC may contribute to the formation of the current distribution pattern. A systematic comparison of epibiotic bacterial communities associated with different Munidopsidae species would help to explore this hypothesis.

Site F is one of the active cold seeps in the South China Sea and supports several macrobenthic communities, including squat lobsters (Xiao et al., 2020). Both *S. crosnieri* and *M. verrilli* are dominant species in Site F. They have distinct differences in their distribution in relation to the cold seep. Zhao et al. found that *S. crosnieri* only congregated in the immediate vicinity of the cold seep at Site F, with very high abundances, reaching up to 300 individuals per square meter (Zhao et al., 2020). *Munidopsis verrilli,* on the other hand, is distributed over many regions of Site F, but not at high densities (Wang X. et al., 2022). These findings reflect the differential distributions of *S. crosnieri* and *M. verrilli* within a relatively small area. The co-occurrences of the two species provide an excellent opportunity for a comparative study of the link between the epibiotic bacterial communities and the distribution of squat lobsters.

The aim of this study was to investigate the epibiotic bacterial communities on squat lobsters with different ecological niches. We used scanning electron microscopy (SEM) to visualize the morphology of the epibiotic bacteria, quantitative real-time PCR to determine the difference in the absolute density of the bacteria, and high-throughput sequencing of 16S rRNA gene to explore the differences in the composition of the epibiotic bacterial communities.

2. Materials and methods

2.1. Sample collection

Squat lobsters were collected from Site F in the South China Sea (N119°17′8.22″ E, 22°06′55.26" N) during a cruise in May, 2021. *Shinkaia crosnieri* was caught around the cold seep, where conspicuous methane bubbles can be observed. *Munidopsis verrilli* was mainly caught at peripheral mussel beds around 10 m away from the cold seep. Specimens were collected using a carousel suction sampler on the remotely operated vehicle (ROV) Faxian on the research vessel "Kexue." They were transported in a homothermic macrofauna carrier which maintained a temperature similar to that at the cold seep, at around 4°C.

All animals were identified as *S. crosnieri* or *M. verrilli via* morphological classification, according to the descriptions given by Baba and Poore (2002) and Baba and Williams (1998). The carapaces of the two squat lobster species ($MV_{carapace}$ and $SC_{carapace}$) and the plumose setae of *S. crosnieri* (SC_{setae}) were rinsed with sterilized seawater and then immediately dissected with scissors on board. Samples for molecular analysis were snap-frozen in liquid nitrogen and stored at −80°C until DNA extraction. Cold seep interface water associated with the community of *S. crosnieri* (designated environment [ENV]), which was used to investigate the bacterioplankton, was filtered using an *in-situ* microbe sampler with a 0.22-μm filter membrane and stored at −80°C.

2.2. SEM

The animal samples for SEM were preserved in glutaraldehyde, underwent replacement of glutaraldehyde after 24 h, and were then stored at 4°C. In the laboratory, the samples were dehydrated in a graded ethanol series, underwent critical-point drying, were coated with gold (sputter/carbon thread; EM ACE200, Leica, Germany), and were then observed using SEM (S-3400 N, Hitachi, Japan).

2.3. Nucleic acid extraction and 16S rRNA gene amplicon sequencing

For 16S amplicon sequencing, we obtained ten different samples. These included three carapace samples of *M. verrilli*, three carapace samples of *S. crosnieri*, three setae samples of *S. crosnieri*, and one environmental water sample for bacterioplankton. We used a DNeasy PowerWater Kit (Qiagen, United States) to extract total DNA from these samples, following the manufacturer's instructions. The DNA was then diluted to 1 ng/μl for PCR amplification. The PCR amplification was performed using the primer pair 341F (5′-CCTAYGGGRBGCASCAG-3′) and 806R (5′-GGACTACNNGGG TATCTAAT-3′), which target the hypervariable regions between V3 and V4 of the prokaryotic 16S rRNA gene. All PCRs were performed with 10 μl Phusion® HighFidelity PCR Master Mix (NEB, United States), 1 μM forward primer, 1 μM reverse primer, and 1 μL template DNA. The thermal cycling program involved initial denaturation at 98°C for 1 min, 30 cycles of denaturation at 98°C for 10 s, annealing at 50°C for 30 s, and extension at 72°C for 30 s, and a final elongation at 72°C for 5 min. Electrophoresis was then performed using 2% agarose gel. Sequencing libraries were generated using an NEBNext® Ultra™ II DNA Library Prep Kit and were quantified by Qubit and qPCR. After that, NovaSeq 6000 (Illumina) was used for on-machine sequencing.

2.4. Quantification of the epibiotic bacteria

Real-time PCR was performed on QuantStudio 1 (Thermo Fisher Scientific, USA) in triplicate. 331F (5′-TCCTACGGGAGGCAG CAGT-3′) and 797R (5′-GGACTACCAGGGTATCTAATCCTGTT-3′) primers were used and each reaction (20 μL) contained 1× SYBR® Premix Ex Taq™ (TaKaRa), 1 μl template DNA, 1 μM forward primer, and 1 μM reverse primer (Nadkarni et al., 2002). The standard curve was constructed based on known amounts of purified PCR product (10^2 to 10^8 copies/μl) obtained from *E. coli* genomic DNA by using the bacterial 16S rRNA gene-specific primers 27F (5′-AGAGTT TGATCMTGGCTCAG-3′) and 1492R (5′-TACGGYTACCTTGTT ACGACTT-3′) (Weisburg et al., 1991). The thermal cycling program involved 95°C for 15 min, followed by 35 cycles of 95°C for 15 s, 58°C for 30 s, and 72°C for 30 s. The wet weight of each sample was recorded using an electronic balance and the number of copies per unit mass (wet weight) was calculated using the standard curve.

2.5. Bioinformatic analyses

Bioinformatic analyses were performed using QIIME 2 (v2022.2) (Bolyen et al., 2019). Raw sequence data were demultiplexed and quality filtered using the q2-demux plugin followed by denoising with DADA2 (Callahan et al., 2016). All amplicon sequence variants (ASVs) were aligned using MAFFT (Katoh and Standley, 2013) and were used to construct a phylogeny using FastTree2 (Price et al., 2010). To minimize differences in sequencing depth among the samples for the alpha and beta diversity analyses, all samples were normalized by subsample at a depth of 32,549. Alpha diversity analysis, beta diversity analysis, and principal coordinate analysis (PCoA) were conducted using q2-diversity. Taxonomy was assigned to ASVs using the q2-feature-classifier (classify-sklearn naïve Bayes taxonomy classifier; Bokulich et al., 2018) and the Silva138 database (Quast et al., 2012). Analysis of variance (ANOVA) and least significant difference (LSD) post-hoc comparisons were applied in SPSS v26 to show the significance of the difference in the alpha diversity index (Shannon index; Fahy et al., 2015). STAMP v2.1.3 was used with Welch's t-test to compare the dominant bacterial orders and ASVs in different groups (Parks et al., 2014). Analysis of similarities (ANOSIM) based on the Bray–Curtis distance was conducted using the 'vegan' package in R v3.5.1 (Liu and Tong, 2017). A bacterial co-occurrence network consisting of the top 200 ASVs was constructed based on a Spearman correlation matrix using the 'ggClusterNet' package (Wen et al., 2022).

3. Results

3.1. Observation of the microbiota on squat lobsters

According to Figures 1C,I, the ventral surface of *S. crosnieri* was covered with numerous plumose setae, whereas the ventral parts of *M. verrilli* was much smoother with only nolittle setae. The SEM images showed that the percentage of surfaces covered by biofilm was significantly higher for SC_{setae} (Figure 1G) than $SC_{carapace}$ and $MV_{carapace}$ (Figures 1F,H). In terms of the morphology, the biofilm on the carapace of both species of squat lobster tended to be dominated by groups <5 μm in length and had a monolayer configuration. In contrast, the SC_{setae} epibiotic bacterial community consisted of diverse morphological groups, ranging from 1 to 200 μm in length, with rod or filament shapes, and the community had a multi-layer configuration. In summary, in the setae, the biofilm was much denser and groups with slender linear shapes were more common (Figure 1).

3.2. Quantification of the microbiota on squat lobsters

We established the standard curve with the R^2 of 0.996 to estimate the abundance of the bacteria for each sample (Supplementary Figure S1). Real-time PCR confirmed the significant difference in the 16S rRNA gene copy number of epibiotic bacteria on the two species of squat lobster. The 16S rRNA gene copy number of SC_{setae} exceeded that of $MV_{carapace}$ and $SC_{carapace}$ by around three orders of magnitude, while the values for $MV_{carapace}$ and $SC_{carapace}$ were close. The results suggest that SC_{setae} might provide epibiotic bacteria with an excellent attachment substrate, leading to the enrichment of various groups, with a multi-layer configuration (Figure 2).

10.3389/fmicb.2023.1197476

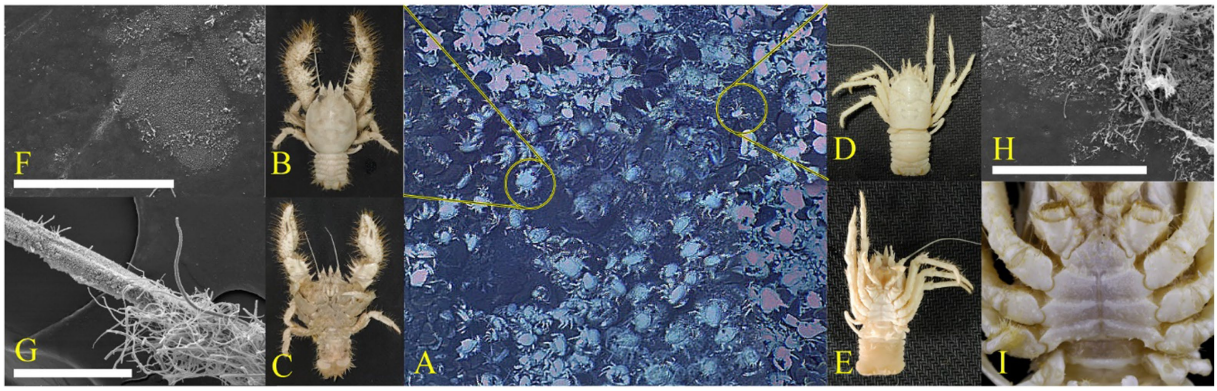

FIGURE 1
Epibiotic microbiota. **(A)** Photographs of squat lobsters at Site F. The dominant squat lobsters were *Shinkaia crosnieri* **(B,C)** and *Munidopsis verrilli* **(D,E)**. Scanning electron microscopy (SEM) images of the morphology of bacteria attached to the *S. crosnieri* carapace ($SC_{carapace}$) **(F)**, *S. crosnieri* ventral setae (SC_{setae}) **(G)**, and *M. verrilli* carapace ($MV_{carapace}$) **(H)**. Dissecting microscope images showing the ventral view of *M. verrilli*, without the setae **(I)**. White scale bar=100 μm **(F–H)**.

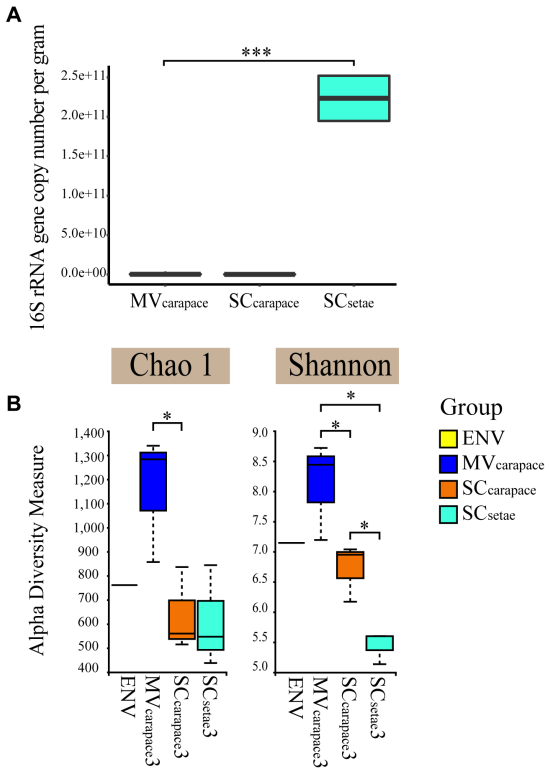

FIGURE 2
(A) Box plots of the 16S rRNA gene copy number of epibiotic bacteria from the *M. verrilli* carapace ($MV_{carapace}$), *S. crosnieri* carapace ($SC_{carapace}$), and *S. crosnieri* setae (SC_{setae}). (***: $p<0.01$). **(B)** Alpha diversity, based on the Shannon index and Chao1 index, of bacterioplankton in cold seep interface water (environment [ENV]) and epibiotic bacteria on *M. verrilli* carapace ($MV_{carapace}$), *S. crosnieri* carapace ($SC_{carapace}$), and *S. crosnieri* setae (SC_{setae}). (*: $p<0.05$).

3.3. Bacterial diversity of different groups

A total of 673,093 reads were generated from the bacterioplankton and epibiotic bacteria associated with $MV_{carapace}$, $SC_{carapace}$, and SC_{setae}, and 2,100 ASVs were retained. All sequences found in this study were bacteria due to the use of bacteria-specific primers. The rarefaction curves based on the sequencing data were stable, indicating that sufficient sequencing depth was achieved (Supplementary Figure S2). Based on comparisons with the Silva 138 bacterial database, 52 microbial phyla were detected in the 10 samples, comprising 143 classes, 354 orders, 591 families, and 1,123 genera.

The alpha diversity of the epibiotic bacterial and bacterioplankton communities were compared. The Shannon index varied from 5.13 to 8.68, and differed significantly among the three groups of epibiotic bacteria. The Shannon index was highest for $MV_{carapace}$ and lowest for SC_{setae}. And samples at $MV_{carapace}$ showed highest Chao1 indexes. The difference in the epibiotic bacterial communities between carapace and setae was significant ($p<0.05$). However, the differences between the bacterioplankton (in the single ENV sample) and the epibiotic bacteria were insignificant.

3.4. Comparison of bacterial orders and ASVs among groups

Regarding the three epibiotic bacterial communities, *Methylococcales* (10.25 to 36.75%), *Campylobacterales* (4.32 to 34.32%), and *Thiotrichales* (6.28 to 51.29%) were all in the top three orders in each community, although their ranks varied. In the SC_{setae} epibiotic bacterial communities, *Thiotrichales* accounted for the highest relative abundance (42.25%). In contrast, in the $MV_{carapace}$ and $SC_{carapace}$ epibiotic bacterial communities, the relative abundance of *Thiotrichales* (14.60 and 10.74%, respectively) was lower than that of *Methylococcales* (24.16% and 29.54, respectively) or *Campylobacterales* (17.37 and 29.26%, respectively). Furthermore, the ranking of the top three orders was similar between the epibiotic bacterial communities of $MV_{carapace}$ and $SC_{carapace}$. The bacterioplankton community in the ENV sample wasdominated by *Alteromonadales* (15.99%), *Campylobacterales* (15.03%), and *Methylococcales* (14.77%). Notably, *Alteromonadales* was only exclusively dominated the bacterioplankton community, and the proportion of *Thiotrichales* was much lower (3.87%; Figure 3).

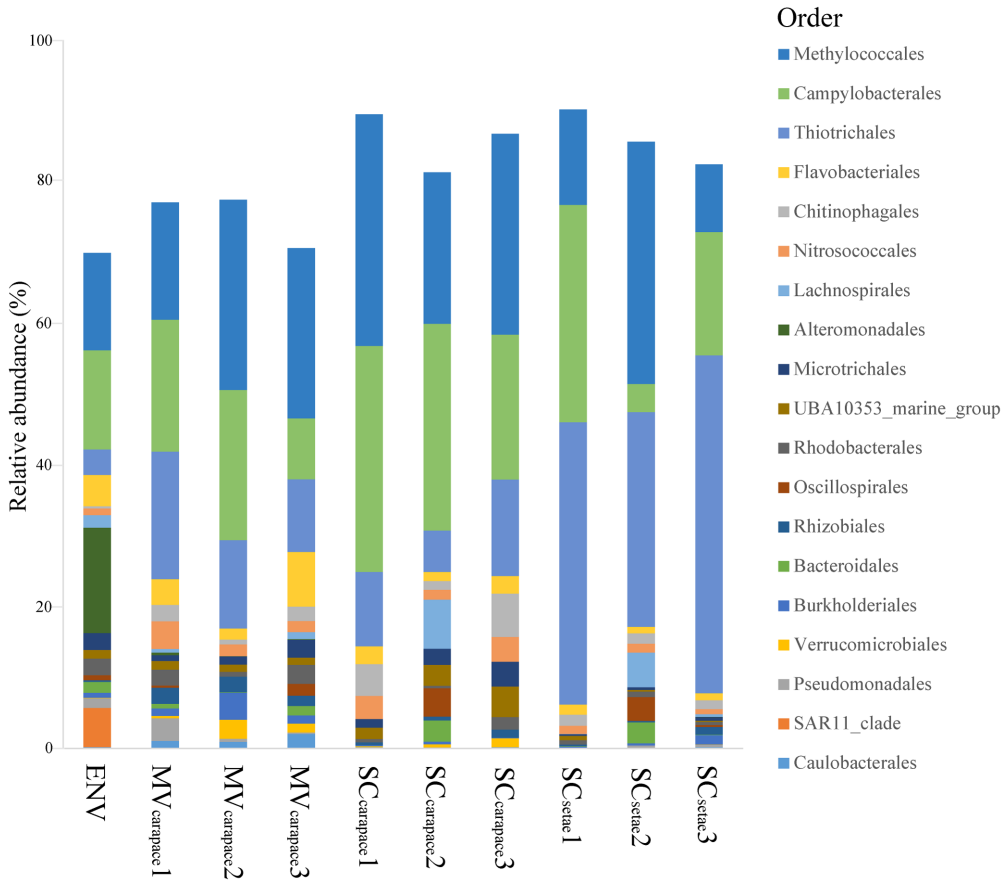

FIGURE 3
Stacked bar chart of relative abundances of bacterial orders. The top 20 orders in the *M. verrilli* carapace ($MV_{carapace}$), *S. crosnieri* carapace ($SC_{carapace}$), and *S. crosnieri* setae (SC_{setae}) samples and the bacterioplankton community in the cold seep interface water (environment [ENV]) sample are shown.

To further explore the compositional differences at the ASV level, PCoA, heatmap analysis, and bacterial co-occurrence network analysis were used (Figure 4). The dominant order *Campylobacterales* mainly involved ASV1 (genus *Sulfurovum*), *Thiotrichales* mainly involved ASV3 (unknown species in order *Thiotrichales*), and *Methylococcales* mainly involved ASV2 (genus Marine_Methylotrophic_Group_2). ANOSIM revealed significant differences in the epibiotic bacterial communities within each of the three groups ($p < 0.01$). The SC_{setae} epibiotic bacterial community was highly separated from the others based on PCoA and heatmap clustering (Figures 4A,B). According to the STAMP analysis, the high abundance of ASV3 (order *Thiotrichales*), associated with sulfide oxidation, in SC_{setae} seemed to be a major source of variation among the groups (Supplementary Figure S3). There was a high degree of similarity between the $MV_{carapace}$ and $SC_{carapace}$ epibiotic bacterial communities, reflected by partial overlaps based on PCoA and heatmap clustering. There were slight differences between individuals in the $MV_{carapace}$ group, as evidenced by the dispersion shown by our results (Figure 4A). The bacterial co-occurrence network, containing 144 nodes and 533 edges, was parsed into various modules, which are groups of tightly connected ASVs. The relative abundance of the module graph_3 (Figure 4C; Supplementary Figure S4), which mainly contained ASV3 (order *Thiotrichales*) associated with sulfur oxidation, was much higher in SC_{setae} than $MV_{carapace}$ and $SC_{carapace}$, which might indicate an enrichment of specific sulfur-oxidizing bacteria in SC_{setae}.

4. Discussion

4.1. Comparison of bacterial orders and ASVs among groups

Cold seeps harbor thriving communities of unique organisms, supported mainly by chemosynthetic microbes (such as *Thiotrichales*, *Methylococcales*, and *Campylobacterales*; Sogin et al., 2021). These microbes produce biomass for the higher trophic levels using energy from reducing gases such as hydrogen sulfide and methane. In this study, we present the first report of the epibiotic bacterial communities associated with *M. verrilli* and the first comparative study of the epibiotic bacterial communities on Munidopsidae species in cold seeps.

Despite the wide distribution of *M. verrilli* in the global deep-sea environment, previous studies on it were limited to morphological identification (Baba and Poore, 2002). Our results showed that chemosynthetic bacteria, including *Thiotrichales*, *Methylococcales*, and *Campylobacterales*, dominated the $MV_{carapace}$ epibiotic bacterial community. *Campylobacterales* species often play a crucial role in the

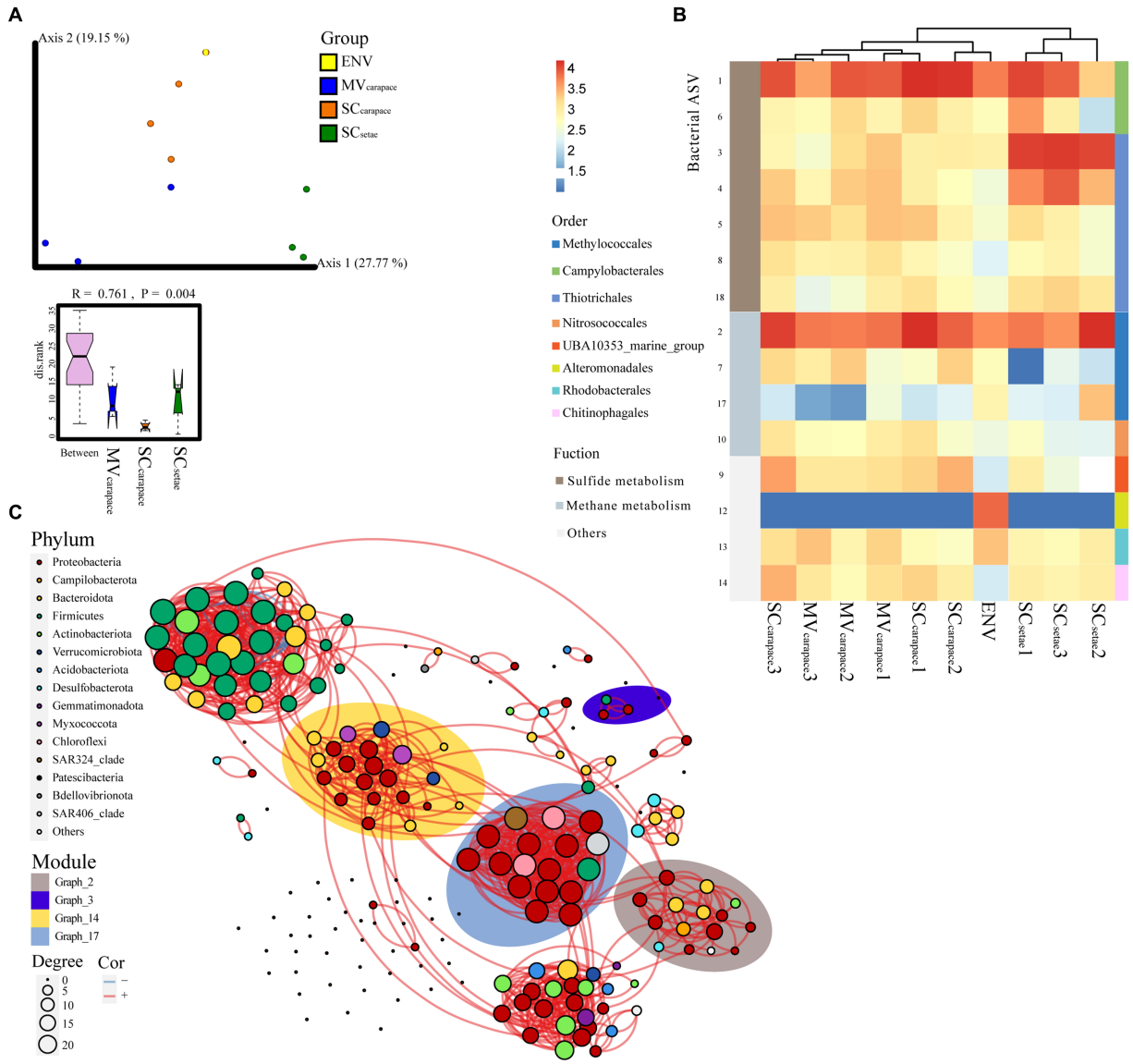

FIGURE 4
(A) PCoA plot of *M. verrilli* carapace ($MV_{carapace}$), *S. crosnieri* carapace ($SC_{carapace}$), and *S. crosnieri* setae (SC_{setae}) epibiotic bacterial communities and the bacterioplankton community in cold seep interface water (environment [ENV]), showing the differences in the epibiotic bacterial and bacterioplankton communities at the ASV level. The SC_{setae} samples were clustered far apart from the others. The rank of the dissimilarities within groups of epibiotic bacteria was estimated using analysis of similarity (ANOSIM), revealing significant differences in the epibiotic bacterial communities within each of the three groups. **(B)** Heatmap of the top 10 ASVs associated with sulfur and methane metabolism. **(C)** Bacterial co-occurrence network based on the top 200 ASVs. Each node represents a bacterial ASV. The size of each node is proportional to the number of correlations and the links represent statistically significant correlations ($|\rho|>0.7$, $p<0.05$). The background color around the nodes indicates the modules (groups of tightly connected ASVs), i.e., graph_2, graph_3, graph_14, and graph_17, that the ASVs are affiliated with.

sulfur, nitrogen, and hydrogen cycles, as oxidizers or reducers (Wang Y. et al., 2022). *Methylococcales* belongs to facultative anaerobic bacteria and exhibits prominent capacity for the anaerobic oxidation of methane (Bhattarai et al., 2019). Research on serpulids at a seep known as Jaco Scar showed that *Methylococcales* dominated the epibiotic bacterial communities (Goffredi et al., 2020). Consistent with our results, epibiotic growth of chemoautotrophic bacteria on invertebrates is quite common in cold seeps (Martin and Haney, 2005). Similar to our results on the $MV_{carapace}$ epibiotic bacterial communities, research on *Munidopsis alvisca* showed that chemosynthetic bacterial families were also the dominant families (Leinberger et al., 2022). Research on Alvinocarididae crustaceans at Site F showed that the epibiotic microbes had a similar composition, including *Methylococcales*, *Campylobacterales*, and *Thiotrichales* (Hui et al., 2022). The high relative abundance of chemosynthetic bacteria in $MV_{carapace}$ in our study was in line with the extreme environment involving high hydrogen sulfide and methane concentrations (Cao et al., 2021). Most of the reported mutualistic relationships in deep-sea chemosynthetic ecosystems involve chemosynthetic bacteria with sulfide-oxidizing or methane-oxidizing activity (Levin et al., 2016). Epibiotic microbes have been reported to contribute to the *Munidopsis alvisca* diet, with bacterial biofilms being a relevant food source for

Munidopsis sp. (Hoyoux et al., 2012). Based on the co-occurrence on *M. verrilli* of methanotrophic and thiotrophic bacteria with high relative abundances, we hypothesize that the epibiotic bacteria might provide nutrition to their hosts, although only a small amount, given their low absolute density.

As for *S. crosnieri,* its epibiotic bacteria have been intensively studied. Watsuji et al. concluded that there is a close relationship between the epibiotic bacteria of *S. crosnieri* and the host in terms of nutrient supply, as the epibiotic bacteria adhering to the setae (including those with sulfide-oxidizing or methane-oxidizing activity) could be scraped by the host to use as food (Watsuji et al., 2017). Our result on the SC_{setae} epibiotic bacterial community composition concurred with previous studies, in which *Thiotrichales*, *Methylococcales*, and *Campylobacterales* made up a large proportion (Xu et al., 2022).

4.2. Absence or presence of setae is the main cause of variation in epibiotic bacterial communities

The significant differences in epibiotic bacterial community morphology, density, and composition of SC_{setae} compared to $MV_{carapace}$ and $SC_{carapace}$ hinted at the function of setae in shaping the epibiotic bacterial communities.

The morphology of the dense epibiotic bacteria on *S. crosnieri* that we observed is consistent with previous studies (Zhang et al., 2018). Microbes often live in consortia bound to substrates, forming biofilms, which are quite common in chemosynthetic systems, e.g., euglenozoans in cold seeps are entirely covered by biofilms of closely packed epibiotic bacteria (Buck et al., 2000). Bacterial communities within a biofilm often have a multi-layered structure (Hansen et al., 2007). In our study, the SC_{setae} bacteria, forming a biofilm, were quite different from other epibiotic bacterial communities, with diverse taxa and a multi-layer configuration. A previous study suggested that a multi-layer biofilm configuration involving metabolic cooperation exhibited increased stability and productivity, increasing biomass accumulation due to optimal nutrient utilization (Elias and Banin, 2012). In addition, pereopods densely covered with specialized setae maximized the adhesion space for epibiotic bacteria and the dense structure intensified the adhesion to the surfaces, thereby reducing loss of the bacteria (Christensen et al., 2002; Federle, 2006). Moreover, chemical intermediates produced by reactions within the chemosynthetic microbiota maintained the stability of the biofilm in the face of temporal heterogeneity (Dolinšek et al., 2016). Research has shown that the stable intermediates of the SC_{setae} epibiotic bacterial community play essential roles in metabolic interactions between the hosts and bacteria in the face of temporal oscillations in resource availability (Xu et al., 2022).

The PCoA analysis revealed slight differences in the epibiotic bacteria on the $MV_{carapace}$ and $SC_{carapace}$, which is possibly caused by their different distribution patterns. However, such difference was not supported by the co-occurrence network results and was not visible in the heatmaps, indicating that the microbiome difference is not as remarkable as the difference between the setae and the carapaces. More research is necessary to fully comprehend whether the setae selectively attach to the biofilms of the SC-symbionts. In addition, the overlapping distribution of some individuals of the two squat lobster species around the vents could reduce the significance of the difference between two carapaces in the statistical analysis. The similarity between the $MV_{carapace}$ and $SC_{carapace}$ groups suggested a weak selection of the carapaces by bacteria.

Epibiotic bacterial communities often reflect the environment and can exchange members with the bacterioplankton community in the surrounding water via direct contact (He et al., 2020). A study of Chinese mitten crabs indicated that the bacterial diversity in the water somewhat shaped the epibiotic bacterial communities (Zhang et al., 2016). In our study, almost all the orders present in the bacterioplankton community were present in the epibiotic bacterial community, The presence of plume setae with a soft texture may increase the three-dimensional space for chemosynthetic bacteria to interact with each other and may provide a more suitable adhesion substrate for certain groups. In addition, the extremely low alpha diversity in the SC_{setae} epibiotic bacterial community in contrast to its high density indicates an enrichment of specific bacterial groups.

To identify the enriched taxa, we performed various analyses at the ASV level. Studies have shown that mutualistic host–microbe relationships likely exist for *S. crosnieri* and *M. verrilli* (Watsuji et al., 2012; Leinberger et al., 2022). Additionally, chemosynthetic bacteria played a crucial role in the adaptation of crustaceans to cold seeps by forming close symbiotic relationships with their hosts (Cowart et al., 2017). Therefore, we focused on these chemosynthetic groups in epibiotic bacterial communities to investigate whether these groups were specifically enriched and thus may be involved in differential adaptive strategies. We found that the chemosynthetic orders (*Thiotrichales*, *Methylococcales*, and *Campylobacterales*) accounted for a high proportion of the epibiotic bacterial communities (>60%), while the proportions of these orders were less in the bacterioplankton community (<40%). These differences indicated that the epibiotic bacteria were not random recruited from the bacterioplankton.

The difference in the relative abundance of ASV3 (order *Thiotrichales*) among the epibiotic bacterial communities is striking. *Thiotrichales*, which are often involved in primary production in chemosynthetic communities (Cambon-Bonavita et al., 2020), can exhibit sulfur-oxidizing activity in the presence of hydrogen sulfide and its spontaneously oxidized compounds and has been widely reported in the deep-sea research field, as sulfur-oxidizing symbionts of invertebrate hosts (Hourdez et al., 2021). Dissolved sulfate and elemental sulfur are regarded as indicators of biochemical processes (Feng et al., 2016). Du et al. detected strong Raman peak of the sulfate and elemental sulfur in the fluids in the chemosynthetic communities at Site F (Du et al., 2018). The presence of these chemicals in the vicinity of cold seep could sustain the high biomass production in epibiotic bacterial communities. The relative abundance of ASV3 (order *Thiotrichales*) was strikingly higher for SC_{setae} than $MV_{carapace}$ and $SC_{carapace}$, which might indicate that sulfide oxidation was quite important in the formation of epibiotic bacterial communities on *S. crosnieri* setae.Notably, a recent study found that chemoautotrophic bacteria belonging to Gammaproteobacteria (including the order *Thiotrichales*) could coevolve with their hosts, whereas Campylobacteria (such as the order *Campylobacterales*) had a weak preference for hosts (Lee et al., 2021). This indicates the possibility of enrichment of ASV3 (order *Thiotrichales*) in SC_{setae} and explains the high relative

abundance, across all samples, of ASV1 (order *Campylobacterales*), which is also a sulfur-oxidizing bacteria like ASV3 (order *Thiotrichales*).

S. crosnieri cluster near the most active cold seeps, where fluids are expelled as a result of geological processes such as sediment compaction (Feng et al., 2018). The chemical fluxes are higher near the seeps with the most active bubble outflows (Sibuet and Olu, 1998). The multi-layer biofilm configuration and high density of the SC_{setae} epibiotic bacterial community helps the host to efficiently utilize the high chemical fluxes around it. Additionally, certain physical behaviors (such as dancing behavior) of the host can indirectly deepen the symbiotic relationship to increase the productivity of its episymbionts and the adaptation of the host, such as the yeti crab *Kiwa puravida* (Thurber et al., 2011). Research suggested that *S. crosnieri* exhibited similar behaviors, allowing it to drive water through the endogenous water flow around its setae (Watsuji et al., 2018). At Site F, there is a vertical gradient regarding the concentration of hydrogen sulfide, with the highest concentration at the bottom interface of the chemosynthetic communities (Cao et al., 2021). Higher concentrations of reducing substances could be produced from the bottom interface due to the endogenous water flow of the hosts. This improves the energy metabolism and the assimilation of chemosynthetic inorganic carbon under the water flow, contributing to an enrichment of sulfur-oxidizing bacteria (such as *Thiotrichales* species) on the setae to support host survival.

As for *M. verrilli*, although the relative abundance of chemoautotrophic bacteria was high, their body surfaces are lacking dense setae, and endogenous water flow and dancing behavior have not been reported or observed. These chemoautotrophic bacteria could not form as dense community as *S. crosnieri*. Previous studies indicated that *M. verrilli* tended to be opportunists and had broader feeding targets (Martin and Haney, 2005). This might indicate that, compared to *S. crosnieri,* a relatively small proportion of the nutrient supply of *M. verrilli* is derived from chemosynthesis by epibiotic microbes utilizing reducing substances (such as sulfide). We hypothesize that the presence of setae shaped the structure of the epibiotic bacterial communities and that the numerous chemosynthetic epibiotic bacteria tightly adhering to SC_{setae} form an ideal biofilm, in contrast to the relatively sparse and simple epibiotic bacterial communities on carapaces, improving metabolic efficiency and the overall primary productivity.

5. Conclusion

In light of the unique composition of the SC_{setae} group and the higher relative abundance of ASV3 (order *Thiotrichales*), we suggest that the morphology of *S. crosnieri* might allow the epibiotic bacterial community to form a bushy jungle in the plumose setae, which improves primary production and provides *S. crosnieri* with sufficient nutrition by selectively obtaining sulfur-oxidizing episymbionts from the environment. Consistently, *S. crosnieri* clusters around the vents in order to use the high chemical fluxes for chemosynthetic reactions. In contrast, *M. verrilli* has a relatively low dependence on epibiotic bacterial communities for its nutrient supply, so they are more dispersed. Our research showed that the different distributions of *S. crosnieri* and *M. verrilli* relate to the differences in their epibiotic bacterial communities, involving differential adaptation mechanisms around cold seeps.

Data availability statement

The data presented in the study are deposited in the NCBI repository, accession number PRJNA947936 and PRJNA954131.

Ethics statement

The studies involving animals were reviewed and approved by the Science and Technology Ethics Committee of the Institute of Oceanology Chinese Academy of Sciences.

Author contributions

WF performed the statistical analysis and wrote the first draft of the manuscript. MW and CL contributed to conception and design of the study. ZX, DD, MH, ZZ, HZ, and LF contributed to sampling. All authors contributed to the article and approved the submitted version.

Funding

This work was supported by the National Natural Science Foundation of China, grant/award number: 42076091 and 41906124, the NSFC Innovative Group Grant (No. 42221005), the National Key R&D Program of China (2022YFC2804003), the Strategic Priority Research Program of the Chinese Academy of Sciences (XDA22050303 and XDB42020401).

Acknowledgments

We thank Weiyue Liu, Longzhao Li, Yujie Yan and Yan Sun for the helping of project implementation.

Conflict of interest

The authors declare that the research was conducted in the absence of any commercial or financial relationships that could be construed as a potential conflict of interest.

Publisher's note

Supplementary material

The Supplementary material for this article can be found online at: https://www.frontiersin.org/articles/10.3389/fmicb.2023.1197476/full#supplementary-material

References

Baba, K., and Fujita, Y. (2017). Squat lobsters of the genus Galathea associated with comatulid crinoids (Decapoda: Anomura: Galatheidae) from the Ryukyu Islands, Japan. *Crustacean Res* 37, 43–62.

Baba, K., and Poore, G. C. B. (2002). Munidopsis (Decapoda, Anomura) from south-eastern Australia. *Crustaceana* 75, 231–252. doi: 10.1163/156854002760095363

Baba, K., and Williams, A. B. (1998). New Galatheoidea (Crustacea, Decapoda, Anomura) from hydrothermal systems in the West Pacific Ocean: Bismarck archipelago and Okinawa trough. *Zoosystema* 20, 143–156.

Bhattarai, S., Cassarini, C., and Lens, P. N. L. (2019). Physiology and distribution of Archaeal Methanotrophs that couple anaerobic oxidation of methane with sulfate reduction. *Microbiol. Mol. Biol. Rev.* 83:e00074-18. doi: 10.1128/MMBR.00074-18

Bokulich, N. A., Kaehler, B. D., Rideout, J. R., Dillon, M., Bolyen, E., Knight, R., et al. (2018). Optimizing taxonomic classification of marker-gene amplicon sequences with QIIME 2's q2-feature-classifier plugin. *Microbiome* 6:90. doi: 10.1186/s40168-018-0470-z

Bolyen, E., Rideout, J., Dillon, M., Bokulich, N., Abnet, C., Al-Ghalith, G., et al. (2019). Reproducible, interactive, scalable and extensible microbiome data science using QIIME 2. *Nat. Biotechnol.* 37:1091. doi: 10.1038/s41587-019-0252-6

Buck, K. R., Barry, J. P., and Simpson, A. G. B. (2000). Monterey Bay cold seep biota: Euglenozoa with chemoautotrophic bacterial epibionts. *Eur. J. Protistol.* 36, 117–126. doi: 10.1016/S0932-4739(00)80029-2

Callahan, B. J., Mcmurdie, P. J., Rosen, M. J., Han, A. W., Johnson, A. J., and Holmes, S. P. (2016). DADA2: high resolution sample inference from Illumina amplicon data. *Nat. Methods* 13, 581–583. doi: 10.1038/nmeth.3869

Cambon-Bonavita, M.-A., Aubé, J., Cueff-Gauchard, V., and Reveillaud, J. (2020). Niche partitioning in the Rimicaris exoculata holobiont: the case of the first symbiotic Zetaproteobacteria. *Microbiome* 9:87. doi: 10.1186/s40168-022-01257-4

Cao, L., Lian, C., Zhang, X., Zhang, H., Wang, H., Zhou, L., et al. (2021). In situ detection of the fine scale heterogeneity of active cold seep environment of the Formosa ridge, the South China Sea. *J. Mar. Syst.* 218:103530. doi: 10.1016/j.jmarsys.2021.103530

Cheng, J., Hui, M., Li, Y. L., and Sha, Z. L. (2020). Genomic evidence of population genetic differentiation in deep-sea squat lobster *Shinkaia crosnieri* (crustacea: Decapoda: Anomura) from northwestern Pacific hydrothermal vent and cold seep. *Deep Sea Res I Oceanogr Res Pap.* 156:103188. doi: 10.1016/j.dsr.2019.103188

Chevaldonne, P., and Olu, K. (1996). Occurrence of anomuran crabs (Crustacea: Decapoda) in hydrothermal vent and cold-seep communities: a review. *Proc. Biol. Soc. Wash.* 109, 286–298.

Christensen, B. B., Haagensen, J. A. J., Heydorn, A., and Molin, S. (2002). Metabolic commensalism and competition in a two-species microbial consortium. *Appl. Environ. Microbiol.* 68, 2495–2502. doi: 10.1128/AEM.68.5.2495-2502.2002

Cowart, D. A., Durand, L., Cambon-Bonavita, M.-A., and Arnaud-Haond, S. (2017). Investigation of bacterial communities within the digestive organs of the hydrothermal vent shrimp Rimicaris exoculata provide insights into holobiont geographic clustering. *PLoS One* 12:e0172543. doi: 10.1371/journal.pone.0172543

Dattagupta, S., Schaperdoth, I., Montanari, A., Mariani, S., Kita, N., Valley, J. W., et al. (2009). A novel symbiosis between chemoautotrophic bacteria and a freshwater cave amphipod. *ISME J.* 3, 935–943. doi: 10.1038/ismej.2009.34

Dolinšek, J., Goldschmidt, F., and Johnson, D. R. (2016). Synthetic microbial ecology and the dynamic interplay between microbial genotypes. *FEMS Microbiol. Rev.* 40, 961–979. doi: 10.1093/femsre/fuw024

Dong, D., and Li, X. (2015). Galatheid and chirostylid crustaceans (Decapoda: Anomura) from a cold seep environment in the northeastern South China Sea. *Zootaxa* 4057, 91–105. doi: 10.11646/zootaxa.4057.1.5

Du, Z., Zhang, X., Luan, Z.-D., Wang, M., Xi, S., Li, L., et al. (2018). In situ Raman quantitative detection of the cold seep vents and fluids in the chemosynthetic communities in the South China Sea. *Geochemistry* 19, 2049–2061. doi: 10.1029/2018GC007496

Elias, S., and Banin, E. (2012). Multi-species biofilms: living with friendly neighbors. *FEMS Microbiol. Rev.* 36, 990–1004. doi: 10.1111/j.1574-6976.2012.00325.x

Fahy, B. G., Vasilopoulos, T., Ford, S., Gravenstein, D., and Enneking, F. K. (2015). A single consent for serial anesthetics in burn surgery. *Anesth. Analg.* 121, 219–222. doi: 10.1213/ANE.0000000000000780

Federle, W. (2006). Why are so many adhesive pads hairy? *J. Exp. Biol.* 209, 2611–2621. doi: 10.1242/jeb.02323

Feng, D., Peng, Y., Bao, H., Peckmann, J., Roberts, H. H., and Chen, D. (2016). A carbonate-based proxy for sulfate-driven anaerobic oxidation of methane. *Geology* 44, 999–1002. doi: 10.1130/G38233.1

Feng, D., Qiu, J.-W., Hu, Y., Peckmann, J., Guan, H., Tong, H., et al. (2018). Cold seep systems in the South China Sea: an overview. *J. Asian Earth Sci.* 168, 3–16. doi: 10.1016/j.jseaes.2018.09.021

Goffredi, S. K., Jones, W. J., Erhlich, H., Springer, A., and Vrijenhoek, R. C. (2008). Epibiotic bacteria associated with the recently discovered yeti crab, *Kiwa hirsuta*. *Environ. Microbiol.* 10, 2623–2634. doi: 10.1111/j.1462-2920.2008.01684.x

Goffredi, S. K., Tilic, E., Mullin, S. W., Dawson, K. S., Keller, A., Lee, R. W., et al. (2020). Methanotrophic bacterial symbionts fuel dense populations of deep-sea feather duster worms (Sabellida, Annelida) and extend the spatial influence of methane seepage. *Sci. Adv.* 6:6. doi: 10.1126/sciadv.aay8562

Hansen, S. K., Haagensen, J., Gjermansen, M., Jørgensen, T. M., Tolker-Nielsen, T., and Molin, S. (2007). Characterization of a *Pseudomonas putida* rough variant evolved in a mixed-species biofilm with *Acinetobacter* sp. strain C6. *J. Bacteriol.* 189, 4932–4943. doi: 10.1128/JB.00041-07

He, D., Ren, L., and Wu, Q. L. (2020). Growing season drives the compositional changes and assembly processes of epiphytic bacterial communities of two submerged macrophytes in Taihu Lake. *FEMS Microbiol. Ecol.* 96:fiaa025. doi: 10.1093/femsec/fiaa025

Hourdez, S., Boidin-Wichlacz, C., Jollivet, D., Massol, F., Rayol, M. C., Bruno, R., et al. (2021). Investigation of *Capitella* spp. symbionts in the context of varying anthropic pressures: first occurrence of a transient advantageous epibiosis with the giant bacteria *Thiomargarita* sp. to survive seasonal increases of sulfides in sediments. *Sci. Total Environ.* 798:149149. doi: 10.1016/j.scitotenv.2021.149149

Hoyoux, C., Zbinden, M., Samadi, S., Gaill, F., and Compère, P. (2009). Wood-based diet and gut microXora of a galatheid crab associated with PaciWc deep-sea wood falls. *Mar. Biol.* 156, 2421–2439. doi: 10.1007/s00227-009-1266-2

Hoyoux, C., Zbinden, M., Samadi, S., Gaill, F., and Compère, P. (2012). Diet and gut microorganisms of Munidopsis squat lobsters associated with natural woods and mesh-enclosed substrates in the deep South Pacific. *Mar. Biol. Res.* 8, 28–47. doi: 10.1080/17451000.2011.605144

Hui, M., Wang, A., Cheng, J., and Sha, Z. (2022). Full-length 16S rRNA amplicon sequencing reveals the variation of epibiotic microbiota associated with two shrimp species of alvinocarididae: possibly co-determined by environmental heterogeneity and specific recognition of hosts. *PeerJ* 10:e13758. doi: 10.7717/peerj.13758

Katoh, K., and Standley, D. M. (2013). MAFFT multiple sequence alignment software version 7: improvements in performance and usability. *Mol. Biol. Evol.* 30, 772–780. doi: 10.1093/molbev/mst010

Komai, T., and Matsuzaki, K. (2016). Two deep-sea decapod crustaceans collected off eastern Hokkaido, Japan: *Sclerocrangon* rex n. sp. (Caridea: Crangonidae) and *Munidopsis verrilli* Benedict, 1902 (Anomura: Munidopsidae). *Zootaxa* 4162, 92–106. doi: 10.11646/zootaxa.4162.1.4

Komai, T., Shank, T. M., and Dover, C. L. V. (2005). A new species of *Alvinocaris* (Crustacea: Decapoda: Caridea: Alvinocarididae) and a new record of *A. muricola* from methane seeps on the Blake ridge Diapir, Northwestern Atlantic. *Zootaxa* 1019, 27–42. doi: 10.11646/zootaxa.1019.1.2

Lee, W.-K., Juniper, S. K., Perez, M., Ju, S.-J., and Kim, S.-J. (2021). Diversity and characterization of bacterial communities of five co-occurring species at a hydrothermal vent on the Tonga arc. *Ecol. Evol.* 11, 4481–4493. doi: 10.1002/ece3.7343

Leinberger, J., Milke, F., Christodoulou, M., Poehlein, A., Caraveo-Patino, J., Teske, A., et al. (2022). Microbial epibiotic community of the deep-sea galatheid squat lobster *Munidopsis alvisca*. *Sci. Rep.* 12:2675. doi: 10.1038/s41598-022-06666-x

Levin, L. A., Baco, A. R., Bowden, D. A., Colaço, A., Cordes, E., Cunha, M. R., et al. (2016). Hydrothermal vents and methane seeps: rethinking the sphere of influence. *Front. Mar. Sci.* 3:72. doi: 10.3389/fmars.2016.00072

Liu, D., and Tong, C. (2017). Bacterial community diversity of traditional fermented vegetables in China. *LWT Food Sci. Technol.* 86, 40–48. doi: 10.1016/j.lwt.2017.07.040

Macavoy, S. E., Carney, R. S., Morgan, E., and Macko, S. A. (2008). Stable isotope variation among the mussel *Bathymodiolus childressi* and associated heterotrophic Fauna at four cold-seep communities in the Gulf of Mexico. *J. Shellfish Res.* 27, 147–151. doi: 10.2983/0730-8000(2008)27[147:SIVATM]2.0.CO;2

Macpherson, E., Jones, W., and Segonzac, M. (2005). A new squat lobster family of Galatheoidea (Crustacea, Decapoda: Anomura) from the hydrothermal vents of the Pacific-Antarctic ridge. *Zoosystema* 27, 709–723.

Martin, J. W., and Haney, T. A. (2005). Decapod crustaceans from hydrothermal vents and cold seeps: a review through 2005. *Zool. J. Linnean Soc.* 145, 445–522. doi: 10.1111/j.1096-3642.2005.00178.x

Mioduchowska, M., Czyż, M. J., Gołdyn, B., Kilikowska, A., Namiotko, T., Pinceel, T., et al. (2018). Detection of bacterial endosymbionts in freshwater crustaceans: the applicability of non-degenerate primers to amplify the bacterial 16S rRNA gene. *Peer J.* 6:e6039. doi: 10.7717/peerj.6039

Nadkarni, M. A., Martin, F. E., Jacques, N. A., and Hunter, N. (2002). Determination of bacterial load by real-time PCR using a broad-range (universal) probe and primers set. *Microbiology* 148, 257–266. doi: 10.1099/00221287-148-1-257

Niemann, H., Linke, P., Knittel, K., Macpherson, E., Boetius, A., Ckmann, W. B., et al. (2013). Methane-carbon flow into the benthic food web at cold seeps – a case study from the Costa Rica Subduction zone. *PLoS One* 8:10. doi: 10.1371/journal.pone.0074894

Parks, D. H., Tyson, G. W., Hugenholtz, P., and Beiko, R. G. (2014). STAMP: statistical analysis of taxonomic and functional profiles. *Bioinformatics* 30, 3123–3124. doi: 10.1093/bioinformatics/btu494

Price, M. N., Dehal, P. S., and Arkin, A. P. (2010). FastTree 2 – approximately maximum-likelihood trees for large alignments. *PLoS One* 5:e9490. doi: 10.1371/journal.pone.0009490

Quast, C., Pruesse, E., Yilmaz, P., Gerken, J., Schweer, T., Yarza, P., et al. (2012). The SILVA ribosomal RNA gene database project: improved data processing and web-based tools. *Nucleic Acids Res.* 41, D590–D596. doi: 10.1093/nar/gks1219

Schwartzman, J. A., Koch, E., Heath-Heckman, E. A. C., Zhou, L., Kremer, N., Mcfall-Ngai, M. J., et al. (2015). The chemistry of negotiation: rhythmic, glycan-driven acidification in a symbiotic conversation. *Proc. Natl. Acad. Sci. U. S. A.* 112, 566–571. doi: 10.1073/pnas.1418580112

Sibuet, M., and Olu, K. (1998). Biogeography, biodiversity and fluid dependence of deep-sea cold-seep communities at active and passive margins. *Deep Sea Res II* 45, 517–567. doi: 10.1016/S0967-0645(97)00074-X

Sogin, M. E., Kleiner, M., Borowski, C., Gruber-Vodicka, H. R., and Dubilier, N. (2021). Life in the dark: phylogenetic and physiological diversity of chemosynthetic symbioses. *Ann. Rev. Microbiol.* 75, 695–718. doi: 10.1146/annurev-micro-051021-123130

Thurber, A. R., Jones, W. J., and Schnabel, K. (2011). Dancing for food in the Deep Sea: bacterial farming by a new species of yeti crab. *PLoS One* 6:e26243. doi: 10.1371/journal.pone.0026243

Tsuchida, S., Fujiwara, Y., and Fujikura, K. (2003). Distribution and population structure of the Galatheid crab *Shinkaia crosnieri* (Decapoda: Anomura: Galatheidae) in the southern Okinawa trough. *Plankon Benthos Res.* 58, 84–88. doi: 10.5179/benthos.58.84

Wang, Y., Bi, H.-Y., Chen, H., Zheng, P., Zhou, Y.-L., and Li, J. (2022). Metagenomics reveals dominant unusual sulfur oxidizers inhabiting active hydrothermal chimneys from the southwest Indian ridge. *Front. Microbiol.* 13:861795. doi: 10.3389/fmicb.2022.861795

Wang, X., Guan, H., Qiu, J.-W., Xu, T., Peckmann, J., Chen, D., et al. (2022). Macro-ecology of cold seeps in the South China Sea. *Geosyst. Geoenviron.* 1:100081. doi: 10.1016/j.geogeo.2022.100081

Warrant, E. J., and Locket, N. A. (2004). Vision in the deep sea. *Biol. Rev.* 79, 671–712. doi: 10.1017/S1464793103006420

Watsuji, T.-O., Motoki, K., Hada, E., Nagai, Y., Takaki, Y., Yamamoto, A., et al. (2018). Compositional and functional shifts in the Epibiotic bacterial Community of *Shinkaia crosnieri* Baba & Williams (a squat lobster from hydrothermal vents) during methane-fed rearing. *Microbes Environ.* 33, 348–356. doi: 10.1264/jsme2.ME18072

Watsuji, T.-O., Nishizawa, M., Morono, Y., Hirayama, H., Kawagucci, S., Takahata, N., et al. (2012). Cell-specific thioautotrophic productivity of epsilon-proteobacterial epibionts associated with *Shinkaia crosnieri*. *PLoS One*:7:e46282. doi: 10.1371/journal.pone.0046282

Watsuji, T.-O., Tsubaki, R., Chen, C., Nagai, Y., Nakagawa, S., Yamamoto, M., et al. (2017). Cultivation mutualism between a deep-sea vent galatheid crab and its chemosynthetic epibionts. *Deep Sea Res. I Oceanogr. Res. Pap.* 127, 13–20. doi: 10.1016/j.dsr.2017.04.012

Watsuji, T.-O., Yamamoto, A., Motoki, K., Ueda, K., Hada, E., Takaki, Y., et al. (2015). Molecular evidence of digestion and absorption of epibiotic bacterial community by deep-sea crab Shinkaia crosnieri. *ISME J.* 9, 821–831. doi: 10.1038/ismej.2014.178

Wehrtmann, I. S., and Acuna, E. (2011). "Squat Lobsters Fisheries," in *The Biology of Squat Lobsters*. eds. G. C. B. Poore, S. Ahyong and J. Taylor (Museum Victoria: CSIRO Publishing), 297–322.

Weisburg, W. G., Barns, S. M., Pelletier, D. A., and Lane, D. J. W. (1991). 16S ribosomal DNA amplification for phylogenetic study. *J. Bacteriol.* 173, 697–703. doi: 10.1128/jb.173.2.697-703.1991

Wen, T., Xie, P., Yang, S., Niu, G., Liu, X., Ding, Z., et al. (2022). ggClusterNet: an R package for microbiome network analysis and modularity-based multiple network layouts. *iMeta*. 1:e32. doi: 10.1002/imt2.32

Williams, A. B., Smith, C. R., and Baco, A. R. (2000). New species of Paralomis (Decapoda, Anomura, Lithodidae) from a sunken whale carcass in the San Clemente Basin off southern California. *J. Crustac. Biol.* 20, 281–285. doi: 10.1163/1937240X-90000030

Xiao, Y., Xu, T., Sun, J., Wang, Y., Wong, W. C., Kwan, Y. H., et al. (2020). Population genetic structure and gene expression plasticity of the Deep-Sea vent and seep squat lobster *Shinkaia crosnieri*. *Front. Mar. Sci.* 7:587686. doi: 10.3389/fmars.2020.587686

Xu, Z., Wang, M., Zhang, H., He, W., Cao, L., Lian, C., et al. (2022). Metabolism interactions promote the overall functioning of the episymbiotic chemosynthetic community of *Shinkaia crosnieri* of cold seeps. *mSystems* 7:4. doi: 10.1128/msystems.00320-22

Zhang, M. L., Sun, Y., Chen, L., Cai, C., Qiao, F., Du, Z. Y., et al. (2016). Symbiotic Bacteria in gills and guts of Chinese mitten crab (*Eriocheir sinensis*) differ from the free-living Bacteria in water. *PLoS One* 11:e0148135. doi: 10.1371/journal.pone.0148135

Zhang, J., Zeng, Z.-G., Chen, S., and Sun, L. (2018). Bacterial communities associated with *Shinkaia crosnieri* from the Iheya north, Okinawa trough: microbial diversity and metabolic potentials. *J. Mar. Syst.* 180, 228–236. doi: 10.1016/j.jmarsys.2017.02.011

Zhao, Y., Xu, T., Law, Y. S., Feng, D., Li, N., Xin, R. J., et al. (2020). Ecological characterization of cold-seep epifauna in the South China Sea. *Deep Sea Res. I Oceanogr. Res. Pap.* 163:103361. doi: 10.1016/j.dsr.2020.103361

frontiers | Frontiers in Microbiology

TYPE Original Research
PUBLISHED 27 July 2023
DOI 10.3389/fmicb.2023.1211649

OPEN ACCESS

EDITED BY
Ruiyong Zhang,
Chinese Academy of Sciences (CAS), China

REVIEWED BY
Yanfei Zhang,
Chinese Academy of Sciences (CAS), China
Minxi Wan,
East China University of Science and Technology, China

*CORRESPONDENCE
Hui Sun
✉ yh_gcc@163.com

RECEIVED 25 April 2023
ACCEPTED 10 July 2023
PUBLISHED 27 July 2023

CITATION
Xu A, Liu C, Zhao S, Song Z and Sun H (2023) Dynamic distribution of *Massilia* spp. in sewage, substrate, plant rhizosphere/phyllosphere and air of constructed wetland ecosystem. *Front. Microbiol.* 14:1211649. doi: 10.3389/fmicb.2023.1211649

Dynamic distribution of *Massilia* spp. in sewage, substrate, plant rhizosphere/phyllosphere and air of constructed wetland ecosystem

Ailing Xu[1], Congcong Liu[1], Shuke Zhao[2], Zhiwen Song[1] and Hui Sun[2]*

[1]School of Environmental and Municipal Engineering, Qingdao Technological University, Qingdao, Shandong, China, [2]Qingdao sub-Center, Shandong Water Transfer Project Operation and Maintenance Center, Qingdao, Shandong, China

Introduction: *Massilia* bacteria are widely distributed and have various ecological functions. Preliminary studies have shown that *Massilia* is the dominant species in constructed wetland ecosystems, but its species composition and distribution in constructed wetlands are still unclear.

Methods: In this paper, the in-house-designed primers were used to construct a 16S rDNA clone library of *Massilia*. The RFLP sequence analysis method was used to analyze the diversity of *Massilia* clone library and the composition of *Massilia* in sewage, substrate, plant rhizosphere, plant phyllosphere and air in a constructed wetland sewage treatment system. Redundancy analysis (RDA) and canonical correspondence analysis (CCA) were used to analyze the correlation between environmental factors and the population characteristics of *Massilia* in the corresponding environment. The dominant species of *Massilia* were analyzed for differences.

Results: The results showed that the 16S rDNA clone library in primer 5 worked well. According to the clone library diversity index analysis, the richness of *Massilia* varied significantly in different environments in different seasons, where the overall summer and autumn richness was higher than that in the spring and winter. The relative abundance of 5 *Massilia* in the constructed wetland ecosystem was greater than 1% in all samples, which were *M. alkalitolerans*, *M. albidiflava*, *M. aurea*, *M. brevitalea*, and *M. timonae*. The seasonal variation of dominant genera was significantly correlated with environmental factors in constructed wetlands.

Discussion: The above results indicated that the species of *Massilia* were abundant and widely distributed in the constructed wetland ecosystem, and there were significant seasonal differences. In addition, the *Massilia* clone library of constructed wetland was constructed for the first time in this study and the valuable data of *Massilia* community structure were provided, which was conducive to the further study of microbial community in constructed wetland.

KEYWORDS

***Massilia bacterial*, clonal library, distribution characteristics, community structure, 16S rDNA extraction**

1. Introduction

Massilia spp. are Gram-negative bacteria that are widely distributed. For example, four species of *Massilia* were isolated from Antarctic streams, lakes and weathering layers (Holochová et al., 2020). *Massilia aquatica* was isolated from a subtropical stream in China (Lu et al., 2020). *Massilia* sp. YMA4 was isolated from the open ocean off Lamay island in Taiwan (Ho et al., 2021), and *M. buxea* was found on rock surfaces (Sun et al., 2017). In addition, *Massilia* spp. can also be found in water, organisms and human clinical specimens. Among those, soil is the main environment of *Massilia* spp (Hye et al., 2022).

Numerous studies have shown that *Massilia* spp. have many functions. Some *Massilia* are able to synthesize violacein (Agematu et al., 2011; Baek et al., 2014), which has a good therapeutic effect on tumors, malaria and diarrhea and has great application potential in the pharmaceutical field. PHAs (as reserve material displayed as intracellular bright granules) is a kind of natural polymer biomaterial, which has good biocompatibility and biodegradability, and has become the most active research focus in the field of biomaterials in recent years. For the first time, Cerrone et al. find majority of the *Massilia* strains were capable to produce significant amounts of PHA under batch culture mode using soluble starch as carbon source (Cerrone et al., 2011). Studies have shown that some *Massilia* spp. were beneficial to environmental modification. For example, *M. aromaticvorans* ML15P13^T can degrade toxic gaseous organic air pollutants, such as benzene, toluene, ethylbenzene and xylene isomers (m, p and o-x) (BTEX) (Son et al., 2021); *M. tieshanensis* TS3 and *M. putida* 6NM-7 are resistant to multiple heavy metals (Du et al., 2012; Feng et al., 2016); *M. phosphatilytica* 12-OD1 has phosphate solubilization and can improve available phosphorus content in soil and improve the soil environment (Zheng et al., 2017); *Massilia* sp. WF1 and *Massilia* sp. WG5 can degrade phenanthrene and repair contaminated soil (Lou et al., 2016; Gu et al., 2021); and *M. chloroacetimidivorans* TA-C7e degrades the chloroacetamide herbicide (Lee et al., 2017). Some *Massilia* bacteria can also promote plant growth and increase the survival rate of plants in harsh environments. Krishnamoorthy et al. found that the combined application of *Massilia* and arbuscular mycorrhizal fungi alleviated the effects of salt stress on plant growth, root colonization, nutrient accumulation and growth in studying the effects of three different salinity on the growth of corn plants in coastal reclamation area (Krishnamoorthy et al., 2016). Turnbull et al. isolated a strain of *Massilia* from potato roots that can produce heteroauxin and cellulose-degrading enzymes to promote plant growth (Turnbull et al., 2012).

In recent years, research on *Massilia* spp. made significant progress. However, the community composition and distribution of *Massilia* spp. in the constructed wetland sewage treatment system has been neglected. Preliminary research on this research group showed that *Massilia* spp. are the dominant bacteria in the air of constructed wetland sewage treatment systems. The pollutant degradation ability of artificial wetland sewage treatment systems is higher than that in natural wetlands and microbes play an important role (Liu et al., 2019; Hu et al., 2022). In consideration of the functions of *Massilia* spp., it is of great significance to study the community composition of *Massilia* bacteria in constructed wetland ecosystems. The culturable microorganism accounts for 1%~5%; therefore, molecular biology has been widely used in microbial community research. Lang et al. and Zhang et al. studied the community structure of constructed wetlands using molecular biology methods (Zhang et al., 2019; Lang et al., 2021). This study was the first to investigate the composition and distribution characteristics of *Massilia* in sewage, substrate, plant rhizosphere, plant phyllosphere and air in a constructed wetland sewage treatment system by two molecular biology methods: construction of a 16S rDNA clone library and RFLP sequence analysis. At the same time, redundancy analysis (RDA) and canonical correspondence analysis (CCA) were used to analyze the correlation between environmental factors and population characteristics of *Masilia*. The compositional differences and dynamic changes of *Massilia* in different environments and seasons were also explored, which is of great significance to reveal the mechanism of degradation of pollutants in the constructed wetlands and is beneficial to the operation of constructed wetlands.

2. Materials and methods

2.1. Sampling sites

The free water surface constructed wetland, located in the interior of the Huangdao district (Qingdao city, Shandong province, China), at a latitude of 35°35′ to 36°08' North and a longitude of 119°30′ to 120°11′ East, is a part of an integrated sewage purification system (Figure 1). This region has a warm temperate continental monsoon climate with a mean annual temperature of 12°C and a mean annual precipitation of 794 mm. The constructed wetland wastewater treatment system had a total area of 76.7 hm^2 and a treatment capability of $3.0 \times 10^4\ m^3 \cdot d^{-1}$ and was surrounded by the Yellow Sea to the east and south. It consisted of 99 treatment beds and received secondary unchlorinated wastewater from the Jiaonan Municipal Wastewater Treatment Facility with an A^2O application as the secondary treatment. All beds were planted with common reed (*Phragmites australis*) and a number of naturally germinated wetland plants (*Typha orientalis*, *Scirpus validus*, and *Lemna minor*). To facilitate the harvest progress of aboveground biomass, sewage did not enter the constructed wetland bed from December to March of the following year.

A total of five sampling points were selected in this experiment, as shown in Figure 2. The soil, wastewater, leaves and air were sampled from April 2018 to January 2019, and the sampling collection frequency was once every month.

2.2. Sampling method

Fifty grams of soil sample and 10 L of water sample were collected from each sample site using sterile sealed bags and sterile bottles, respectively. After removing the fine roots in the soil samples, the water and soil samples were transferred to the laboratory immediately. After samples were dewatered by centrifugation, a fraction of the soil samples was stored at −20°C for molecular analysis.

The rhizosphere samples of 3 reed plants were randomly selected at each sampling point. Large soil was removed from the roots, the roots were soaked in sterile water, and the difficult soil on the roots was rinsed with sterile water. The collected water samples were mixed evenly, concentrated by centrifugation and placed in a sterile centrifuge tube to extract DNA.

FIGURE 1
Schematic diagram of the geographic location of the study area.

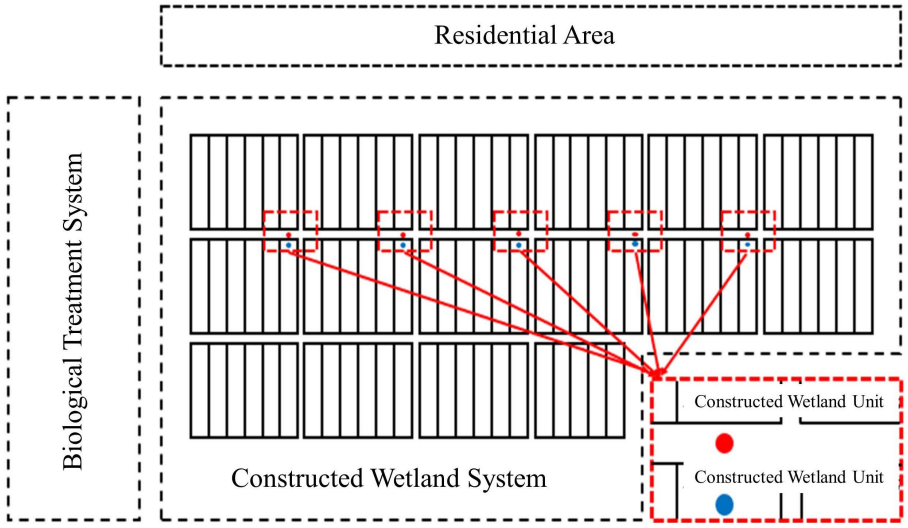

FIGURE 2
Schematic diagram of the sampling location of the constructed wetland. For the specific location of 5 sampling points, air samples, leaf interval, sewage, substrate and rhizome samples.

Leaves of the reed plants were aseptically collected from different locations within the experimental unit and placed in Ziploc bags or Whirl-Pak bags by using new gloves for each replicate and by applying an ethanol disinfection of the pruning shears between samples. Samples were then transported back to the laboratory at 4°C. One hundred milliliters of sterile water was added to the bags, and the samples were agitated for 1 min by hand and then sonicated for 2 min. The microfloral wash was then transferred to polypropylene tubes and centrifuged at 30,000 ×*g* overnight at 4°C. The pellet was then transferred to a microcentrifuge tube and stored at −80°C until DNA extraction was performed.

The bacterial activity samples in TSP were collected via two KC-1000 high-flow air samplers with fixed Teflon membranes. The samples were placed 1.5 m from the ground, and the TSP samples were collected on the membranes at a sampling flow rate of 1250 L/min. After 24 h of sample collection, the membranes of the samples were quickly sent back to the laboratory and stored at −80°C until subsequent analysis.

2.3. Experimental methods

2.3.1. DNA extraction

Sterile distilled water was used to rinse the surface of the Teflon membrane to obtain the particulate matter. After centrifugation, the particulate matter was transferred to a sterile 2 mL centrifuge tube. The sample quality was maintained at 0.2 ~ 0.3 g. Using the E.Z.N.A. VR Soil DNA Kit (Omega Bio-Tek, USA), DNA samples were obtained according to the manufacturer's instructions. An ultramicro spectrophotometer (IMPLEN, Germany) was used to detect the concentration.

2.3.2. PCR amplification of the gene fragment

Five in-house-designed primers were amplified for 16S rDNA, and the community diversity of *Massilia* was analyzed by RFLP (Table 1). The PCR amplification procedure was as follows: 94°C for 5 min; 94°C for 30 s, annealing temperature Tm°C for 30 s, and 72°C for 1 min (36 cycles), and 72°C extension for 10 min.

Five pairs of primers were designed according to the 16S rRNA of *Massilia* spp. The PCR had a total volume of 25 μL, including 5 μL 5_ reaction buffer, 5 μL 5_GC buffer, 2 μL dNTP (2.5 mmol L-1), 1 μL forward primer (10 lmol L-1), 1 μL reverse primer (10 lmol L-1), 2 μL DNA template, 8.75 μL ddH2O, and 0.25 μL Q5 DNA polymerase. The PCR system was initially denatured at 94°C for 5 min, followed by 29 cycles at 94°C for 30 s, 56°C for 30 s, and 72°C for 45 s, then extension at 72°C for 5 min, and finally samples were kept at 4°C. The Illumina MiSeq platform (Illumina, San Diego, CA, USA) provided by Personalbio (Shanghai, China) was selected for the sequencing of the PCR products.

2.3.3. Construction of a 16S rDNA clone library and RFLP sequence analysis and sequencing

PCR products were purified by a PCR product Purification Kit (OMEGA). Purified PCR products were inserted into the T-vectors by a T4 ligase cloning kit (MBI Fermen-tas). The recombinant was transformed into *Escherichia coli* (Top10) cells. The cells were cultured on LB plate medium with X-Gal/IPTG resistance screening, and the white bacterial colonies were selected and a cloned library was constructed. The vector primers M13 were used for the sequencing reactions according to the manufacturer's instructions. The new PCR products were digested by the restriction endonucleases HhaI and RsaI, and the digested products were detected by agarose gel electrophoresis. The DNA fingerprints were analyzed, and the types were designated.

After analyzing the enzyme digestion map, an OTU clone was selected to prepare the puncture tube, which was cultured for 16 h and sent to Shenggong Bioengineering (Shanghai) Co., LTD for sequencing. The sequencing results were inputed into the BLAST program in NCBI to compare with the sequences in the database, and the coverage (C), Shannon diversity index (H′), Simpson index (D) and richness (R) of the clone library were calculated.

2.3.4. Environmental factors in constructed wetland sewage, substrate and air

The wastewater environmental factors of constructed wetland: NH_3-N, NO_2^--N, NO_3^--N, pH, DO, Water temperature and Redox potential.

Physicochemical indexes of sewage: Ammonia nitrogen (NH_3-N) was determined by Nessler 's reagent spectrophotometry. Nitrite nitrogen (NO_2^--N) was determined by N-(1-naphthyl) ethylenediamine spectrophotometry. Nitrate nitrogen (NO_3^--N) was determined by ultraviolet spectrophotometry. The pH, DO, water temperature and redox potential were measured by a multi-parameter water quality analyzer (HQ30d, HACH, USA).

The soil environmental factors of constructed wetland: pH, Organic matter, Water content, TP, TN, TK.

TABLE 1 The primers used in the RFLP.

Number	Primers	Primer sequences (5′ - 3′)	Temperature/°C	Amplified fragment length/bp
1	Forward	GATAACGTAGCGAAAGTTACGCTAATAC	55	1606
	Reverse	CTCCTTGCGGTTAAGCTACCTACT		
2	Forward Reverse	TAGCAGAGTTCTGCGCAATCC GGCAGCACGGGCTTCGGCCTGGT	53	963
3	Forward Reverse	GGACGACCAGCCACACTGGGACTGAGACA TGGTAAAACCCGCTCCCATGGAGAGAG	58	1491
4	Forward Reverse	TAAGCTACCTACTTCTGGTAAAACCCA CCAAGAGTGGGGGATAACGTAGCGAAAGTT	52	1132
5	Forward Reverse	GACACGGTCCAGACTCCTAC TGTGAAGCCCTACCCATAA	53	903

TABLE 2 Physicochemical properties of constructed wetland sewage.

Sampling time	NH_3-N ($mg·L^{-1}$)	NO_2^--N ($mg·L^{-1}$)	NO_3^--N ($mg·L^{-1}$)	DO ($mg·L^{-1}$)	φ (V)	pH	T (°C)
201804	0.79 ± 0.09	0.11 ± 0.01	18.9 ± 0.33	16.11 ± 1.04	220.1 ± 3.46	7.92 ± 0.62	20.1 ± 1.5
201805	0.66 ± 0.12	0.13 ± 0.03	9.45 ± 0.80	11.45 ± 0.92	238.83 ± 8.25	7.81 ± 0.27	21.6 ± 2.1
201806	0.55 ± 0.04	0.02 ± 0.01	4.6 ± 0.34	6.27 ± 1.06	144.07 ± 9.98	7.66 ± 0.32	27.3 ± 1.4
201807	0.43 ± 0.08	0.06 ± 0.01	5.96 ± 0.44	5.59 ± 0.54	197.93 ± 4.15	7.72 ± 0.19	28.8 ± 1.1
201808	0.47 ± 0.05	0.05 ± 0.01	3.27 ± 0.29	5.06 ± 0.56	62.57 ± 9.54	7.59 ± 0.07	29.8 ± 0.8
201809	0.41 ± 0.03	0.06 ± 0.01	4.11 ± 0.53	4.84 ± 0.95	146.83 ± 3.26	7.75 ± 0.16	24.9 ± 1.9
201810	0.39 ± 0.1	0.02 ± 0.01	9.12 ± 0.94	7.14 ± 1.84	118.03 ± 8.35	7.84 ± 0.24	13.3 ± 0.6
201811	0.72 ± 0.03	0.02 ± 0.01	11.39 ± 1.18	9.11 ± 0.35	185 ± 9.3	7.84 ± 0.24	6.0 ± 1.4
201812	1.22 ± 0.07	0.68 ± 0.06	8.98 ± 0.59	5.86 ± 1.26	145.9 ± 5.01	7.06 ± 0.17	2.6 ± 0.3

TABLE 3 Physical and chemical indexes of soil samples.

Sampling time	pH	Water content(%)	Organic matter ($g·kg^{-1}$)	TN ($mg·kg^{-1}$)	TP ($mg·kg^{-1}$)	TK ($mg·kg^{-1}$)	T (°C)
201804	7.49 ± 0.20	22.24 ± 1.86	15.52 ± 0.85	78.67 ± 3.28	74.93 ± 1.84	71.84 ± 5.73	19.6 ± 1.8
201805	7.85 ± 0.24	29.05 ± 1.48	21.12 ± 0.73	130.34 ± 6.46	112.21 ± 4.17	21.12 ± 1.30	21.6 ± 2.1
201806	6.94 ± 0.99	29.71 ± 1.01	24.25 ± 0.87	109.39 ± 5.11	75.43 ± 4.16	24.25 ± 1.75	26.9 ± 1.0
201807	7.43 ± 0.22	30.1 ± 0.61	21.96 ± 0.78	131.04 ± 2.36	106.02 ± 3.02	21.96 ± 1.47	28.1 ± 0.8
201808	7.61 ± 0.37	27.88 ± 1.55	20.06 ± 1.06	127.08 ± 10.75	126.48 ± 4.91	22.39 ± 1.23	29.1 ± 0.7
201809	7.45 ± 0.29	23.8 ± 0.50	12.58 ± 1.11	67.73 ± 2.81	99.43 ± 5.26	12.58 ± 1.11	24.8 ± 1.5
201810	7.42 ± 0.33	37.05 ± 1.66	36 ± 1.13	154.05 ± 5.86	32.61 ± 1.73	181.48 ± 5.87	13.6 ± 0.5
201811	7.36 ± 0.70	30.4 ± 0.92	39.36 ± 2.34	128.2 ± 6.26	36.45 ± 1.74	157.78 ± 9.94	6.2 ± 1.3
201812	7.59 ± 0.70	25.58 ± 1.31	53.07 ± 3.18	235.1 ± 15.74	34.74 ± 3.35	219.51 ± 7.59	6.1 ± 0.2
201901	8.02 ± 0.30	27.33 ± 1.36	15.45 ± 1.08	108.93 ± 1.25	59.19 ± 3.41	15.45 ± 1.09	3.1 ± 0.9

The physical and chemical indexes of the substrate: The pH was determined by HI2221 pH meter. Organic matter was determined by potassium dichromate volumetric method. The water content was measured by drying at 105°C to constant weight. Total phosphorus (TP) was determined by molybdenum antimony colorimetric method. Total nitrogen (TN) was determined by micro-Kjeldahl method. Total potassium (TK) was determined by flame photometric method.

The air environmental factors of constructed wetland: Temperature (T), Humidity (H), Wind speed (V), O_3, SO_2, NO, NO_2, CO.

The ambient temperature and humidity of the sampling points were measured by TASI-620 digital thermometer and hygrometer. The wind speed was measured by TASI-641 anemometer. Gaseous pollutants O_3, SO_2, NO and NO_2 were measured in real time online by 49C ozone analyzer, 43C sulfur dioxide analyzer and 42C nitrogen oxide analyzer of American thermoelectric company, and CO was monitored in real time by 300 EU CO analyzer.

The above environmental factors were measured using different instruments and methods, as shown in Tables 2–4.

2.3.5. The structural differential analysis method of the *Massilia* species group

OriginPro 9.1 was used to draw the analysis map differences of *Massilia* species number and dominance, and the R language tool was used to draw and analyze the Venn diagram of *Massilia*'s population structure correlation.

Redundancy analysis (RDA) and canonical correspondence analysis (CCA) were used to analyze the correlation between environmental factors and the population characteristics of *Massilia* in the corresponding environment. Canoco 5 software was used to analyze the discriminant components of the data. If the length of the first axis was greater than 4.0, CCA should be selected. If between 3.0 and 4.0, RDA and CCA can be selected; if less than 3.0, RDA results are better than CCA. Finally, the RDA or CCA analysis chart is drawn. The contribution rate of environmental factors to the change of population structure was obtained by VPA analysis of R language. The experimental data were analyzed by SPSS 20.0 software.

3. Results

3.1. Effects of different pairs of primers on the 16S rDNA amplification of *Massilia* spp.

The 16S rDNA amplification products of *Massilia* 16S rDNA amplified by different primers were detected by 1% agarose gel electrophoresis (Figure 3 in the Additional files). The result shows that Primers 2, 3 and 4 all had nonspecific amplication production. Primers 1 and 5 had better amplification effects and can be used for 16S rDNA clone library construction.

10.3389/fmicb.2023.1211649

TABLE 4 Environmental factors of sampling sites.

Sampling time	T (°C)	H (%)	V (m/s)	SO_2 (μg/m³)	NO_2 (μg/m³)	CO (μg/m³)	O_3 (μg/m³)	$PM_{2.5}$ (μg/m³)	PM_{10} (μg/m³)
201804	18.8 ± 1.5	52.1 ± 6.3	2.25 ± 0.85	11.0 ± 0.3	39.3 ± 0.6	0.31 ± 0.02	75.7 ± 1.5	29.1 ± 1.0	98.7 ± 3.8
201805	20.3 ± 2.1	62.4 ± 3.4	1.33 ± 0.80	6.7 ± 0.1	18.3 ± 0.4	0.58 ± 0.04	88.7 ± 0.7	28.3 ± 0.9	41 ± 3.0
201806	26 ± 1.4	84.1 ± 5.1	2.56 ± 0.50	7.0 ± 0.1	19.7 ± 0.5	0.50 ± 0.03	119.7 ± 2.3	26.3 ± 0.4	44.4 ± 1.2
201807	27.5 ± 1.1	94.2 ± 0.9	2.25 ± 0.35	4.0 ± 0.2	8.5 ± 0.5	0.26 ± 0.03	43.5 ± 1.3	8.0 ± 0.2	25.5 ± 0.6
201808	28.5 ± 0.8	86 ± 0.8	2.82 ± 0.18	3.7 ± 0.2	11.0 ± 0.3	0.29 ± 0.03	72.7 ± 1.3	16.0 ± 0.3	30.6 ± 0.9
201809	23.6 ± 1.9	73.5 ± 5.5	2.97 ± 0.27	5.5 ± 0.2	39.5 ± 0.5	0.55 ± 0.02	59 ± 1.1	31.0 ± 1.1	51.0 ± 0.9
201810	12 ± 0.6	63.5 ± 3.4	4.21 ± 0.30	6.1 ± 0.3	26.0 ± 0.3	0.37 ± 0.02	71 ± 0.8	25.0 ± 0.5	52.0 ± 1.1
201811	4.7 ± 1.4	54.3 ± 3.5	6.46 ± 0.60	20.3 ± 1.2	51.3 ± 0.8	1.29 ± 0.03	54.1 ± 0.8	84.3 ± 1.2	139.7 ± 2.8
201812	6 ± 0.3	39.2 ± 2.4	5.22 ± 0.69	20.0 ± 1.3	78.7 ± 0.4	1.41 ± 0.03	25.0 ± 0.8	94.0 ± 1.0	159.7 ± 4.6
201901	4.3 ± 1.5	29.7 ± 2.2	7.74 ± 1.24	18.3 ± 0.2	63.0 ± 1.1	1.60 ± 0.12	29.7 ± 0.6	138.7 ± 0.7	200.0 ± 5.3

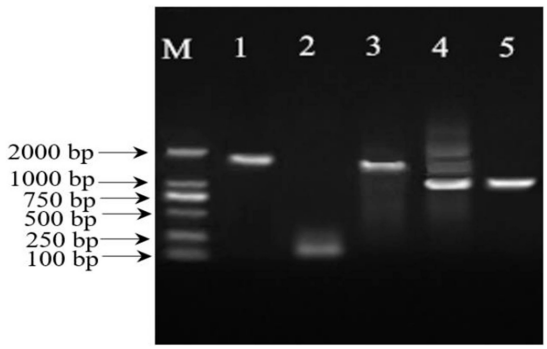

FIGURE 3
Electrophoresis analysis of PCR products with the five different primers.

3.2. Analysis of the enzyme digestion products for the amplification of two pairs of primers

The 16S rDNA of *Massilia* spp. was amplified by using primers No. 5 and No. 1. Then, the amplified products were digested with the endonucleases RsaI and HhaI, and the digested products were detected by 3% agarose gel electrophoresis. The results shows that the digested products of 16S rDNA in the clone library amplified by primer No. 1 had similar fragments (Figure 4A in the Additional files), while the digested products of 16S rDNA amplified by primer No. 5 had discrepancies (Figure 4B).

Figure 5 shows the OTUs in the constructed 16S rDNA clone libraries amplified by primers No. 1 and No. 5. There were 6 OTUs in the clone library amplified by primer No. 1, while there were 24 OTUs in the clone library amplified by primer No. 5. This indicated that the 16S rDNA amplified products of primer No. 5 were better in distinguishing the diversity of *Massilia* spp. Therefore, primer No. 5 was chosen for 16S rDNA clone library construction of *Massilia* spp.

3.3. Diversity analysis of the *Massilia* spp. in constructed wetlands

The specific alpha diversity indices are shown in Table 5. Through the coverage index, the coverage of the 16S rDNA clone libraries of *Massilia* spp. in the constructed wetland was greater than 86%, which indicated that most of the *Massilia* spp. were included in the constructed clone libraries. Large differences in the richness of *Massilia* spp. could be observed every month. The sampling in summer had the highest abundance, while the lowest abundance was in the samples collected in the winter. The richness of *Massilia* spp. was obviously different in the constructed wetland in different seasons and was higher in the summer and autumn than in the spring and winter. The Shannon index and Simpson index were selected to estimate the diversity of *Massilia* spp. According to the Shannon index and Simpson index, the samples in the summer had the highest community diversity.

3.4. The community structure of *Massilia* spp. in a constructed wetland sewage treatment system

3.4.1. The community structure of *Massilia* spp. in sewage of constructed wetland

A total of 23 *Massilia* species were found in constructed wetland sewage (Figure 6). There were significant differences in the number of dominant species of *Massilia* spp. in different months. There was a significant temporal variation in the distribution of dominant *Massilia* spp. The relative abundance of *M. albidiflava* was the highest in November. From June to August, the relative abundance was less than 1%, which was different from that in other seasons. The relative abundance of *M. alkalitolerans* was the highest in September, which was no more than 0.5% relative abundance from June to August. The relative abundance of *M. aurea* was more than 7% over the year, and there was no significant difference in different months. The relative abundance of *M. brevitalea* was highest in the summer and lowest in the autumn, which was similar to the variation in *M. brevitalea* in the substrate and rhizosphere. The relative abundance of *M. timonae* was highest in the summer, with approximately 20% relative abundance in other seasons. The relative abundance of *M. umbonata* was lowest in May and highest in December, and the seasonal variation was insignificant.

The data were analyzed with Canoco 5 software. The findings indicated that the RDA linear model should be chosen for analysis because the length of the first axis was less than 3.0. The findings reveal that the first axis' interpretation rate is 40.35%, the second axis' interpretation rate is 23.63%, and the combined

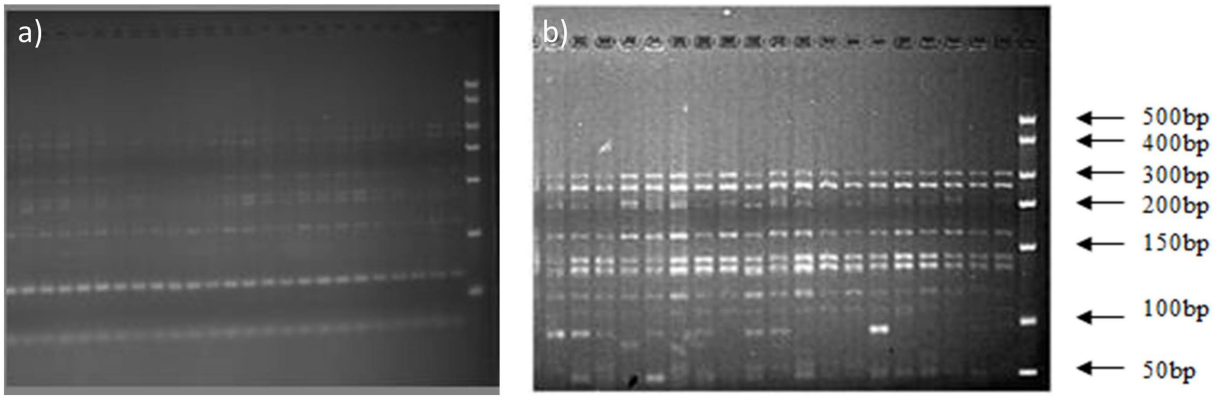

FIGURE 4
Electrophoresis analysis of amplified 16S rDNA digested by HhaI and RsaI. **(A)** Electrophoretic Strips of 16S rDNA Fragments Amplified by Primer 1; **(B)** Electrophoretic Strips of 16S rDNA Fragments Amplified by Primer 5.

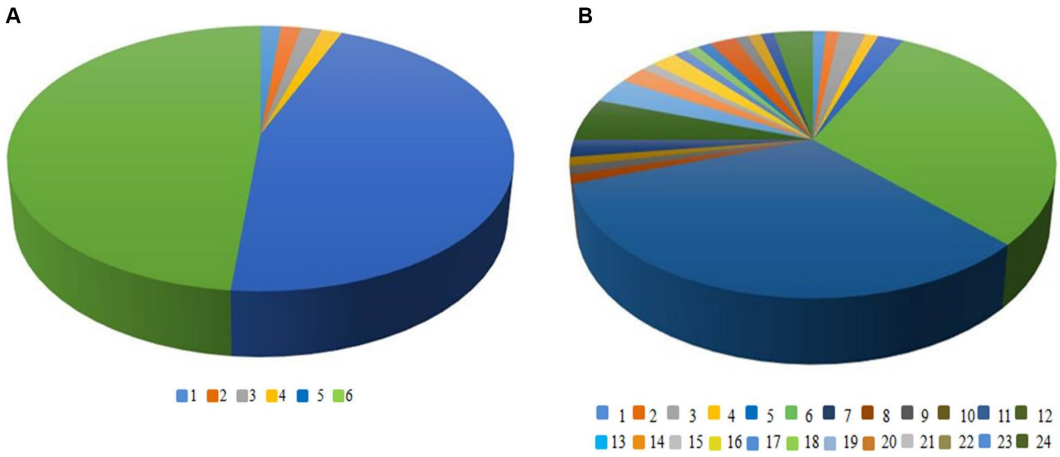

FIGURE 5
OTUs in the constructed 16S rDNA clone libraries amplified by different pairs of primers. **(A)** Amplification of OTU in 16S rDNA clone library with primer 1; **(B)** Amplification of OTU in 16S rDNA clone library with primer 5.

interpretation rate of the two axes is 63.9%. It demonstrates that the structure of *Massilia* species is significantly influenced by environmental factors in constructed wetland sewage. According to Figure 7 and Table 6, the dominant species *M. timonae* was highly significantly positively correlated with T ($p < 0.01$), and highly significantly negatively correlated with NH_3-N and NO_3^--N ($p < 0.01$). *M. brevitalea* was highly significantly positively correlated with NH_3-N, NO_3^--N, DO and φ ($p < 0.01$). *M. albiflava* was highly significantly negatively correlated with T ($p < 0.01$). *M. aurea* was significantly positively correlated with φ ($p < 0.05$). *M. plicata* and *M. aerilata* were significantly negatively correlated with NH_3-N and φ ($p < 0.05$). The results of the VPA analysis showed that the four factors with the highest contribution rates were NH_3-N, T, DO and NO_3^--N, which were 26.5, 22.2, 21.8 and 21.8%. The findings revealed that the aforementioned four factors had the greatest influence on the composition and distribution of the *Massilia* community in constructed wetland sewage.

3.4.2. The community structure of *Massilia* spp. in constructed wetland substrate

A total of 24 *Massilia* species were found in the constructed wetland substrate (Figure 8). The dominant species in the constructed wetland substrate were *M. albidiflava*, *M. alkalitolerans*, *M. aurea*, *M. brevitalea*, *M. timonae* and *M. umbonata*. The relative abundance of *M. albidiflava* was the lowest in the summer, which was significantly different from other seasons. There was no significant difference in the relative abundance of *M. albidiflava* in the other seasons. The relative abundance of *M. alkalitolerans* in the substrate decreased in order from autumn to winter to spring to summer. The relative abundance of *M. aurea* was higher in the spring and summer than in the autumn. The relative abundance of *M. brevitalea* was highest in the spring and winter and lowest in the autumn, and there were obvious seasonal differences. The relative abundance of *M. timonae* in the summer was significantly higher than that in the other three seasons. There was no significant difference in the relative abundance of *M. timonae* between months in the same season. The relative abundance of *M. umbonata* was lower all year.

10.3389/fmicb.2023.1211649

TABLE 5 The diversity index of *Massilia* based on bacteria clone libraries in different environment of constructed wetland.

Number	Sample name	Coverage(%)	Richness(R)	Shannon(H′)	Simpson(D)
1	AprA	91.38	6.67	3.28	0.9
2	AprL	86.85	8.22	3.52	0.89
3	AprW	95.55	8.16	3.36	0.94
4	AprS	89.77	7.48	2.97	0.87
5	AprR	90.74	7.35	3.15	0.86
6	MayA	93.02	8.04	3.64	0.91
7	MayL	94.1	7.68	3.85	0.93
8	MayW	94.07	7.15	3.91	0.92
9	MayS	95.27	9.23	3.83	0.89
10	MayR	94.23	8.64	3.77	0.91
11	JunA	94.69	7.89	3.56	0.94
12	JunL	93.75	8.74	3.28	0.89
13	JunW	95.16	8.16	3.36	0.92
14	JunS	92.42	7.66	3.47	0.9
15	JunR	93.79	7.98	3.69	0.94
16	JulA	93.5	9.32	3.84	0.88
17	JulL	92.91	10.49	3.91	0.86
18	JulW	90.12	12.56	4.35	0.95
19	JulS	97.41	13.11	5.54	1
20	JulR	93.2	13.08	5.01	0.96
21	AugA	91.03	10.27	4.98	1
22	AugL	91.41	12.32	5.32	0.97
23	AugW	91.28	11.09	5.47	0.99
24	AugS	93.38	12.46	5.66	0.99
25	AugR	99.22	11.45	5.73	1
26	SepA	88.59	12.74	5.97	0.98
27	SepL	92.5	12.12	5.82	0.97
28	SepW	96.98	12.88	5.43	1
29	SepS	96.73	12.65	4.9	0.99
30	SepR	95.92	12.37	4.58	1
31	OctA	96.69	9.97	3.92	0.91
32	OctL	95.81	9.78	3.58	0.89
33	OctW	96.4	9.61	3.74	0.92
34	OctS	93.63	9.54	3.65	0.91
35	OctR	91.24	8.76	3.94	0.93
36	NovA	97.22	7.54	3.22	0.86
37	NovL	91.18	8.55	3.14	0.9
38	NovW	92.68	7.31	3.26	0.91
39	NovS	95.12	6.98	3.43	0.89
40	NovR	97.31	7.85	3.59	0.92
41	DecA	96.87	8.52	3.62	0.86
42	DecW	97.23	7.68	3.57	0.87
43	DecS	94.25	7.94	3.63	0.89
44	DecR	95.49	8.26	3.59	0.91
45	JanA	93.68	8.23	3.31	0.9
46	JanS	93.86	9.57	3.53	0.89
47	JanR	91.82	8.85	3.25	0.88

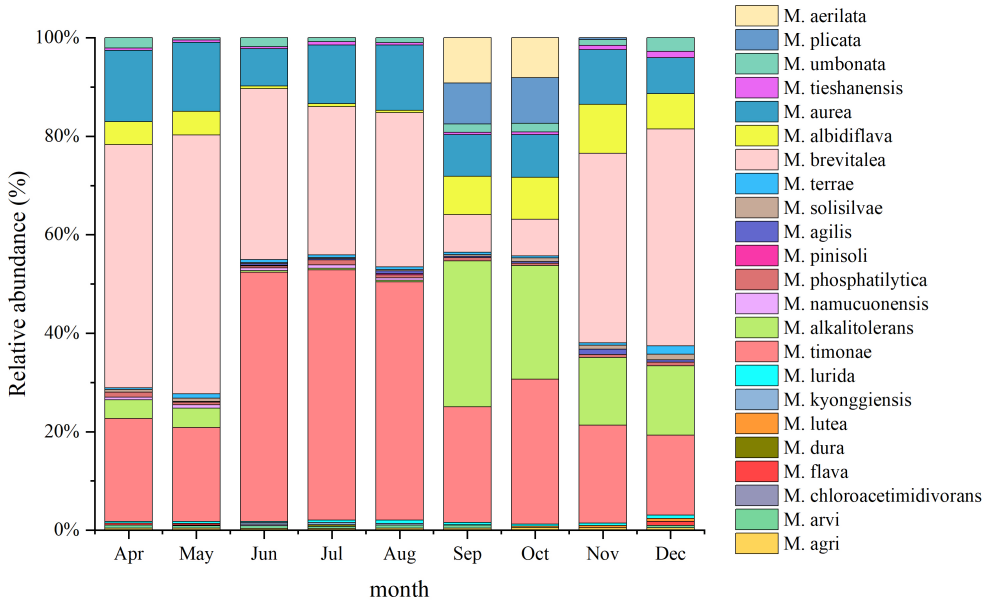

FIGURE 6
Analysis of the 16S rDNA clone library based on microbes in sewage.

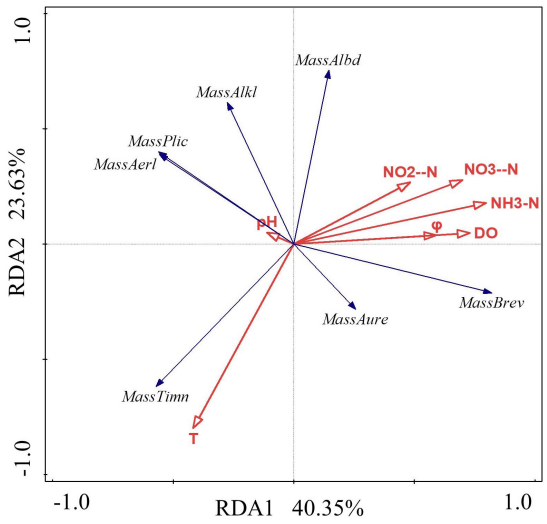

FIGURE 7
Redundancy analysis of *Massilia* and environmental factors in wastewater.

The RDA linear model was used to analyze the data. The results show that the interpretation rate of the first axis is 31.57%, the second axis is 21.18%, and the common interpretation rate of the two axes is 52.75%. It shows that environmental factors in the constructed wetland substrate have a significant effect on the structure of *Massilia* spp. According to Figure 9 and Table 7, the dominant species *M. timonae* was very significantly positively correlated with T and TP content ($p < 0.01$). *M. alkalitolerans* was significantly negatively correlated with TP ($p < 0.05$). *M. brevitalea* was highly significantly positively correlated with TN ($p < 0.01$). *M. albiflava* was very significantly positively correlated with TN ($p < 0.01$), and highly significantly negatively correlated with TP and T ($p < 0.01$). *M. aurea* was significantly positively correlated with TP ($p < 0.05$). *M. plicata* and *M. aerilata* were positively correlated with water content and T. The results of the VPA analysis showed that the three factors with the highest contribution rates were T, TP and TN, which were 19.1, 14.1 and 9.7%. The findings revealed that the aforementioned three factors had the greatest influence on the composition and distribution of the *Massilia* community in constructed wetland substrate.

3.4.3. The community structure of *Massilia* spp. in the rhizosphere sample of constructed wetland plants

A total of 24 *Massilia* species were found in the rhizosphere of constructed wetland plants (Figure 10). The dominant species in the rhizosphere sample of constructed wetland plants were *M. albidiflava*, *M. alkalitolerans*, *M. aurea*, *M. brevitalea*, *M. timonae*, and *M. umbonata*. The relative abundance of *M. albidiflava* was higher in the autumn and winter than in the spring and summer. The relative abundance of *M. albidiflava* was lowest in July and highest in December. The variation in the relative abundance of *M. albidiflava* in the rhizosphere sample of plants was similar to that in the substrate sample of the constructed wetland. The relative abundance of *M. alkalitolerans* was higher in the autumn and winter than in the spring and summer, and the relative abundance was lowest in the summer (less than 1%). The variation in relative abundance for *M. aurea* was relatively slight. The relative abundance of *M. aurea* was higher in spring and summer than in autumn and winter, and the relative abundance was lowest in January and highest in May. The relative abundance of *M. brevitalea* was higher in the spring and summer than in the autumn and winter, and the relative abundance was highest in the summer, at nearly 50%. In the autumn, the relative abundance of *M. brevitalea* was lower in September and October, at approximately 8%. The relative abundance of *M. timonae* was the highest from June to August, up to approximately 47%. The relative abundance in the

TABLE 6 Correlation analysis of dominant species of *Massilia* and environmental factors in sewage.

	NH_3-N	DO	NO_3^--N	NO_2^--N	φ	pH	*T*
M. timonae	−0.577**	−0.324	−0.541**	−0.183	−0.248	0.078	0.728**
M. alkalitolerans	−0.029	0.114	0.273	0.052	−0.149	0.210	−0.378
M. brevitalea	0.579**	0.537**	0.511**	0.118	0.629**	−0.060	−0.174
M. albidiflava	0.112	0.194	0.371	−0.061	−0.044	0.243	−0.725**
M. aurea	0.209	0.287	0.280	−0.006	0.392*	0.291	0.249
M. plicata	−0.423*	−0.216	−0.124	−0.058	−0.427*	0.201	−0.050
M. aerilata	−0.433*	−0.218	−0.127	−0.077	−0.419*	0.195	−0.027

**Significant correlation at 0.01 level (bilateral); *Significant correlation at the 0.05 level (bilateral).

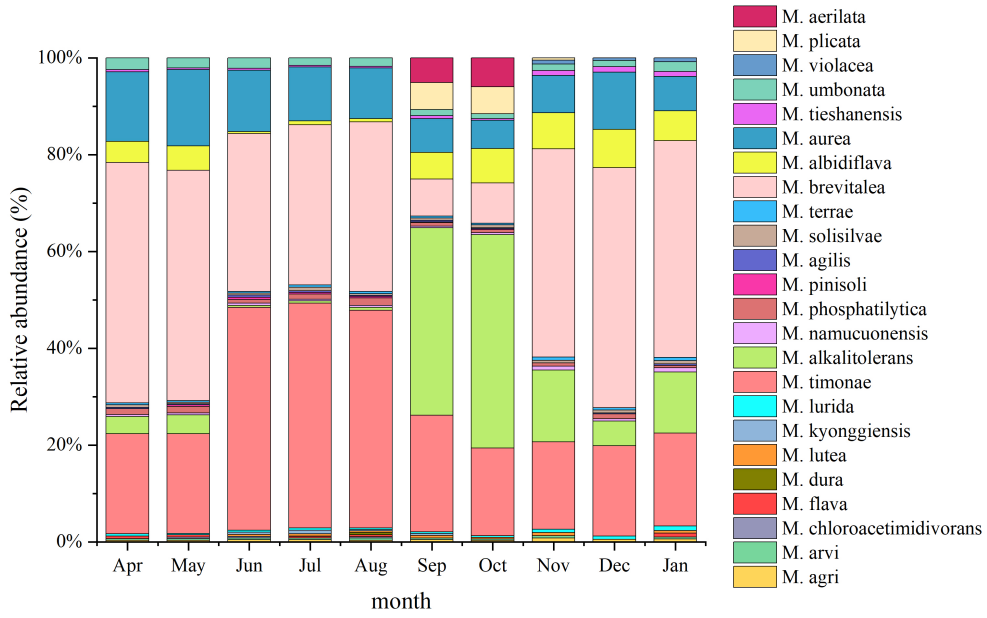

FIGURE 8
Analysis of the 16S rDNA clone library based on soil microbes.

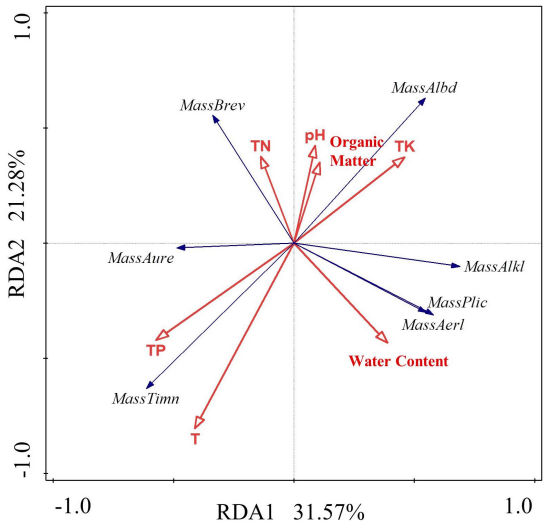

FIGURE 9
Redundancy analysis of *Massilia* and environmental factors in soil.

other months was approximately 20%. The variation in the relative abundance of *M. timonae* in the rhizosphere sample of plants was similar to that in the substrate sample of constructed wetland. The relative abundance of *M. umbonata* was lower than 2.5% all year, and was higher in the spring and winter than in the summer and autumn.

3.4.4. The community structure of *Massilia* spp. in the phyllosphere sample of constructed wetland plants

A total of 18 *Massilia* species were found in the phyllosphere sample of constructed wetland plants (Figure 11). The relative abundance of *M. albidiflava* in the phyllosphere sample decreased in an order from autumn to spring to summer. The relative abundance of *M. albidiflava* was highest in the autumn and lowest in the summer. The variation regularity of the relative abundances of *M. alkalitolerans* was similar to that of *M. albidiflava* in the phyllosphere sample. There was no obvious seasonal variation in the relative abundance of *M. aurea*. The relative abundance of *M. brevitalea* exhibited significant differences between seasons, with the highest relative abundance observed in the spring and the lowest relative abundance observed in

TABLE 7 Correlation analysis of dominant species of *Massilia* and environmental factors in soil.

	pH	TN	Water content	TK	TP	Organic matter	*T*
M. timonae	−0.346	−0.027	−0.161	−0.360	0.570**	−0.132	0.749**
M. alkalitolerans	0.145	−0.127	0.191	0.108	−0.461*	0.004	−0.208
M. brevitalea	0.205	0.840**	−0.173	0.269	−0.138	0.059	−0.315
M. albidiflava	0.137	0.534**	0.124	0.318	−0.613**	0.112	−0.780**
M. aurea	0.053	−0.026	−0.243	0.054	0.362*	−0.054	0.344
M. plicata	−0.088	−0.140	0.130	−0.040	−0.164	−0.030	0.062
M. aerilata	−0.109	−0.134	0.132	−0.040	−0.158	−0.032	0.044

**Significant correlation at 0.01 level (bilateral); *Significant correlation at the 0.05 level (bilateral).

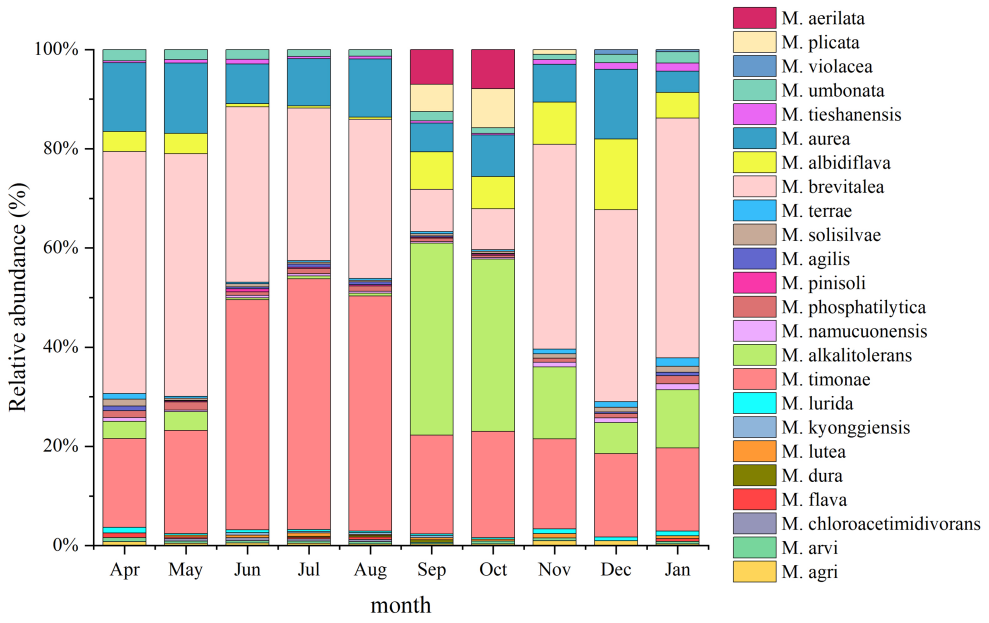

FIGURE 10
Analysis of the 16S rDNA clone library based on rhizosphere microbes.

autumn. There were obvious seasonal differences in the relative abundance of *M. timonae*; the highest relative abundance was approximately 50% in the summer, and the lowest relative abundance was approximately 19% in the spring and autumn. The relative abundance of *M. umbonata* was similar to that in the other environments of constructed wetlands, and its relative abundance was lower.

3.4.5. The community structure of *Massilia* spp. in the air sample of constructed wetland plants

A total of 16 *Massilia* species were found in the air sample of the constructed wetland (Figure 12). The relative abundances of *M. albidiflava* and *M. alkalitolerans* exhibited significant seasonal variation; the relative abundance was higher in the autumn and winter, while the species were not detected in the summer. The variation in the relative abundance of *M. aurea* between seasons was not obvious; the relative abundance was highest in April, May, July and December (approximately 16%), while it was lowest in January. The relative abundance of *M. brevitalea* was similar to that in other environments of constructed wetlands, with the highest relative abundance observed in January and the lowest relative abundance observed in September and October. The relative abundance of *M. timonae* exhibited obvious seasonal variation, with the highest relative abundance observed in the summer, while there were no significant differences among the spring, autumn and winter.

The data in Table 4 and Figure 12 were examined using the RDA model. The results show that the first axis interpretation rate is 48.03%, the second axis interpretation rate is 29.67%, and the combined interpretation rate of the two axes is 77.69%. It was discovered that the air environmental factors of the constructed wetland had a substantial impact on the community structure of *Massilia*. As shown in Figure 13 and Table 8, the dominant species of the genus *M. timonae* in the air of constructed wetlands was highly significantly positively correlated with temperature, humidity and O_3 ($p < 0.01$), highly significantly negatively correlated with SO_2, NO_2, CO, $PM_{2.5}$ and PM_{10} ($p < 0.01$), and significantly negatively correlated with wind speed ($p < 0.05$); *M. alkalitolerans* showed a highly significant positive correlation with wind speed ($p < 0.01$), a significant positive correlation with NO_2 ($p < 0.05$), and a highly significant negative correlation with humidity ($p < 0.01$); *M. albidiflava* showed highly significant positive correlations ($p < 0.01$) with SO_2, NO_2

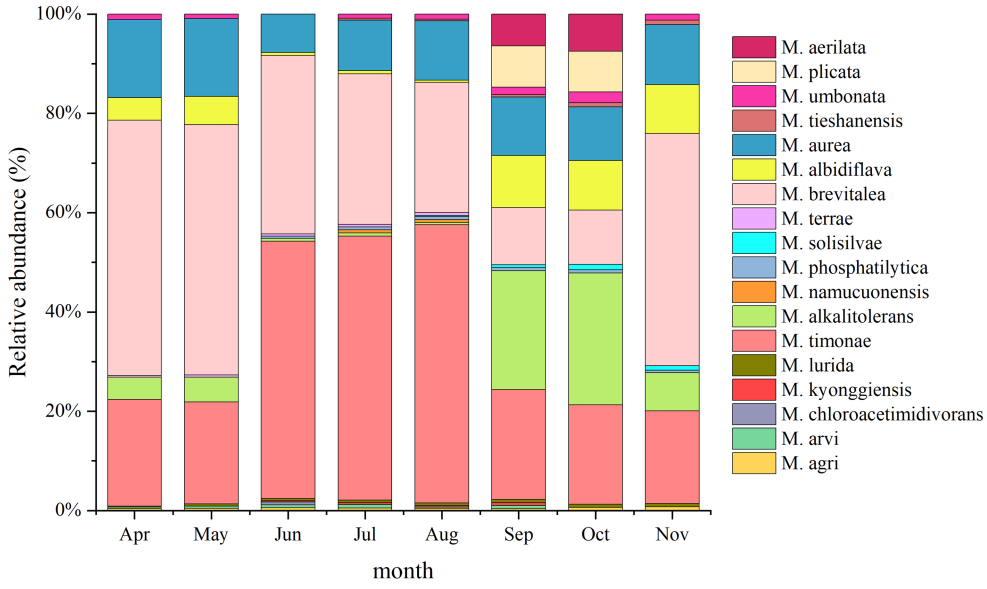

FIGURE 11
Analysis of the 16S rDNA clone library based on phyllosphere microbes.

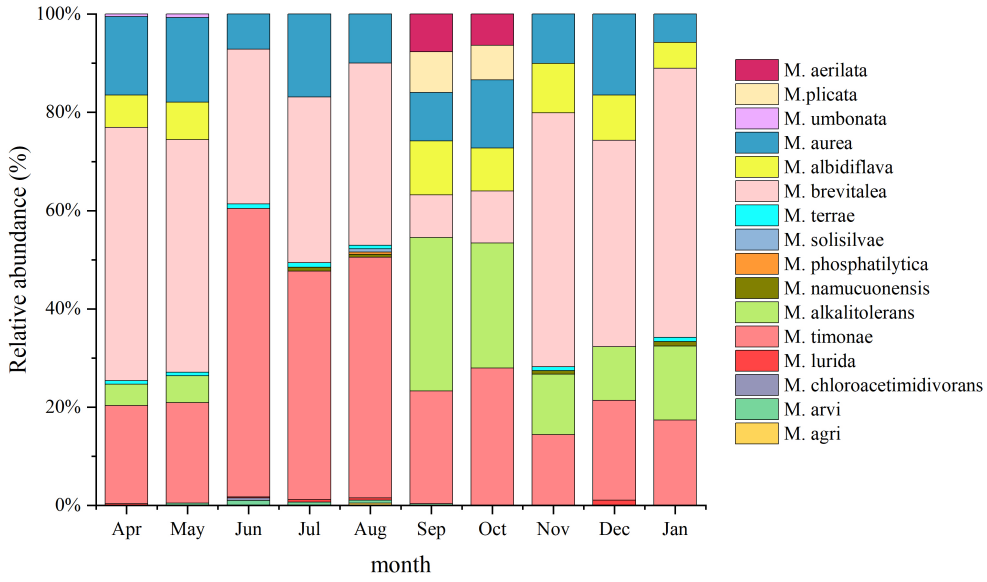

FIGURE 12
Analysis of the 16S rDNA clone library based on airborne microbes.

and PM_{10}, significant positive correlations ($p < 0.05$) with $PM_{2.5}$ and CO, and highly significant strong negative correlations ($p < 0.01$) with temperature and humidity; *M. aurea* showed highly significant negative correlations ($p < 0.01$) with wind speed and $PM_{2.5}$ and significant negative correlations ($p < 0.05$) with CO and PM_{10}. The results obtained from the VPA analysis showed that humidity, NO_2, temperature and SO_2 were the four factors that explained the greatest contribution with values of 40.1, 11.4, 15.2 and 5.1%. The findings revealed that the community composition and distribution of *Massilia* in the air of the constructed wetland is most influenced by the above four factors.

3.5. The influence of environmental factors on the structure of the *Massilia* spp. community in constructed wetlands

The structure of *Massilia* spp. in different seasons and different environments was analyzed by a Venn diagram (Figure 14). The species numbers of *Massilia* spp. in the constructed wetland sewage, substrate, plant rhizosphere, plant phyllosphere and air samples were 15, 16, 16, 10 and 8 species, respectively in the spring, 17, 20, 21, 14 and 7 species, respectively in the summer, and 13, 19, 19, 13 and 7 species, respectively

in the autumn. The species number of *Massilia* spp. in the substrate and rhizosphere in the winter was 18, while it was 7 in the air. The above results show that the species of *Massilia* in the air samples were all found in the other environments of the constructed wetland. Therefore, it can be concluded that *Massilia* spp. in the air were probably from the underlying surface of the constructed wetland.

PCA was employed to analyze the composition of *Massilia* species in each environmental sample of the constructed wetland, and the distribution characteristics among the samples were described by two-dimensional images, as shown in Figure 15. The results showed that there were significant differences in the composition of *Massilia* spp. among different environmental samples, while the differences in different seasons were small. Most interestingly, the study found that the similarity of *Massilia* spp. in different environmental samples within the same season was higher than that in the same environmental sample within different seasons.

4. Discussion

Since *Massilia* was first discovered by La Scola in 1998, scholars from all over the world have successfully discovered other *Massilia* from different regions and environments and studied them. In 2003, Wery et al. studied the microbial community in Antarctic soil, isolated a strain capable of producing protease, used universal primers to amplify 16S rDNA by PCR, and determined the phylogenetic relationship of the strain by gene sequencing, and classified it as belonging to the *Massilia* genus (Wery et al., 2003). Weon et al. and Feng et al. also used the same molecular biology approach to study *Massilia* found in other environments (Weon et al., 2009; Feng et al., 2016). It can be seen that there are many studies on *Massilia*, but its community structure composition and dynamic changes in different environments are rarely reported. This study was the first to systematically study the composition and distribution of *Massilia* spp. in constructed wetlands using the method of cloning library construction. Five pairs of primers designed in-house were innovatively used to amplify the 16S rDNA of *Massilia* spp. and further analyzed using agarose gel electrophoresis. The detection showed that the amplification effect of primer No. 5 was the best, and the electrophoresis bands of the restriction map of RFLP were abundant. Therefore, primer No. 5 was finally selected to construct a *Massilia* clone library and conduct RFLP sequence analysis. The coverage rate of the clone library constructed by primer No. 5 was greater than 86%, indicating that the clone library constructed by the primer contained most of the *Massilia spp.* in the wetland, which could more fully reflect the diversity of the *Massilia* community. The construction of the clone library can obtain a more systematic and comprehensive understanding of the community structure of *Massilia* in the constructed wetland, which provides valuable experience for studying the community composition of *Massilia* in other environments and provides data support for the construction and operation of the constructed wetland.

Previous studies have shown that the higher the H′ is, the lower the D is, and the higher the microbial diversity. The Shannon index and Simpson index of *Massilia* in the constructed wetland were analyzed, and the results showed that the variation range of Shannon index and Simpson index was 2.97–5.97 and 0.86–1.00, which were the highest in summer and significantly higher than that in winter, and the difference between spring and autumn was not significant. According to the clone library diversity index analysis, the abundance of *Massilia* in different environments of constructed wetlands in different seasons was significantly different, and the overall abundance in the summer was higher than that winter, indicating that there is a significant seasonal fluctuation in the structure and diversity of microbial communities in wetland ecosystems. When Chazarenc studied the vertical flow constructed wetland in France, he found that the degree of bacterial activity varied with seasonal temperature, the highest in June, and the

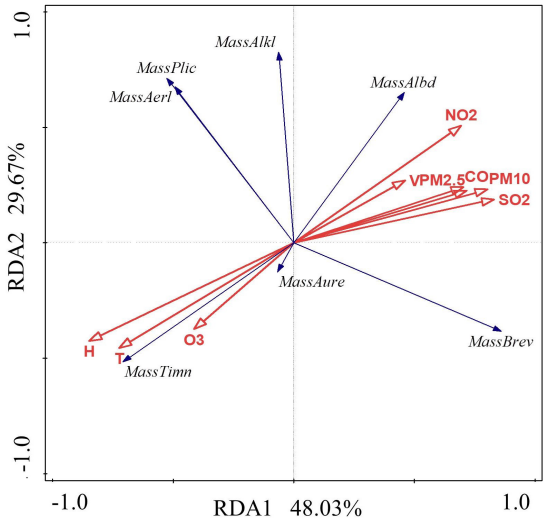

FIGURE 13
Redundancy analysis of *Massilia* and environmental factors in air.

TABLE 8 Correlation analysis of dominant species of *Massilia* and environmental factors in the air.

	T	*H*	*V*	SO_2	NO_2	CO	O_3	$PM_{2.5}$	PM_{10}
M. timonae	0.731**	0.778**	−0.377*	−0.664**	−0.729**	−0.588**	0.475**	−0.587**	−0.658**
M. alkalitolerans	−0.36	−0.503**	0.500**	0.15	0.430*	0.233	−0.324	0.225	0.208
M. brevitalea	−0.463**	−0.683**	0.276	0.659**	0.420*	0.539**	−0.222	0.562**	0.628**
M. albidiflava	−0.607**	−0.568**	0.262	0.503**	0.641**	0.457*	−0.357	0.428*	0.474**
M. aurea	0.338	0.297	−0.702**	−0.318	−0.339	−0.443*	0.18	−0.507**	−0.430*
M. plicata	0.022	0.144	0.109	−0.343	−0.068	−0.262	0.026	−0.247	−0.275
M. aerilata	0.016	0.147	0.093	−0.323	−0.062	−0.244	0.024	−0.234	−0.261

**Significant correlation at 0.01 level (bilateral); *Significant correlation at the 0.05 level (bilateral).

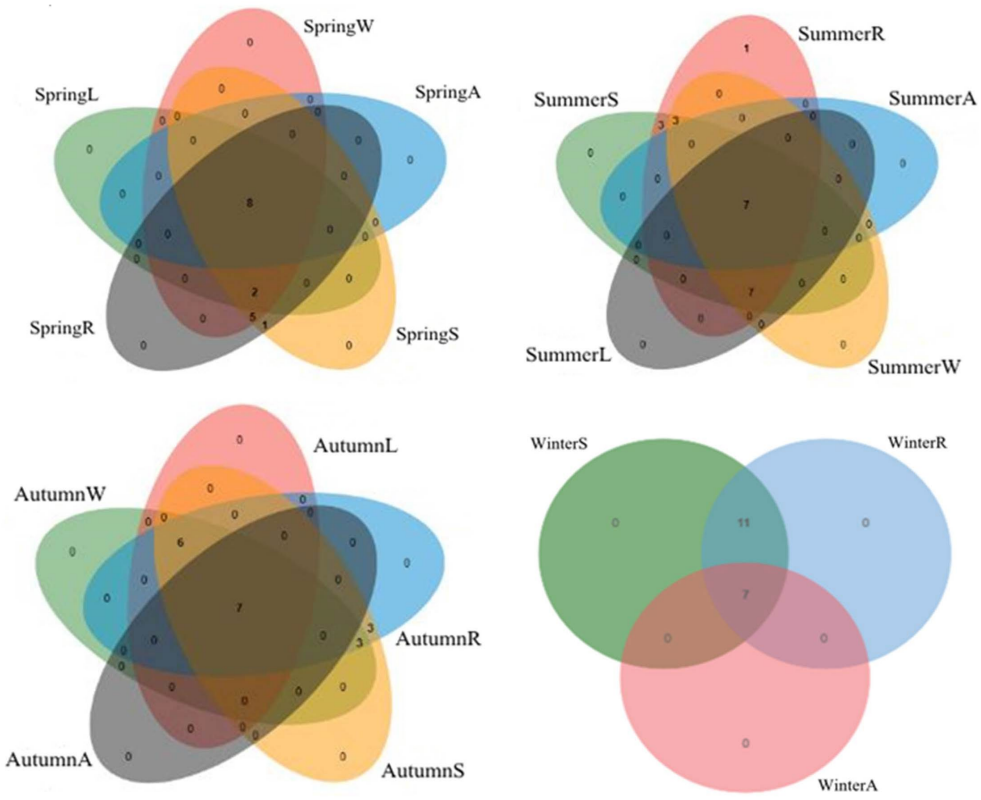

FIGURE 14
Correlation of *Massilia* spp. in four seasons. (A): *Massilia* in the Air; (L): *Massilia* in the Leaf (Phyllosphere); (W): *Massilia* in the Water (Sewage); (S): *Massilia* in the Substrate (Soil); (R): *Massilia* in the Rhizosphere.

lowest in late winter and autumn (Chazarenc et al., 2010), which was similar to the results of this study. This may be due to the low temperature in winter and low microbial activity, so the microbial abundance is low. According to the correlation analysis of environmental factors, T was the most significant factor affecting the community structure of *Massilia* in constructed wetlands. After the beginning of spring, with the increase of temperature, the microbial activity increases, and the reproduction speed also accelerates, so the number of microorganisms gradually increases, reaching the peak in summer. The temperature in autumn is also high, so the microorganisms continue to grow, and then the number of microorganisms starts to decrease after the temperature decreases in late autumn, until it drops to the lowest point in winter. Buckeridge et al. research found that the number of bacteria in the soil microbial community of arctic tundra decreased significantly from the peak in the late thawing period to the low point in spring, and then increased to a level similar to that in autumn in midsummer, which is different from this study (Buckeridge et al., 2013). The reason may be that the climate types and ecosystems of the two places are different. The Arctic has a long winter and freezes all the year round; Qingdao is located in the mid latitude region, with four distinct seasons and short winter. This indicates that the seasonal variation of the composition of *Massilia* in the constructed wetland may be related to the environment and climate of the area where the constructed wetland is located, and the microbial community structure of the constructed wetland in different areas is different.

This study found that *Massilia* were distributed and abundant in sewage, substrate, plant rhizosphere, phyllosphere and air in constructed wetlands, but their proportions in each environment were different. A total of 24 species of *Massilia* were detected in the constructed wetland system, and the number of species was in the following order: substrate and rhizosphere samples > sewage samples > phyllosphere samples > air samples. Moreover, the species of *Massilia* in air samples were found in other environments of the constructed wetland, indicating that the substrate (soil) and plant rhizosphere of the constructed wetland were important sources of *Massilia*. It may diffuses into the air from the underlying surface of the constructed wetland. In addition, previous studies have reported that the microbial community in the rhizosphere of constructed wetland plants is the most abundant and that plant root exudates can have a positive effect on microorganisms indicating that the constructed wetland substrate (soil) was an important source of *Massilia*. It diffuses into the air from the underlying surface of the constructed wetland (Chaparro et al., 2013; Wu et al., 2017).

Through Venn diagram comparison, we found that *Massilia* and dominant bacteria were similar in sewage samples, substrate samples, plant rhizosphere and phyllosphere samples and showed that the number of *Massilia* species in plant rhizosphere samples was slightly greater than that in substrates. This may be due to artificial wetlands using substrates, plants, microorganisms of physical, chemical and biological sewage treatment triple synergy (Stottmeister et al., 2003), and aquatic plants as an indispensable part of the purification process. This increase in the type of bacteria in constructed wetland system substrates and plant rhizospheres enhances the growth of microbial communities to create a favorable environment (Cao et al., 2017); for example, a variety of useful compounds are released into the rhizosphere

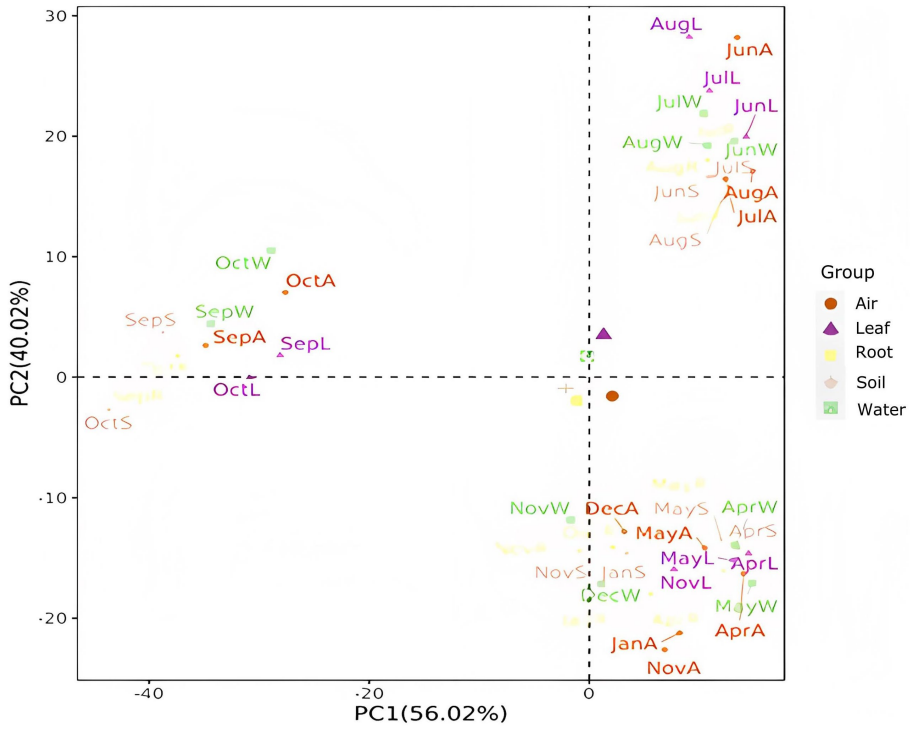

FIGURE 15
PCA of the *Massilia* population composition in different months and environments. (Air): *Massilia* in the Air; (Leaf): *Massilia* in the Phyllosphere; (Root): *Massilia* in the Rhizosphere; (Soil): *Massilia* in the Substrate; (Water): *Massilia* in the Sewage.

(Olanrewaju et al., 2019). *Massilia* can secrete auxin, accelerate the growth of plants and increase the concentration of cations such as iron (Kuffner et al., 2010), calcium and magnesium in plant roots (Hrynkiewicz et al., 2010), improve the nutrient supply of plant roots, and improve the survival rate of plants under adversity. *Massilia* and aquatic plants complement each other, and the two act synergistically, so there are more species of *Massilia* in the rhizosphere than in the substrate.

This study found that there are 6 dominant species of *Massilia* in different environmental samples of constructed wetlands, with obvious seasonal differences, namely, *M. albidiflava, M. alkalitolerans, M. aurea, M. brevitalea, M. timonae* and *M. umbonata*. This shows that the dominant species of *Massilia* have multiple ecological functions. Among them, *M. timonae* was the most important of the six dominant bacteria, with the highest relative abundance of 58.75%. Because of its significant positive correlation with T, the relative abundance of *M. timonae* was higher in summer and autumn, and lower in winter and spring. In 2009, Faramarzi et al. found that the most dominant species, *M. timonae,* could produce chitinase in a medium containing colloidal chitin as the only carbon and nitrogen source, which greatly reduced the production cost of chitinase (Faramarzi et al., 2009). The relative abundance of the second largest species *M. brevitalea* was higher in winter and spring, reaching 54.76%. The correlation analysis of environmental factors showed that it was significantly negatively correlated with T, so it was a low temperature resistant *Massilia*. In 2008, Zul et al. isolated a strain of *M. brevitalea* from the substrate and found that it can hydrolyze starch and casein and has salt tolerance, and in this study, it was found that its relative abundance was high in the winter (Zul et al., 2008). In addition, *M. brevitalea* was once isolated from organic fertilizers as the dominant strain of ammonification, indicating that it is more suitable for survival in environments with higher organic matter and nitrogen content, and its abundance was positively correlated with total nitrogen and organic matter. There is little difference between *M. alkalitolerans* and *M. aurea*, but *M. alkalitolerans* is slightly dominant, and the relative abundance can reach 44.12%, while the highest relative abundance of *M. aurea* is 17.24%. *M. alkalitolerans* has alkali resistance (Xu et al., 2005), and *M. aurea* can produce auxin (indoleacetic acid) (Gallego et al., 2006). The relative abundances of *M. albidiflava* and *M. umbonata* were low. *M. umbonata* can produce poly-β-hydroxybutyrate (Rodriguez-Diaz et al., 2014). *M. albidiflava* was positively correlated with total nitrogen, which may be related to its nitrogen fixation activity (Zhang et al., 2006).

In addition, the environmental factors in the constructed wetland have a significant impact on the composition, distribution and seasonal variation of the community structure of the *Massilia* dominant bacteria. In this study, we found that *M. albidiflava* and *M. brevitalea*, the dominant species of *Massilia*, were positively correlated with NH_3-N, NO_2^--N and NO_3^--N, consistent with their having nitrate reductase activity; *M. timonae* and *M. aurea* were positively correlated with TP content, which proved that *Massilia* had phosphorus solubilization; *M. aurea* absorbed the fungal secretion; The photosynthetic products secreted by the fungus were absorbed by *M. aurea*, which promoted the mineralization and transformation of organic phosphorus in the substrate. The substrate with high phosphorus content was more suitable for its survival (Wang et al., 2016). When studying the correlation between microbial community structure and environmental factors in Poyang Lake wetland profile, it was found that water content and pH were the main factors affecting bacterial community structure (Ma et al., 2018), which was consistent with the results of this study. Since airborne bacteria are usually attached to the surface of atmospheric particles and can easily spread with the wind. Many air environment factors affect atmospheric particulate matter, which in

turn affects the composition and function of the microbial community attached to its surface (Hwang and Park, 2014). Therefore, the air environmental factors investigated in this study, such as temperature, humidity, wind speed, $PM_{2.5}$ and PM_{10}, all had an impact on the seasonal variation and community structure of the *Massilia* dominant strains (Maron et al., 2006; Cao et al., 2014). In summary, the study of *Massilia* dominant species in the constructed wetland will help us to analyze the main functions of the constructed wetland and adjust its operation status, which can make it treat sewage more efficiently.

Although the genus *Massilia* has multiple environmental functions, clinical medical studies have found that infection with one of the dominant species, *M. timonae*, has the potential to lead to multiple human health-threatening diseases, such as septicemia, osteomyelitis, and encephalitis (Scola et al., 1998; Van Craenenbroeck et al., 2011), but the infection mechanism is unknown. Song recently isolated a *Massilia oculi* sp. nov. of type strain CCUG 43427^T from the eyes of an endophthalmitis patient, and analyzed its genome. It was found that it contains pathogenic genes, indicating that the strain has posed a threat to human health (Song et al., 2019). The above results indicate that some *Massilia* bacteria have evolved a wide range of pathogenicity, and the air mosaic bacteria in constructed wetlands can spread with the air to the surrounding environment, which is one of the important ways of *Massilia* transmission. Therefore, studying the community composition of *Massilia* bacteria is important for the safety evaluation of artificial wetlands, as well as for public health and ecological safety.

5. Conclusion

In conclusion, self-designed primers were used to construct a 16S rDNA clone library, and RFLP sequence analysis was used to determine the composition of the *Massilia* community in sewage, substrate, plant rhizosphere, plant leaf and air in an artificial wetland sewage treatment system. The overall community of *Massilia* bacteria in the artificial wetland sewage treatment system was higher in the summer and autumn than in the spring and winter, while the relative abundance of the dominant species had obvious seasonal differences. There were significant seasonal differences in the relative abundance of dominant species in sewage, substrate, plant rhizosphere and plant leaf sphere. Environmental factors in the sewage, substrate and air of the constructed wetland had a great influence on the composition and seasonal variation of *Massilia's* community structure. The diversity of *Massilia* bacteria in the artificial wetland air was less different than in the environmental samples, and the overlap rate of the total OTUs with the remaining samples was 100%, indicating that *Massilia* spp. in the air were probably from the underlying surface of the constructed wetland. In different seasons, the composition of *Massilia* spp. was significantly different in the same environment. In the same season, the similarity of *Massilia* spp. in different environments was high, and there was homology.

Data availability statement

The original contributions presented in the study are included in the article/supplementary material, further inquiries can be directed to the corresponding author.

Author contributions

AX wrote the review and editing. CL wrote the original draft preparation. All authors contributed to the article and approved the submitted version.

Funding

This research was funded by the Key R&D projects of Shandong Province (2018GSF117022), the Youth Foundation of Shandong Natural Science Foundation (ZR2020QC027), and the Shandong Natural Science Foundation (ZR2023MC193).

Acknowledgments

We thank the experimental materials provided by the Key Laboratory of Eco-environmental Engineer and Pollution Remediation in Shandong Province. We also thank the reviewers for their remarks and suggestions.

Conflict of interest

The authors declare that the research was conducted in the absence of any commercial or financial relationships that could be construed as a potential conflict of interest.

Publisher's note

References

Agematu, H., Suzuki, K., and Tsuya, H. (2011). *Massilia* sp. BS-1, a novel violacein-producing bacterium isolated from soil. *Biosci. Biotechnol. Biochem.* 75, 2008–2010. doi: 10.1271/bbb.100729

Baek, H. J., Lee, C. M., Sim, J. S., Koo, B. S., Yoon, S. H., Hahn, B. S., et al. (2014). Production of violacein by a novel bacterium, *Massilia* sp. EP15224 strain. *Korean J. Microbiol. Biotechnol.* 42, 317–323. doi: 10.4014/kjmb.1410.10006

Buckeridge, K. M., Banerjee, S., Siciliano, S. D., and Grogan, P. (2013). The seasonal pattern of soil microbial community structure in mesic low arctic tundra. *Soil Biol. Biochem.* 65, 338–347. doi: 10.1016/j.soilbio.2013.06.012

Cao, C., Jiang, W. J., Wang, B. Y., Fang, J. H., Lang, J. D., Tian, G., et al. (2014). Inhalable microorganisms in Beijing's PM2.5 and PM10 pollutants during a severe smog event. *Environ. Sci. Technol.* 48, 1499–1507. doi: 10.1021/es4048472

Cao, Q. Q., Wang, H., Chen, X. C., Wang, R. Q., and Liu, J. (2017). Composition and distribution of microbial communities in natural river wetlands and corresponding constructed wetlands. *Ecol. Eng.* 98, 40–48. doi: 10.1016/j.ecoleng.2016.10.063

Cerrone, F., Sánchez-Peinado, M. M., Rodríguez-Díaz, M., González-López, J., and Pozo, C. (2011). PHAs production by strains belonging to *Massilia* genus from starch. *Starch* 63, 236–240. doi: 10.1002/star.201000132

Chaparro, J. M., Badri, D. V., Bakker, M. G., Sugiyama, A., Manter, D. K., and Vivanco, J. M. (2013). Root exudation of phytochemicals in Arabidopsis follows specific patterns that are developmentally programmed and correlate with soil microbial functions. *PLoS One* 8:e55731. doi: 10.1371/journal.pone.0055731

Chazarenc, F., Brisson, J., and Merlin, G. (2010). Seasonal and spatial changes of microorganism communities in constructed wetlands: a community level physiological profiling analysis. *Int. J. Chem. Eng.* 2010, 1–6. doi: 10.1155/2010/490240

Du, Y., Yu, X., and Wang, G. (2012). *Massilia tieshanensis* sp. nov., isolated from mining soil. *Int. J. Syst. Evol. Microbiol.* 62, 2356–2362. doi: 10.1099/ijs.0.034306-0

Faramarzi, M. A., Fazeli, M., Yazdi, M. T., Adrangi, S., Ahmadi, K. J. A., Tasharrofi, N., et al. (2009). Optimization of cultural conditions for production of chitinase by a soil isolate of *Massilia timonae*. *Biotechnology* 8, 93–99. doi: 10.3923/biotech.2009.93.99

Feng, G. D., Yang, S. Z., Li, H. P., and Zhu, H. H. (2016). *Massilia putida* sp. nov., a dimethyl disulfide-producing bacterium isolated from wolfram mine tailing. *Int. J. Syst. Evol. Microbiol.* 66, 50–55. doi: 10.1099/ijsem.0.000670

Gallego, V., Sanchez-Porro, C., Garcia, M. T., and Ventosa, A. (2006). *Massilia aurea* sp. nov., isolated from drinking water. *Int. J. Syst. Evol. Microbiol.* 56, 2449–2453. doi: 10.1099/ijs.0.64389-0

Gu, H., Yan, K., You, Q., Chen, Y., Pan, Y., Wang, H., et al. (2021). Soil indigenous microorganisms weaken the synergy of *Massilia* sp. WF1 and *Phanerochaete chrysosporium* in phenanthrene biodegradation. *Sci. Total Environ.* 781:146655. doi: 10.1016/j.scitotenv.2021.146655

Ho, S. T., Ho, Y. N., Lin, C., Hsu, W. C., Lee, H. J., Peng, C. C., et al. (2021). Integrated omics strategy reveals cyclic lipopeptides empedopeptins from *Massilia* sp. YMA4 and their biosynthetic pathway. *Mar. Drugs* 19:209. doi: 10.3390/md19040209

Holochová, P., Mašlaňová, I., Sedláček, I., Švec, P., Králová, S., Kovařovic, V., et al. (2020). Description of *Massilia rubra* sp. nov., *Massilia aquatica* sp. nov., *Massilia mucilaginosa* sp. nov., *Massilia frigida* sp. nov., and one *Massilia* genomospecies isolated from Antarctic streams, lakes and regoliths. *Syst. Appl. Microbiol.* 43:126112. doi: 10.1016/j.syapm.2020.126112

Hrynkiewicz, K., Baum, C., and Leinweber, P. (2010). Density, metabolic activity, and identity of cultivable rhizosphere bacteria on *Salix viminalis* in disturbed arable and landfill soils. *J. Plant Nutr. Soil Sci.* 173, 747–756. doi: 10.1002/jpln.200900286

Hu, S. W., He, R. J., Zeng, J., Zhao, D. Y., Wang, S. R., He, F., et al. (2022). Lower compositional variation and higher network complexity of rhizosphere bacterial community in constructed wetland compared to natural wetland. *Microb. Ecol.* 85, 965–979. doi: 10.1007/s00248-022-02040-6

Hwang, S. H., and Park, J. B. (2014). Comparison of culturable airborne bacteria and related environmental factors at underground subway stations between 2006 and 2013. *Atmos. Environ.* 84, 289–293. doi: 10.1016/j.atmosenv.2013.11.064

Hye, B. J., Woonhee, B., Wenting, R., Su, J. H., Chul, L. S., and Ok, J. C. (2022). *Massilia soli* sp. nov., isolated from soil. *Int. J. Syst. Evol. Microbiol.* 72. doi: 10.1099/ijsem.0.005227

Krishnamoorthy, R., Kim, K., Subramanian, P., Senthilkumar, M., Anandham, R., and Sa, T. (2016). Arbuscular mycorrhizal fungi and associated bacteria isolated from salt-affected soil enhances the tolerance of maize to salinity in coastal reclamation soil. *Agric. Ecosyst. Environ.* 231, 233–239. doi: 10.1016/j.agee.2016.05.037

Kuffner, M., De Maria, S., Puschenreiter, M., Fallmann, K., Wieshammer, G., Gorfer, M., et al. (2010). Culturable bacteria from Zn- and Cd-accumulating *Salix caprea* with differential effects on plant growth and heavy metal availability. *J. Appl. Microbiol.* 108, 1471–1484. doi: 10.1111/j.1365-2672.2010.04670.x

Lang, X. L., Xu, A. L., Wang, Y. H., and Song, Z. W. (2021). Seasonal variation of aerosol fungal community structure in reed constructed wetlands. *Environ. Sci. Pollut. Res. Int.* 29, 19420–19431. doi: 10.1007/s11356-021-17138-6

Lee, H., Kim, D. U., Park, S., Yoon, J. H., and Ka, J. O. (2017). *Massilia chloroacetimidivorans* sp. nov., a chloroacetamide herbicide-degrading bacterium isolated from soil. *Antonie Van Leeuwenhoek* 110, 751–758. doi: 10.1007/s10482-017-0845-3

Liu, F. F., Fan, J., Du, J., Shi, X., Zhang, J., and Shen, Y. (2019). Intensified nitrogen transformation in intermittently aerated constructed wetlands: removal pathways and microbial response mechanism. *Sci. Total Environ.* 650, 2880–2887. doi: 10.1016/j.scitotenv.2018.10.037

Lou, J., Gu, H., Wang, H., An, Q., and Xu, J. (2016). Complete genome sequence of *Massilia* sp. WG5, an efficient phenanthrene-degrading bacterium from soil. *J. Biotechnol.* 218, 49–50. doi: 10.1016/j.jbiotec.2015.11.026

Lu, H. B., Deng, T. C., and Xu, M. Y. (2020). *Massilia aquatica* sp. nov., isolated from a subtropical stream in China. *Curr. Microbiol.* 77, 3185–3191. doi: 10.1007/s00284-020-02104-1

Ma, M. C., Zhou, J., Ongena, M., Liu, W. Z., Wei, D., Zhao, B. S., et al. (2018). Effect of long-term fertilization strategies on bacterial community composition in a 35-year field experiment of Chinese Mollisols. *AMB Express* 8:20. doi: 10.1186/s13568-018-0549-8

Maron, P. A., Mougel, C., Lejon, D. P. H., Carvalho, E., Bizet, K., Marck, G., et al. (2006). Temporal variability of airborne bacterial community structure in an urban area. *Atmos. Environ.* 40, 8074–8080. doi: 10.1016/j.atmosenv.2006.08.047

Olanrewaju, O. S., Ayangbenro, A. S., Glick, B. R., and Babalola, O. O. (2019). Plant health: feedback effect of root exudates-rhizobiome interactions. *Appl. Microbiol. Biotechnol.* 103, 1155–1166. doi: 10.1007/s00253-018-9556-6

Rodriguez-Diaz, M., Cerrone, F., Sanchez-Peinado, M., Santa Cruz-Calvo, L., Pozo, C., and Lopez, J. G. (2014). *Massilia umbonata* sp. nov., able to accumulate poly-beta-hydroxybutyrate, isolated from a sewage sludge compost-soil microcosm. *Int. J. Syst. Evol. Microbiol.* 64, 131–137. doi: 10.1099/ijs.0.049874-0

Scola, B. L., Birtles, R. J., Mallet, M. N., and Raoult, D. (1998). *Massilia timonae* gen. nov., sp. nov., isolated from blood of an immunocompromised patient with cerebellar lesions. *J. Clin. Microbiol.* 36, 2847–2852. doi: 10.1128/JCM.36.10.2847-2852.1998

Son, J., Lee, H., Kim, M., Kim, D. U., and Ka, J. O. (2021). *Massilia aromaticivorans* sp. nov., a BTEX degrading bacterium isolated from Arctic soil. *Curr. Microbiol.* 78, 2143–2150. doi: 10.1007/s00284-021-02379-y

Song, W., Wang, S., Shen, J., and Zhu, B. (2019). Complete genome sequence of *Massilia oculi* sp. nov. CCUG 43427(T) (=DSM 26321(T)), the type strain of *M. oculi*, and comparison with genome sequences of other *Massilia* strains. *Curr. Microbiol.* 76, 1082–1086. doi: 10.1007/s00284-018-1597-7

Stottmeister, U., Wiessner, A., Kuschk, P., Kappelmeyer, U., Kastner, M., Bederski, O., et al. (2003). Effects of plants and microorganisms in constructed wetlands for sewage treatment. *Biotechnol. Adv.* 22, 93–117. doi: 10.1016/j.biotechadv.2003.08.010

Sun, L. N., Yang, E. D., Cui, D. X., Ni, Y. W., Wang, Y. B., Sun, D. D., et al. (2017). *Massilia buxea* sp. nov., isolated from a rock surface. *Int. J. Syst. Evol. Microbiol.* 67, 4390–4396. doi: 10.1099/ijsem.0.002301

Turnbull, A. L., Liu, Y., and Lazarovits, G. (2012). Isolation of Bacteria from the rhizosphere and rhizoplane of potato (*Solanum tuberosum*) grown in two distinct soils using semi selective media and characterization of their biological properties. *Am. J. Potato Res.* 89, 294–305. doi: 10.1007/s12230-012-9253-4

Van Craenenbroeck, A. H., Camps, K., Zachee, P., and Wu, K. L. (2011). *Massilia timonae* infection presenting as generalized lymphadenopathy in a man returning to Belgium from Nigeria. *J. Clin. Microbiol.* 49, 2763–2765. doi: 10.1128/JCM.00160-11

Wang, F., Shi, N., Jiang, R. F., Zhang, F. S., and Feng, G. (2016). In situ stable isotope probing of phosphate-solubilizing bacteria in the hyphosphere. *J. Exp. Bot.* 67, 1689–1701. doi: 10.1093/jxb/erv561

Weon, H. Y., Kim, B. Y., Hong, S. B., Jeon, Y. A., Koo, B. S., Kwon, S. W., et al. (2009). *Massilia niabensis* sp. nov. and *Massilia niastensis* sp. nov., isolated from air samples. *Int. J. Syst. Evol. Microbiol.* 59, 1656–1660. doi: 10.1099/ijs.0.006908-0

Wery, N., Gerike, U., Sharman, A., Chaudhuri, J. B., Hough, D. W., and Danson, M. J. (2003). Use of a packed-column bioreactor for isolation of diverse protease-producing bacteria from antarctic soil. *Appl. Environ. Microbiol.* 69, 1457–1464. doi: 10.1128/AEM.69.3.1457-1464.2003

Wu, H., Wang, X., He, X., Zhang, S., Liang, R., and Shen, J. (2017). Effects of root exudates on denitrifier gene abundance, community structure and activity in a micro-polluted constructed wetland. *Sci. Total Environ.* 598, 697–703. doi: 10.1016/j.scitotenv.2017.04.150

Xu, P., Li, W. J., Tang, S. K., Zhang, Y. Q., Chen, G. Z., Chen, H. H., et al. (2005). *Naxibacter alkalitolerans* gen. nov., sp. nov., a novel member of the family 'Oxalobacteraceae' isolated from China. *Int. J. Syst. Evol. Microbiol.* 55, 1149–1153. doi: 10.1099/ijs.0.63407-0

Zhang, Y. Q., Li, W. J., Zhang, K. Y., Tian, X. P., Jiang, Y., Xu, L. H., et al. (2006). *Massilia dura* sp. nov., *Massilia albidiflava* sp. nov., *Massilia plicata* sp. nov. and *Massilia lutea* sp. nov., isolated from soils in China. *Int. J. Syst. Evol. Microbiol.* 56, 459–463. doi: 10.1099/ijs.0.64083-0

Zhang, L., Lv, W., Li, S., Geng, Z., and Yao, H. (2019). Nitrogen removal characteristics and comparison of the microbial community structure in different anaerobic Ammonia oxidation reactors. *Water* 11:230. doi: 10.3390/w11020230

Zheng, B. X., Bi, Q. F., Hao, X. L., Zhou, G. W., and Yang, X. R. (2017). *Massilia phosphatilytica* sp. nov., a phosphate solubilizing bacteria isolated from a long-term fertilized soil. *Int. J. Syst. Evol. Microbiol.* 67, 2514–2519. doi: 10.1099/ijsem.0.001916

Zul, D., Wanner, G., and Overmann, J. (2008). *Massilia brevitalea* sp. nov., a novel betaproteobacterium isolated from lysimeter soil. *Int. J. Syst. Evol. Microbiol.* 58, 1245–1251. doi: 10.1099/ijs.0.65473-0

frontiers | Frontiers in Microbiology

TYPE Original Research
PUBLISHED 20 September 2023
DOI 10.3389/fmicb.2023.1250330

OPEN ACCESS

EDITED BY
Ruiyong Zhang,
Chinese Academy of Sciences (CAS), China

REVIEWED BY
Santosh Kumar,
University of Wisconsin-Madison, United States
Hongchang Liu,
Central South University, China

*CORRESPONDENCE
Jianqun Lin
✉ jianqunlin@sdu.edu.cn
Xin Pang
✉ pangxin@sdu.edu.cn

†These authors have contributed equally to this work

RECEIVED 30 June 2023
ACCEPTED 09 August 2023
PUBLISHED 20 September 2023

CITATION
Shi Y, Wu W, Yang Y, Liu X, Lin J, Liu X, Lin J and Pang X (2023) Gene knockout of glutathione reductase results in increased sensitivity to heavy metals in *Acidithiobacillus caldus*. *Front. Microbiol.* 14:1250330. doi: 10.3389/fmicb.2023.1250330

Gene knockout of glutathione reductase results in increased sensitivity to heavy metals in *Acidithiobacillus caldus*

Yuping Shi†, Wei Wu†, Yinghui Yang, Xiao Liu, Jianqiang Lin, Xiangmei Liu, Jianqun Lin* and Xin Pang*

State Key Laboratory of Microbial Technology, Shandong University, Qingdao, China

Acidithiobacillus caldus plays an important role in bioleaching of low-grade metal ore. It can promote the release of heavy metals in mining-associated habitats and survive in high concentrations of heavy metals. Functions of glutathione reductase (GR) in cell defense against reactive oxygen species caused by heavy metals have been elucidated in some eukaryotic cells and bacteria; however, no information is available in *A. caldus*. In this research, the methods of bioinformatics, gene expression, GR activity assays were used to detect and characterize the glutathione reductase gene from the *A. caldus* MTH-04 strain. Then, *A. caldus gr* knockout mutant and *gr* overexpression strain were constructed, and the heavy metal tolerant properties and transcriptional levels of ROS related genes of them were compared to study the function of GR. The results showed that, a putative *gr* gene F0726_RS04210 was detected in the genome of *A. caldus* MTH-04. The purified recombinant protein of F0726_RS04210 showed remarkable GR activity at optimal pH 7.0 and 30°C using *in vitro* assay. The evolutionary relationship of GR from *A. caldus* MTH-04 was close to that from *Escherichia coli* K12. Gene knockout or overexpression of *gr* in *A. caldus* did not affect the growth rate on S^0 medium, suggesting that GR did not play a key role in the activation of sulfur. Deletion of *gr* resulted in increased sensitivity to heavy metals (Cu^{2+} and Zn^{2+}) in *A. caldus*, and the *gr* overexpression strain showed enhanced tolerance to heavy metals. Furthermore, transcription analysis also revealed strong correlations between GR and the antioxidant pathway. The above results suggest that GR can play an important role in heavy metal tolerance in *A. caldus*.

KEYWORDS

glutathione reductase, *Acidithiobacillus caldus*, heavy metal tolerance, bioleaching, antioxidation

1. Introduction

At present, many polymetallic ores, such as zinc ore and copper ore, are sulfide minerals, which complicate the production of high-grade metal ores and increase the production cost. *Acidithiobacillus caldus* is an important acidophilic, chemolithoautotrophic sulfur-oxidizing bacterium that is widely used in the bioleaching industry. It can obtain energy and reduce power to achieve autotrophic growth by sulfur oxidation (Hallberg and Lindström, 1994, 1996; Kamimura et al., 1999; Edwards et al., 2000; Okibe et al., 2003). *Acidithiobacillus caldus* can play an important role in processing low-grade concentrates

of non-ferrous metals. During the bioleaching process, the released heavy metals are toxic to the leaching microorganisms, and the stress tolerance process of the microorganisms will result in the production of reactive oxygen species (ROS) inside the cells (Stadtman and Oliver, 1991; Natarajan et al., 1994). In eukaryotic cells, ROS can be scavenged using the glutathione system, including glutathione (GSH), glutathione S-transferases (GST), glutathione synthetase (GS), and glutathione reductase (GR) (Foyer et al., 1991). However, limited studies have been conducted on *A. caldus* (Dopson et al., 2003; Luo et al., 2008).

GSH, which is widely found in bacteria and eukaryotic cells (Meister and Anderson, 1983; Smith et al., 1990), can protect cells from ROS by providing reducing equivalents for antioxidant defense enzymes or scavenging hydroxyl radicals directly (Noctor and Foyer, 1998). GR can catalyze the conversion of glutathione disulfide (GSSG) to GSH (Scruton et al., 1990; Rice-Evans et al., 1996). By keeping high GSH/GSSG ratios, GR plays a key role in cell defense against ROS (Schirmer et al., 1989; Creissen et al., 1994; Mullineaux and Creissen, 1997). Recently, the glutathione system was reported to participate in the heavy metal tolerance of *Acidithiobacillus ferrooxidans* (Xia et al., 2011; Zheng et al., 2015, 2016); however, the heavy metal tolerance mechanisms of *A. caldus* are poorly understood compared with that of *A. ferrooxidans*.

In this research, we characterized a glutathione reductase gene from *A. caldus* MTH-04 using the methods of bioinformatic, gene expression, and GR activity assays. Then, we reported the construction of a *gr* knockout mutant and a *gr* overexpression strain of *A. caldus* MTH-04. Finally, we compared the heavy metal tolerance properties of the *A. caldus* mutants with its wild type and discussed the potential role of *gr* gene in heavy metal tolerance in *A. caldus* MTH-04.

2. Materials and methods

2.1. Bacterial strains, plasmids, media and growth conditions

The bacterial strains and plasmids used in this study are presented in Table 1. The strains of *A. caldus* were cultured at 40°C shaken at 150 rpm in liquid Starkey-S^0 medium (pH 2.5) or on solid Starkey-$Na_2S_2O_3$ medium (pH 4.8) (Jin et al., 1992). The liquid Starkey medium contained S^0 (8 g/L, boiling sterilized) as the energy source. Kanamycin (200 μg/ml), streptomycin (200 μg/ml), or chloromycetin (68 μg/ml) was used in liquid Starkey-S^0 when required, and kanamycin (80 μg/ml), streptomycin (80 μg/ml), or chloromycetin (27.2 μg/ml) was used in the solid Starkey-$Na_2S_2O_3$ medium for selection. *Escherichia coli* strains were grown at 37°C shaken at 170 rpm in liquid Luria–Bertani (LB) broth or on solid LB

TABLE 1 Bacterial strains and plasmids used in this study.

Strain or plasmid	Genotype or description	Source or reference
Strains		
Acidithiobacillus caldus		
MTH-04	Wild type strain	Liu et al., 2004
Δ*gr*	MTH-04, ΔF0726_RS04210	This study
Escherichia coli		
JM109	*recA1 endA1 gyrA96 thi-1 hsdR17supE44 relA1*Δ*(lac-proAB)*/F' [traD36proAB + lacIqlacZΔM15]	TaKaRa
BL21(DE3)	F^- *dcm ompThsdS*($r_B^- m_B^-$) *gal*λ(DE3)	Novagen
SM10	Km^r *thi-1 thr leu tonA acy supE rec*ARP4-2-Tc::Mu	Simon et al., 1983
Plasmids		
pET28a	Km^r	Novagen
pUC19	Ap^r, ColE1 replicon, cloning vector	TaKaRa
pET28a-*gr*	pET28a containing F0726_RS04210	This study
pSDUDI	Ap^r Km^r, $oriT_{RP4}$, ColE1 replicon	Wang et al., 2016
pSDUDI-*gr*	pSDUDI carrying both homologous fragments of F0726_RS04210	This study
pSDU1-I-Sce I	pSDU1 containing the I-Sce I gene	Wang et al., 2016
pJRD215	Kmr; Smr; IncQ replicon; mob^+	Davison et al., 1987
pJRD215-tac-*cup*	pJRD215 containing *cup*	Cui, 2011
pJRD215-*tac-gr*	pJRD215 containing F0726_RS04210	This study

medium, and ampicillin (100 μg/ml), kanamycin (100 μg/ml), streptomycin (100 μg/ml), or chloromycetin (34 μg/ml) was added when required.

2.2. Bioinformatics

NCBI BLASTP (http://blast.ncbi.nlm.nih.gov/Blast.cgi) was used to search for GR homolog in the sequenced genome of *A. caldus* MTH-04 (CGMCC 1.15711). The protein molecular masses of the homologous proteins and the isoelectric points (pI) were predicted by using an ExPASy Compute pI/Mw tool (http://web.expasy.org/compute_pi/). ClustalX version 1.81 was used to perform the multiple sequence alignment. The phylogenetic tree was constructed by ClustalX version 1.81 and MEGA version 5, with a *p*-distance distribution, pairwise deletion, and bootstrap analysis of 10,000 repeats. Subcellular localization of protein was predicted using SignalP 4.1 (http://www.cbs.dtu.dk/services/SignalP/), Softberry ProtCompB tool (http://linux1.softberry.com/berry.phtml?topic=pcompb&group=programs&subgroup=proloc), and PSORTB v3.0 (http://www.psort.org/psortb/).

2.3. Genetic manipulations

General molecular biological techniques, including restriction enzyme digestion, ligation, gel electrophoresis, and transformation of the plasmids, were conducted according to the standard protocols (Sambrook and Russell, 2001). The genomic DNA of *A. caldus* was isolated using the TIANamp Bacteria DNA Kit of TIANGEN. Plasmids were isolated using the TIANprep Mini Plasmid Kit of TIANGEN. DNA fragments were recovered from agarose gels using the OMEGA E.Z.N.A.® Gel Extraction Kit of Omega Bio-Tek. DNA polymerase, restriction enzymes, and T4 DNA ligase were purchased from TaKaRa, and primers were generated by Invitrogen.

2.4. Expression and purification of GR

The strains and plasmids used to clone the potential GR gene are presented in Table 1, and the primers are presented in Table 2. To express and purify the recombinant protein of F0726_RS04210, the coding sequence was amplified using primers F-*gr* and R-*gr*. The fragment was digested by *Nde*I and *Xho*I and inserted into *Nde*I-*Xho*I-treated pET28a, to generate recombinant plasmid pET28a-*gr*. Successful insertion of the coding sequences of target genes was confirmed by sequencing; then, the recombinant plasmids were transformed into *E. coli* BL21(DE3) cells. Isopropyl-β-D-thiogalactopyranoside (IPTG) was added to the final concentration of 0.4 mM to induce the expression of recombinant protein at 25°C for at least 5 h. Recombinant proteins were analyzed using 10% SDS-PAGE and purified using HisTrap™ HP Crude Columns (GE Health) and AmiconUltra-15 Centrifugal Filter Units with Ultracel-3 membranes (Merck Millipore). Finally, the protein concentrations were determined using a Pierce® BCA Protein Assay Kit.

TABLE 2 Primers used in this study.

Primer	Sequence(5′-3′)
F-*gr*	GGAATTCCATATGTCCCATCACCACGAATTT
R-*gr*	CCGCTCGAGCTAGCGCATGGTGACGAAC
*gr*UF	ACGCGTCGACGCATTGTTGGCATCATTGGC
*gr*UR	GCTCTAGATGGCTTGCTTGAAGAGGGA
*gr*DF	GCTCTAGACATCGTTGACGGAGATACAGAG
*gr*DR	CCCAAGCTTCGACATGGACTCGACCCTACT
oriTF	CCGCCTTTTCCTCAATCGCTCTTC
oriTR	GCATCGTCTCTCGCCTGTCCC
*gr*IF	CGGGACCGCTGACTTT
*gr*IR	GGTGAGCCAACTCCTCTTG
*gr*OF	GTGGAGGTGGATTATGTGGGTCT
*gr*OR	GAGGAGAACGCCATGAGCAGTA
O-F	CCGGAATTCATGTCCCATCACCACGAATTTGACT
O-R	CGCGGATCCCTCAGTGATGATGATGATGATGCTAGCGCATGGTGACGAC

2.5. GR activity assays

GR can catalyze the reaction as follows: $NADPH + H^+ + GSSG \rightarrow NADP^+ + 2GSH$, and the oxidation of NADPH can be measured by the decrease in absorbance at 340 nm ($\varepsilon = 6.22 \times 10^3 M^{-1} \cdot cm^{-1}$). Purified GR was used in GR activity measurement using the method reported by Greer with minor modifications (Greer and Perham, 1986). In brief, the assay mixture (200 μl) contained 0.1 mM NADPH, 1.2 mM GSSG, and an appropriate amount of purified GR in 1 mM phosphate buffer (pH 7.0) at room temperature. Values of absorbance at 340 nm were recorded every 1 min and continued for at least 5 min. The reaction was started by the addition of NADPH. All reactions were performed with three independent biological replicates. Heat inactivated purified GR was used as the control for each reaction. Specific GR activity was measured as units of GR activities per mg of purified GR protein. Moreover, 1 unit of GR activity is defined as that can reduce 1 μmol of GSSG in 1 min at room temperature.

2.6. pH and temperature dependence

The effects of pH and temperature on GR activity were determined using the method described above. The optimum pH of GR was determined using purified GR in 1 mM citrate buffer solution (pH 3–5), 1 mM phosphate buffer solution (pH 6–8), or 1 mM Tris–HCl buffer solution (pH 9–10), respectively. The purified GR was incubated in the above buffers for 60 min at

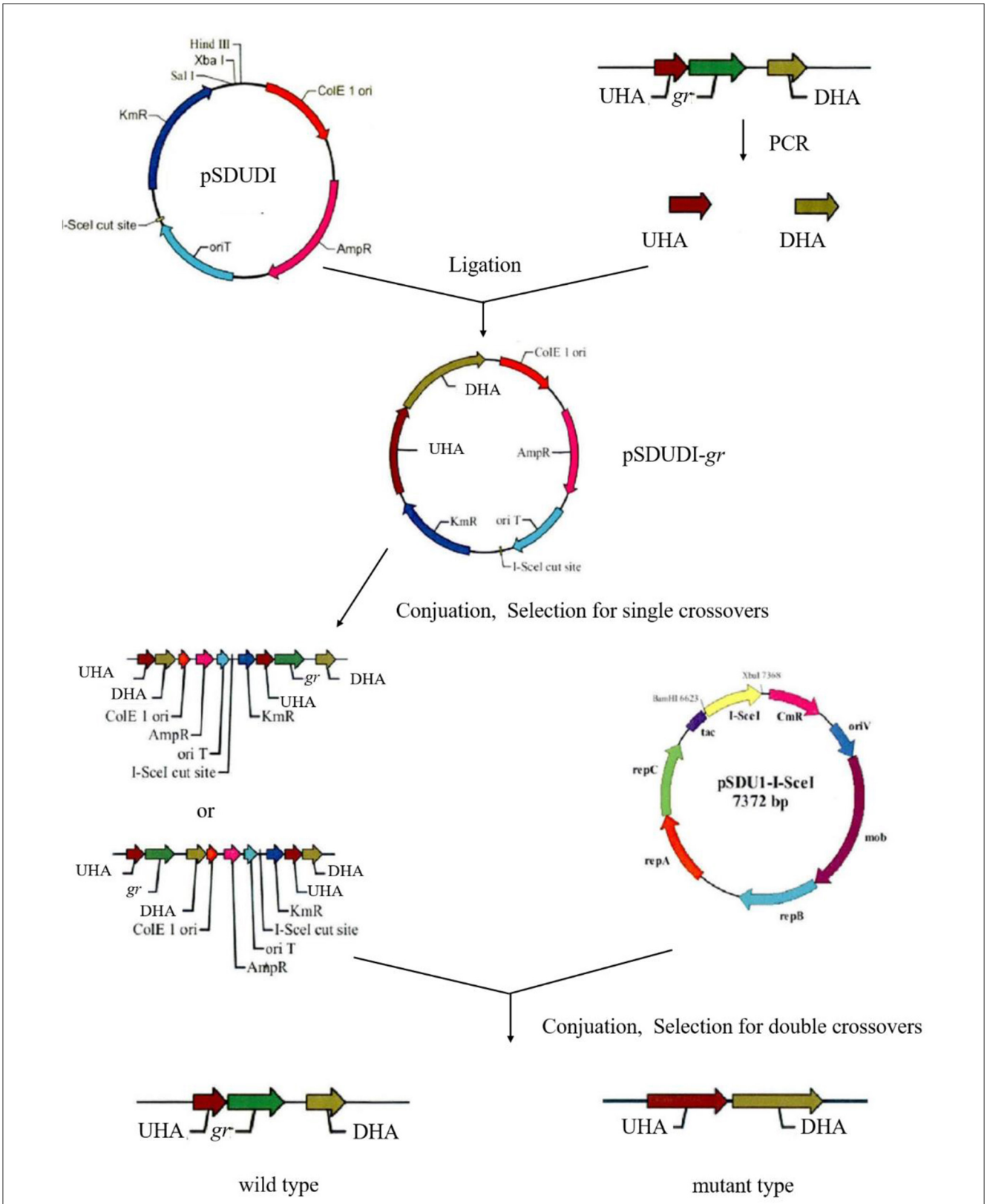

FIGURE 1
Construction process of the *A. caldus* knockout strain. UHA represents the upstream homologous arm, and DHA represents the downstream homologous arm, respectively.

room temperature before measuring the activity at various pH conditions. The optimum temperature of GR was measured using purified GR within the range of 20–50°C at pH 7.0. The purified GR was incubated at the same temperature for 60 min before the activity measurement at each temperature.

TABLE 3 Primers used qPCR in this study.

Primer	Sequence (5′-3′)
00165F	GACCACCCTTGGCTACCTG
00165R	TGCTGGGCAAAGGGTAGG
02000F	CTTGTCCTACTTCTACGGGTGC
02000R	GCGTGAATGTGGGTGTCG
02905F	GCAATACGGTGGTCGTCTCC
02905R	CGGGCAATGCTCTTGGTCAG
04210F	GACACGGACCCGATGTTC
04210R	GCAGTTATGCGCTGTATGG
04255F	GACGCGACCCGTGAACT
04255R	GGTGACCGCCTGACGATAGA
04480F	TGCTGATGCGTAAGGACC
04480R	TGCTCGCCCAAGAAGG
10185F	ATGGAGCAGCGGCACAG
10185R	GGCAAATCCCAGGAGAAACT
12050F	GATCCAGCCCGACCACTT
12050R	TTCAGCGACACCTCCCAC
13530F	ACCTGCTACGGTCGCTATGC
13530R	TATGGCGGGTGCTATCTTCT
*ala*SF	GACACCGACCTCTTCCAACC
*ala*SR	ACATAGCCACGCCGTTCATT

2.7. Inhibition studies

The effect of metal ions (Cu^{2+}, Zn^{2+}, Cd^{2+}, Ag^{+}, Fe^{2+}, Co^{2+}, Mg^{2+}, Sn^{2+}, and Mn^{2+}) on GR activity was determined by measuring its specific activity in the presence of 0.5 mM, 1 mM, or 1.5 mM of each reagent. The purified GR was incubated in the above reagent for 60 min before the GR activity measurement. The *p*-value was calculated using a *t*-test.

2.8. Generation of the markerless *gr* knockout mutant of *A. caldus*

Markerless *gr* knockout mutant was generated as described previously with minor modifications (as shown in Figure 1) (Wang et al., 2016). The plasmids used in generating markerless *gr* knockout mutants are presented in Table 1, and the primers are presented in Table 2.

The upstream and downstream homologous arms of *gr* were amplified by PCR using primer pairs of *gr*UF/*gr*UR [819 bp upstream homologous arm (UHA)] and *gr*DF/*gr*DR [933 bp downstream homologous arm (DHA)]. The amplified sequences were inserted into the suicide vector pSDUDI after digestion with appropriate restriction enzymes. The sequences of the resulting plasmids pSDUDI-*gr* were confirmed by sequencing.

The suicide vector pSDUDI-*gr* was transformed into *E. coli* SM10, and the generated transformant was used as the donor. *Acidithiobacillus caldus* MTH-04 was used as the recipient to construct Δ*gr*. Plasmid pSDUDI-*gr* was transferred from *E. coli* SM10 to *A. caldus* by conjugation, as described earlier (Wu et al., 2017). Colonies on selective Starkey-$Na_2S_2O_3$ plates containing kanamycin were selected and analyzed using colony PCR. Primer pairs oriTF/oriTR were used to detect the single crossover of Δ*gr*, where a fragment of 465 bp was expected in the case of a single crossover, and no fragment was expected in wild type or Δ*gr*. Colonies with the correct PCR fragments were inoculated into a liquid Starkey-S^0 medium, and the genomic DNA of each

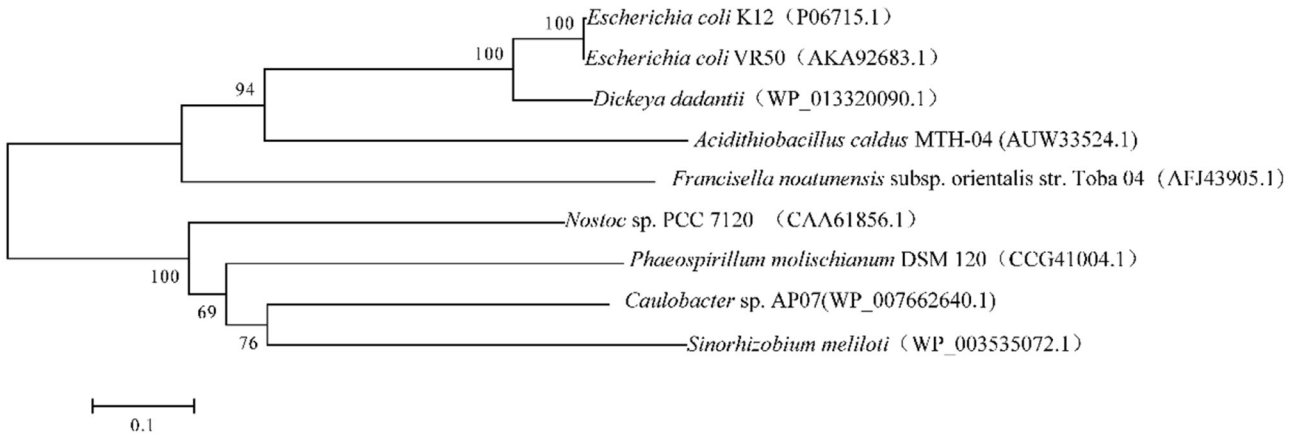

FIGURE 2
Neighbor-joining tree of GRs from eukaryotic and prokaryotic species. GenBank accession numbers are presented in parentheses.

10.3389/fmicb.2023.1250330

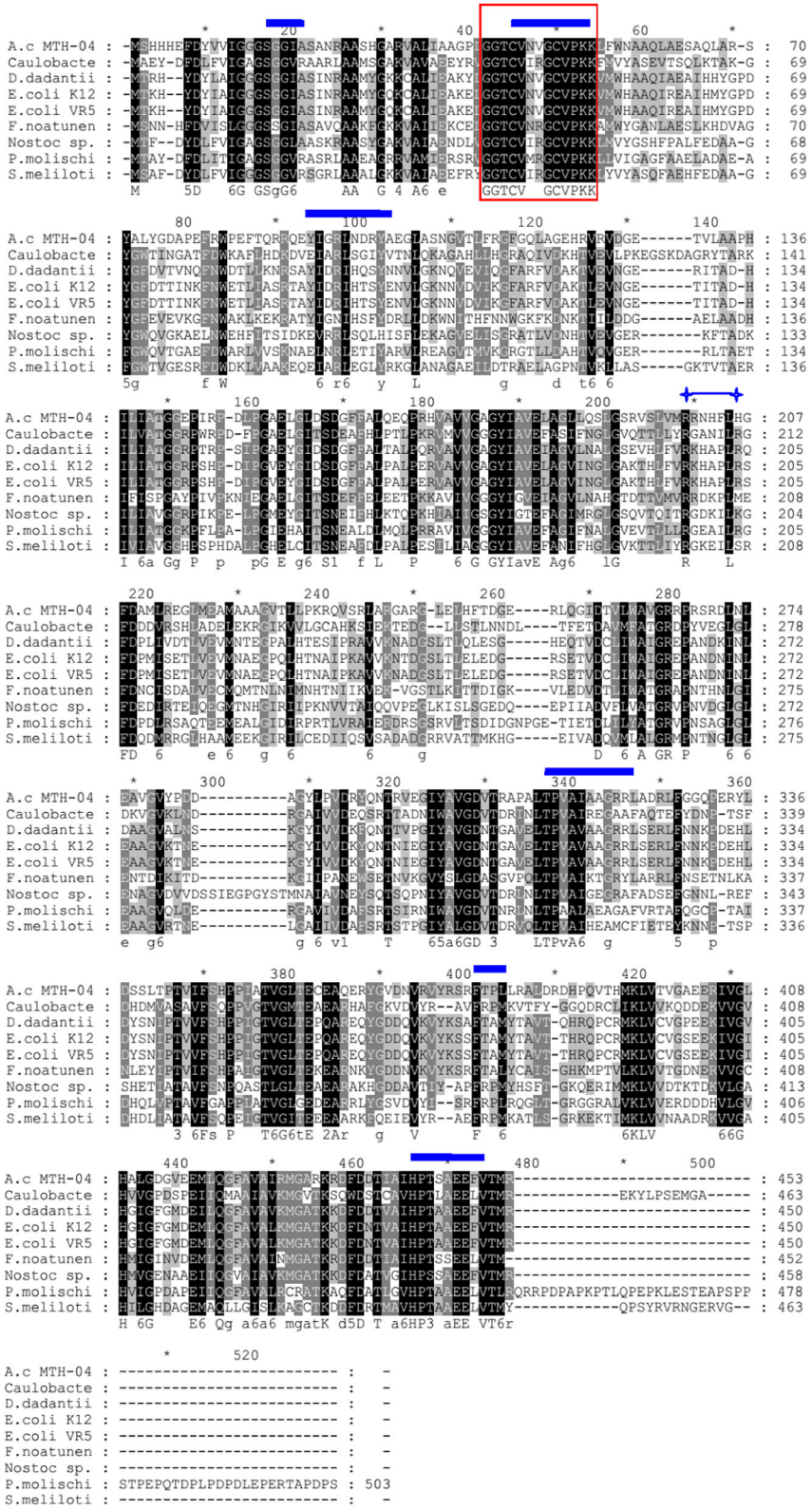

FIGURE 3
Sequence alignment of protein sequences homologous to GR. The protein encoded by F0726_RS04210 from *Acidithiobacillus caldus* MTH-04 is abbreviated to *A.c* MTH-04 (AUW33524.1). The GRs from *Caulobacter* sp. AP07, *Dickeya dadantii, Escherichia coli* K12, *Escherichia coli* VR50, *Francisella noatunensis* subsp. *orientalis* str. Toba 04, *Nostoc* sp. PCC 7120, *Phaeospirillum molischianum* DSM 120, and *Sinorhizobium meliloti* are abbreviated to Caulobacter (WP_007662640.1), *D. dadantii* (WP_013320090.1), *E. coli* K12 (P06715.1), *E. coli* VR50 (AKA92683.1), *F. noatunensis* (AFJ43905.1), *Nostoc* sp. (CAA61856.1), *P. molischianum* (CCG41004.1), and *S. meliloti* (WP_003535072.1), respectively. Identical amino acid residues are highlighted in black. The box indicates the redox-active disulfide bond domain (CXXXXC), the glutathione-binding residues are marked with ▬, and the conserved arginine residues required for NADP binding are indicated by ✦—✦, respectively. The symbol * indicates the position of a multiple of 10.

selected colony was isolated for PCR analysis to confirm the single-recombination event. Primer pairs *gr*IF/*gr*IR were used to confirm the single crossover of Δ*gr*, where both fragments of 3,088 bp and 1,054 bp were expected in the case of a single crossover.

Plasmid pSDU1-I-Sce I was then transferred to the single crossover cells of *A. caldus* to induce a second homologous recombination, thereby generating the knockout mutants or wild type individuals. The Δ*gr* strain was identified using colony PCR based on screening colonies grown on selective Starkey-$Na_2S_2O_3$ plate containing chloromycetin using primer pairs *gr*IF/*gr*IR, as described above. A 1,054 bp fragment was expected in the Δ*gr* strain, and a 3,088 bp fragment was expected for wild type cells. Primer pairs oriTF/oriTR, *gr*IF/*gr*IR, and *gr*OF/*gr*OR were used to confirm the deletion of *gr*. For the primer pairs *gr*OF/*gr*OR, a 2,963 bp fragment was expected in *gr* knockout mutant, and a 4,325 bp fragment was expected in the wild type cells. The amplified fragment from *gr* knockout mutant using primer pairs *gr*OF/*gr*OR was sequenced to confirm the mutants.

The pSDU1-I-Sce I plasmid in mutant cells was eliminated by spontaneous loss, as described earlier (Wu et al., 2017).

2.9. Southern blot analysis of *gr* gene knockout mutant of *A. caldus*

A Southern blot analysis was performed, as described earlier (Wen et al., 2014), using Sac I digests of the genomic DNA of the Δ*gr* mutant and wild type of *A. caldus*. The downstream homologous arm of *gr* gene was labeled with digoxigenin and used as the probe.

2.10. Construction of *A. caldus gr* overexpression strain

The strains and plasmids used to construct the *gr* gene overexpression strain of *A. caldus* are presented in Table 1, and the primers are presented in Table 2. The coding sequence of *gr* along with its SD sequence was amplified using primer pairs O-F/O-R. The amplified fragment was first cloned into plasmid pUC19 for sequencing, after digestion with *Bam*H I and *Eco*R I. The fragment pJRD215-tac was obtained from plasmid pJRD215-tac-*cup* after digestion with *Bam*H I and *Eco*R I. Then, the confirmed *gr*-coding sequence was obtained from its sequenced recombinant plasmid by digestion with *Bam*H I and *Eco*R I and ligated with pJRD215-tac to produce pJRD215-tac-*gr*. Plasmid pJRD215-tac-*gr* and the control plasmid pJRD215 were transformed into *E. coli* SM10. The plasmids were then transformed into *A. caldus* MTH-04 through conjugation as described earlier (Wu et al., 2017).

2.11. Heavy metal tolerance assays

The *A. caldus* MTH-04 wild type, Δ*gr*, control strain (wild type carrying plasmid pJRD215), and *gr* overexpression strain (wild type carrying plasmid pJRD215-tac-*gr*) were grown in the Starkey-S^0 medium. All the strains were grown in the Starkey-S^0 medium for 7 days, and then the cells were collected by centrifugation and adjusted to the same cell concentration (OD_{600} = 20.0). An aliquot (150 μl) of the treated cells was inoculated into 150 ml of fresh Starkey-S^0 medium, added with different amounts of $CuSO_4$ with the final concentrations of 0 mM, 5 mM, 10 mM, and 20 mM or different amounts of $ZnSO_4$ with the final concentrations of 0 mM, 40 mM, 80 mM, and 160 mM, respectively, cultivated at 40°C, and shaken at 150 rpm. After low-speed centrifugation at 400 × *g* for 5 min to remove the solid sulfur (Wang et al., 2016), the growth of *A. caldus* cultured in different concentrations of $CuSO_4$ or $ZnSO_4$ was monitored by measuring the optical density at 460 or 600 nm, respectively. All measurements were performed in triplicate, and error bars correspond to the standard deviations.

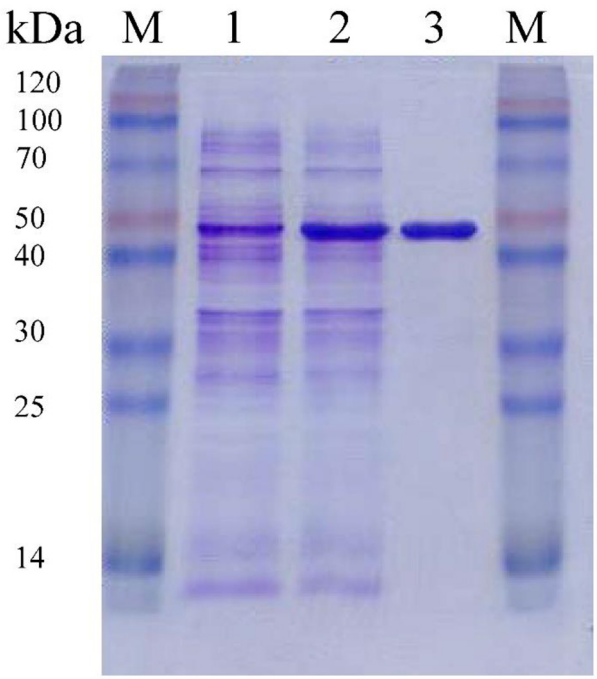

FIGURE 4
Purification of recombinant F0726_RS04210 from *E. coli* BL21(DE3). The proteins are loaded on 10% (wt/vol) SDS-PAGE gel and stained with Coomassie Brilliant Blue R-250. The protein extract of *E. coli* BL21(DE3) cells containing pET28a-*gr* without induction (1), induced with IPTG (2) and the purified recombinant F0726_RS04210 protein (3), is indicated, respectively. M: Blue Plus™ II Protein Marker (TransGen Biotech).

2.12. RNA extraction and RT-qPCR

Wild type, Δ*gr*, the control strain (wild type carrying plasmid pJRD215) and the *gr* overexpression strain (wild type carrying plasmid pJRD215-tac-*gr*) of *A. caldus* were grown for 7 days in Starkey-S^0 medium without heavy metals and used to measure the transcriptional levels of the glutathione-related genes. The cells were first collected

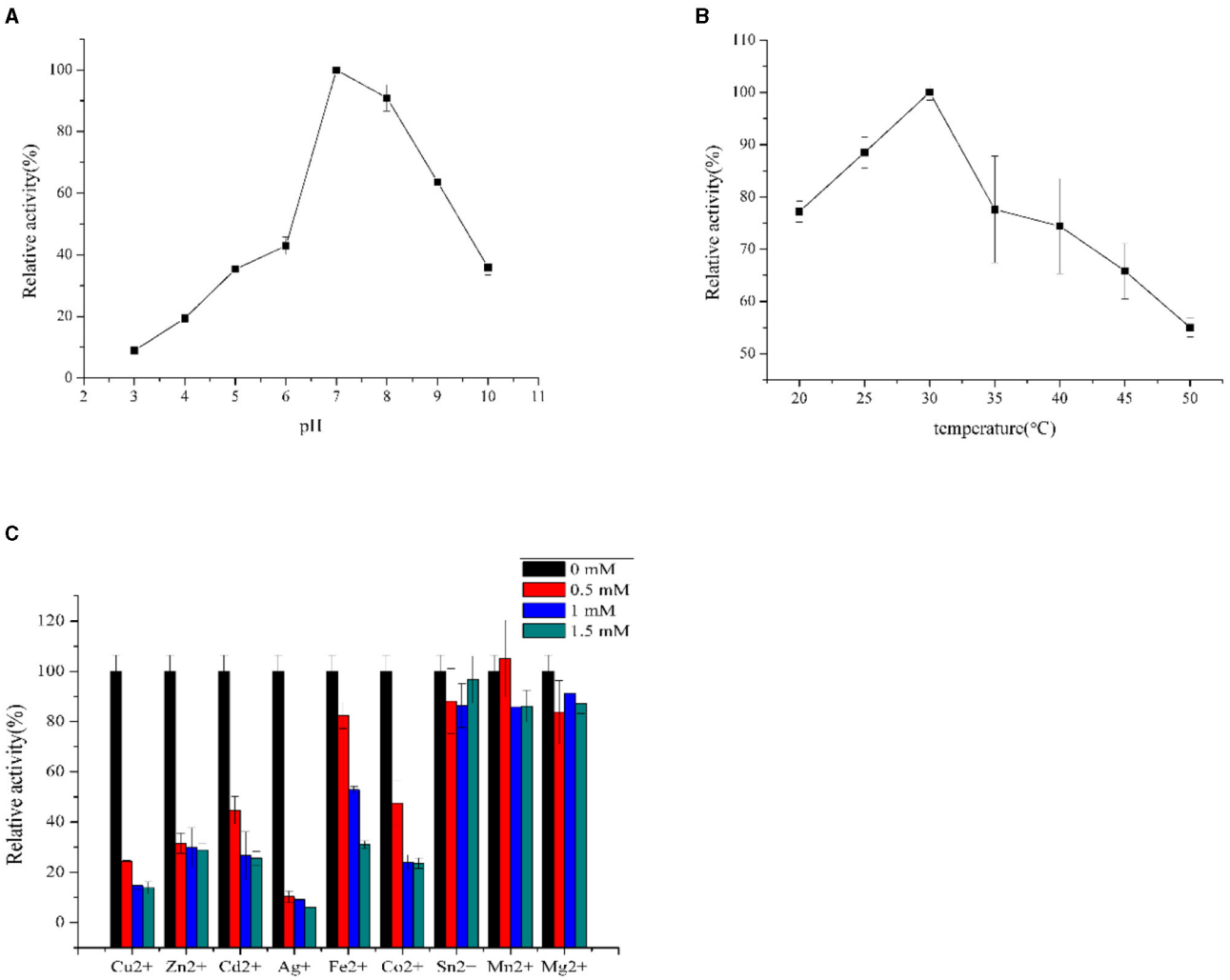

FIGURE 5
Influence of pH **(A)**, temperature **(B)**, and inhibitors **(C)** on GR activities of purified recombinant F0726_RS04210.

by centrifugation at 12,000 × *g* for 5 min, resuspended in RNA*later*® Solution (Ambion), and harvested from the RNA*later*® suspension by centrifugation after overnight storage at 4°C.

To study the responses of the glutathione-related genes to the heavy metal stress at different time points, above *A. caldus* strains grown for 7 days without heavy metals were supplemented with $CuSO_4$ (final concentration: 5 mM) or $ZnSO_4$ (final concentration: 40 mM), respectively, incubated at 40°C and shaken at 150 rpm. Cells were collected at two time intervals (1 h and 2 h) and treated as described above.

Overall, 100 μl of lysis buffer (1 mg/ml lysozyme, 10 mM Tris, and 1 mM EDTA, pH 8.0) was used to resuspend the cells and then incubated at 26°C for 6 min. TRIzol® Reagent (Ambion) was used to extract total RNA following the manufacturer's instruction. Denaturing formaldehyde agarose gel electrophoresis was used to examine RNA quality, and a NanoDrop-1000 spectrophotometer (NanoDrop Technologies) was used to determine the concentration of RNA. A PrimeScript™ RT Reagent Kit with gDNA Eraser (Perfect Real Time; TAKARA) was used to remove the genomic DNA and synthesize the cDNA.

RT-qPCR was performed with the LightCycler® 480 system (Roche), following the manufacturer's instruction with SYBR® Premix Ex Taq (TaKaRa). In this study, all RT-qPCR reactions were performed in triplicate with at least three independent biological replicates. All primers used for RT-qPCR are presented in Table 3. Gene *alaS* was used for normalization, and transcriptional results were calculated and shown in $2^{-\Delta\Delta CT}$ (Livaka and Schmittgenb, 2001; Wu et al., 2017). The *p*-value was calculated using a *t*-test. The relative mRNA levels of these genes were measured using the *gr* knockout strain with the wild type as the control or using the gr overexpression strain with the wild type carrying vacant pJRD215 plasmid as the control. Fold change ≥ 2 and *p*-value ≤ 0.05 were considered to be upregulated, while fold change ≤ 0.5 and *p*-value ≤ 0.05 were considered to be downregulated.

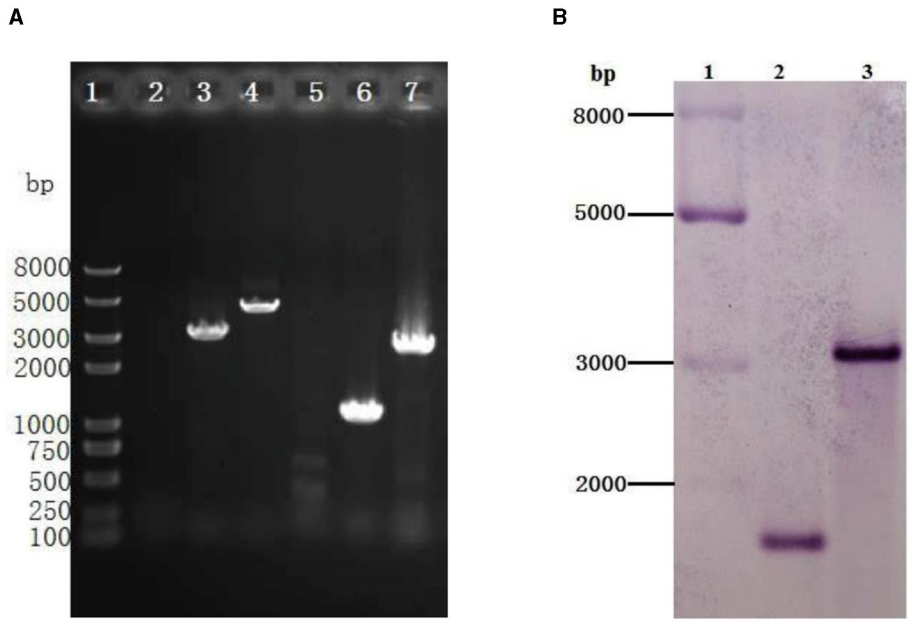

FIGURE 6
Identification of the *gr* knockout mutant of *Acidithiobacillus caldus* MTH-04 using PCR **(A)** and Southern blot hybridization **(B)**. **(A)** Specific primer pairs oriTF/oriTR (2, 5), *gr*IF/*gr*IR (3, 6), and *gr*OF/*gr*OR (4, 7) were used to detect the presence of corresponding sequence on genomic DNA of *A. caldus* MTH-04 wild type (2, 3, 4) and Δ*gr* (5, 6, 7). The numbers on the left indicate the sizes of the fragments based on the molecular size marker (lane 1). **(B)** Line 2: Sac I-digested genomic DNA from Δ*gr*, line 3: Sac I-digested genomic DNA from wild type. The molecular size marker was loaded on the left lane, and the sizes of its fragments are indicated (lane 1).

3. Results

3.1. Identification of *gr* gene in *A. caldus* MTH-04

We found a putative glutathione reductase encoding gene F0726_RS04210 in the genome of *A. caldus* MTH-04 by conducting an online BLASTN search. The ORF of F0726_RS04210 encoades a 453 amino acid glutathione disulfide reductase with a theoretical isoelectric point of 6.58 and molecular mass of 49.2 kDa. F0726_RS04210 shareas sequence identity with known GRs. These include *Dickeya dadantii* (53% identity), *E. coli* K12 (54% identity), *E. coli* VRa50 (53% identity), *Francisella noatunensis* subsp. *orientalis* str. Toba 04 (45% identity), *Nostoc* sp. PCC 7120 (40% idaentity), *Phaeospirillum molischianum* DSM 120 (41% identity), *Caulobacter* sp. AP07 (38% identity), and *Sinorhizobaium meliloti* (38% identity), respectively. An unrooted phylogenetic tree was constructed with F0726_RS04210 and the above mentioned GRs to better uanderstand the relationship between the reported GRs and the putative GR detected in *A. caldus* MTH-04. The evolutionary relationship of F0726_RS04210 is close to the glutathione reductase from *E. coli* K12, one of the best-understood GR, with a high identitay (54%; Figure 2). By alignment with known GRs, F0726_RS04210 has the highly conserved functional motifs characterized for GR, indicating the close relationship among GRs (Figure 3).

F0726_RS04210 was then expressed and purified from *E. coli* BL21(DE3) (Figure 4). We observed the GR activity of recombinant protein F0726_RS04210 *in vitro*. The GR activity of F0726_RS04210 was 415.8 U/mg, which was similar to that from *E. coli* (Nigel et al., 1987). Based on the activity we detected in the *in vitro* assays, we designated F0726_RS04210 as glutathione reductase. The optimum pH for the GR was 7.0 (Figure 5A), and the optimum temperature was 30°C (Figure 5B). The effect of metal ions on GR activity was also studied. Cu^{2+}, Zn^{2+}, Cd^{2+}, Ag^{+}, Fe^{2+}, and Co^{2+} were found to strongly inhibit the activity of GR ($P < 0.05$), while GR activity was not obviously affected by Mg^{2+}, Mn^{2+}, and Sn^{2+} (Figure 5C). Similar phenomena were also reported in rainbow trout liver, *E. coli*, *Phaeodactylum tricornutum*, and *Spinacia oleracea* L. Leaves (Asnis, 1955; Michail and James, 1977; Diego et al., 2010; Ekinci and Sentürk, 2013).

In addition, the predicted subcellular localization of GR was analyzed using ProtCompB, SignalP 4.1, and PSORTB v3.0, and no signal peptide or transmembrane region was found, suggesting that it may be cytoplasmic protein, which is consistent with the neutral optimum pH of GR.

3.2. Construction and characterization of *gr* knockout mutant and *gr* overexpression strain of *A. caldus* MTH-04

To better understand the function of GR in *A. caldus*, we used a markerless gene knockout system to generate *gr* knockout mutant Δ*gr* (as shown in Figure 1). We identified

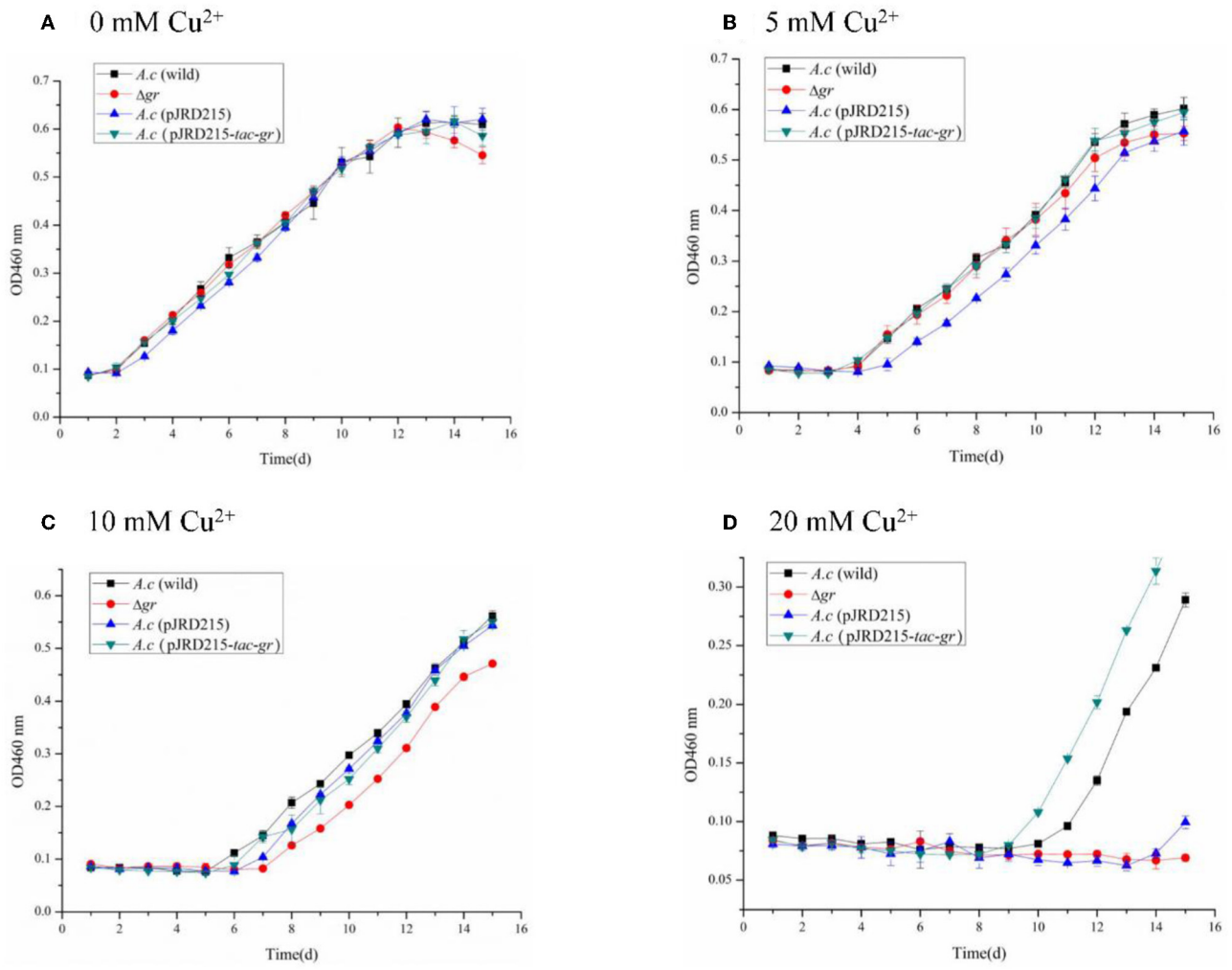

FIGURE 7
Growth curves of the *Acidithiobacillus caldus* MTH-04 wild type, *gr* knockout mutant, *gr* overexpression strain, and control strain (wild type carrying pJRD215) grown in S^0 medium under copper stress. *A. caldus* (wild) represents the wild type, Δ*gr* represents the *gr* knockout mutant, *A. caldus* (pJRD215) represents the control strain, and *A. caldus* (pJRD215-*tac*-*gr*) represents the *gr* overexpression strain of *A. caldus* MTH-04, respectively. The concentrations of copper are indicated as well. **(A)** 0 mM Cu^{2+}; **(B)** 5 mM Cu^{2+}; **(C)** 10 mM Cu^{2+}; **(D)** 20 mM Cu^{2+}. OD_{460nm} indicates the optical density at 460 nm, all measurements were performed in triplicate, and error bars correspond to the standard deviations.

the candidate Δ*gr* mutant firstly by observing fragment size in a PCR analysis, and all observed PCR fragments were in accordance with the predicted sizes as described in the Materials and Methods section (Figure 6A). Then, Southern blot hybridization was performed using the downstream homologous arm as the probe. After digestion by using *Sac* I, the expected bands of 1,683 and 3,045 bp were obtained for Δ*gr* mutant and the wild type, respectively, which indicates the successful knockout of the *gr* gene from *A. caldus* MTH-04 (Figure 6B). Finally, the obtained Δ*gr* mutant was confirmed by sequencing the mutated region. The *gr* overexpression strain and a control strain (wild type carrying plasmid pJRD215) were also successfully constructed using the method described in the previous section.

To study the effect of *gr* gene on heavy metal tolerance of *A. caldus*, Δ*gr*, the *gr* overexpression strain and the control strains of wild type and the wild type carrying plasmid pJRD215 of *A. caldus* were grown in the Starkey-S^0 medium with different concentrations of $CuSO_4$ or $ZnSO_4$. Without heavy metals, knockout or overexpression of *gr* did not affect the growth curves on S^0 compared with the control strains (Figure 7A), suggesting that GR did not play a key role in the growth on S^0.

All strains showed obvious growth lags under low concentrations of copper ions, and the inhibition was increased with the increase in copper ion concentrations. The growth of Δ*gr* mutant was completely inhibited under 20 mM copper ions, while the *gr* overexpression strain showed a growth advantage over the wild type (Figure 7). The high sensitivity to copper ions of the Δ*gr* mutant and the enhanced tolerance to copper ions of the *gr* overexpression strain indicated the involvement of *gr* gene in copper tolerance in *A. caldus* MTH-04.

The zinc tolerance of *A. caldus* strains was investigated as well. The increased growth inhibitions with the concentration of zinc

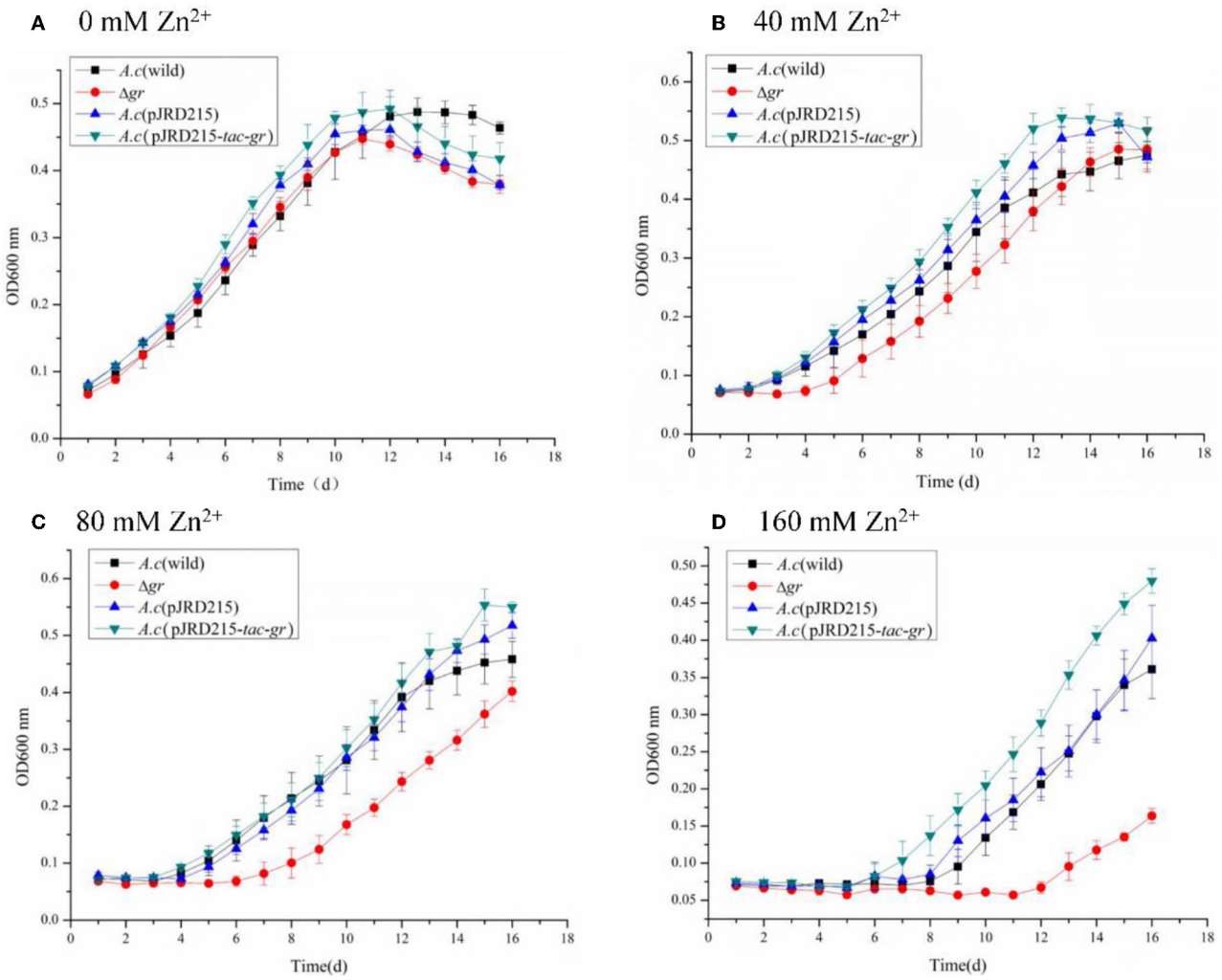

FIGURE 8
Growth curves of *Acidithiobacillus caldus* MTH-04 wild type, *gr* knockout mutant, *gr* overexpression strain, and control strain (wild type carrying pJRD215) grown in S^0 medium under zinc stress. *Acidithiobacillus caldus* (wild) represents the wild type, Δ*gr* represents the *gr* knockout mutant, *A. caldus* (pJRD215) represents the control strain, and *A. caldus* (pJRD215-*tac*-*gr*) represents the *gr* overexpression strain of *A. caldus* MTH-04, respectively. The concentrations of zinc are indicated as well. **(A)** 0 mM Zn^{2+}; **(B)** 40 mM Zn^{2+}; **(C)** 80 mM Zn^{2+}; **(D)** 160 mM Zn^{2+}. OD_{600nm} indicates the optical density at 600 nm, all measurements were performed in triplicate, and error bars correspond to the standard deviations.

ions were also observed in all *A. caldus* strains. Moreover, the Δ*gr* mutant grew lowest with a longer growth delay, while the *gr* overexpression strain grew highest with a shorter growth delay under the same concentration of zinc ions (Figure 8). The above results indicated the important role of the *gr* gene in zinc tolerance in *A. caldus* MTH-04.

3.3. Transcriptional analysis of *gr* knockout and overexpression strains

To further understand how *gr* may influence the expression patterns of glutathione-related genes in *A. caldus*, the relative mRNA levels of these genes were measured using the *gr* knockout strain with the wild type as the control or using the *gr* overexpression strain with the wild type carrying vacant pJRD215 plasmid as the control using the RT-qPCR measurement method. Without heavy metal stress, *gr* knockout resulted in increased expression levels of glutathione synthetase and glutathione peroxidase, while *gr* overexpression resulted in increased expression levels of glutathione reductase, thioredoxin reductase, and heterodisulfide reductase subunit C and decreased expression levels of peroxiredoxin, glutathione synthetase, and glutathione S-transferase (Table 4). These results suggest that the GR activity was involved in the glutathione system in *A. caldus* during elemental sulfur oxidization.

When the strains were incubated with $CuSO_4$, as shown in Table 5, most of the investigated genes were apparently upregulated in Δ*gr* compared with the wild type. On the other hand, the increased expression levels of the genes were somewhat different from others. For instance, the expression levels of peroxiredoxin, thioredoxin-disulfide reductase, and heterodisulfide reductase subunit C were increased after incubation for either 1 or 2 h, while the expression levels of thiol peroxidase and sulfur dioxygenase

TABLE 4 Changes in the expression of genes in *Acidithiobacillus caldus* MTH-04 in *gr* knockout and *gr* overexpression strains.

Locus	Gene description	Fold change (SD)[a]	
		Δ*gr*	OE-*gr*
F0726_RS00165	Peroxiredoxin	1.1	1.0
F0726_RS02905	Peroxiredoxin, AhpC/Tsa family	1.4	**0.3**
F0726_RS04210	Glutathione reductase	–	**5.4**
F0726_RS04255	Thioredoxin reductase	1.3	**2.0**
F0726_RS04480	Glutathione synthetase	**3.4**	**0.4**
F0726_RS10185	Glutathione S-transferase	0.7	**0.4**
F0726_RS13530	Glutathione peroxidase	**2.2**	1.1
F0726_RS02000	Sulfur dioxygenase	1.7	1.2
F0726_RS12050	Heterodisulfide reductase subunit C	1.7	**3.1**

[a] Δ*gr* represents the *gr* knockout mutant; OE-gr represents the gr overexpression strain of *Acidithiobacillus caldus* MTH-04.
The expression of gene F0726_RS04210 was not detectable in gr knockout mutant and was shown as "–." Fold change ≥ 2 and p-value ≤ 0.05 were considered to be upregulated, while fold change ≤ 0.5 and p-value ≤ 0.05 were considered to be downregulated and highlighted in bold.

only increased after incubation for 1 h. When the *gr* overexpression strain was compared with the control strain (wild type carrying plasmid pJRD215), the expression levels of glutathione reductase and heterodisulfide reductase subunit C were increased after incubation for 1 and 2 h, respectively, while the expression levels of thioredoxin-disulfide reductase and sulfur dioxygenase were decreased after incubation for 1 h, and the expression levels of peroxiredoxin were decreased after incubation for 2 h, respectively.

Table 6 presents the responses of the selected genes to $ZnSO_4$. It shows that when compared with the wild type, the deletion of *gr* resulted in the upregulation of peroxiredoxin and heterodisulfide reductase subunit C and the downregulation of thioredoxin reductase, glutathione S-transferase, and sulfur dioxygenase after incubation for 1 h. The absence of *gr* also resulted in the upregulation of thiol peroxidase, peroxiredoxin, and thioredoxin reductase after incubation for 2 h. When compared with the control strain (wild type carrying plasmid pJRD215), the overexpression of *gr* resulted in the upregulation of glutathione reductase and heterodisulfide reductase subunit C after incubation for either 1 or 2 h and downregulation of peroxiredoxin after incubation for 2 h. The above results suggest that the GR activity was involved in heavy metal tolerance in *A. caldus*.

4. Discussion

A putative *gr* gene (F0726_RS04210) was detected in the genome of *A. caldus* MTH-04 by conducting a BLASTP search. The proteins with GR activity contain conserved functional motifs, including an NADPH binding site, a GSSG binding site, and a redox-active disulfide bond domain (Figure 3). Most of the GR homologs contain a highly conserved NADPH binding site sequence (RX5R). Moreover, the first arginine residue in the RX5R motif is conserved up to 100%, while the last arginine residue is replaced by different residues in different strains. In F0726_RS04210, a histidine residue replaces the last conserved arginine residue (RX5H). Similar phenomena were also reported in *F. noatunensis* subsp. *orientalis* str. Toba 04 (RX5M), *S. meliloti* (RX5S), and *Nostoc* sp. PCC7120 (RX5K). Replacing arginine with other basic amino acids (H or K) may affect the affinity of NADPH and result in a wider range of electronic sources, such as NADPH and NADH. In addition, the evolutionary relationship of F0726_RS04210 is close to the glutathione reductase from *E. coli* K12. Finally, we detected GR activity in the protein of F0726_RS04210. The above results indicate that F0726_RS04210 is a GR and may play a similar role as the reported GRs.

It is well established that *A. caldus* can obtain energy by oxidizing reduced inorganic sulfur compounds (RISCs) during chemolithoautotrophic growth in acidic environments. Oxidation of RISCs requires elemental sulfur (S^0) as the initial primary and intermediate metabolite; however, limited information is available on the activation of elemental sulfur. Previous studies have proposed that elemental sulfur may be activated by GSH in *Acidithiobacillus* (Silver and Lundgren, 1968). However, the Δ*gr* mutant of *A. caldus* still grew well when using elemental sulfur as the sole energy substrate. The results indicate that GR is not fatal in the oxidation of elemental sulfur in *A. caldus*.

In biometallurgy, ore leaching microorganisms are in an environment of high osmotic pressure and high concentration of heavy metals. Our recent research has explained the essential role of OmpR in *A. caldus* adapting to the high osmolarity (Chen et al., 2022), but little is known about the mechanism of heavy metal resistance. A copper-sensitive operon repressor was identified in *A. caldus*, which might be involved in putative copper resistance mechanisms (Hou et al., 2021). Due to the lack of effective genetic tools, this specific mechanism still needs to be verified. Heavy metals accumulate during the bioleaching process, and the stress tolerance process will result in reactive oxygen species (ROS) (Stadtman and Oliver, 1991; Natarajan et al., 1994). Recently, GR was reported to participate in the heavy metal tolerance of *A. ferrooxidans* (Xia et al., 2011; Zheng et al., 2015, 2016), so the role of GR in the heavy metal tolerance of *A. caldus* was investigated in this research. Deletion of *gr* resulted in increased sensitivity to heavy metals, while the overexpression of *gr* enhanced tolerance to heavy metals, which suggests the involvement of the *gr* gene in heavy metal tolerance in *A. caldus* MTH-04. Moreover, enzymes involved in the antioxidant pathway (for instance, thioredoxin reductase) and GSH-producing pathway (for instance, glutathione synthetase and heterodisulfide reductase subunit C) were altered when *gr* was deleted or overexpressed in *A. caldus* under heavy metal stress. Previous studies also reported that GR plays a key role in heavy metal tolerance by keeping high GSH/GSSG ratios (Schirmer et al., 1989; Creissen et al., 1994; Mullineaux and Creissen, 1997). The results indicate that GR may play a key role in heavy metal tolerance in *A. caldus* by sustaining the reduced status of glutathione.

TABLE 5 Changes in the expression of genes in *Acidithiobacillus caldus* MTH-04 in *gr* knockout and *gr* overexpression strains under copper stress.

Locus	Gene description	Fold change (SD)[a]			
		Δ*gr*		OE-*gr*	
		Incubation for 1 h	Incubation for 2 h	Incubation for 1 h	Incubation for 2 h
F0726_RS00165	Peroxiredoxin	**2.4**	1.4	0.7	0.6
F0726_RS02905	Peroxiredoxin, AhpC/Tsa family	**2.5**	**2.2**	0.8	**0.5**
F0726_RS04210	Glutathione reductase	–	–	**2.5**	1.6
F0726_RS04255	Thioredoxin reductase	**4.7**	**2.2**	**0.5**	0.8
F0726_RS10185	Glutathione S-transferase	0.6	0.8	0.8	1.3
F0726_RS13530	Glutathione peroxidase	1.7	**2.0**	1.5	1.1
F0726_RS02000	Sulfur dioxygenase	**2.9**	0.9	**0.5**	1.6
F0726_RS12050	Heterodisulfide reductase subunit C	**2.3**	**2.4**	1.4	**2.7**

[a] Δ*gr* represents the *gr* knockout mutant; OE-gr represents the gr overexpression strain of *Acidithiobacillus caldus* MTH-04.
The expression of gene F0726_RS04210 was not detectable in gr knockout mutant and was shown as "–." Fold change ≥ 2 and p-value ≤ 0.05 were considered to be upregulated, while fold change ≤ 0.5 and p-value ≤ 0.05 were considered to be downregulated and highlighted in bold.

TABLE 6 Changes in the expression of genes in *Acidithiobacillus caldus* MTH-04 in *gr* knockout and *gr* overexpression strains under zinc stress.

Locus	Gene description	Fold change (SD)[a]			
		Δ*gr*		OE-*gr*	
		Incubation for 1 h	Incubation for 2 h	Incubation for 1 h	Incubation for 2 h
F0726_RS00165	Peroxiredoxin	0.9	**2.5**	0.6	1.0
F0726_RS02905	Peroxiredoxin, AhpC/Tsa family	**6.1**	**2.2**	0.6	**0.5**
F0726_RS04210	Glutathione reductase	–	–	**5.3**	**3.0**
F0726_RS04255	Thioredoxin reductase	**0.5**	**2.1**	1.3	1.0
F0726_RS10185	Glutathione S-transferase	0.1	1.1	1.2	1.0
F0726_RS13530	Glutathione peroxidase	1.3	1.6	0.9	1.0
F0726_RS02000	Sulfur dioxygenase	**0.3**	1.8	1.6	1.7
F0726_RS12050	Heterodisulfide reductase subunit C	**3.7**	1.7	**6.3**	**6.2**

[a] Δ*gr* represents the *gr* knockout mutant; OE-gr represents the gr overexpression strain of *Acidithiobacillus caldus* MTH-04.
The expression of gene F0726_RS04210 was not detectable in gr knockout mutant and was shown as "–." Fold change ≥ 2 and p-value ≤ 0.05 were considered to be upregulated, while fold change ≤ 0.5 and p-value ≤ 0.05 were considered to be downregulated and highlighted in bold.

5. Conclusion

We detect a *gr* gene in *A. caldus* and provide the report characterizing the *gr* gene by constructing a *gr* knockout mutant and a *gr* overexpression strain. We found that *gr* knockout results in increased sensitivity to heavy metals (Cu^{2+} and Zn^{2+}) and revealed the strong correlations between GR and the antioxidant pathway in *A. caldus*. Finally, we propose the function of GR is to play an important role in heavy metal tolerance. Our findings provide a template for further investigation of GR in other microorganisms and can be further used to construct improved bioleaching strains.

Data availability statement

The original contributions presented in the study are included in the article/supplementary material, further inquiries can be directed to the corresponding authors.

Author contributions

YS, YY, and XiaoL: methodology. JianqiL: formal analysis. XianL: validation. JianquL and XP: investigation and supervision.

WW: initial draft and revised draft writing and editing. JianquL and XP: funding acquisition. All authors have read and agreed to the published version of the manuscript.

Funding

This study was supported by grants from the National Natural Science Foundation of China (30800011 and 31872621), the State Key Laboratory of Microbial Technology Foundation (M2017-01), the Natural Science Foundation of Shandong Province (ZR2020MC006), People's Republic of China, the Instrument Improvement Funds of Shandong University Public Technology Platform (ts20220104), the State Key Laboratory of Microbial Technology Open Projects Fund (Project No. M2022-03), and the Cooperation Project on Bioleaching Between Shandong University and Guangxi Senhe High-tech Co., Ltd.

Acknowledgments

The authors would like to thank the Core Facilities Sharing Platform for Life and Environment Sciences of Shandong University, including Cheng-Jia Zhang and Nan-Nan Dong for providing the bacteriological incubator and Zhi-Feng Li for RT-qPCR instruction.

Conflict of interest

The authors declare that the research was conducted in the absence of any commercial or financial relationships that could be construed as a potential conflict of interest.

Publisher's note

All claims expressed in this article are solely those of the authors and do not necessarily represent those of their affiliated organizations, or those of the publisher, the editors and the reviewers. Any product that may be evaluated in this article, or claim that may be made by its manufacturer, is not guaranteed or endorsed by the publisher.

References

Asnis, R. E. (1955). A glutathione reductase from *Escherichia coli*. *J. Biol. Chem.* 213, 77–85. doi: 10.1016/S0021-9258(18)71046-6

Chen, L., Liu, X., Gao, C., Guan, Y., Lin, J., Liu, X., et al. (2022). The essential role of OmpR in *Acidithiobacillus caldus* adapting to the high osmolarity and its regulation on the tetrathionate-metabolic pathway. *Microorganisms* 11, 35. doi: 10.3390/microorganisms11010035

Creissen, G., Edwards, E. A., and Mullineaux, P. (1994). "Glutathione reductase and ascorbate peroxidase," in *Causes of Photooxidative Stress and Amelioration of Defense Systems in Plants*, eds C. H. Foyer, and P. M. Mullineaux (Boca Raton, FL: CRC Press), 343–364. doi: 10.1201/9781351070454-13

Cui, S. (2011). *Function Comparison and Analysis of Gene-cox, Cup, Iro of Acidithiobacillus ferrooxidans in Ferrous Iron Oxidation* [M.Sc]. Jinan: Shandong University.

Davison, J., Heusterspreute, M., Chevalier, N., Ha-Thi, V., and Brunei, F. (1987). Vectors with restriction site banks V. pJRD215, a wide-host-range cosmid vector with multiple cloning sites. *Gene* 51, 275–280. doi: 10.1016/0378-1119(87)90316-7

Diego, G. A., Vanina, E. M., Alejandro, J. B., Sergio, A. G., and Alberto, A. I. (2010). Purification and characterization of a glutathione reductase from *Phaeodactylum tricornutum*. *Protist* 161, 91–101. doi: 10.1016/j.protis.2009.06.001

Dopson, M., Baker-Austin, C., Koppineedi, P. R., and Bond, P. L. (2003). Growth in sulfidic mineral environments: metal resistance mechanisms in acidophilic micro-organisms. *Microbiology* 149, 1959–1970. doi: 10.1099/mic.0.26296-0

Edwards, K. J., Bond, P. L., and Banfield, J. F. (2000). Characteristics of attachment and growth of *Thiobacillus caldus* on sulphide minerals: a chemotactic response to sulphur minerals? *Environ. Microbiol.* 2, 324–332. doi: 10.1046/j.1462-2920.2000.00111.x

Ekinci, D., and Sentürk, M. (2013). Assessment of metal inhibition of antioxidant enzyme glutathione reductase from rainbow trout liver. *J. Enzyme Inhib. Med. Chem.* 28, 11–15. doi: 10.3109/14756366.2011.615745

Foyer, C., Lelandais, M., Galap, C., and Kunert, K. J. (1991). Effects of elevated cytosolic glutathione reductase activity on the cellular glutathione pool and photosynthesis in leaves under normal and stress conditions. *Plant Physiol.* 97, 863–872. doi: 10.1104/pp.97.3.863

Greer, S., and Perham, R. N. (1986). Glutathione reductase from *Escherichia coli*: cloning and sequence analysis of the gene and relationship to other flavoprotein disulfide oxidoreductases. *J. Biochem.* 25, 2736–2742. doi: 10.1021/bi00357a069

Hallberg, K. B., and Lindström, E. B. (1994). Characterization of *Thiobacillus caldus* sp.nov., a moderately thermophilic acidophile. *Microbiology* 140, 3451–3456. doi: 10.1099/13500872-140-12-3451

Hallberg, K. B., and Lindström, E. B. (1996). Multiple serotypes of the moderate thermophile *Thiobacillus caldus*, a limitation of immunological assays for biomining microorganisms. *Appl. Environ. Microbiol.* 62, 4243–4246. doi: 10.1128/aem.62.11.4243-4246.1996

Hou, S., Tong, Y., Yang, H., and Feng, S. (2021). Molecular insights into the copper-sensitive operon repressor in *Acidithiobacillus caldus*. *Appl. Environ. Microbiol.* 87, e0066021. doi: 10.1128/AEM.00660-21

Jin, S., Yan, W., and Wang, Z. (1992). Transfer of IncP plasmids to extremely acidophilic *Thiobacillus thiooxidans*. *Appl. Environ. Microbiol.* 58, 429–430. doi: 10.1128/aem.58.1.429-430.1992

Kamimura, K., Okayama, T., Murakami, K., and Sugio, T. (1999). Isolation and characterization of a moderately thermophilic sulfur-oxidizing bacterium. *Microbios* 99, 7–18.

Liu, Y., Qi, F., Lin, J., Tian, K., and Yan, W. (2004). Isolation and phylogenetic analysis of a moderately thermophilic acidophilic sulfur oxidizing bacterium. *Acta Microbiol. Sin.* 44, 382–385. doi: 10.13343/j.cnki.wsxb.2004.03.025

Livaka, K. J., and Schmittgenb, T. D. (2001). Analysis of relative gene expression data using real-time quantitative PCR and the 2-[Delta][Delta] CT method. *Methods* 25, 402–408. doi: 10.1006/meth.2001.1262

Luo, Y., Liu, Y., Zhang, C., Luo, H., Guan, H., Liao, H., et al. (2008). Insights into two high homogenous genes involved in copper homeostasis in *Acidithiobacillus ferrooxidans*. *Curr. Microbiol.* 57, 274–280. doi: 10.1007/s00284-008-9189-6

Meister, A., and Anderson, M. E. (1983). Glutathione. *Ann. Rev. Biochem.* 52, 711–760. doi: 10.1146/annurev.bi.52.070183.003431

Michail, S., and James, A. B. (1977). Chloroplast glutathione reductase. *J. Plant Physiol.* 59, 1011–1012. doi: 10.1104/pp.59.5.1011

Mullineaux, P. M., and Creissen, G. P. (1997). "Glutathione reductase: regulation and role in oxidative stress," in *Oxidative Stress and the Molecular Biology of Antioxidant Defenses* ed J. Scandalios (New York, NY: Cold Spring Harbor Laboratory Press), 667–713.

Natarajan, K. A., Sudeesha, K., and Rao, G. R. (1994). Stability of copper tolerance in *Thiobacillus ferrooxidans*. *Antonie Van Leeuwenhoek* 66, 303–306. doi: 10.1007/BF00882764

Nigel, S. S., Alan, B., and Richard, N. P. (1987). Purification and characterization of glutathione reductase encoded by a cloned and over-expressed gene in *Escherichia coli*. *J. Biol. Chem.* 245, 875–880. doi: 10.1042/bj2450875

Noctor, G., and Foyer, C. H. (1998). Ascorbate and glutathione: keeping active oxygen under control. *Ann. Rev. Plant Physiol. Plant Biol. Med.* 49, 249–279. doi: 10.1146/annurev.arplant.49.1.249

Okibe, N., Gericke, M., Hallberg, K. B., and Johnson, D. B. (2003). Enumeration and characterization of acidophilic microorganisms isolated from apilot plant stirredtank bioleaching operation. *Appl. Environ. Microbiol.* 69, 1936–1943. doi: 10.1128/AEM.69.4.1936-1943.2003

Rice-Evans, C. A., Miller, N. J., and Paganga, G. (1996). Structure-antioxidant activity relationships of flavonoids and phenolic acids. *Free Rad. Biol. Med.* 20, 933–956. doi: 10.1016/0891-5849(95)02227-9

Sambrook, J., and Russell, D. W. (2001). *Molecular Cloning: A Laboratory Manual*, 3rd ed. Cold Spring Harbor, NY: Cold Spring Harbor Laboratory Press.

Schirmer, R. H., Krauth-Siegel, R. L., and Schulz, G. E. (1989). "Glutathione reductase," in *Coenzymes and Cofactors: Glutathione*, Vol. 3, eds D. Dolphin, O. Avaramovic, and R. Poulson (New York, NY: Wiley), 553–596.

Scruton, N. S., Berry, A., and Perham, R. N. (1990). Redesign of the coenzyme specificity of a dehydrogenase by protein engineering. *Nature* 343, 38–43. doi: 10.1038/343038a0

Silver, M., and Lundgren, D. G. (1968). Sulfur-oxidizing enzyme of *Ferrobacillus ferrooxidans* (*Thiobacillus ferrooxidans*). *Biochem. Cell Biol.* 46, 1215–1220. doi: 10.1139/o68-069

Simon, R., Priefer, U., and Pühler, A. (1983). A broad host range mobilization system for *in vivo* genetic engineering: transposon mutagenesis in gram negative bacteria. *Nat. Biotechnol.* 1, 784–791. doi: 10.1038/nbt1183-784

Smith, I. K., Polle, A., and Rennenberg, H. (1990). "Glutathione," in *Stress Responses in Plant Adaptation and Acclimation Mechanisms*, eds R. G. Alscher, and J. R. Cumming (New York, NY: Wiley-Liss), 201–215.

Stadtman, E. R., and Oliver, C. N. (1991). Metal-catalyzed oxidation of proteins. *J. Biol. Chem.* 266, 2005–2008. doi: 10.1016/S0021-9258(18)52199-2

Wang, Z., Li, Y., Lin, J., Pang, X., Liu, X., Liu, B., et al. (2016). The two-component system RsrS-RsrR regulates the tetrathionate intermediate pathway for thiosulfate oxidation in *Acidithiobacillus caldus*. *Front. Microbiol.* 7, 1755. doi: 10.3389/fmicb.2016.01755

Wen, Q., Liu, X., Wang, H., and Lin, J. (2014). A versatile and efficient markerless gene disruption system for *Acidithiobacillus thiooxidans*: application for characterizing a copper tolerance related multicopper oxidase gene. *Environ. Microbiol.* 16, 3499–3514. doi: 10.1111/1462-2920.12494

Wu, W., Pang, X., Lin, J., Liu, X., Wang, R., Lin, J., et al. (2017). Discovery of a new subgroup of sulfur dioxygenases and characterization of sulfur dioxygenases in the sulfur metabolic network of *Acidithiobacillus caldus*. *PLoS ONE* 12, e0183668. doi: 10.1371/journal.pone.0183668

Xia, J. L., Wu, S., Zhang, R. Y., Zhang, C. G., He, H., Jiang, H. C., et al. (2011). Effects of copper exposure on expression of glutathione-related genes in *Acidithiobacillus ferrooxidans*. *Curr. Microbiol.* 62, 1460–1466. doi: 10.1007/s00284-011-9881-9

Zheng, C., Chen, M., Tao, Z., Zhang, L., Zhang, X. F., Wang, J. Y., et al. (2015). Differential expression of sulfur assimilation pathway genes in *Acidithiobacillus ferrooxidans* under Cd^{2+} stress: evidence from transcriptional, enzymatic, and metabolic profiles. *Extremophiles* 19, 429–4436. doi: 10.1007/s00792-014-0728-8

Zheng, C., Chen, M., Wang, D., Zhang, L., Wang, J., Zhang, X., et al. (2016). Interplay between expression of sulfur assimilation pathway genes and Zn(2+) and Pb(2+) stress in *Acidithiobacillus ferrooxidans. Curr. Microbiol.* 73, 527–533. doi: 10.1007/s00284-016-1083-z

frontiers | Frontiers in Microbiology

TYPE Original Research
PUBLISHED 20 November 2023
DOI 10.3389/fmicb.2023.1277349

OPEN ACCESS

EDITED BY
Ruiyong Zhang,
Chinese Academy of Sciences (CAS), China

REVIEWED BY
Egbert Schwartz,
Northern Arizona University, United States
Lichao Fan,
Northwest A&F University, China

*CORRESPONDENCE
Alon Angert
✉ angert@huji.ac.il

RECEIVED 14 August 2023
ACCEPTED 30 October 2023
PUBLISHED 20 November 2023

CITATION
Weiner T, Tamburini F, Keren N, Keinan J and Angert A (2023) Does metabolic water control the phosphate oxygen isotopes of microbial cells?
Front. Microbiol. 14:1277349.
doi: 10.3389/fmicb.2023.1277349

Does metabolic water control the phosphate oxygen isotopes of microbial cells?

Tal Weiner[1], Federica Tamburini[2], Nir Keren[3], Jonathan Keinan[1] and Alon Angert[1]*

[1]The Institute of Earth Sciences, The Hebrew University of Jerusalem, Jerusalem, Israel, [2]Institute of Agricultural Science, ETH Zürich, Zurich, Switzerland, [3]Department of Plant and Environmental Science, The Alexander Silberman Institute of Life Sciences, The Hebrew University of Jerusalem, Jerusalem, Israel

The oxygen isotopes ratio ($\delta^{18}O$) of microbial cell water strongly controls the $\delta^{18}O$ of cell phosphate and of other oxygen-carrying moieties. Recently it was suggested that the isotopic ratio in cell water is controlled by metabolic water, which is the water produced by cellular respiration. This potentially has important implications for paleoclimate reconstruction, and for measuring microbial carbon use efficiency with the ^{18}O-water method. Carbon use efficiency strongly controls soil organic matter preservation. Here, we directly tested the effect of metabolic water on microbial cells, by conducting experiments with varying the $\delta^{18}O$ of headspace O_2 and the medium water, and by measuring the $\delta^{18}O$ of cell phosphate. The latter is usually assumed to be in isotopic equilibrium with the cell's water. Our results showed no correlation between the $\delta^{18}O$ of O_2 and that of the cell phosphate, contradicting the hypothesis that metabolic water is an important driver of $\delta^{18}O$ of microbial cell water. However, our labeled ^{18}O water experiments indicated that only 43% of the oxygen in the cell's phosphate is derived from equilibration with the medium water, during late-log to early-stationary growing phase. This could be explained by the isotopic effects of intra-and extra-cellular hydrolysis of organic compounds containing phosphate.

KEYWORDS

metabolic water, oxygen stable isotopes, ambient water, carbon use efficiency, microbial cells

Introduction

The oxygen isotope ratios in biominerals from hard tissues have been used extensively to reconstruct paleo-temperatures, paleo-environments, and the isotopic composition of the water in the environment. The studied hard tissues are usually composed of carbonates and phosphates and the measurements have been mainly of the isotopic ratio of $^{18}O/^{16}O$ (expressed in the delta notation as $\delta^{18}O$), but expanded recently also to $^{17}O/^{16}O$ (Tudge, 1960; Shackleton, 1967; Pearson, 2012; Passey and Levin, 2021). Other studies have focused on other chemical species, such as sulfates and nitrates, and the isotopic composition of oxygen in these species was used to reconstruct past environments and study ecosystem processes (Fritz et al., 1989; Casciotti et al., 2002). Implicit assumptions made for all these applications are that (1) the oxygen isotopic composition of intracellular water is transferred to oxygen-bearing chemical species, and (2) while intracellular water of large animals is isotopically different from ambient water, the

intracellular water of small organisms (i.e., bacteria, plankton) and the ambient water exchange fast enough to be practically identical in terms of isotopic composition.

The assumption of isotopically identical ambient and intracellular water, however, might not be valid if the water inside the living cell is strongly controlled by metabolic water. Metabolic water is produced as a result of the aerobic cellular respiration process. In this process, oxygen atoms are transferred from O_2 to H_2O, following the canonical equation for respiration:

$$C_6H_{12}O_6 + 6O_2 \rightarrow 6CO_2 + 6H_2O$$

Since the isotopic composition of atmospheric O_2 is usually different from that of the water in the same environment, the contribution of metabolic water can change the intracellular water isotopic composition. The isotopic composition can then be carried over to the oxygen-bearing compounds of interest, like phosphates, carbonates and nitrates. The effect of metabolic water was recognized decades ago in the case of large land organisms like mammals, birds, and plants, which have limited exchange of cell water with the environment (Luz and Kolodny, 1985; Yakir, 1992; Sabat et al., 2021). However, for micro-organisms, the implicit assumption of fast exchange and negligible contribution of metabolic water was dominant until recently challenged with a series of experiments in which bacteria were grown in media with varying water oxygen isotopic compositions (Li et al., 2016). At the end of each experiment (during the late-log to early-stationary growing phase), the bacteria biomass was collected and the $\delta^{18}O$ of phosphate ($\delta^{18}O_P$) from DNA and from the total biomass (which includes inorganic cytosolic phosphate and organic-P) was measured. Based on the assumption that all the cell phosphate (i.e., cytosolic phosphate and phosphate bound to organic compounds) was in equilibrium with the cell water, this study concluded that ~30% of the oxygen in DNA, and 40% of the total biomass phosphate of cells in this growing phase are derived from metabolic water. Based on this indirect finding, it was suggested that metabolic water strongly controls the isotopic composition of water in microbial cells.

The indirect evidence for the contribution of metabolic water to cell water was supported by previous research (Kreuzer-Martin et al., 2005), which measured the stable oxygen isotopes in water distilled from filtered microbial (*Escherichia coli*) "cell cakes." These "cell cakes" contained both intercellular and medium water, and isotope labeling was used to distinguish between the two. That led to the conclusion that 70% of the intracellular water in log-phase *E. coli* cells was of metabolic origin.

Here, we directly tested the hypothesis that metabolic water has a significant effect on the cell water isotopic composition, and hence the total biomass $\delta^{18}O_P$, by conducting experiments in which the bacteria were exposed not only to varying water isotopic composition, but also to varying headspace O_2 isotopic composition. This approach was used in a recent study and proven successful to trace the incorporation of labeled O_2 from the headspace to the metabolic water (Koch and Schwartz, 2023). The labeling of the headspace, which was not done in the previous phosphate studies, is expected to lead to changes in metabolic water oxygen isotopes ratios, and enables to test the hypothesis that the metabolic water signal has strong control over the cell water and hence the biomass $\delta^{18}O_P$.

Materials and methods

Pseudomonas putida was grown in a 1 L gas-tight Tedlar bag, equipped with a one-way Luer check-valve to release gas pressure buildup. Similarly to Li et al. (2016), the bacteria were grown in 200 mL LB medium composed of 2 g Tripton, 1 g yeast extract, 2 g NaCl and 0.2 mL 1 M NaOH, in either natural or $\delta^{18}O$ enriched water (+108.5‰, all isotopic values are given vs. V-SMOW). An aliquot of the water used for the medium preparation was taken for oxygen stable isotopes analysis. A headspace of 800 mL gas was pre-introduced to the bag. The headspace was either air ($\delta^{18}O$ of 23.9‰; Barkan and Luz, 2005) or a mixture of 632 mL N_2 and 168 mL O_2 a with a $\delta^{18}O$ of −13.0‰. The bags with the medium and bacteria were shaken at 30°C for 17–21 h until late-log/early-stationary phase. At the end of the incubation, air from the headspace was sampled into glass flasks and measured for CO_2 and O_2 concentrations, in a system consisting of an infra-red gas analyzer (IRGA) for CO_2 measurement and a fuel-cell based analyzer for measuring O_2 (Hilman and Angert, 2016). This procedure was done in order to validate that the conditions remained aerobic and that O_2 was consumed from the headspace.

The biomass was isolated through centrifugation (3,500 RPM for 15 min), rinsed with 0.03 M HEPES buffer (Sigma-Aldrich), and transferred to quartz vessels for UV radiation digestion. The digestion took place in DDW with 2–3 mL phosphate-free H_2O_2 (Sigma Aldrich) under UVC irradiation (18 lamps with a total power of 30 W). To evaluate the release of phosphate from the organic-P, one of the experiments was performed in duplicates, one in deionized water with $\delta^{18}O$ of +0.2‰, and the second in water with $\delta^{18}O$ of +97.1‰, the measured $\delta^{18}O_P$ was 24.4‰ and 32.8‰ respectively. This enables us to calculate by an isotopic mass balance approach, the percentage of oxygen that was incorporated into the released phosphate from the water during the UV-induced mineralization (Liang and Blake, 2006). We used the following equations for calculation assuming x and y are equal in both samples:

$$x \times y + (1 - x) \times 97.1 = 32.8 \quad (1)$$

$$x \times y + (1 - x) \times 0.2 = 24.4 \quad (2)$$

Where x is the percentage of oxygen that originated from the biomass, $1 - x$ is the percentage of incorporated oxygen that originated from water, and y is the $\delta^{18}O$ of the biomass. The percentage of incorporated oxygen that originated from water was found to be 9%, and the value of biomass $\delta^{18}O_P$ was corrected accordingly in all other samples.

After the digestion of the biomass, the samples were kept refrigerated for 2 weeks. We found this stage useful for preventing precipitation of MoO_3 during the next steps, which might be produced due to an excited state caused by the UVC radiation. The samples were acidified with 1 M HCl to prevent growth of microorganisms and were shaken with SuperliteTM DAX-8 resin (Sigma Aldrich) to remove any remaining organic matter.

The phosphate was purified according to Tamburini et al. (2010). Briefly, the phosphate was precipitated as ammonium phospho-molybdate (APM) using 35% NH_4NO_3 and 10% NH_4Mo,

vacuum filtered, rinsed with 5% NH_4NO_3, and finally dissolved in citric acid-NH_4OH solution. The phosphate was re-precipitated as struvite using a magnesium-based reagent composed of $MgCl_2$•$6H_2O$, NH_4Cl, and HCl, and 1:1 ammonia solution, vacuum filtered and rinsed with 1:20 ammonia solution and dissolved in 0.5 M HNO_3. A cation resin AG50 × 8 resin (Bio-Rad) was used for removal of cations. The purification was followed by precipitation as silver phosphate using a mixture of 1.1 M $AgNO_3$ and 2.72 M NH_4OH, while KOH and HNO_3 were added to adjust the pH (Mine et al., 2017). The precipitates were rinsed in water after centrifugation (3,500 RPM, 15 min) and were dried at 50°C. Phosphate concentrations were determined by colorimetry (Murphy and Riley, 1962).

The water samples were analyzed for $\delta^{18}O$ by either headspace equilibration using Thermo Scientific GasBench II coupled to a Thermo Finnigan Delta Plus XL isotope-ratio mass spectrometer (at UC Davis), or by cavity ringdown spectroscopy using a Picarro L2140-i isotopic water analyzer (at the Hebrew University), described in detail by Keinan and Goldsmith (2023). In brief, liquid water samples were stored in 2 mL glass vials capped with blue polypropylene caps with red PTFE/white silicone septum and injected with a liquid autosampler (Picarro A0325) into a vaporizer module (Picarro A0211), using pure nitrogen (99.999%) as the carrier gas. Sample isotope ratios were standardized using a range of reference waters which have been calibrated against IAEA reference waters (VSMOW2, and SLAP2). For $\delta^{18}O_P$ the Ag_3PO_4 was measured in a TC/EA (thermal conversion elemental analyzer, Vario Pyro Cube, Elementar GmbH, Germany) in pyrolysis mode, coupled in continuous flow with an IRMS (isotope ratio mass spectrometer, Isotprime, Elementar, GmbH, Germany). Two benzoic acid standards (IAEA 601: $\delta^{18}O = 23.1‰$, IAEA 602 $\delta^{18}O = 71.3‰$), an internal Ag_3PO_4 standard (Acros Organics, Geel, Belgium, $\delta^{18}O = 14.2‰$), and in-house standards were used for instrumental drift correction and isotopic calibration.

Results and discussion

The headspace gases measurements showed considerable consumption of O_2. The average O_2 concentration in the incubation bags at the end of an experiment dropped from 20.95 to 7.5% ± 3.6%, while the average CO_2 concentration increased from 0.04 to 7.8% ± 2.3% (Table 1). These concentration values correspond to a respiratory quotient (increase in CO_2 divided by the decrease in O_2) of 0.6 ± 0.1. These values indicate that aerobic respiration was dominant during the experiments despite the considerable oxygen consumption, since anaerobic respiration is associated with values above 1.0. Simple calculations showed the amount of O_2 in the solution is small compared to the amount consumed from the headspace, since the medium contains less than 0.05 mmol of dissolved O_2, while the headspace contains about 7 mmol of gaseous O_2. Hence, the O_2 consumed during the experiment is almost entirely derived from the headspace, and if metabolic water has a strong contribution to the cell water, the $\delta^{18}O$ of the cell water should be affected by the $\delta^{18}O$ of O_2 in the headspace (which was varied between experiments).

TABLE 1 Results of headspace gases measurements at the end of each experiment.

Exp.	Exp. duration (h)	CO_2 (%)	O_2 (%)	RQ
1	19.91	4.0	14.3	0.59
2	19.91	5.8	11.6	0.62
3	19.91	5.6	11.3	0.58
4	19.91	4.9	12.5	0.57
5	18.42	8.1	6.6	0.56
6	18.42	9.9	7.1	0.71
7	18.42	5.8	10.4	0.55
8	18.42	6.6	8.5	0.53
9	18.92	6.8	6.0	0.45
10	18.92	7.5	7.0	0.54
11	18.92	7.1	7.5	0.53
12	20.92	10.8	0.9	0.54
13	20.92	11.1	1.3	0.56
14	20.92	9.8	1.2	0.49
15	20.92	11.4	1.5	0.59
16	17.08	1.8	14.3	0.26
17	17.08	9.5	6.1	0.64
18	17.08	8.8	5.6	0.57
19	17.08	0.4	18.5	0.14

RQ is the respiratory quotient (increase in CO_2 divided by the decrease in O_2, ΔCO2/−ΔO2).

The isotopic results are summarized in Table 2. To calculate the value of $\delta^{18}O$ in phosphate in equilibrium with medium water, we used the equation from Chang and Blake (2015):

$$1000^{*} \ln \alpha = 14.43^{*}1000 / T(K) - 26.54 \quad (3)$$

And then used the relationship:

$$\delta^{18}O_P(\text{equilibrium}) = \delta^{18}O_{\text{medium water}} + 1000^{*} \ln \alpha \quad (4)$$

To check for possible effect of metabolic water, we calculate the equilibrium not just with the medium water, but also with assumed cell water composed of 70% medium water and 30% metabolic water (Table 2), as asserted in Li et al. (2016). The $\delta^{18}O$ of metabolic water was calculated based on the $\delta^{18}O$ value of the O_2 in the bag headspace, and the known −20‰ fractionation of the consumed O_2 during aerobic respiration (Guy et al., 1989; Bender et al., 1994). It should be noted that this is a simple approach, which ignore possible effect of fractionation in the gas-water interface and the effect of slow diffusion through this interface, as well as the consumption effect on the $\delta^{18}O$ of the

10.3389/fmicb.2023.1277349

TABLE 2 Summary of all the isotopic data, grouped by experiments blocks.

Exp.	Headspace O_2 $\delta^{18}O$	Medium water $\delta^{18}O$	$\delta^{18}O_P$ measured	$\delta^{18}O_P$ corrected for UV-introduced oxygen	Calculated equilibrium with medium water	Calculated equilibrium with 30% metabolic water
1	23.9	0.0	19.6	21.4	21.3	22.4
2	23.9	0.0	20.9	22.9	21.3	22.4
3	−13.0	0.0	21.1	23.0	21.3	11.4
4	−13.0	0.0	22.1	24.1	21.3	11.4
5	23.9	11.9	21.0	22.0	33.2	30.8
6	23.9	11.9	19.1	20.9	33.2	30.8
7	−13.0	11.9	20.2	22.0	33.2	19.7
8	−13.0	11.9	22.9	25.0	33.2	19.7
9	−13.0	0.3	19.2	21.1	21.6	11.6
10	23.9	0.3	19.5	21.1	21.6	22.7
11	23.9	0.3	19.3	21.3	21.6	22.7
12	23.8	3.3	26.1	28.3	24.5	24.7
13	23.8	3.3	23.1	25.1	24.5	24.7
14	−13.0	3.3	25.3	27.4	24.5	13.7
15	−13.0	3.3	27.2	29.5	24.5	13.7
16	23.8	87.2	50.7	55.4	108.5	83.5
17	23.8	87.2	56.1	61.5	108.5	83.5
18	−13.0	87.2	53.6	58.6	108.5	72.4
19	−13.0	87.2	59.1	64.7	108.5	72.4

All isotopic values are in delta permil vs. V-SMOW. The experiments were performed with both DDW water at natural abundance and ^{18}O-labeled DDW water, and both with air headspace and light-O_2 headspace. The value of "$\delta^{18}OP$ corrected for UV introduced oxygen," is the measured value with correction for 9% contribution from water oxygen incorporation during the UV treatment (see methods). See text for explanations of equilibrium calculations. Note that the light-O_2 headspace do not cause lighter $\delta^{18}OP$, in contrast to the calculated equilibrium value when assuming 30% contribution of metabolic water.

remaining O_2. However, these effects are not related to the $\delta^{18}O$ of the O_2 in the headspace, and hence, the calculated difference between the metabolic water under different headspace O_2 is a good estimate.

Considering metabolic water made the calculated equilibrated $\delta^{18}O_P$ lighter (Table 2). This effect on the calculation was weaker in the experiment in which the headspace was air (with $\delta^{18}O$ of O_2 of 23.9‰), but, as expected, had a marked effect when light-O_2 ($\delta^{18}O$ of −13.0‰) was used in the headspace. This calculation shows that if metabolic water was indeed contributing 30% of the internal cell water, the $\delta^{18}O_P$ should have been 11‰ lighter in the experiments in which light-O_2 was in the headspace than in the experiments with atmospheric air. However, this is not the case (Table 2; Figure 1). This result suggests that fast exchange between the cell and the ambient water might have erased the contribution of metabolic water to the cell water.

The experiments with no ^{18}O-labeled water additions to the medium show $\delta^{18}O_P$ values which are close to equilibrium with the medium water. On average, the difference between the calculated equilibrium between phosphate and medium water and the measured value (after correction for oxygen introduced during UV treatment) is only 2.7‰, but with quite a large standard deviation of 2.4‰. However, for the experiments in which ^{18}O-labeled water was added to the medium and enriched it to 87.2‰, this difference is one order of magnitude larger (Table 2) and is 48.5% ± 4.0‰. A known approach to estimate the control of ambient water on the phosphate oxygen isotopes, is to plot the measured $\delta^{18}O_P$ versus the calculated $\delta^{18}O_P$ in equilibrium with ambient water (Li et al., 2016). In our experiments the fitted linear slope on this plot is 0.43 (Figure 2), indicating that only 43% of the oxygen atoms in the cell phosphate originate from the medium water, while the rest must have another source.

The results from the experiments with ^{18}O-labeled water in the medium are in general agreement with (Li et al., 2016), who reported that ~40% of the O in biomass PO_4 is not derived from extracellular water. In their paper, they suggested that the gap between the measured values and the values calculated by assuming equilibrium with medium water, could be explained if

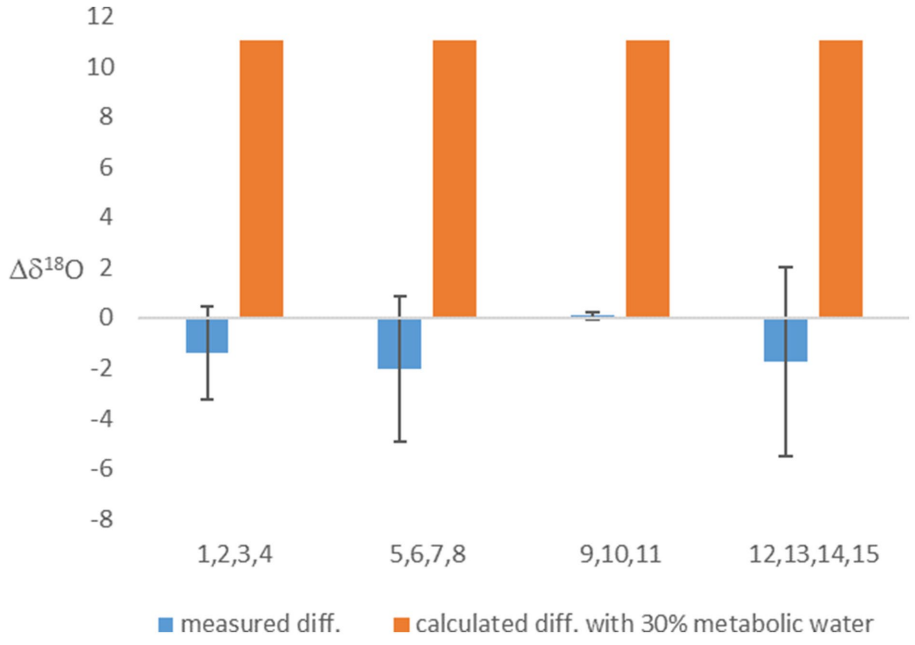

FIGURE 1
The difference between the $\delta^{18}O_P$ of experiments with headspace of air-O_2 and light O_2. Presented are the measured values, and calculated values based on the assumption that 30% of cell water is metabolic water. Averages (based on experiments numbers indicated in the x-axis and grouped in blocks) and error bars are shown.

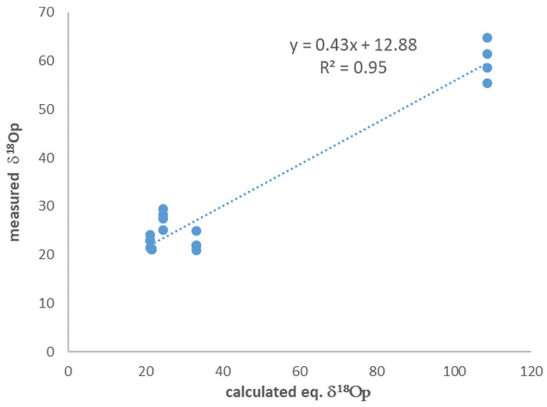

FIGURE 2
The measured $\delta^{18}O_P$ vs. the calculated $\delta^{18}O_P$ in equilibrium with ambient water. The slope indicate that only 43% of the phosphate oxygen is derived from the water.

40% of the biomass phosphate oxygen came from metabolic water with $\delta^{18}O = -3.5‰$ (Li et al., 2016). We can calculate the expected value for metabolic water from the measured $\delta^{18}O$ of atmospheric O_2, which is 23.9‰ (Barkan and Luz, 2005), and the known isotopic fractionation during respiration which is ~−20‰. This yields an estimate of ~3.9‰ (23.9–20), which is ~7‰ heavier than the value of −3.5‰ estimated by Li et al. (2016). The additional isotopic effects on the metabolic water, discussed above, will only increase this mismatch. Thus, this mismatch strengthens our conclusion that metabolic water is not a significant contributor to cell water, and that the deviations from the calculated equilibrium with ambient water are due to other reasons.

What can drive this deviation from the expected equilibrium? One major assumption of most studies dealing with intracellular ^{18}O in phosphate is that the oxygen isotopes in the cell P (biomass plus cytosolic phosphate) are only controlled by equilibrium with the cell-water. This ignores many intracellular reactions (e.g., ATP driven energy conversion reactions, organic P synthesis by phosphotransferases, phosphorylation and dephosphorylation of molecules and proteins), which are known to have possible isotope effects (see Hengge, 2002 and refs therein), but are not yet characterized for their isotopic fractionation. One possible explanation for the deviation from equilibrium observed in our experiments could be the activity of other enzymatic reactions (Figure 3). Indeed, phosphate released from the cleavage of organic P is known to be affected by enzyme-specific kinetic fractionation, on top of the carried inherent signature of the phosphate from the organic molecule (Liang and Blake, 2006; Liang and Blake, 2009; von Sperber et al., 2014). The medium in which the bacteria were grown during our experiments (and also in Li et al., 2016) included yeast extract, which is a complex nutrient-rich source and contains about 2.5% of organic P (Dzurendova et al., 2020). Previous research (Pistocchi et al., 2020) also found that in some soils the oxygen isotopic ratios in microbial P (mainly cytosolic) can be far from equilibrium and attributed this to the intracellular enzymatic release of phosphate from organic-P. In addition, phosphate uptake by microbial cells high-efficiency transporter was shown to involve isotopic fractionation (Lis et al., 2019). It has to be noted that both the

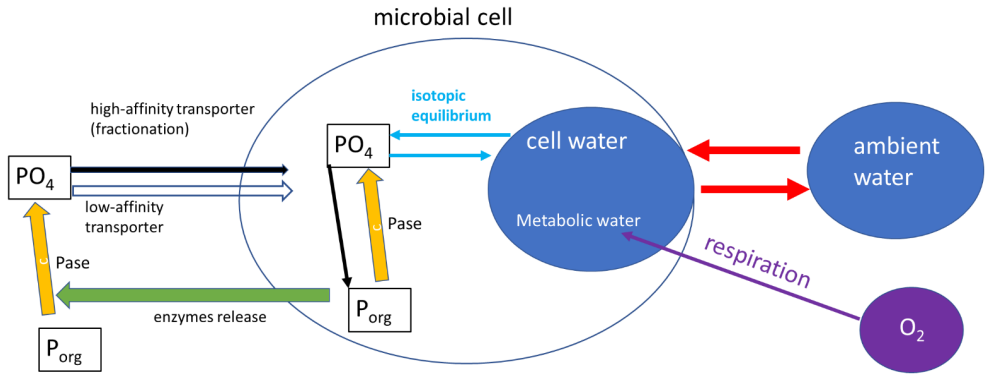

FIGURE 3
Schematic representation (after Pistocchi et al., 2020) of the reactions affecting phosphate oxygen isotopes in a microbial cell. This included inherence from organic-P sources, fractionation by phosphatases (Pase) and isotopic equilibrium with cell water. The cell water is controlled by exchange with ambient water which is fast, and a slow contribution of metabolic water.

current and the previously cited works targeting metabolic water and ^{18}O in phosphate, targeted the sum of cytosolic and organic (UV-degradable) phosphate. Different results might be expected if these phosphate pools could be separately analyzed.

These results are important not only for paleoclimate reconstructions, but also for measurements of carbon turnover in soils, which strongly controls atmospheric CO_2 and hence climate. Recent modeling efforts showed that the amount of carbon stored in soils is highly sensitive to carbon use efficiency (CUE) which is the ratio between the carbon used for microbial growth and the carbon emitted in microbial respiration (Manzoni et al., 2012; Tao et al., 2023). The CUE is often measured by labeling the soil water with ^{18}O, and tracing this label incorporation into the microbial DNA. While our results showed that metabolic water production do not dilute this label (in agreement with Wang et al., 2022), the incorporation to the DNA of phosphate which inherent it oxygen atoms from organic-P, will invalidate this method assumptions (Pold et al., 2020). However, it should be noted that the DNA $\delta^{18}O$ is also controlled by the oxygen atoms in the deoxyribose sugars and in the DNA bases, with unknown direct contribution of ambient water to this oxygen. Hence, the fraction of oxygen derived from ambient water in total DNA should be tested in future studies, because of its implication for CUE measurements.

In conclusion, our experiments directly show that the deviation from isotopic equilibrium between the ambient water and the oxygen in phosphate is not derived from the contribution of metabolic water to the cell water. We suggest that this deviation is most likely the result of intracellular enzyme activity, which is associated with fractionation and inheritance isotopes effects. However, more research is needed to clarify the various processes which control the phosphate oxygen isotopes in microbial cells.

Data availability statement

The original contributions presented in the study are included in the article/supplementary material, further inquiries can be directed to the corresponding author.

Author contributions

TW: Writing – original draft, Writing – review & editing, Data curation, Investigation. FT: Writing – original draft, Writing – review & editing, Conceptualization. NK: Writing – review & editing, Resources. JK: Resources, Writing – review & editing. AA: Writing – review & editing, Conceptualization, Funding acquisition, Project administration, Supervision, Visualization, Writing – original draft.

Funding

The author(s) declare financial support was received for the research, authorship, and/or publication of this article. This research was supported by the Israel Science Foundation (grant #773/19).

Acknowledgments

We thank Hagit Zer for help with bacteria growing.

Conflict of interest

The authors declare that the research was conducted in the absence of any commercial or financial relationships that could be construed as a potential conflict of interest.

The author(s) declared that they were an editorial board member of Frontiers, at the time of submission. This had no impact on the peer review process and the final decision.

Publisher's note

References

Barkan, E., and Luz, B. (2005). High precision measurements of 17O/16O and 18O/16O ratios in H2O. *Rapid Commun. Mass Spectrom.* 19, 3737–3742. doi: 10.1002/rcm.2250

Bender, M., Sowers, T., and Labeyrie, L. (1994). The dole effect and its variations during the last 130,000 years as measured in the Vostok ice core. *Global Biogeochem. Cycles* 8, 363–376. doi: 10.1029/94GB00724

Casciotti, K. L., Sigman, D. M., Hastings, M. G., Böhlke, J., and Hilkert, A. (2002). Measurement of the oxygen isotopic composition of nitrate in seawater and freshwater using the denitrifier method. *Anal. Chem.* 74, 4905–4912. doi: 10.1021/ac020113w

Chang, S. J., and Blake, R. E. (2015). Precise calibration of equilibrium oxygen isotope fractionations between dissolved phosphate and water from 3 to 37°C. *Geochim. Cosmochim. Acta* 150, 314–329. doi: 10.1016/j.gca.2014.10.030

Dzurendova, S., Zimmermann, B., Tafintseva, V., Kohler, A., Ekeberg, D., and Shapaval, V. (2020). The influence of phosphorus source and the nature of nitrogen substrate on the biomass production and lipid accumulation in oleaginous Mucoromycota fungi. *Appl. Microbiol. Biotechnol.* 104, 8065–8076. doi: 10.1007/s00253-020-10821-7

Fritz, P., Basharmal, G., Drimmie, R., Ibsen, J., and Qureshi, R. (1989). Oxygen isotope exchange between sulphate and water during bacterial reduction of sulphate. *Chem. Geol.* 79, 99–105.

Guy, R. D., Berry, J. A., Fogel, M. L., and Hoering, T. C. (1989). Differential fractionation of oxygen isotopes by cyanide-resistant and cyanide-sensitive respiration in plants. *Planta* 177, 483–491. doi: 10.1007/BF00392616

Hengge, A. C. (2002). Isotope effects in the study of phosphoryl and sulfuryl transfer reactions. *Acc. Chem. Res.* 35, 105–112. doi: 10.1021/ar000143q

Hilman, B., and Angert, A. (2016). Measuring the ratio of CO2 efflux to O2 influx in tree stem respiration. *Tree Physiol.* 36, 1422–1431. doi: 10.1093/treephys/tpw057

Keinan, J., and Goldsmith, Y. (2023). A simple method for rapid removal of the memory effect in cavity ring-down spectroscopy water isotope measurements. *Rapid Commun. Mass Spectrom.* 37:e9600.

Koch, G. W., and Schwartz, E. (2023). Isotopic labeling of metabolic water with 18O2. *Rapid Commun. Mass Spectrom.* 37:e9447. doi: 10.1002/rcm.9447

Kreuzer-Martin, H. W., Ehleringer, J. R., and Hegg, E. L. (2005). Oxygen isotopes indicate most intracellular water in log-phase *Escherichia coli* is derived from metabolism. *Proc. Natl. Acad. Sci.* 102, 17337–17341. doi: 10.1073/pnas.0506531102

Li, H., Yu, C., Wang, F., Chang, S. J., Yao, J., and Blake, R. E. (2016). Probing the metabolic water contribution to intracellular water using oxygen isotope ratios of PO_4. *Proc. Natl. Acad. Sci.* 113, 5862–5867. doi: 10.1073/pnas.1521038113

Liang, Y., and Blake, R. E. (2006). Oxygen isotope signature of P-i regeneration from organic compounds by phosphomonoesterases and photooxidation. *Geochim. Cosmochim. Acta* 70, 3957–3969. doi: 10.1016/j.gca.2006.04.036

Liang, Y., and Blake, R. E. (2009). Compound-and enzyme-specific phosphodiester hydrolysis mechanisms revealed by [delta]18O of dissolved inorganic phosphate: implications for marine P cycling. *Geochim. Cosmochim. Acta* 73, 3782–3794. doi: 10.1016/j.gca.2009.01.038

Lis, H., Weiner, T., Pitt, F. D., Keren, N., and Angert, A. (2019). Phosphate uptake by Cyanobacteria is associated with kinetic fractionation of phosphate oxygen isotopes. *ACS Earth Space Chem* 3, 233–239. doi: 10.1021/acsearthspacechem.8b00099

Luz, B., and Kolodny, Y. (1985). Oxygen isotope variations in phosphate of biogenic apatites, IV. Mammal teeth and bones. *Earth Planet. Sci. Lett.* 75, 29–36. doi: 10.1016/0012-821X(85)90047-0

Manzoni, S., Taylor, P., Richter, A., Porporato, A., and Ågren, G. I. (2012). Environmental and stoichiometric controls on microbial carbon-use efficiency in soils. *New Phytol.* 196, 79–91. doi: 10.1111/j.1469-8137.2012.04225.x

Mine, A., Waldeck, A., Olack, G., Hoerner, M., Alex, S., and Colman, A. (2017). Microprecipitation and δ18O analysis of phosphate for paleoclimate and biogeochemistry research. *Chem. Geol.* 460, 1–14. doi: 10.1016/j.chemgeo.2017.03.032

Murphy, J., and Riley, J. P. (1962). A modified single solution method for the determination of phosphate in natural waters. *Anal. Chim. Acta* 27, 31–36. doi: 10.1016/S0003-2670(00)88444-5

Passey, B. H., and Levin, N. E. (2021). Triple oxygen isotopes in meteoric waters, carbonates, and biological apatites: implications for continental paleoclimate reconstruction. *Rev. Mineral. Geochem.* 86, 429–462. doi: 10.2138/rmg.2021.86.13

Pearson, P. N. (2012). Oxygen isotopes in foraminifera: overview and historical review. *Paleontol Soc Papers* 18, 1–38. doi: 10.1017/S1089332600002539

Pistocchi, C., Mészáros, É., Frossard, E., Bünemann, E. K., and Tamburini, F. (2020). In or out of equilibrium? How microbial activity controls the oxygen isotopic composition of phosphate in Forest organic horizons with low and high phosphorus availability. *Front Environ Sci.* 8:778. doi: 10.3389/fenvs.2020.564778

Pold, G., Domeignoz-Horta, L. A., and DeAngelis, K. M. (2020). Heavy and wet: the consequences of violating assumptions of measuring soil microbial growth efficiency using the 18O water method. *Elem Sci Anth* 8:069. doi: 10.1525/elementa.069

Sabat, P., Newsome, S. D., Pinochet, S., Nespolo, R., Sanchez-Hernandez, J. C., Maldonado, K., et al. (2021). Triple oxygen isotope measurements (Δ'17O) of body water reflect water intake, metabolism, and δ18O of ingested water in passerines. *Front. Physiol.* 12:26. doi: 10.3389/fphys.2021.710026

Shackleton, N. (1967). Oxygen isotope analyses and Pleistocene temperatures re-assessed. *Nature* 215, 15–17. doi: 10.1038/215015a0

Tamburini, F., Bernasconi, S. M., Angert, A., Weiner, T., and Frossard, E. (2010). A method for the analysis of the δ18O of inorganic phosphate extracted from soils with HCl. *Eur. J. Soil Sci.* 61, 1025–1032. doi: 10.1111/j.1365-2389.2010.01290.x

Tao, F., Huang, Y., Hungate, B. A., Manzoni, S., Frey, S. D., Schmidt, M. W. I., et al. (2023). Microbial carbon use efficiency promotes global soil carbon storage. *Nature* 618, 981–985. doi: 10.1038/s41586-023-06042-3

Tudge, A. (1960). A method of analysis of oxygen isotopes in orthophosphate—its use in the measurement of paleotemperatures. *Geochim. Cosmochim. Acta* 18, 81–93. doi: 10.1016/0016-7037(60)90019-3

von Sperber, C., Kries, H., Tamburini, F., Bernasconi, S. M., and Frossard, E. (2014). The effect of phosphomonoesterases on the oxygen isotope composition of phosphate. *Geochim. Cosmochim. Acta* 125, 519–527. doi: 10.1016/j.gca.2013.10.010

Wang, Z., Yang, J., Wang, C., and Bai, E. (2022). Oxygen gas derived oxygen does not affect the accuracy of 18O-labelled water approach for microbial carbon use efficiency. *Soil Biol. Biochem.* 168:108649. doi: 10.1016/j.soilbio.2022.108649

Yakir, D. (1992). Variations in the natural abundance of oxygen-18 and deuterium in plant carbohydrates. *Plant Cell Environ.* 15, 1005–1020. doi: 10.1111/j.1365-3040.1992.tb01652.x

frontiers | Frontiers in Microbiology

TYPE Mini Review
PUBLISHED 23 November 2023
DOI 10.3389/fmicb.2023.1304703

OPEN ACCESS

EDITED BY
Yizhi Sheng,
China University of Geosciences, China

REVIEWED BY
Long Hao,
Corrosion and Protection Center of Materials, Institute of Metal Research, Chinese Academy of Sciences, China
Qiao Yanxin,
Jiangsu University of Science and Technology, China

*CORRESPONDENCE
Yishan Jiang
jys130@126.com
Xin Zhao
13156239571@163.com

RECEIVED 29 September 2023
ACCEPTED 03 November 2023
PUBLISHED 23 November 2023

CITATION
Zhang Q, Jiang Y, Zhao X, Duan J, Chen L and Xu Y (2023) A new research proposal to prevent hydrogen embrittlement for nuclear waste container by bacteria-a mini review. *Front. Microbiol.* 14:1304703. doi: 10.3389/fmicb.2023.1304703

A new research proposal to prevent hydrogen embrittlement for nuclear waste container by bacteria-a mini review

Qichao Zhang[1,2], Yishan Jiang[1]*, Xin Zhao[1]*, Jizhou Duan[2], Luning Chen[1] and Ying Xu[1]

[1]Navy Submarine Academy, Qingdao, China, [2]CAS Key Laboratory of Marine Environment of Corrosion and Bio-fouling, Institute of Oceanology, Chinese Academy of Sciences, Qingdao, China

A large amount of nuclear waste produced in the process of nuclear energy utilization has always been a key problem to be solved urgently for nuclear safety. At present, "deep geological disposal" is a feasible method and generally accepted by many countries. The oxygen content in the near field environment of the waste container will decrease to anaerobic conditions, and hydrogen will permeation into the internal materials of container for a long time. Hydrogen evolution corrosion may cause a risk of hydrogen embrittlement. The harm of hydrogen embrittlement in metal container is far more severe than predictable uniform corrosion. It is a research hotspot that the microorganisms impact on the corrosion behavior of container materials in the deep geological environment. Microbial corrosion in deep geological environments can be divided into two types: aerobic microbial corrosion and anaerobic microbial corrosion. There is a type of hydrogen consuming microorganism in the natural environment that uses the oxidation of hydrogen as the energy for its life activities. This provides a new approach for us to study reducing the hydrogen embrittlement sensitivity of nuclear waste container materials.

KEYWORDS

microbial corrosion, hydrogen embrittlement, hydrogen consuming microorganisms, deep geological disposal, nuclear waste

Introduction

Nuclear energy has been widely used in fields such as medicine, national defense, agriculture, and industry due to its advantages of low cost, high efficiency and no greenhouse gas generation, greatly improving human life. However, high-level nuclear waste is an inevitable waste generated during the process of nuclear energy utilization, with characteristics such as high radioactivity, long half-life and high toxicity. The various high radioactive elements pose great harm to the human body and the biosphere. For example, technetium (Tc) is a problematic fission product, as its long half-life, high fission rate and environmental mobility of high technetium salts make long-term disposal of nuclear waste more complex (Lukens and Saslow, 2017). At present, countries are vigorously developing nuclear power plants, and the rapid development of nuclear power will inevitably generate more high-level nuclear waste. For China, it is expected to produce 3,000 m^2 high-level nuclear waste by 2030. Therefore, countries around the world have regarded efficient disposal of high-level nuclear waste as an important challenge for the development of the nuclear energy industry (Wang et al., 2004).

Regarding the disposal plan for high-level nuclear waste, researchers have proposed "deep seabed disposal," "frozen disposal," "hydraulic cage disposal," "space disposal" and "deep geological disposal" (Arup, 1985; Milnes, 1985; Pang, 1989; Gao, 1995; Bradley, 1997; Shen, 2002). At present, the widely accepted solution in various countries is the deep geological disposal method, which means that high-level nuclear waste is disposed of in a suitable rock mass storage warehouse at a depth of about 500–1,000 meters from the surface, forming a "multi-barrier system" consisting of solidified high-level nuclear waste, metal container and buffer backfill materials, as well as surrounding rock and its geological environment, forming a natural barrier (SKB, 2001; Wang et al., 2005; Duquette et al., 2009). Metal container is particularly important as the first barrier for nuclear waste. Titanium and its alloys are one of the alternative materials for container due to their excellent corrosion resistance. Canada and Japan have used titanium and its alloys as alternative materials for container and have conducted extensive research (Tsujikawa and Kojima, 1990; He et al., 2002). Currently, the United States plans to use titanium droplet shields on nickel alloy containers at Yucca Mountain (Hua et al., 2005a,b, 2008; Mon, 2008; Rebak, 2009). Carbon steel has also been used as an alternative material for container in Japan, South Korea and Canada due to its advantages of simple processing and low cost (King and Padovani, 2011).

The container corrosion is closely related to the surrounding environment. The factors that affect container corrosion in deep geological environments mainly include oxygen content (partial interception of oxygen by the closed storage), temperature (decay heat release of nuclear waste), radiation (strong radioactivity of nuclear waste), microbial activity, etc. However, the near field environment of the container may change over time, for example, the oxygen content may decrease to anaerobic conditions. Winsley et al. (2011) believe that when the oxygen content around the container decreases to low oxygen concentration environmental conditions, hydrogen evolution corrosion dominates. Long term permeation of hydrogen into the interior of container materials may cause a risk of hydrogen embrittlement (HE). The good corrosion resistance of titanium and its alloys depends on the formation of a stable oxide film on their surface. If exposed to hydrogen environments, titanium is highly susceptible to hydrogen absorption. Dwivedi and Vishwakarma classified titanium as a material susceptible to HE (Dwivedi and Vishwakarma, 2018). Meanwhile, hydrogen will react with titanium and hydrides formed (Qiao et al., 2021). The titanium hydrides show brittleness. Research has shown that hydrogen ions can also be reduced and hydrogen can penetrate into carbon steel under aerobic corrosion conditions (Huang and Zhu, 2005; Tsuru et al., 2005). Therefore, hydrogen evolution corrosion will accompany the whole process of container corrosion. The harm of HE in metal container is far more severe than predictable uniform corrosion, so it is particularly important to reduce the HE sensitivity of metal container materials.

Microbial corrosion of container

The impact of microorganisms on the corrosion behavior of container materials in the deep geological environment is currently a research hotspot. Microbial corrosion refers to the life activities of microorganisms attached to the biofilm on the surface of a material, leading to or promoting the corrosion and destruction of the material. The attachment of biofilms and the presence of metabolites alter the anodic or cathodic reaction kinetics at the metal/solution interface, leading to accelerated corrosion of metal materials (Ornek et al., 2002).

Corrosive microorganisms are often participants in the iron sulfur cycle in the environment (Huang et al., 2017). According to the types and functions of bacteria, they can be divided into sulfate reducing bacteria (SRB), sulfur oxidizing bacteria (SOB), acid producing bacteria (APB), iron oxidizing bacteria (IOB), iron reducing bacteria (IRB), nitrate reducing bacteria (NRB) and slime producing bacteria (SFB).

There are currently several main mechanisms of microbial corrosion.

(1) Cathodic depolarization theory

The cathodic depolarization theory (von Wolzogen and van der Vlugt, 1934) suggests that a "hydrogen film" will adhere to the metal surface in anaerobic environments due to the cathodic hydrogen evolution reaction, ultimately hindering the metal corrosion. This obstruction is often referred to "polarization." SRB can be adsorbed on metal surfaces and utilize the cathodic hydrogen on the metal surface through hydrogenase in the body to reduce local hydrogen partial pressure. This "depolarization" makes metal corrosion continue. The hydrogen consumption of SRB plays a role in cathodic depolarization. The relevant reactions are as follows:

Anode reaction

$$8H_2O \rightarrow 8H^+ + 8OH^- \quad (1)$$

$$4Fe + 8H^+ \rightarrow 4Fe^{2+} + 8[H] \quad (2)$$

Hydrogen depolarization of hydrogenase

$$H_2SO_4 + 8[H] \rightarrow H_2S + H_2O \quad (3)$$

Corrosion products

$$3Fe^{2+} + 6OH^- \rightarrow 3Fe(OH)_2 \quad (4)$$

Total reaction

$$4Fe + H_2SO_4 + 2H_2O \rightarrow 3Fe(OH)_2 + FeS \quad (5)$$

(2) Metabolite corrosion mechanism

Microorganisms have metabolic diversity. Therefore, the metabolites of microorganisms also have diversity, including some metabolites that can promote corrosion. For example, the metabolite H_2S of SRB can react quickly with metal iron to generate FeS (Li et al., 2014), accelerating corrosion. The sulfide metabolites of microorganisms can also react with Fe^{2+} generated during the corrosion process to form a loose iron sulfur (FeS_x) composite layer, which has no protective effect on metals compared to a dense FeS protective film (Liu et al., 2009). In addition, the acidic metabolites of acid producing bacteria can reduce the pH value in the environment, which is prone to serious pore corrosion and pore leakage.

(3) Concentration cell mechanism

The growth and metabolism process of microorganisms can establish various concentration batteries on metal surfaces, such as oxygen concentration batteries, metal ion concentration batteries, activation and passivation batteries, etc. The presence of concentration batteries can cause local corrosion of metals. For example, that an oxygen concentration cell with a positive potential in the rich oxygen region as the cathode and a negative potential in the poor oxygen region as the anode is formed because of the differences in oxygen consumption among different bacterial colonies within the biofilm leads to accelerated corrosion in the poor oxygen region (Abdolahi et al., 2014).

(4) Direct or indirect electronic transmission

Some microorganisms can utilize cytochrome C proteins on the surface of cell membranes and biological nanowires to directly obtain electrons from metal surfaces (Dinh et al., 2004; Reguera et al., 2005), thereby accelerating corrosion. In addition, some microorganisms can efficiently indirectly transfer extracellular electrons through reversible redox active electron mediators, For example, the phenazine like substances of Pseudomonas and the flavin like substances secreted by Shewanella (Huang et al., 2017) perform efficient indirect extracellular electron transfer, thereby accelerating metal corrosion.

Overall, there are two types of microbial corrosion in the deep geological environment of nuclear waste container. One is that in the early stages of disposal, there is a high oxygen content in the deep geological environment and aerobic microbial corrosion occurs; One is that in the medium to long term of disposal, the oxygen content decreases to an anaerobic environment, resulting in anaerobic microbial corrosion. Figure 1 shows the variation of microbial corrosion types with oxygen concentration in deep geological environments.

Aerobic conditions will certainly prevail during the repository operating phase. Many aerobic bacteria produce metabolites which can be corrosive for metallic materials in general and steels in particular (Féron and Crusset, 2014). An estimation of corrosion due to ferro-oxidizing bacteria was made on a carbon steel (Pitonzo et al., 2004) exposed to synthetic solutions representative of the waters of Yucca Mountain site (same pH, same redox and same concentration of main ions). Electrochemical measurements showed decreasing corrosion rates with time. After 1 month of testing, the mean rate of corrosion is 58 mm/year (while corrosion rate of around 30 mm/year is found on carbon steel coupons immersed in the same synthetic aqueous solutions without bacteria). Shrestha et al. examined microbial corrosion of carbon steel in synthetic bentonite pore water inoculated with natural underground water containing microorganisms over a period of 780-days under sterile and anaerobic conditions (Shrestha et al., 2021). The results indicate that nitrate-reducing bacteria could represent a potential threat to waste canisters under nuclear repository conditions.

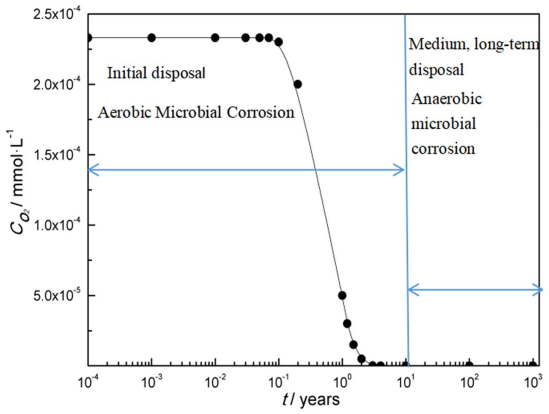

FIGURE 1
Microbial corrosion types vary with oxygen content.

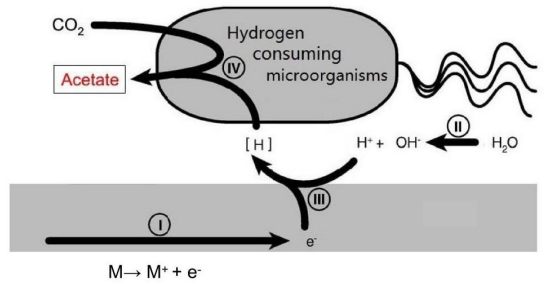

FIGURE 2
Schematic illustration of the mutual effects between hydrogen consuming organisms and metal surface.

Hydrogen consuming microorganisms reduce hydrogen embrittlement sensitivity

Currently, most research is focused on the issue of microbial accelerated corrosion of nuclear waste container. However, there is little research on whether certain microorganisms exist in deep geological environments that can reduce the corrosion rate of container materials. There is a type of hydrogen consuming microorganism in the natural environment that uses hydrogen oxidation as the energy for its life activities. This provides a new approach for us to study reducing the HE sensitivity of nuclear waste container materials (Figure 2).

Collet et al. (2005) studied the effect of hydrogen consuming microorganisms on the metabolism of Clostridium thermophilum. Experiments have shown that hydrogen consuming microorganisms such as Methanothermophyter thermophilus and Moorella thermophilica increase acetic acid production by three times. Thermophilic Lactobacillus not only produces acetic acid but also by-products such as hydrogen, carbon dioxide, and lactic acid when metabolizing lactose. Thermophilic autotrophic methane bacteria play an important role as effective hydrogen removal agents, which can significantly reduce the partial pressure of hydrogen in the system and convert hydrogen into methane. Moorella thermautotrophica converts hydrogen, lactic acid, and carbon dioxide into acetic acid. Hoehler et al. (2001) involved a hydrogen consuming microbial methane producing archaea when studying the apparent minimum free energy required by microorganisms in hypoxic marine sediments. Homoacetic acid bacteria are also hydrogen consuming microorganisms, and Kotsyurbenko et al. (2001) studied their competitive behavior with methanogenic archaea for hydrogen in

anaerobic environments. Lin et al. (2014) suggests that basalt aquifers on the seafloor can support hydrogen driven ecosystems. Feng et al. (2014) and Zhao (2012) conducted an experimental research on the enhancement of methane production during anaerobic digestion of sludge by adding 0 valent iron. The reason for the enhancement was that hydrogen consuming bacteria utilized hydrogen produced by iron corrosion. Mori et al. (2010) isolated 26 microbial species from petroleum facilities. The hydrogen consuming microorganisms do not have a strong promoting effect on the corrosion of iron, while the other non hydrogen consuming microorganisms cause severe corrosion of iron. These are the only literature found on hydrogen consuming microbial corrosion. Nybo et al. (2015) reviewed the use of chemotrophic autotrophic microorganisms to immobilize greenhouse gasses in the production of fuels and chemical products, which also require hydrogen consumption. There are also literature (Giblin et al., 2000; Libert et al., 2011) on the research of microbial engineering using hydrogen consuming microorganisms. It can be seen that hydrogen consuming microorganisms are widely present in nature. If the hydrogen consumption effect of these hydrogen consuming microorganisms can be utilized to consume the hydrogen generated during natural corrosion processes and reduce the diffusion of hydrogen into the metal interior, the HE possibility in metal materials can be reduced. Although microorganisms do not have a significant impact on the corrosion behavior of titanium and its alloys, if hydrogen consuming microorganisms in deep geological environments can consume excess hydrogen atoms on their surfaces, this will reduce the combination hydride of hydrogen and titanium, which is the main cause of HE in titanium and its alloys.

Conclusion

In summary, the cathodic reaction of corrosion has shifted from oxygen absorption corrosion to hydrogen evolution corrosion due to the continuous consumption of oxygen, so there is a possibility of long-term HE in metal container during nuclear waste disposal. Unpredictable HE often has a more severe impact on nuclear waste container materials than predictable uniform corrosion. Hydrogen consuming microorganisms exist in deep geological environments, which use hydrogen oxidation as their energy for life activities. If these hydrogen consuming microorganisms can consume the hydrogen atoms generated during the natural corrosion process of the container material, thereby preventing hydrogen from permeation into the interior of the container material, greatly reducing the possibility of HE. However, most current research has focused on microbial accelerated corrosion rate of container materials in deep geological environments, only considering the adverse factors of microorganisms. However, the presence of hydrogen consuming microorganisms provides a new approach for studying the reduction of HE sensitivity for nuclear waste container materials.

Author contributions

QZ: Writing – original draft. YJ: Funding acquisition, Supervision, Writing – review & editing. XZ: Supervision, Writing – review & editing. JD: Investigation, Supervision, Writing – review & editing. LC: Writing – review & editing. YX: Writing – review & editing.

Funding

The author(s) declare financial support was received for the research, authorship, and/or publication of this article. This work was financially supported by the Natural Science Foundation of Shandong Province under grant no. ZR2022QE131.

Conflict of interest

The authors declare that the research was conducted in the absence of any commercial or financial relationships that could be construed as a potential conflict of interest.

Publisher's note

References

Abdolahi, A., Hamzah, E., Ibrahim, Z., and Hashim, S. (2014). Microbially influenced corrosion of steels by *Pseudomonas aeruginosa*. *Corros. Rev.* 32, 129–141. doi: 10.1515/corrrev-2013-0047

Arup, O. (1985). *Ocean disposal of radioactive waste by penetrator emplacement*. Graham & Trotman Ltd.. London

Bradley, D. J. (1997). Behind the nuclear curtain: radioactive waste management in the former soviet union. *Phys. Today* 51:63. doi: 10.1063/1.882248

Collet, C., Gaudard, O., Péringer, P., and Schwitzguébel, J. P. (2005). Acetate production from lactose by Clostridium thermolacticum and hydrogen-scavenging microorganisms in continuous culture—effect of hydrogen partial pressure. *J. Biotechnol.* 118, 328–338. doi: 10.1016/j.jbiotec.2005.05.011

Dinh, H. T., Kuever, J., Mußmann, M., Hassel, A. W., Stratmann, M., and Widdel, F. (2004). Iron corrosion by novel anaerobic microorganisms. *Nature* 427, 829–832. doi: 10.1038/nature02321

Duquette, D. J., Latanision, R. M., di Bella, C. A. W., and Kirstein, B. E. (2009). Corrosion issues related to disposal of high-level nuclear waste in the yucca mountain repository-peer reviewer's perspective. *Corrosion* 65, 272–280. doi: 10.5006/1.3319133

Dwivedi, S. K., and Vishwakarma, M. (2018). Hydrogen embrittlement in different materials: a review. *Int. J. Hydrog. Energy* 43, 21603–21616. doi: 10.1016/j.ijhydene.2018.09.201

Feng, Y., Zhang, Y., Quan, X., and Chen, S. (2014). Enhanced anaerobic digestion of waste activated sludge digestion by the addition of zero valent iron. *Water Res.* 52, 242–250. doi: 10.1016/j.watres.2013.10.072

Féron, D., and Crusset, D. (2014). Microbial induced corrosion in French concept of nuclear waste underground disposal. *Corros. Eng. Sci.* 49, 540–547. doi: 10.1179/1743278214Y.0000000193

Gao, Z. L. (1995). Send nuclear waste into space. *Rev. World Inv.* 11, 12–15.

Giblin, T. L., Herman, D. C., and Frankenberger, W. T. (2000). Removal of Perchiorate from ground water by hydrogen-utilizing Bacteria. *J. Environ. Qual.* 29, 1057–1062. doi: 10.2134/jeq2000.00472425002900040004x

He, X., Noël, J. J., and Shoesmith, D. W. (2002). Temperature dependence of crevice corrosion initiation on titanium grade-2. *J. Electrochem. Soc.* 149, B440–B449. doi: 10.1149/1.1499501

Hoehler, T. M., Alperin, M. J., Albert, D. B., and Martens, C. S. (2001). Apparent minimum free energy requirements for methanogenic Archaea and sulfate-reducing bacteria in an anoxic marine sediment. *FEMS Microbiol. Ecol.* 38, 33–41. doi: 10.1111/j.1574-6941.2001.tb00879.x

Hua, F., De, G. C., and Gordon, G. M., (2005a). *Hydrogen induced cracking of titanium alloys in environments anticipated in Yucca Mountain nuclear waste repository*. Houston, Texas: Paper presented at the corrosion.

Hua, F., Mon, K., De, G., Gordon, G., and Andresen, P. L. (2008). The potential for the SCC of titanium alloys under repository-relevant environments for US nuclear waste. *JOM* 60, 66–72. doi: 10.1007/s11837-008-0010-6

Hua, F., Mon, K., Pasupathi, P., Gordon, G., and Shoesmith, D. (2005b). A review of corrosion of titanium grade 7 and other titanium alloys in nuclear waste repository environments. *Corrosion* 61, 987–1003. doi: 10.5006/1.3280899

Huang, Y., Liu, S. J., and Jiang, C. Y. (2017). Microbiologically influenced corrosion and mechanisms. *J. Microbiol.* 44, 1699–1713.

Huang, Y. L., and Zhu, Y. Y. (2005). Hydrogen ion reduction in the process of iron rusting. *Corros. Sci.* 47, 1545–1554. doi: 10.1016/j.corsci.2004.07.044

King, F., and Padovani, C. (2011). Review of the corrosion performance of selected canister materials for disposal of UK HLW and/or spent fuel. *Corros. Eng. Sci. Techn.* 46, 82–90. doi: 10.1179/1743278211Y.0000000005

Kotsyurbenko, O. R., Glagolev, M. V., Nozhevnikova, A. N., and Conrad, R. (2001). Competition between homoacetogenic bacteria and methanogenic archaea for hydrogen at low temperature. *FEMS Microbiol. Ecol.* 38, 153–159. doi: 10.1111/j.1574-6941.2001.tb00893.x

Li, D. P., Zhang, L., Yang, J. W., Lu, M. X., Ding, J. H., and Liu, M. L. (2014). Effect of H_2S concentration on the corrosion behavior of pipeline steel under the coexistence of H_2S and CO_2. *Int. J. Miner. Metall.* 21, 388–394. doi: 10.1007/s12613-014-0920-y

Libert, M., Bildstein, O., Esnault, L., Jullien, M., and Sellier, R. (2011). Molecular hydrogen: an abundant energy source for bacterial activity in nuclear waste repositories. *Phys. Chem. Earth* 36, 1616–1623. doi: 10.1016/j.pce.2011.10.010

Lin, H. T., Cowen, J. P., Olson, E. J., Lilley, M. D., Jungbluth, S. P., Wilson, S. T., et al. (2014). Dissolved hydrogen and methane in the oceanic basaltic biosphere. *Earth Planet. Sci. Lett.* 405, 62–73. doi: 10.1016/j.epsl.2014.07.037

Liu, T., Liu, H., Hu, Y., Zhou, L., and Zheng, B. (2009). Growth characteristics of thermophile sulfate-reducing bacteria and its effect on carbon steel. *Mater. Corros.* 60, 218–224. doi: 10.1002/maco.200805063

Lukens, W. W., and Saslow, S. A. (2017). Aqueous synthesis of technetium-doped titanium dioxide by direct oxidation of titanium powder, a precursor for ceramic nuclear waste forms. *Chem. Mater.* 29, 10369–10376. doi: 10.1021/acs.chemmater.7b03567

Milnes, A. G. (1985). *Geology and Radwaste*. New York: Academic Press INC.

Mon, K. G. (2008). "Potential SCC initiation and propagation in titanium alloys under U.S. nuclear waste repository environmental conditions." *17th International Corrosion Congress*. Las Vegas, Nevada.

Mori, K., Tsurumaru, H., and Harayama, S. (2010). Iron corrosion activity of anaerobic hydrogen-consuming microorganisms isolated from oil facilities. *J. Biosci. Bioeng.* 110, 426–430. doi: 10.1016/j.jbiosc.2010.04.012

Nybo, S. E., Khan, N. E., Woolston, B. M., and Curtis, W. R. (2015). Metabolic engineering in chemolithoautotrophic hosts for the production of fuels and chemicals. *Metab. Eng.* 30, 105–120. doi: 10.1016/j.ymben.2015.04.008

Ornek, D., Wood, T. K., Hsu, C., Sun, Z., and Mansfeld, F. (2002). Pitting corrosion control of aluminum 2024 using protective biofilms that secrete corrosion inhibitors. *Corrosion* 58, 761–767. doi: 10.5006/1.3277659

Pang, W. K. (1989). Introduction of nuclear waste treatment method. *Geol. Sci. Technol. Inf.* 1, 143–148.

Pitonzo, B. J., Castro, P., Amy, P. S., Southam, G., Jones, D. A., and Ringelberg, D. (2004). Microbiologically influenced corrosion capability of bacteria isolated from Yucca mountain. *Corrosion* 60, 64–74. doi: 10.5006/1.3299233

Qiao, Y., Xu, D., Wang, S., Ma, Y., Chen, J., Wang, Y., et al. (2021). Effect of hydrogen charging on microstructural evolution and corrosion behavior of Ti-4Al-2V-1Mo-1Fe alloy. *J. Mater. Sci. Technol.* 60, 168–176. doi: 10.1016/j.jmst.2020.06.010

Rebak, R. B. (2009). Corrosion testing of nickel and titanium alloys for nuclear waste disposition. *Corrosion* 65, 252–271. doi: 10.5006/1.3319132

Reguera, G., McCarthy, K. D., Mehta, T., Nicoll, J. S., Tuominen, M. T., and Lovley, D. R. (2005). Extracellular electron transfer via microbial nanowires. *Nature* 435, 1098–1101. doi: 10.1038/nature03661

Shen, Z. Y. (2002). Method to treatment and disposal HLW. *Radiat. Protecti. Bull.* 22, 37–39.

Shrestha, R., Černoušek, T., Stoulil, J., Kovářová, H., Sihelská, K., Špánek, R., et al. (2021). Anaerobic microbial corrosion of carbon steel under conditions relevant for deep geological repository of nuclear waste. *Sci. Total Environ.* 800:149539. doi: 10.1016/j.scitotenv.2021.149539

SKB. (2001). *Sea disposal of radioactive wastes (technical report TR-01-30)*. Vienna: IAEA Bulletin.

Tsujikawa, S., and Kojima, Y. (1990). Repassivation method to predict long term integrity of low alloy titanium for nuclear waste package. *Mater. Res. Soc. symp. proc.* 212, 261–268. doi: 10.1557/PROC-212-261

Tsuru, T., Huang, Y. L., Ali, M. R., and Nishikata, A. (2005). Hydrogen entry into steel during atmospheric corrosion process. *Corros. Sci.* 47, 2431–2440. doi: 10.1016/j.corsci.2004.10.006

von Wolzogen, K. C. A. H., and van der Vlugt, I. S. (1934). The graphitization of cast iron as an electrobiochemical process in anaerobic soils. *Water* 1934, 147–165.

Wang, J., Fan, X. H., and Xu, G. G.. (2004). *Ten years progress of geological disposal of high level radioactive waste in China*. Beijing: Atomic Energy Press.

Wang, J., Xu, G. Q., and Fang, H. L. (2005). Geological disposal of high level radioactive waste in China: Progress during 1985-2004. *World Nucl. Geosci.* 22, 5–16.

Winsley, R. J., Smart, N. R., Rance, A. P., Fennell, P. A. H., Reddy, B., and Kursten, B. (2011). Further studies on the effect of irradiation on the corrosion of carbon steel in alkaline media. *Corros. Eng. Sci. Techn.* 46, 111–116. doi: 10.1179/1743278210Y.0000000010

Zhao, D. (2012). *Experimental study on hydrogen evolution enhancement of methane yield in iron corrosion*. Beijing Institute of Architecture and Engineering. Beijing

frontiers | Frontiers in Microbiology

TYPE Original Research
PUBLISHED 17 May 2024
DOI 10.3389/fmicb.2024.1352792

OPEN ACCESS

EDITED BY
Ruiyong Zhang,
Chinese Academy of Sciences (CAS), China

REVIEWED BY
Carolina Keim,
Federal University of Rio de Janeiro, Brazil
Yizhi Sheng,
China University of Geosciences, China

*CORRESPONDENCE
Markus Gastauer
✉ markus.gastauer@itv.org

RECEIVED 08 December 2023
ACCEPTED 26 April 2024
PUBLISHED 17 May 2024

CITATION
da Silva RdSS, Cardoso AF, Angelica RS, Bitencourt JAP, Moreira JCF, Lucheta AR, Prado IGdO, Candela DRS and Gastauer M (2024) Enhancing iron biogeochemical cycling for *canga* ecosystem restoration: insights from microbial stimuli. *Front. Microbiol.* 15:1352792. doi: 10.3389/fmicb.2024.1352792

Enhancing iron biogeochemical cycling for *canga* ecosystem restoration: insights from microbial stimuli

Rayara do Socorro Souza da Silva[1,2], Aline Figueiredo Cardoso[3], Rômulo Simões Angelica[2], José Augusto P. Bitencourt[3], Julio Cezar Fornazier Moreira[1], Adriano Reis Lucheta[1], Isabelle Gonçalves de Oliveira Prado[3], Dalber Ruben Sanchez Candela[4] and Markus Gastauer[3]*

[1]Instituto SENAI de Inovação em Tecnologias Minerais, Belém, Brazil, [2]Instituto de Geociências, Universidade Federal do Pará, Belém, Brazil, [3]Instituto Tecnológico Vale, Belém, Brazil, [4]Instituto de Física, Universidade Federal Fluminense, Rio de Janeiro, Brazil

Introduction: The microbial-induced restoration of ferruginous crusts (*canga*), which partially cover iron deposits and host unique ecosystems, is a promising alternative for reducing the environmental impacts of the iron mining industry.

Methods: To investigate the potential of microbial action to accelerate the reduction and oxidation of iron in substrates rich in hematite and goethite, four different microbial treatments (water only as a control – W; culture medium only – MO; medium + microbial consortium – MI; medium + microbial consortium + soluble iron – MIC) were periodically applied to induce iron dissolution and subsequent precipitation. Except for W, all the treatments resulted in the formation of biocemented blocks.

Results: MO and MI treatments resulted in significant goethite dissolution, followed by precipitation of iron oxyhydroxides and an iron sulfate phase, due to iron oxidation, in addition to the preservation of microfossils. In the MIC treatment, biofilms were identified, but with few mineralogical changes in the iron-rich particles, indicating less iron cycling compared to the MO or MI treatment. Regarding microbial diversity, iron-reducing families, such as Enterobacteriaceae, were found in all microbially treated substrates.

Discussion: However, the presence of Bacillaceae indicates the importance of fermentative bacteria in accelerating the dissolution of iron minerals. The acceleration of iron cycling was also promoted by microorganisms that couple nitrate reduction with Fe(II) oxidation. These findings demonstrate a sustainable and streamlined opportunity for restoration in mining areas.

KEYWORDS

duricrust, biocementation, microfossils, iron minerals, sustainable mining, Serra dos Carajás

Highlights

- Iron-rich particles aggregate in response to different microbial stimuli by forming biofilms.
- Microbial action alters the levels of iron oxyhydroxides and results in the formation of biominerals.
- The growth of biofilms between grains consolidates *canga* fragments.
- Cellular structures provide active sites for mineral nucleation.
- Microorganisms with fermentative and respiratory metabolisms concomitantly contribute to the formation of biocements.

1 Introduction

Some of the largest iron ore deposits in the world are covered by ferruginous crusts generally outcropping on mountaintops, such as those in the Iron Quadrangle and the Serra dos Carajás, Brazil, or the Province of Hamersley, Australia (Dorr, 1964; Hagemann et al., 2016). These ferruginous crusts, also known as duricrust, *canga*, ferricrete, or ironstone, consist of a variety of materials bound together by iron oxyhydroxides, making them resistant to erosion (Dorr, 1964; Freyssinet et al., 2005; Shuster et al., 2012). Unique, ancient, and mega-diverse savanna-type ecosystems, containing dozens of microendemic species (Giulietti et al., 2019), have developed under the restricted environmental conditions provided by *canga* (Gibson et al., 2010; Jacobi and do Carmo, 2011). To reduce the impacts of mining on biodiversity and ecosystem services and make iron mining more sustainable, effective methods for *canga* duricrust restoration are needed (Gastauer et al., 2019).

Geochemical and geochronological evidence suggests that the ferruginous crusts from the Iron Quadrangle and Serra dos Carajás were formed through repeated cycles of iron mineral dissolution and reprecipitation triggered by, among other factors, iron-reducing microorganisms (biocementation). Goethite formation within *cangas* ranges from ~80 Ma to 1 Ma, with younger ages closer to the surface and progressively older ages toward the saprolite, indicating the importance of biological processes for iron cycling (Monteiro et al., 2014, 2018; Gagen et al., 2019a). Near the surface, locally anaerobic conditions facilitate the dissolution of iron oxyhydroxides through iron reduction induced by microorganisms. During this process, Fe(III) serves as an electron acceptor in microbial respiration, oxidizing hydrogen or carbon compounds (Lovley, 1991; Kappler et al., 2021; Dong et al., 2023). As the environment shifts toward aerobic conditions, Fe(II) oxidizes back to ferric iron and precipitates, generating biocements (Zammit et al., 2015). Although the natural cycling of iron minerals in ferruginous crusts has developed over millions of years, laboratory experiments have demonstrated that this process can be accelerated by microbial activity (Gagen et al., 2020; Levett et al., 2020a).

Recent studies have identified the presence of iron-reducing bacteria in Serra dos Carajás across various environments, suggesting their widespread distribution (Gagen et al., 2020; Cardoso et al., 2023). The cultivation of these microorganisms can be promising for *canga* restoration, thereby fostering sustainable mining. Here, we aimed to examine the mineralogical alterations in an iron-rich substrate subjected to repeated cycles of irrigation and desiccation in the laboratory using three different microbial stimuli and a control treatment (W: water as a control, MO: culture medium only, MI: culture medium + iron reducing microbial consortium, MIC: culture medium + iron reducing microbial consortium + dissolved iron). We examined alterations in substrate texture using stereomicroscopy and scanning electron microscopy and carried out chemical analysis of the substrates from the distinct treatments. Furthermore, we used XRD and Mössbauer spectroscopy to track alterations in mineralogical composition. Additionally, we analyzed the composition of the iron-reducing microbial consortium, as well as the composition of the bacterial communities in the iron-rich substrate. We expected that the stimulation of microorganisms together with repeated cycles of dissolution and subsequent precipitation of iron in all treatments except W would trigger alterations of the substrates and lead to their cementation and cohesion.

2 Materials and methods

2.1 Experimental setup

To induce biocementation under controlled conditions, we irrigated an iron-rich substrate three times per week to simulate short cycles of waterlogging (anaerobic conditions for iron reduction) and desiccation (aerobic conditions for iron precipitation) for 5 months. We used a control treatment (W: water only) and three different microbial stimuli (MO: culture medium only, MI: culture medium + iron-reducing microbial consortium, MIC: culture medium + consortium + dissolved iron). All treatments were tested in triplicate; replicates were placed in an incubator (Innova® 42) throughout the experiment at 28°C (Supplementary Figure S1).

The culture media for the MO, MI, and MIC treatments were DSMZ 579 (2.5 gL^{-1} $NaHCO_3$; 1.5 gL^{-1} NH_4Cl; 0.60 gL^{-1} NaH_2PO_4; 0.1 gL^{-1} KCl), supplemented with 10 mL.L^{-1} of each vitamin and micronutrient [DSMZ 141: 10 gL^{-1} $ZnSO_4.7H_2O$; 1.0 gL^{-1} $CuSO_4.5H_2O$; 1.0 gL^{-1} $MnSO_4.4H_2O$; 1.0 gL^{-1} $CoSO_4.7H_2O$; 0.5 gL^{-1} $Cr_2(SO_4)_3.15H_2O$; 0.6 gL^{-1} H_3BO_3; 0.5 gL^{-1} $Na_2MoO_4.2H_2O$; 1.0 gL^{-1} $NiSO_4.6H_2O$; 1.0 gL^{-1} $Na_2SeO_4.10H_2O$; 0.1 gL^{-1} $Na_2WO_4.2H_2O$; 0.1 gL^{-1} $NaVO_3$]. The culture media was sterilized by autoclaving for 15 min at 121°C. The MO and MI treatments were supplemented with a glucose solution (10 mM), while the MIC was enriched with Fe(III) citrate (50 mM) and Na-acetate (30 mM). The pH of the solutions was adjusted to 6.8 using 1 M H_2SO_4, and oxygen was removed to maintain anaerobic conditions by flushing N_2 (filtered through Millex® filter 0.22 µm) into the system with a purge. All treatments were set up using carefully sealed 1 L Schott bottles.

The microbial consortia utilized in both the MI and MIC treatments consisted of a blend of 4-SS and 6-SN consortia, which were previously chosen for their iron-reducing capabilities (Cardoso et al., 2023). Each treatment was inoculated with 50 mL of each consortium, with a starting concentration of at least 2×10^5 CFU mL^{-1}. The total volume was adjusted to 1 L with the culture medium described above. These microbial cultures were then incubated in a shaker chamber at a constant temperature of 28°C and 163 rpm throughout the experiment.

The concentration of dissolved Fe(II) from the MI and MIC cultures was measured monthly by spectrophotometry using the modified ferrozine assay of Lovley and Phillips (1986). For

evaluation, 0.1 mL samples were taken in triplicate from the microbial cultures and acidified with 5 mL of 0.5 M HCl. Additionally, a control sample consisting of the same culture medium but without the microbial consortium was prepared following the same protocol. After allowing the samples to rest for 15 min, 0.2 mL of the mixture was homogenized with 2 mL of ferrozine (1 gL^{-1} in 50 mM HEPES) and filtered through a filter with a pore size of 0.2 µm. The absorbance was measured at 562 nm and compared with that of known standard concentrations of Fe(II) prepared with ferrous sulfate. In the MIC culture, the Fe(II) concentration oscillated between 2 and 3 mM, while the dissolved Fe(II) in the MI culture was below detection limit throughout the experiment (Supplementary Figure S1).

For biocementation, crushed ferruginous crusts from one of the Serra Norte mining fronts were selected as substrates. Prior to the experiment, an XRD analysis (for methodological details, see section 2.2) of the substrate indicated the presence of hematite, goethite, gibbsite, and anatase in its composition (Supplementary Figure S2). Prior to the experiment, the substrate was sieved with an electromechanical shaker to withdraw particles larger than 4 mm. Subsequently, approximately 8.4 kg of this fraction was split in equal parts into 12 plastic containers (3 cm × 11 cm × 11 cm).

Each plastic container received 15 mL of one of the solutions described above per application (3x per week); this corresponds to a precipitation of 1.3 Lm^{-2} per application. This process was sufficient to humidify the substrate and create local anaerobic conditions to trigger iron reduction. After 5 months of periodic irrigation, the boxes remained for 1 month without receiving irrigation, aiming at dehydration for the final consolidation of the substrates. After this period, samples were collected for subsequent analyses.

2.2 X-ray diffraction (XRD)

To quantify the mineralogical changes of the substrates in each treatment, analysis was performed by X-ray diffraction (XRD) using the powder method and backloading preparation. The analysis was performed with a PANalytical Empyrean diffractometer (CoTube, 1 = 1.78901 Å; Long Fine Focus, Fe Kβ Filter, PIXcel3D-Medpix3 1×1 detector) in scanning mode with a voltage of 40 kV and current of 30 mA. For the Rietveld refinement, the following parameters were used: step size of 0.0130° in 2θ, scan from 4° to 109° in 2θ, time/step of 68.6 s, divergent slit: 1/8° and anti-scattering: 1/4°, and mask: 10 mm. The mineral phases were identified and quantified using the International Center for Diffraction Data (ICDD) database with X'Pert HighScore 3.0 software.

2.3 Mössbauer spectroscopy

^{57}Fe Mössbauer spectroscopy was performed to quantify the major iron-bearing phases (>1%) in the transmission geometry. For that, the samples were kept at 4 K inside a close cycle Janis cryostat with the Co-57 source (in the Rh-matrix) moving sinusoidally at room temperature. All the isomer shift IS values were obtained relative to those of metallic iron. These tests were performed in the laboratory of the Physics Institute of the Fluminense Federal University.

2.4 Microtextural analysis

Petrographic sections from consolidated samples (treatments MO, MI, and MIC), polished to a thickness of 30 µm, were embedded in Araldite resin. Sections were analyzed under a Zeiss SteREO Discovery V12 stereomicroscope coupled with a Zeiss Axiocam 712 camera (12 megapixels). These samples were then analyzed with a scanning electron microscope (Zeiss, Sigma-VP) equipped with energy dispersion X-ray spectroscopy (EDS, IXRF Sedona-SD) at an acceleration voltage of 20 kV.

To image biofilms after the experiment, millimetric pieces of consolidated and unconsolidated samples from all treatments were fixed in 2.5% glutaraldehyde with phosphate buffer solution (PBS) for at least 2 h, followed by rinsing with PBS. Dehydration was carried out with different concentrations of ethyl alcohol (50, 60, 70, 80, 90%, and 2 × 100%), with subsequent drying at the critical point (Leica CPD 300). To improve the electrical conductivity, all the samples were previously coated with 15 nm of gold using an Emitech K550X sputter coater. Measurements of the cell structures in the SEM images were carried out with ImageJ software.

2.5 Whole-substrate chemistry

Chemical analysis of the total sample to determine the major, minor, and trace elements, including rare earth elements, was performed by SGS Laboratories. To investigate the chemical behavior under different stimuli. The major elements (SiO_2, Al_2O_3, Fe_2O_3, CaO, MgO, Na_2O, K_2O, TiO_2, MnO, and P_2O_5) were determined by X-ray Fluorescence (XRF), after fusion of the samples with lithium tetraborate (SGS analytical code XRF79C). The loss on ignition (LOI) was obtained by calcination at 1000°C (SGS analytical code PHY01E). The concentrations of trace elements (Be, Sc, V, Cr, Co, Cu, Zn, Ga, Ge, As, Rb, Y, Zr, Nb, Mo, Ag, Cd, In, Sb, Cs, Ba, Hf, W, Hg, Pb, Bi, Th, and U) were determined via inductively coupled plasma–mass spectrometry (ICP–MS) and inductively coupled plasma–optical emission spectrometry (ICP–OES) after digestion by aqua regia (SGS analytical code ICM14B). Other elements, such as Ni and rare earth elements (La, Ce, Pr, Nd, Sm, Eu, Gd, Tb, Dy, Ho, Er, Tm, Yb, and Lu), were analyzed via ICP–MS. Other parameters, such as total carbon and sulfur content, were obtained using a LECO Carbon Sulphur Analyzer (SGS analytical code CSA17V).

2.6 DNA extraction, sequencing, and sequence analysis

DNA extraction was carried out from the two microbial cultures utilized and from 12 substrate samples (three from each treatment). For the microbial cultures, a volume of 15 mL was filtered through 0.22 µm sterile filter membranes (Millipore, Merck KGaA, Darmstadt, Germany). Subsequently, these membranes were manually cut into small pieces with a sterile scalpel. Approximately 300 mg of each substrate sample was collected for analysis after the completion of the experiment.

For both the microbial cultures and substrates, DNA extraction was performed using a PowerSoil DNA Isolation Kit (QIAGEN) according to the manufacturer's instructions. DNA samples were

quantified using a Qubit 3.0 fluorometer (Thermo Fisher Scientific, Inc.), and the DNA quality was checked via electrophoresis on a 1% agarose gel.

Bacterial diversity was evaluated by sequencing the V3–V4 region of the 16S rRNA gene using the Illumina MiSeq platform. For this purpose, approximately 5 ng μL^{-1} extracted DNA was subjected to PCR. The gene-specific sequences used targeted the V3–V4 region of the 16S rRNA gene (Klindworth et al., 2013). Illumina adapter overhang nucleotide sequences were added, and this region was amplified using the full-length primer set 16S Forward Primer = 5′ TCGTCGGCAGCGTCAGATGTGTATAAGAGACAGCCTACGGG NGGCWGCAG 3′ and 16S Reverse Primer = 5′ GTCTCGT GGGCTCGGAGATGTGTAAGAGACAGGACTACHVGGGTATCT AATCC 3′. The PCR mixture was combined with ultrapure water to prepare a final volume of 25 µL. The mixture contained 1.25 µL of dNTPs (2 mM), 2.0 µL of $MgCl_2$ (25 mM), 0.5 µL of each primer (10 µM), 1 µL of DNA (5 ng), 1 µL of Platinum™ Taq DNA polymerase (0.1 U) (Invitrogen, Waltham, MA, United States), and 5 µL of 10× Buffer. Amplification was performed in an Applied Biosystems thermocycler with an initial cycle of 3 min at 95°C; 25 cycles of 30 s at 95°C, 30 s at 57°C, and 30 s at 72°C; and a final cycle of 5 min at 72°C. The amplicons were quantified using a Qubit 3.0 fluorometer (Thermo Fisher Scientific, Inc.), and the quality was measured on a 1% agarose gel.

Then, the amplicon libraries for the bacteria were prepared according to the Illumina 16S Metagenomic Sequencing Library Preparation Protocol (Illumina, San Diego, CA, United States). The PCR products were prepared in a final volume of 25 µL. The PCR mixture contained 12.5 µL of 2x Kappa Hifi HotStart Ready Mix (Sigma–Aldrich, St. Louis, MI, United States), 10 µL of Index primer, 2.5 µL of DNA, and 5 µL of PCR water. The PCR cycle for bacteria consisted of an initial denaturation of 3 min at 95°C, followed by 8 cycles of denaturation at 95°C for 30 s, annealing at 57°C for 30 s, extension to 72°C for 30 s, and a final extension to 72°C for 5 min.

The size and quality of the PCR fragments were estimated on an Agilent 2100 Bioanalyzer (Agilent Technologies, Santa Clara, CA, United States) using a DNA 1000 chip. The PCR products were purified with an AMPure XP purification kit (Beckman Coulter, Brea, CA, United States), and the libraries were further processed with a Nextera XT kit (Illumina). The libraries were standardized to a concentration of 4 nM and processed following Illumina 16S Metagenomic Sequencing Library Preparation (Illumina). The 16S rDNA gene libraries were sequenced on the MiSeq-Illumina platform using the MiSeq V3 reagent kit (600 cycles; Illumina) at Instituto Tecnológico Vale – ITV-DS (Belém, PA, Brazil).

Bioinformatic analysis was performed using Quantitative Insights Into Microbial Ecology Software (QIIME) according to the Pipeline for MetaBarcoding Analysis (PIMBA) (Oliveira et al., 2021) for 16S rRNA sequences. The sequences were trimmed and filtered by quality and converted to FASTA using Prinseq v0.20.4. VSEARCH v2.15.2 was used to dereplicate and discard singletons, trim reads, and group reads into operational taxonomic units (OTUs) with 97% similarity and remove chimeras. Taxonomic assignment was performed using the ribosomal RNA database (Quast et al., 2013). After that, the data were filtered in R software, and OTUs that were not categorized as bacteria were removed. For functional characterization of the detected taxa, we applied the Functional Annotation of Prokaryotic Taxa prediction tool (FAPROTAX, version 1.2.4). The FAPROTAX database maps the metabolic functions of bacterial OTUs into putative functional profiles, enabling the ecological interpretation of 16S marker gene data. The analysis was performed using the collapse_table.py script (Louca et al., 2016).

3 Results

3.1 Consolidation and mineralogy of *canga*

The experiments with unconsolidated *canga* resulted in different degrees of response to each applied treatment, as follows. The substrate of treatment W remained unconsolidated, with no evidence of biocementation. Conversely, treatments MO, MI, and MIC led to the formation of cohesive and compact ferruginous samples (Figure 1). The obtained blocks have a detrital aspect containing clasts composed mostly of hematite, followed by iron oxyhydroxide (hematite and goethite) and minor amounts of gibbsite (Table 1).

In microtextural terms, a matrix with fine debris (<1 mm) of iron oxyhydroxide surrounded by an authigenic cement that adheres to other debris of different size proportions was common among the consolidated treatments (Figure 1). Some of these debris exhibited irregular edges indicative of dissolution, filled with iron-aluminous cements.

Hematite clasts with diameters greater than 2 mm are evidenced by dissolution features, preferably along relict banding (Figures 1C,E), and are individualized by cement that indicates the continuity of these particles. Some clasts are even replaced by this recent cement, preserving only the mineral habit. The intraparticle porosities exhibited very regular shapes that resembled those of bacteriomorphs, demonstrating secondary porosity (Figure 1E).

Gibbsite crystals are also frequent along the cavities and at the edges of the cemented debris (Supplementary Figure S3). Occasionally, there are zones of Fe oxyhydroxide intercalated with gibbsite, indicating dissolution and reprecipitation of both minerals during the process.

The mineralogical composition of the MO, MI, and MIC treatments differed quantitatively from that of the W treatment (control) (Table 1). The concentrations of goethite decreased, while those of hematite increased in the MO and MI treatments, unlike in the MIC treatment, in which there was an increase in goethite. The gibbsite also varies, with higher concentrations in the MI and lower concentrations in the MIC. Anatase exhibited almost no changes.

The concentrations of the iron phases detected by Mössbauer spectroscopy (>1%) (Figure 2) varied only between the MO and MI treatments compared to W, with the decrease in goethite being greater in the MO treatment.

The low-temperature Mössbauer spectroscopy data indicate that the samples from all the treatments produced two sextets, corresponding to hematite, and one sextet, corresponding to goethite. However, hyperfine magnetic field values varied according to treatment (Supplementary Table S1).

3.2 Biofilm formation

Scanning electron microscopy (SEM) revealed biofilm formation under the different conditions during which the

10.3389/fmicb.2024.1352792

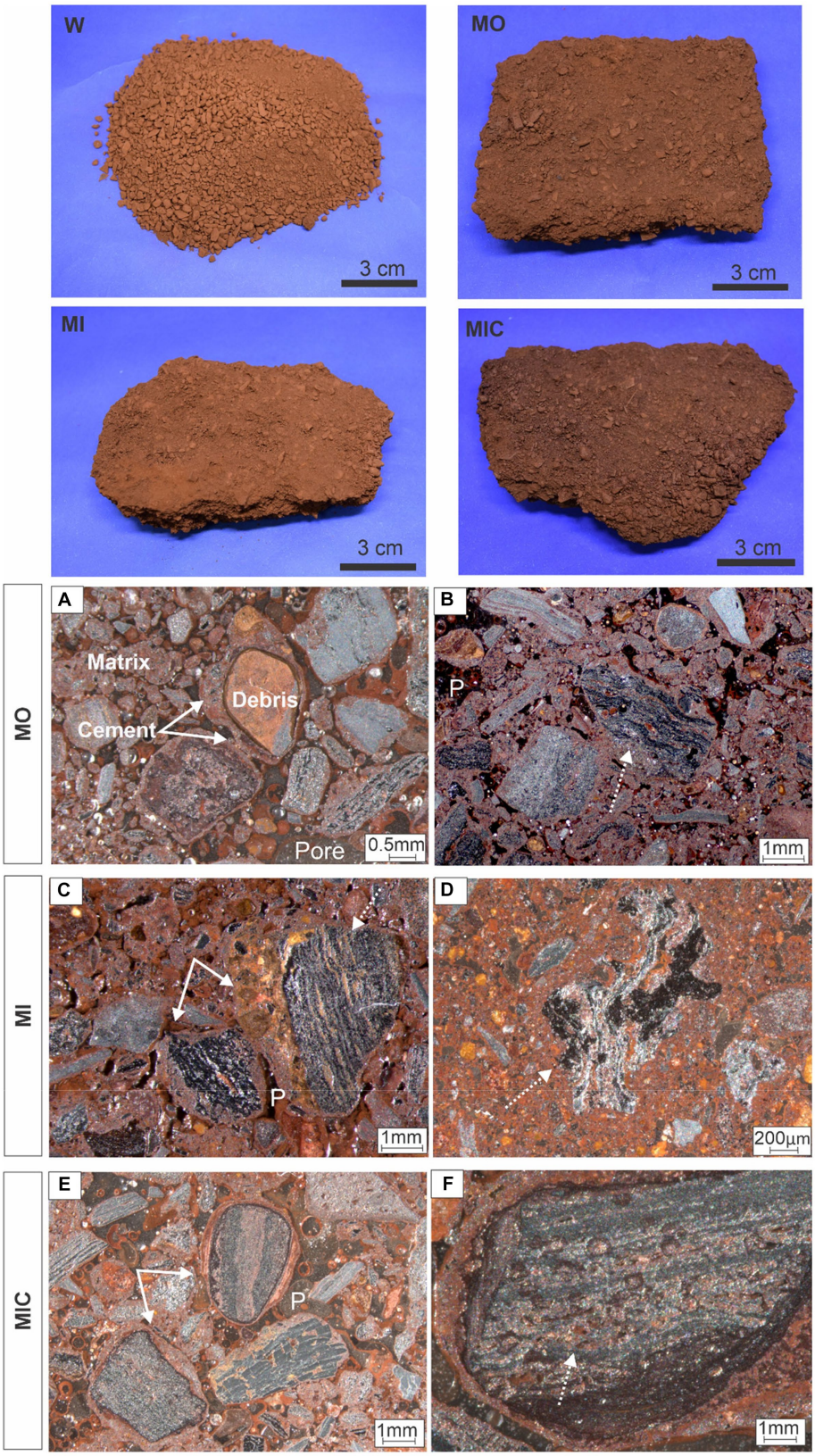

FIGURE 1
Consolidation of *canga* fragments after 6 months of experimentation (upper block) and textural aspects under different biocementation conditions. Hematitic debris (>2 mm) interconnected by the newly formed cemented material **(A)** and with dissolution along the relict structures **(B-D)**. Cement overgrown over hematite debris **(E)**. Secondary porosity of the cellular molds **(F)**.

TABLE 1 Mineral phases quantified by Rietveld refinement for each treatment and their respective Rietveld indices (GOF is the goodness-of-fit, and R_{WP} is the weighted profile parameter) for the treatment: water (W, control), culture medium only (MO), medium + microbial consortium (MI), and medium + microbial consortium + soluble iron (MIC).

Phases	W	MO	MI	MIC
Hematite (%)	64.1	67.8	65.6	63.8
Goethite (%)	32.9	30	30.7	34.2
Gibbsite (%)	2.8	2.1	3.4	1.8
Anatase (%)	0.3	0.1	0.3	0.3
GOF	1.35	1.32	1.30	1.26
R_{WP}	5	4.89	4.84	5

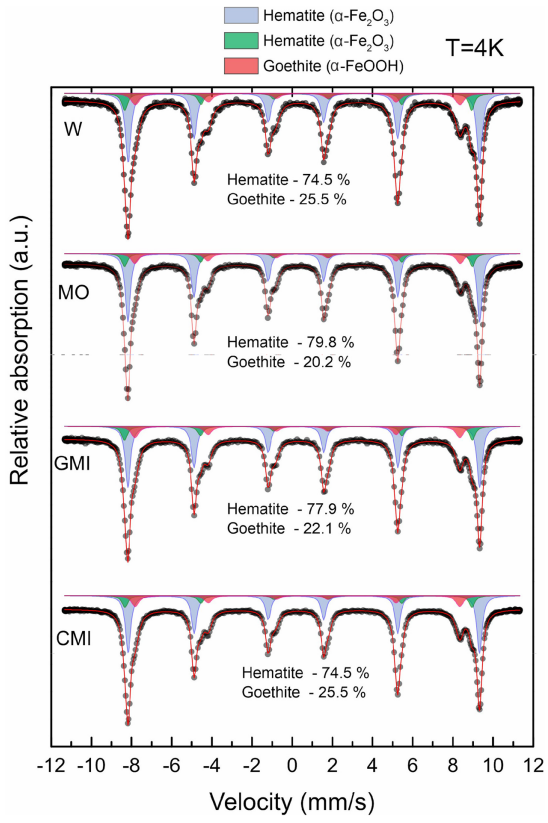

FIGURE 2
Distribution of iron minerals in samples from each treatment, according to Mössbauer spectra at 4 K. W, water (control); MO, culture medium; MI, culture medium + iron reducing microbial consortium; MIC, culture medium + consortium + dissolved iron.

biogeochemical cycle of Fe was stimulated, except for treatment W. Unlike all other treatments, the iron-rich particles in treatment W remained loose, with rough relief (Figures 3A,B). In the MO and MI treatments, sets of well-preserved cells were observed coating the Fe oxyhydroxide particles. Some of these sets of cells appear to be bound to extracellular polymeric substances (EPS), which aid in the attachment of cells to Fe oxyhydroxide surfaces, resulting in smooth relief. The presence of cells is clearer in Figure 3C, where one can see fossilized cells with an average size of 0.8 µm in the form of rods, partially embedded in EPS; and in Figure 3E, with 0.3 µm cell filaments, completely embedded in EPS. EDS revealed the presence of carbon and iron associated with fossilized cells (Figures 3D,F).

Iron-bearing sulfate compounds (with sodium and potassium) were detected by EDS in the biofilms from the MO and MI treatments. The sodium-rich variety exhibited a fibrous set with a radial arrangement (Figures 4A,B). Conversely, the potassium-rich variety occurs as fibrous veins (Figures 4C,D) and small fragments dispersed in the cement.

In the MIC treatment, iron-bearing sulfate compounds were not detected, and Fe-oxyhydroxide precipitates filled part of the cavities associated with biofilm structures, which comprised rods and filament-shaped cells (Figure 3G). In general, after Fe(III) citrate treatment (MIC), the microbial cells in the biofilms were more likely to be bacteriomorphic molds with little cell envelope structure, as shown via the polished section (Figure 3H). On the hematite surface, several pores, left by cellular structures reaching 0.3 µm in diameter, are frequent (Figure 5F), features also visible in the glucose-enriched substrate samples (MO and MI).

In addition to the cellular structures, another aspect observed in all the treatments (except for W) was the formation of meniscus-like structures that interconnected the substrate particles (Figures 5A,C,E), forming microaggregates. At the edge of the particles (cement), the cell envelopes frequently formed nucleation surfaces for the precipitation of iron oxyhydroxides (Figures 5B,D).

3.3 Chemical composition of the substrates

In the substrates of all treatments, Fe_2O_3 was the most abundant oxide (90–90.5%), followed by Al_2O_3 (2.9–3%), TiO_2 (0.3–0.4%), SiO_2 (0.4–0.7%) and P_2O_5 (0.3–0.4%, Supplementary Tables S2 and S3). The concentrations of other oxides were lower than 0.1%, which is the detection limit. Despite this similarity, there was a difference between the control treatment and the other treatments ($p = 0.011$), as highlighted in Figure 6A. The trace element concentrations indicate that the main differences in the concentrations of C, S, Co, Cu, Zn, Mo, Cr, and W occur at ratios between 1 and 3 when these concentrations are normalized as a function of the W treatment (Figure 6B).

3.4 Microbial communities

A total of 681,662 sequences were obtained from the two microbial culture samples, and 393,259 sequences were recorded

10.3389/fmicb.2024.1352792

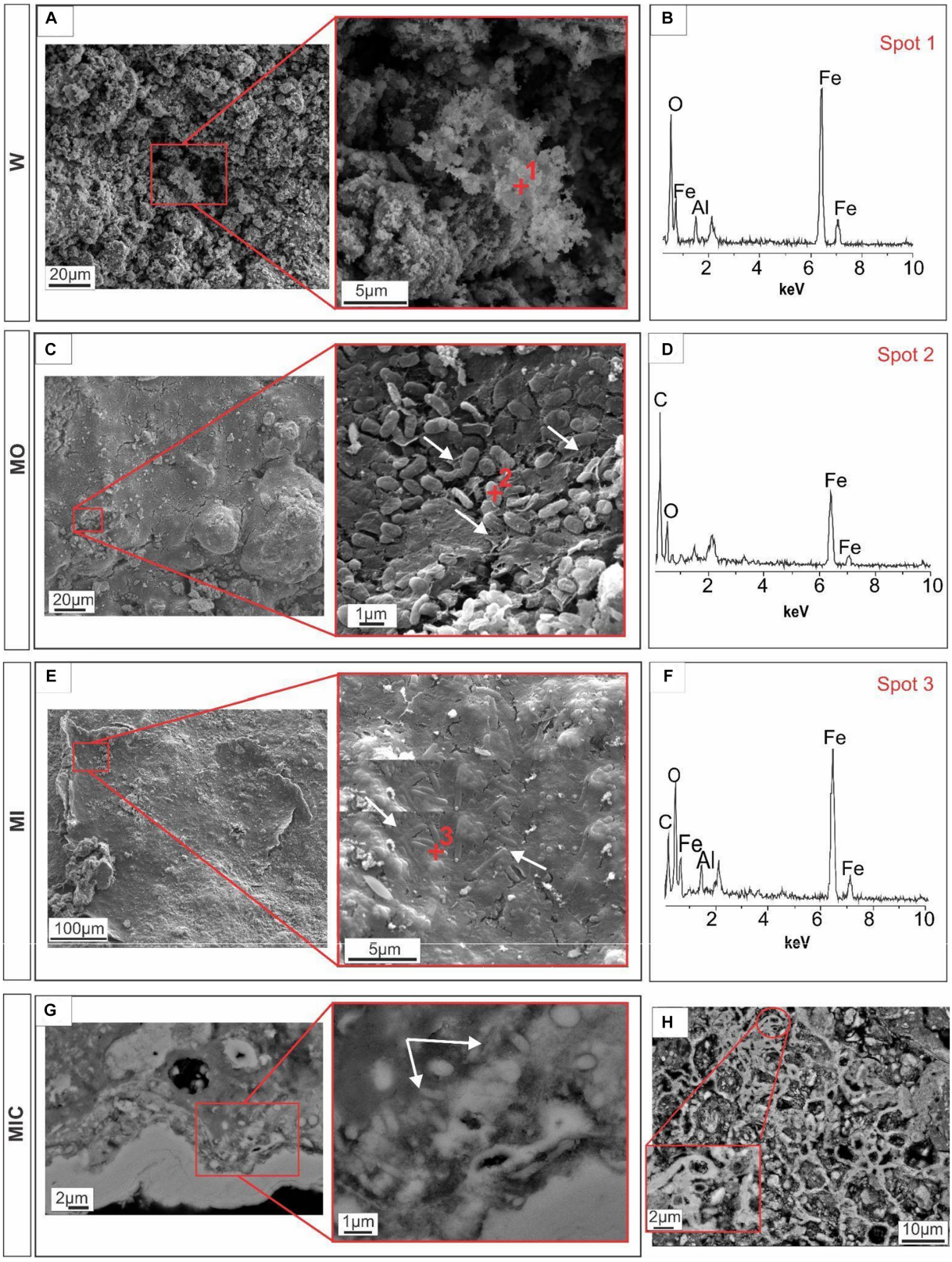

FIGURE 3
Microtexture (SEM) and chemical composition (EDS) of biofilms produced during the experiment. W, control: Control group, displaying iron-rich loose particles **(A,B)**. MO treatment: compact surface of EPS (extracellular polymeric substances) with iron oxyhydroxides, partly embedding rod-shaped cells **(C),** and respective EDS spectrum **(D)**. MI treatment: Filamentous cells embedded in EPS and iron oxyhydroxides **(E)** and the corresponding EDS spectrum **(F)**. MIC treatment: Biofilms in the cavity; details of the cell envelopes are shown (arrows) **(G)**; and biofilms with preserved cellular structures are shown **(H)**.

10.3389/fmicb.2024.1352792

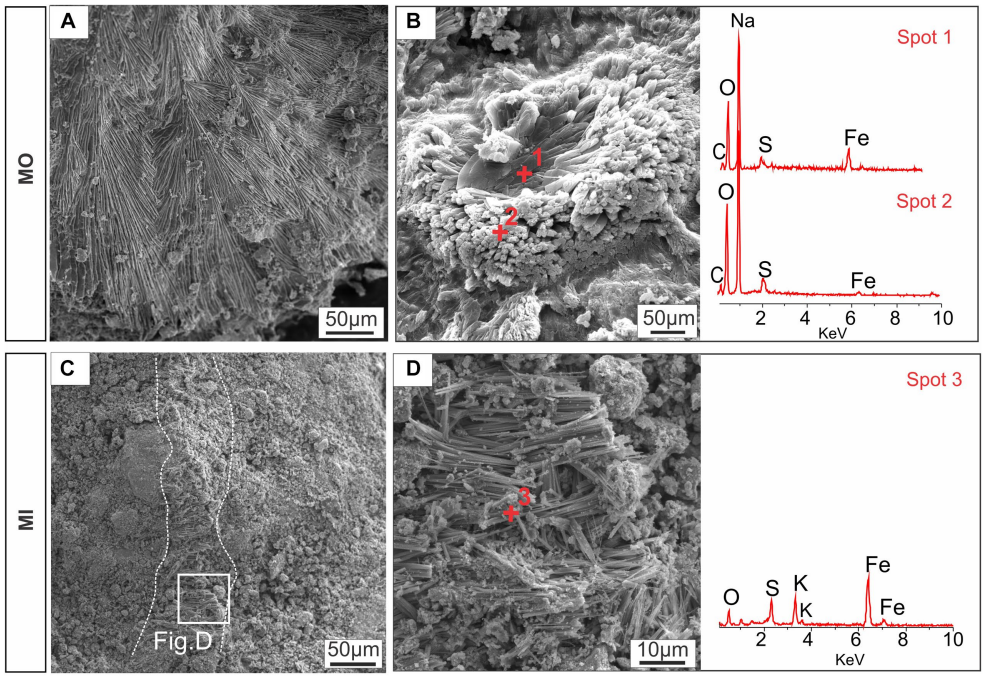

FIGURE 4
Textural aspects of the iron-bearing sulfate compounds detected by SEM–EDS: sodium-iron-bearing sulfate compounds with fibroradial habits **(A)** and nucleation of elongated structures **(B)**; and potassium-iron-bearing sulfate along a vein feature **(C)** and with a fibrous appearance **(D)**. MO, culture medium only; MI, medium + microbial consortium.

from the 12 substrate samples. After quality filtering and removal of sequences not linked to bacteria, we obtained 298 OTUs in the glucose microbial culture (MI) and 316 OTUs in the Fe(III) citrate microbial culture (MIC, Supplementary Table S4). In both microbial cultures, a predominance of OTUs classified into the families Rhizobiaceae, Enterobacteriaceae, and Burkholderiaceae was identified (Figure 7A).

Among the substrates, 240 OTUs were identified in the W treatment, 262 OTUs were identified in the MO treatment, 268 OTUs were identified in the MI treatment, and 187 OTUs were identified in the MIC treatment. The microbial community profiles of the samples collected from the microbial cultures and from the substrates at the end of the experiment were proportionally different. In the microbial culture samples, the Enterobacteriaceae family was predominant, and the family Rhizobiaceae was more abundant in the substrates.

The composition of the microbial communities was influenced by the treatment to which the substrate was subjected (Figure 7A). The treatment that includes only the culture medium comprised the Burkholderiacea family, which was also identified in the W treatment. In addition, the Xanthomonadaceae family was found only in the MO treatment, while the Sporolactobacillaceae family was identified exclusively in the MIC treatment. To a lesser extent, the Enterobacteriaceae, Microbacteriaceae, and Bacillaceae families were identified among the substrates of the MO, MI, and MIC treatments.

The predicted microbial metabolic functional groups based on 16S rDNA sequences indicated differences between microbial cultures and substrates (Figure 7B). In bacteria that grow in microbial cultures, the dominant metabolic pathways are related to anaerobic activity, with most organisms putatively performing activities related to chemotaxis and fermentation and, secondarily, pathways related to the cycling of ammonia, as well as nitrite and nitrate. For substrates, the predicted metabolic pathways of the control treatment (W) were less diverse and based on aerobic chemoheterotrophy, in addition to recycling of nitrogenous excreta (ureolysis) and carbon (methylotrophy). Conversely, in the substrates treated with glucose without a consortium (MO), the native microorganisms presented more evident nitrate reduction activities, in addition to aerobic chemoheterotrophy. In the substrates that received microbial culture (MI and MIC), the metabolic pathways were mainly related to chemoheterotrophy but had lower nitrate reduction activities in relation to MO.

4 Discussion

Within our experiment, various conditions were manipulated to stimulate the biogeochemical cycle of iron, ultimately leading to the formation of biocemented blocks. By supplying micro-and macronutrients, along with carbohydrates, and subjecting the system to repeated cycles of irrigation and subsequent desiccation, we induced alterations in the microbial community and triggered mineralogical and textural changes in *canga* fragments. Notably, nodules surrounded by authigenic cements were observed, with these nodules adhering to debris of varying sizes, likely stemming from the dissolution of iron minerals. The evidence of bacterial dissolution molds on the surface of these minerals further supported this hypothesis. Additionally, the presence of microfossils within the authigenic cements indicated their role in aggregating the enveloped particles, ultimately contributing to the formation of biocemented blocks within the tested systems.

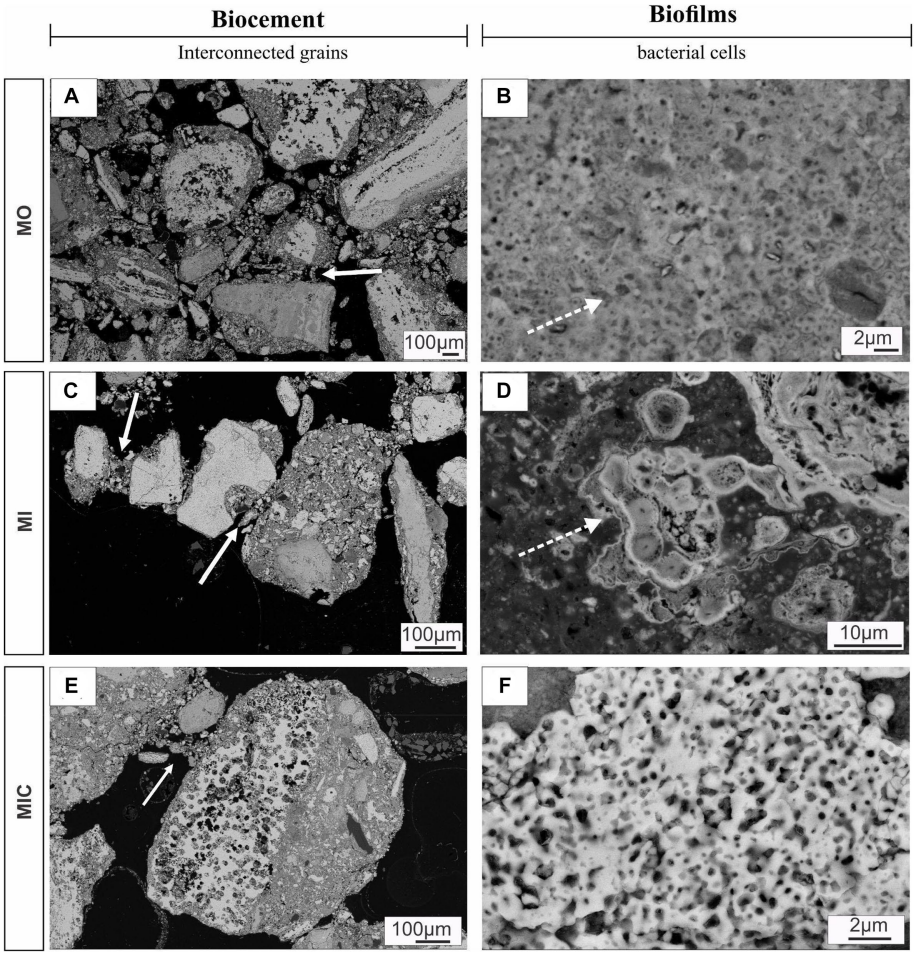

FIGURE 5
SEM images of polished sections displaying biocements and biofilms. Panels **(A,C,E)** show different debris layers interconnected by meniscus-type cements (solid arrows), while **(B,D)** indicate the nucleation of iron oxyhydroxides on the surface of cell envelopes (solid arrows). Panel **(F)** illustrates a set of bacteriomorphs in MIC treatment. Culture medium only (MO), medium + microbial consortium (MI), and medium + microbial consortium + soluble iron (MIC).

4.1 Mineralogical and chemical modifications

Our experiments revealed substantial mineralogical changes within the treated substrates, reflecting the intensification of iron mineral dissolution-precipitation cycles compared to seasonal changes in natural *canga* environments (Monteiro et al., 2014; Levett et al., 2016, 2020b; Spier et al., 2018; Gagen et al., 2019a; Parker et al., 2022). These changes were revealed independently by two distinct methods, Mössbauer spectroscopy and Rietveld refinement. Values differ slightly between methods because Rietveld refinement quantifies all phases in the sample, while Mössbauer spectroscopy only quantifies iron-bearing phases. Additionally, Mössbauer results can be affected by crystal size, which affect the intensity of the hyperfine field, especially in cryptocrystalline materials. Nevertheless, both methods indicate the same tendencies in our analysis. While iron oxide phases differ between treatments, the amount of accessory anatase remained unchanged across all treatments, and gibbsite displayed point changes in all treatments, except for W, due to solubilization by microbial activity amid pH and organic chemistry changes (Levett et al., 2020b).

The manipulation of microbial stimuli and carbon sources significantly influenced the iron cycle, with notable goethite dissolution observed principally in treatments enriched with glucose (MO and MI). These treatments promoted the development of fermentative and anaerobic bacteria that supply hydrogen to the system during the breakdown of glucose and organic byproducts. Hydrogen served as an electron donor for direct iron reduction, facilitating iron mineral dissolution (particularly goethite), as previously demonstrated by Gagen et al. (2019b). Goethite is poorly crystalline and more soluble than more ordered minerals such as hematite and thus has a notably greater dissolution susceptibility (Cornell and Schwertmann, 2003; Bird et al., 2011).

In the MO and MI treatments, the resultant availability of Fe(II), along with its subsequent oxidation to Fe(III), likely precipitated newly formed minerals, including iron sulfates, amid acidic microenvironments promoted by glucose fermentation. The formation of sodium-and potassium-bearing iron sulfates may have been catalyzed by the decomposition of chemical compounds present in the culture medium (Nazari et al., 2014; Cruells and

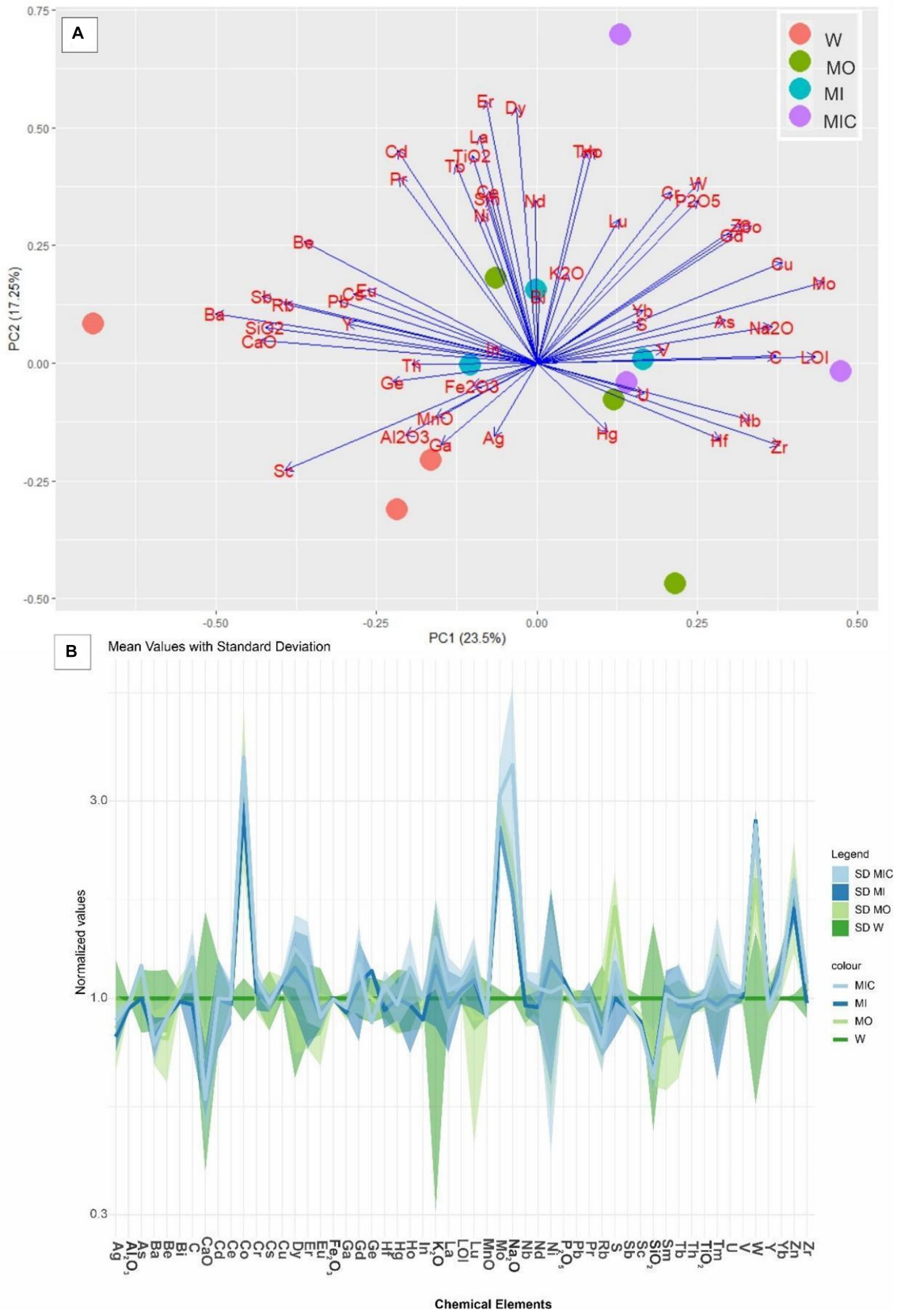

FIGURE 6
(A) Principal component analysis (PCA) of the total chemical composition of the substrates of the different treatments. **(B)** Distribution pattern of the concentrations of the trace elements in the treatment groups normalized to those in the control group. Treatments: Water (W, as a control), culture medium only (MO), medium + microbial consortium (MI), and medium + microbial consortium + soluble iron (MIC).

10.3389/fmicb.2024.1352792

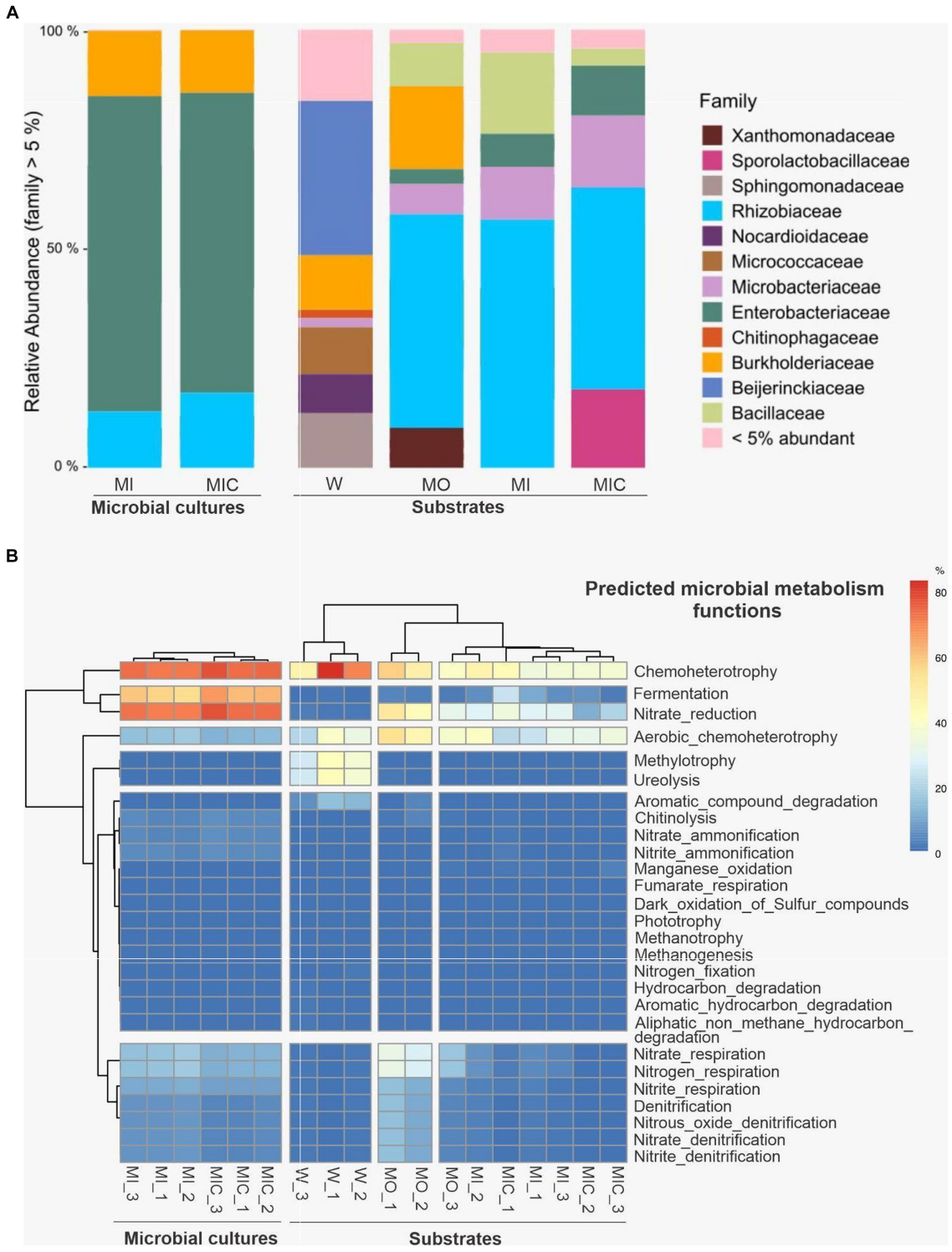

FIGURE 7
Illumina 16S rRNA sequence data were extracted from substrates and microbial cultures; only bacterial data were accessed. **(A)** Average relative abundance of microbial cultures and substrates at the family level. **(B)** Cluster analysis of predicted microbial metabolism functions of microbial cultures and substrates. Treatments: Water (W, as a control), culture medium only (MO), medium + microbial consortium (MI), and medium + microbial consortium + soluble iron (MIC).

Roca, 2022), which is thus the result of biomineralization associated with iron-oxidating/reducing bacteria (Lazaroff, 1997), highlighting the multifaceted role of microbial communities in mineral cycling.

The reduction of Fe(III) from goethite and hematite by microbial cultures in the presence of acetate/Fe(III) citrate (MIC treatment) was lower than that in the glucose treatments (MO and MI). This finding is consistent with that observed by Lentini et al. (2012) and

Castillo-Zacarías et al. (2020), who found that feeding microbes with alternative carbon source had observed low iron reduction compared to feeding them with glicose. Furthermore, the applied concentration of Fe(III) citrate (50 mM) in the MIC treatment may be toxic to studied microorganisms (Chen et al., 2013). Before introducing the microbial culture into the substrate, the bacteria interacted with Fe(III) citrate, resulting in the consumption of Fe(III) and the release of Fe(II). Prolonged exposure of cell surfaces to soluble Fe(II) may have inhibited their activity (e.g., Roden and Urrutia, 2002; Zhang et al., 2020).

The high contents of C, S, Co, Zn, Mo, Cr, W, and Cu in blocks from different treatments indicate that chemical components applied as nutrients were, at least partially, fixed as newly formed minerals or adsorbed by the precipitated iron oxyhydroxides (Weber et al., 2006; Alfadaly et al., 2021; Keim et al., 2021). Moreover, free-floating bacteria can produce siderophores, organic compounds known for their strong affinity for metals that function to chelate bioavailable iron(III) and various other metals from minerals (Gadd, 2004; Lies et al., 2005; Sheng et al., 2023).

4.2 Biocements

Our study revealed that fossilized bacteria acted as nucleation sites for iron oxide minerals in all treatments except control (W). MO and MI treatments resulted in well-preserved cell envelopes, while in MIC treatment, cell-shaped holes (bacteriomorphs) prevale. Differences in cell preservation between treatments may result from varying levels of exposure to aqueous iron through cellular permineralization (Southam and Donald, 1999; Levett et al., 2020a).

These observations were accompanied by the development of biofilms on the surface and between grains, resulting in the formation of meniscus-shaped biocements. Biofilms, as highlighted in investigations of natural crusts, play a crucial role in enhancing permeability and water transport, thereby facilitating biogeochemical iron cycling (Benard et al., 2019; Gagen et al., 2019a; Levett et al., 2020a; Paz et al., 2021). In our biocemented blocks from the MO, MI, and MIC treatments, the presence of biofilms embedded in iron oxide indicated successful microbial colonization of the substrate. This colonization likely occurred due to a combination of factors, including the high surface porosity and availability of nutrients. Furthermore, biofilms contribute to iron oxyhydroxide precipitation through local changes in ionic mobility and nucleation of minerals within EPS (Levett et al., 2020a; Paz et al., 2021; Wu et al., 2023).

4.3 Microorganism communities

In comparing the microbial composition of iron-reducing cultures with post experiment substrate communities, notable shifts in relative abundance were observed. Specifically, the families Burkholderiaceae and Enterobacteriaceae exhibited decreased abundance in substrates receiving microbial cultures, with only Burkholderiaceae persisting in the control (W) and culture medium (MO) conditions, while Rhizobiaceae increased in all treatments except the control (W). This suggests competitive interactions between the introduced microbial cultures and the native substrate communities.

The influence of carbon sources on microbial communities for accelerating the biogeochemical iron cycle in *canga* systems was investigated. The carbon source plays a crucial role in shaping microbial communities and functional groups. Compared to treatment with iron citrate (III) and acetate (MIC), glucose-enriched treatments (MO and MI) resulted in a higher abundance of *Serratia* spp. from the Enterobacteriaceae family. Notably, some strains of *Serratia* isolated from iron-rich environments demonstrate the ability to couple different carbon source oxidations to iron reduction (Castillo-Zacarías et al., 2020), distinguishing them from other more common strains that rely on iron reduction during glucose and lactate fermentation (Lentini et al., 2012). In this study, it was noted that the increased dissolution of iron oxides in the presence of glucose reflects a pattern in the fermentative ability of *Serratia* spp., consistent with another study indicating a preference of this strain for glucose over acetate when faced with insoluble iron oxides (Castillo-Zacarías et al., 2020).

Additional microbial groups may further have indirectly contributed to the solubilization of iron oxides during the decomposition of organic compounds. Within the glucose treatments (MO and MI), fermenters from the Bacillaceae and Burkholderiaceae groups are highlighted (Valverde et al., 2006; Parker et al., 2018; da Silva et al., 2022). Conversely, in the treatment with Fe(III) citrate/acetate, the Sporolactobacillaceae family is prominent, known for its capacity to produce lactic acid (Chang and Stackebrandt, 2014). This emphasizes that microbial behavior is influenced by the available type of carbon source.

The biocementation of iron-rich fragments involves other bacterial taxa and functional groups. Specifically, this study identified certain groups, such as *Acidovorax* and *Enterobacter*, that have already been recorded as capable of nitrate-reducing activity coupled with Fe(II) oxidation (Carlson et al., 2013; Li et al., 2022). Furthermore, aerobic microorganisms such as Xanthomonadaceae may obtain energy from the reduction of oxygen, coupled with the oxidation of Fe(II) (Neubauer et al., 2002; Grettenberger et al., 2017). The predominant reaction observed in this context was the reduction of nitrates, particularly evident in substrates containing glucose (MO and MI).

These findings highlight the complexity of microbial interactions and metabolic pathways involved in biocementation processes. Understanding the optimization of the biogeochemical iron cycle and its application on larger scales, such as in post mining landscapes, requires further research. Identifying oxidation/reduction cycles is crucial for understanding biocementation processes and evaluating sustainable carbon sources for field applications. Advancements in these areas will enhance our understanding of the mechanisms involved, facilitating the replication and acceleration of the cementing process.

5 Conclusion

Our study demonstrated that accelerating the biogeochemical iron cycle is a promising strategy for restoring ferruginous crusts (*canga*). In summary, microorganism feeding and the creation of repeated cycles of anaerobic and aerobic conditions (to stimulate iron reduction and precipitation) are the most important factors triggering the formation of biocemented blocks, accompanied by high rates of textural and mineralogical changes. Although further research and development are required to scale up biocementation in field applications, our study underscores its potential in consolidating iron-rich substrates, highlighting its significance for the restoration of *canga* ecosystems in postmining scenarios.

Data availability statement

The original contributions presented in the study are included in the article/Supplementary material, further inquiries can be directed to the corresponding author.

Ethics statement

The manuscript presents research on animals that do not require ethical approval for their study.

Author contributions

RS: Conceptualization, Data curation, Formal analysis, Investigation, Writing – original draft, Writing – review & editing. AC: Data curation, Formal analysis, Investigation, Writing – review & editing. RA: Writing – review & editing. JB: Conceptualization, Formal analysis, Writing – review & editing. JM: Formal analysis, Writing – review & editing. AL: Writing – review & editing. IP: Data curation, Writing – review & editing, Formal analysis. DC: Data curation, Writing – review & editing. MG: Writing – review & editing, Conceptualization, Data curation, Formal analysis, Funding acquisition, Investigation, Project administration, Validation.

Funding

The authors declare that financial support was received for the research, authorship, and publication of this article. This study was supported by Vale SA and the Vale Institute of Technology. MG holds a CNPq productivity scholarship (310865/2022–0).

Acknowledgments

Authors are grateful for logistic support and analysis by the SENAI Institute of Innovations in Mineral Technologies and the Microanalysis Laboratory of the Geosciences Institute of the Federal University of Pará. The authors appreciate the valuable contributions of two Frontiers's reviewers and the editors.

Conflict of interest

The authors declare that the research was conducted in the absence of any commercial or financial relationships that could be construed as a potential conflict of interest.

The author(s) declared that they were an editorial board member of Frontiers, at the time of submission. This had no impact on the peer review process and the final decision.

Publisher's note

All claims expressed in this article are solely those of the authors and do not necessarily represent those of their affiliated organizations, or those of the publisher, the editors and the reviewers. Any product that may be evaluated in this article, or claim that may be made by its manufacturer, is not guaranteed or endorsed by the publisher.

Supplementary material

The Supplementary material for this article can be found online at: https://www.frontiersin.org/articles/10.3389/fmicb.2024.1352792/full#supplementary-material

References

Alfadaly, R. A., Elsayed, A., Hassan, R. Y. A., Noureldeen, A., Darwish, H., and Gebreil, A. S. (2021). Microbial sensing and removal of heavy metals: bioelectrochemical detection and removal of chromium(VI) and cadmium(II). *Molecules* 26:2549. doi: 10.3390/molecules26092549

Benard, P., Zarebanadkouki, M., Brax, M., Kaltenbach, R., Jerjen, I., Stampanoni, M., et al. (2019). *Microhydrological niches in soils: how mucilage and EPS Alter the biophysical properties of the rhizosphere and other biological hotspots*, vol. *18*, 1–10 doi: 10.2136/vzj2018.12.0211

Bird, L. J., Bonnefoy, V., and Newman, D. K. (2011). Bioenergetic challenges of microbial iron metabolisms. *Trends Microbiol.* 19, 330–340. doi: 10.1016/j.tim.2011.05.001

Cardoso, A. F., da Silva, R. S. S., Prado, I. G. O., Bitencourt, J. A. P., and Gastauer, M. (2023). Acquiring Iron-reducing enrichment cultures: environments. *Meth. Quality Assess. Microorg.* 11:448. doi: 10.3390/microorganisms11020448

Carlson, H. K., Clark, I. C., Blazewicz, S. J., Iavarone, A. T., and Coates, J. D. (2013). Fe(II) oxidation is an innate capability of nitrate-reducing Bacteria that involves abiotic and biotic reactions. *J. Bacteriol.* 195, 3260–3268. doi: 10.1128/JB.00058-13

Castillo-Zacarías, C., Cantú-Cárdenas, M. E., López-Chuken, U. J., Parra-Saldívar, R., Garza-Gonzalez, M. T., de Jesús Rostro-Alanis, M., et al. (2020). Dissimilatory reduction of Fe(III) by a novel *Serratia marcescens* strain with special insight into the influence of prodigiosin. *Int. Microbiol.* 23, 201–214. doi: 10.1007/s10123-019-00088-y

Chang, Y.-H., and Stackebrandt, E. (2014). "The Family Sporolactobacillaceae," in *The Prokaryotes*. Eds. Rosenberg, E., DeLong, E.F., Lory, S., Stackebrandt, E., Thompson, F. (Springer, Berlin, Heidelberg).

Chen, Q., Li, J., Wu, Y., Shen, F., and Yao, M. (2013). Biological responses of gram-positive and gram-negative bacteria to nZVI (Fe^0), Fe^{2+} and Fe^{3+}. *RSC Adv.* 3:13835. doi: 10.1039/c3ra40570b

Cornell, R., and Schwertmann, U. (2003). *The Iron oxides (2nd ed.)*. Structure, Properties, Reactions, Occurrences, and Uses (Wiley: Weinheim, Germany).

Cruells, M., and Roca, A. (2022). Jarosites: formation, structure. *React. Environ. Metals* 12:802. doi: 10.3390/met12050802

da Silva, L. M., Giese, E. C., de Medeiros, G. A., Fernandes, M. T., and de Castro, J. A. (2022). Evaluation of the use of *Burkholderia caribensis* Bacteria for the reduction of phosphorus content in Iron ore particles. *Mater. Res.* 25:e20210427. doi: 10.1590/1980-5373-MR-2021-0427

Dong, H., Zeng, Q., Sheng, Y., Chen, C., Yu, G., and Kappler, A. (2023). Coupled iron cycling and organic matter transformation across redox interfaces. *Nat. Rev. Earth Environ.* 4, 659–673. doi: 10.1038/s43017-023-00470-5

Dorr, J. V. N. (1964). Supergene iron ores of Minas Gerais, Brazil. *Econ. Geol.* 59, 1203–1240. doi: 10.2113/gsecongeo.59.7.1203

Freyssinet, P. H., Butt, C. R. M., Morris, R. C., and Piantone, P. (2005). "Ore-forming processes related to lateritic weathering" in *One Hundredth Anniversary Volume*. 681–722. doi: 10.5382/AV100.21

Gadd, G. M. (2004). Microbial influence on metal mobility and application for bioremediation. *Geoderma* 122, 109–119. doi: 10.1016/j.geoderma.2004.01.002

Gagen, E. J., Levett, A., Paz, A., Bostelmann, H., Borges, R., Augusto, J., et al. (2020). Accelerating microbial iron cycling promotes recementation of surface crusts in iron ore regions. *Microb. Biotechnol.* 13, 1960–1971. doi: 10.1111/1751-7915.13646

Gagen, E. J., Levett, A., Paz, A., Gastauer, M., Caldeira, C. F., Valadares, R. B. S., et al. (2019a). Biogeochemical processes in canga ecosystems: armoring of iron ore against erosion and importance in iron duricrust restoration in Brazil. *Ore Geol. Rev.* 107, 573–586. doi: 10.1016/j.oregeorev.2019.03.013

Gagen, E. J., Zaugg, J., Tyson, G. W., and Southam, G. (2019b). Goethite reduction by a neutrophilic member of the Alphaproteobacterial genus Telmatospirillum. *Front. Microbiol.* 10:2938. doi: 10.3389/fmicb.2019.02938

Gastauer, M., Souza Filho, P. W. M., Ramos, S. J., Caldeira, C. F., Silva, J. R., Siqueira, J. O., et al. (2019). Mine land rehabilitation in Brazil: Goals and techniques in the context of legal requirements. *Ambio* 48, 74–88. doi: 10.1007/s13280-018-1053-8

Gibson, N., Yates, C. J., and Dillon, R. (2010). Plant communities of the ironstone ranges of South Western Australia: hotspots for plant diversity and mineral deposits. *Biodivers. Conserv.* 19, 3951–3962. doi: 10.1007/s10531-010-9939-1

Giulietti, A. M., Giannini, T. C., Mota, N. F. O., Watanabe, M. T. C., Viana, P. L., Pastore, M., et al. (2019). Edaphic endemism in the Amazon: vascular plants of the canga of Carajás. *Brazil. Bot. Rev.* 85, 357–383. doi: 10.1007/s12229-019-09214-x

Grettenberger, C. L., Pearce, A. R., Bibby, K., Jones, D. B., Burgos, W. D., and Macalady, J. L. (2017). Efficient low-pH Iron removal by a microbial Iron oxide mound ecosystem at scalp level run. *Appl. Environ. Microbiol.* 83:e00015–17. doi: 10.1128/aem.00015-17

Hagemann, S. G., Angerer, T., Duuring, P., Rosière, C. A., Figueiredo e Silva, R. C., Lobato, L., et al. (2016). BIF-hosted iron mineral system: a review. *Ore Geol. Rev.* 76, 317–359. doi: 10.1016/j.oregeorev.2015.11.004

Jacobi, C. M., and do Carmo, F. F. (2011). Life-forms, pollination and seed dispersal syndromes in plant communities on ironstone outcrops, SE Brazil. *Acta Bot. Brasil.* 25, 395–412. doi: 10.1590/s0102-33062011000200016

Kappler, A., Bryce, C., Mansor, M., Lueder, U., Byrne, J. M., and Swanner, E. D. (2021). An evolving view on biogeochemical cycling of iron. *Nat. Rev. Microbiol.* 19, 360–374. doi: 10.1038/s41579-020-00502-7

Keim, C. N., Serna, J. D. P., Acosta-Avalos, D., Neumann, R., Silva, A. S., Jurelevicius, D. A., et al. (2021). Dissimilatory Iron-reducing microorganisms are present and active in the sediments of the Doce River and tributaries impacted by Iron mine tailings from the collapsed Fundão dam (Mariana, MG, Brazil). *Fortschr. Mineral.* 11:244. doi: 10.3390/min11030244

Klindworth, A., Pruesse, E., Schweer, T., Peplies, J., Quast, C., Horn, M., et al. (2013). Evaluation of general 16S ribosomal RNA gene PCR primers for classical and next-generation sequencing-based diversity studies. *Nucleic Acids Res.* 41:e1. doi: 10.1093/nar/gks808

Lazaroff, N. (1997). Mineral leaching, iron precipitation, and the sulfate requirement for chemolithotrophic iron oxidation. *Stud. Environ. Sci.* 66, 61–75. doi: 10.1016/s0166-1116(97)80035-0

Lentini, C. J., Wankel, S. D., and Hansel, C. M. (2012). Enriched Iron(III)-reducing bacterial communities are shaped by carbon substrates and Iron oxide mineralogy. *Front. Microbiol.* 3:404. doi: 10.3389/fmicb.2012.00404

Levett, A., Gagen, E. J., Shuster, J., Rintoul, L., Tobin, M. J., Vongsvivut, J., et al. (2016). Evidence of biogeochemical processes in iron duricrust formation. *J. S. Am. Earth Sci.* 71, 131–142. doi: 10.1016/j.jsames.2016.06.016

Levett, A., Gagen, E. J., Zhao, Y., Vasconcelos, P. M., and Southam, G. (2020a). Biocement stabilization of an experimental-scale artificial slope and the reformation of iron-rich crusts. *Proc. Natl. Acad. Sci.* 117, 18347–18354. doi: 10.1073/pnas.2001740117

Levett, A., Vasconcelos, P. M., Gagen, E. J., Rintoul, L., Spier, C., Guagliardo, P., et al. (2020b). Microbial weathering signatures in lateritic ferruginous duricrusts. *Earth Planet. Sci. Lett.* 538:116209. doi: 10.1016/j.epsl.2020.116209

Lies, D. P., Hernandez, M. E., Kappler, A., Mielke, R. E., Gralnick, J. A., and Newman, D. K. (2005). *Shewanella oneidensis* MR-1 uses overlapping pathways for Iron reduction at a distance and by direct contact under conditions relevant for biofilms. *Appl. Environ. Microbiol.* 71, 4414–4426. doi: 10.1128/aem.71.8.4414-4426.2005

Li, M.-J., Wei, M.-Y., Fan, X.-T., and Zhou, G.-W. (2022). Underestimation about the contribution of nitrate reducers to Iron cycling indicated by Enterobacter strain. *Molecules* 27:5581. doi: 10.3390/molecules27175581

Louca, S., Parfrey, L. W., and Doebeli, M. (2016). Decoupling function and taxonomy in the global ocean microbiome. *Science* 353, 1272–1277. doi: 10.1126/science.aaf4507

Lovley, D. R. (1991). Dissimilatory Fe(III) and Mn(IV) reduction. *Microbiol. Rev.* 55, 259–287. doi: 10.1128/mr.55.2.259-287.1991

Lovley, D. R., and Phillips, E. J. P. (1986). Organic matter mineralization with reduction of ferric Iron in anaerobic sediments. *Appl. Environ. Microbiol.* 51, 683–689. doi: 10.1128/aem.51.4.683-689.1986

Monteiro, H. S., Vasconcelos, P. M., Farley, K. A., Spier, C. A., and Mello, C. L. (2014). (U–Th)/he geochronology of goethite and the origin and evolution of Cangas. *Geochim. Cosmochim. Acta* 131, 267–289. doi: 10.1016/j.gca.2014.01.036

Monteiro, H. S., Vasconcelos, P. M. P., Farley, K. A., and Lopes, C. A. M. (2018). Age and evolution of diachronous erosion surfaces in the Amazon: combining (U-Th)/he and cosmogenic 3He records. *Geochim. Cosmochim. Acta* 229, 162–183. doi: 10.1016/j.gca.2018.02.045

Nazari, B., Jorjani, E., Hani, H., Manafi, Z., and Riahi, A. (2014). Formation of jarosite and its effect on important ions for *Acidithiobacillus ferrooxidans* bacteria. *Trans. Nonferrous Metals Soc. China* 24, 1152–1160. doi: 10.1016/s1003-6326(14)63174-5

Neubauer, S. C., Emerson, D., and Megonigal, J. P. (2002). Life at the energetic edge: kinetics of circumneutral iron oxidation by lithotrophic iron-oxidizing bacteria isolated from the wetland-plant rhizosphere. *Appl. Environ. Microbiol.* 68, 3988–3995. doi: 10.1128/aem.68.8.3988-3995.2002

Parker, C. W., Auler, A. S., Barton, M. D., Sasowsky, I. D., Senko, J. M., and Barton, H. A. (2018). Fe(III) reducing microorganisms from Iron ore caves demonstrate fermentative Fe(III) reduction and promote cave formation. *Geomicrobiol J.* 35, 311–322. doi: 10.1080/01490451.2017.1368741

Parker, C. W., Senko, J. M., Auler, A. S., Sasowsky, I. D., Schulz, F., Woyke, T., et al. (2022). Enhanced terrestrial Fe(II) mobilization identified through a novel mechanism of microbially driven cave formation in Fe(III)-rich rocks. *Sci. Rep.* 12:17062. doi: 10.1038/s41598-022-21365-3

Paz, A., Gagen, E. J., Levett, A., and Southam, G. (2021). Ferrugination of biocrusts grown on crushed ferricrete: potential for slope stabilization. *Ore Geol. Rev.* 135:104239. doi: 10.1016/j.oregeorev.2021.104239

Quast, C., Pruesse, E., Yilmaz, P., Gerken, J., Schweer, T., Yarza, P., et al. (2013). The SILVA ribosomal RNA gene database project: improved data processing and web-based tools. *Nucleic Acids Res. (Database issue)* D590–6. doi: 10.1093/nar/gks1219

Roden, E. E., and Urrutia, M. M. (2002). Influence of biogenic Fe(II) on bacterial crystalline Fe(III) oxide reduction. *Geomicrobiol J.* 19, 209–251. doi: 10.1080/01490450252864280

Sheng, Y., Baars, O., Guo, D., Whitham, J., Srivastava, S., and Dong, H. (2023). Mineral-bound trace metals as cofactors for anaerobic biological nitrogen fixation. *Environ. Sci. Technol.* 57, 7206–7216. doi: 10.1021/acs.est.3c01371

Shuster, D. L., Farley, K. A., Vasconcelos, P. M., Balco, G., Monteiro, H. S., Waltenberg, K., et al. (2012). Cosmogenic 3He in hematite and goethite from the Brazilian "canga" duricrust demonstrates the extreme stability of these surfaces. *Earth Planet. Sci. Lett.* 329-330, 41–50. doi: 10.1016/j.epsl.2012.02.017

Oliveira, R. R. M., Silva, R., Nunes, G. L., and Oliveira, G. (2021).PIMBA: A PIpeline for MetaBarcoding Analysis. in Advances in Bioinformatics and Computational Biology. BSB 2021. *Lecture Notes in Computer Science*, Eds. P. F. Stadler, M. E. M. T. Walter, M. Hernandez-Rosales and M. M. Brigido. 13063. (Springer, Cham).

Southam, G., and Donald, R. (1999). Structural comparison of bacterial microfossils vs. 'nanobacteria' and nanofossils. *Earth Sci. Rev.* 48, 251–264. doi: 10.1016/S0012-8252(99)00057-4

Spier, C. A., Levett, A., and Rosière, C. A. (2018). Geochemistry of canga (ferricrete) and evolution of the weathering profile developed on itabirite and iron ore in the Quadrilátero Ferrífero. *Minas Gerais Brazil. Mineral. Deposit.* 54, 983–1010. doi: 10.1007/s00126-018-0856-7

Valverde, A., Delvasto, P., Peix, A., Velázquez, E., Santa-Regina, I., Ballester, A., et al. (2006). *Burkholderia ferrariae* sp. nov., isolated from an iron ore in Brazil. *Int. J. Syst. Evol. Microbiol.* 56, 2421–2425. doi: 10.1099/ijs.0.64498-0

Weber, K. A., Achenbach, L. A., and Coates, J. D. (2006). Microorganisms pumping iron: anaerobic microbial iron oxidation and reduction. *Nat. Rev. Microbiol.* 4, 752–764. doi: 10.1038/nrmicro1490

Wu, C., Chen, Y., Qian, Z., Chen, H., Li, W., Li, Q., et al. (2023). The effect of extracellular polymeric substances (EPS) of iron-oxidizing bacteria (Ochrobactrum EEELCW01) on mineral transformation and arsenic (as) fate. *J. Environ. Sci.* 130, 187–196. doi: 10.1016/j.jes.2022.10.004

Zammit, C. M., Shuster, J. P., Gagen, E. J., and Southam, G. (2015). The geomicrobiology of supergene metal deposits. *Elements* 11, 337–342. doi: 10.2113/gselements.11.5.337

Zhang, X., Zhang, H., Wang, C., Chen, Q., Zhao, Y., Zhou, Q., et al. (2020). Isolation of two iron-reducing facultative anaerobic electricity generation methods and probing of their application performance in eutrophication water. *Ann. Microbiol.* 70:21. doi: 10.1186/s13213-020-01568-7

Frontiers in Microbiology

Explores the habitable world and the potential of microbial life

The largest and most cited microbiology journal which advances our understanding of the role microbes play in addressing global challenges such as healthcare, food security, and climate change.

Discover the latest Research Topics

See more →

Frontiers

Avenue du Tribunal-Fédéral 34
1005 Lausanne, Switzerland
frontiersin.org

Contact us

+41 (0)21 510 17 00
frontiersin.org/about/contact